

Chapter 1

Introduction

The Need for Novel Antibiotics

The 1960s saw the discovery of many firsts among current classes of antibiotics to fight pathogenic infections, such as the quinolones, cephalosporins, and nitroimidazoles, to name a few. However, resistance has been documented in the target microorganisms for most classes of antibiotics, and the number of new classes has been steadily waning. At present, most new therapies are based on modification of known drugs, but this approach generally suffers the same fate as the parent molecule when subject to microbial evolution under selective pressure. This is primarily due to random mutation in amino acid sequence that changes the binding pocket on the protein where the drug otherwise docks. The proliferation of antibiotic resistance in microorganisms is exacerbated by horizontal transfer of resistance genes [1] between species [2], and across genera [3, 4]. Some of the microbes that are of top concern for multi-drug resistance are *E. faecium*, *S. aureus*, *K. pneumoniae*, *A. baumanii*, *P. aeruginosa*, and *Enterobacter* species [5].

What are AMPs?

Gramicidin, an AMP, was among the first antibiotics in commercial use. Recently there

has been a renewed interest in this large and diverse class of antibiotics as apparent by the frequent report of novel AMPs (AMP databank: URL: (<http://aps.unmc.edu/AP/main.php>)). AMPs are sequences of amino acids endogenous to mammals, birds, reptiles, amphibians, fish, insects, plants, and bacteria [6]. They are often derived from the innate immune system of an organism, or from toxins in venom. They are relatively short (less than 120 amino acids), and often cationic [7]. Most AMPs adopt some secondary and higher order structural motifs that segregate hydrophobic and hydrophilic side-chains to create highly amphipathic [8] structures.

Why look to AMPs?

AMPs are thought to be more difficult for microbes to evolve against, due to their inherent ability to permeabilize cell membranes. The efficacy of AMPs often spans multiple species of bacteria, or fungi, or viruses [7]. Their anionic character confers selectivity towards bacteria due to the presence of anionic phosphatidylglycerol (PG) lipids not found in eukaryotic cell membranes.

Debates Over Mechanism of Action

The mechanism by which AMPs kill bacteria is highly debated. There are two prevailing theories that are not mutually exclusive. AMPs have been shown to disrupt the structure, and modify the properties of lipid bilayers. Recently, however, AMPs have also been shown to function additionally as traditional antibiotics, by entering the cytosol and interacting with cellular components, including DNA [9].

The membrane based model of action is attractive as it would partially explain AMPs' broad spectrum activity. AMPs may disrupt the membrane in numerous ways including pore formation [10, 11], perturbation of lipid packing [12], bilayer thinning [13], lipid phase separation [14], generation of curvature strain [15], as well as micellization [16]. AMP activity

is generally described as pore formation, or by the carpet model in which peptides act like detergents [17], or with the interfacial activity model [12] (perturbation of lipid packing).

A Versatile Candidate

In general, high AMP concentrations are required to kill bacteria via membrane disruption [18]. Naturally occurring AMPs therefore serve largely as templates for design of synthetic AMPs [16]. In the absence of complete knowledge of the relationship between peptide sequence, structure, and function, design methodology has proceeded more significantly via combinatorial approaches [19, 20, 21, 22, 23] than via the rational design approach [24]. These primarily involve supplanting residues with similar or dissimilar residues.

An AMP's candidacy as a prototype antibiotic is first evaluated based on its cell specificity in a given environmental setting [16]. Second, it is evaluated based on its ability to induce various perturbations to the target membrane [16]. Lastly, an AMP is evaluated based on whether adjustments can be made to increase potency [16].

The lytic peptide melittin (GIGAVL-KVLTTGLPALISWI-KRKRQQ-amide), a 26 residue peptide constituent of bee venom [25] has emerged as a versatile candidate in the design of membrane targeting antibiotics. Historically melittin has served as an important biological peptide of reference. Melittin has been compared to intramembrane domains of glycophorin, phage coat protein, cytochrome b_5 [26], and cytochrome oxidase [27]. Voltage-dependent pore formation by melittin has made it a model for voltage-gated ion channels [28, 29]. Melittin is similar in many regards to known AMPs including magainin [30], and cecropin [31]. More recently, melittin has been called a prototype for anti-microbial peptides [32]. Melittin is able to completely lyse vesicles [33] and cells [34, 35] at micromolar concentration [18, 36], and has a greater affinity for vesicles that contain anionic lipids, particularly those with the PG head-group, than for neutral membranes [37]. Selectivity towards bacteria over mammalian cells can be achieved with as few as one amino acid substitution [21]. In addition,

there exist multiple routes to increasing its efficacy [20, 22, 23].

Studies to investigate details of the overall mechanism involving model membranes, generally in the form of vesicles, reveal melittin's activity is highly contextual [38]. Melittin is more active in pure phosphatidylglycerol (PG) membranes than in pure zwitterionic phosphatidylcholine (PC) membranes [20]. In membranes with purely anionic headgroups melittin behaves more like a detergent [39]. In zwitterionic and membranes of mixed composition melittin induces formation of transient [40] pores [41]. Anionic headgroups in mixed membranes and cholesterol have an inhibitory effect [20]. AFM experiments on the supported 1-palmitoyl-2-oleoyl-glycero-3-phosphocholine (POPC) bilayer show melittin is unable to remodel the membrane [42]. Naito et *al.* show the mechanism's temperature dependence in 1,2-dimyristoyl-sn-glycero-3-phosphocholine (DMPC) GUVs by differential interference contrast microscopy; DMPC GUV fusion occurs at 298.15K; pores are generated at 288.15K, and micellization takes place at 283.15K [43].

Krauson et *al.* define equilibrium pores as those from which leakage remains detectable for one hour [20]. Melittin forms equilibrium pores above peptide to lipid ratio of one to 200 ($P/L=1:200$) in POPC large unilamellar vesicles (LUVs) with the majority of peptides adsorbed on the membrane surface, and has very low activity at $P/L=1:2000$ [20]. Melittin pores have a wide distribution in size [41], and increase in size with concentration [41, 44]. Dextran leakage in POPC LUVs estimates the mean inner pore diameter as 25–30 Å at $P/L=1:50$, with 10–15 monomers [41] lining the pore assuming a barrel-stave pore structure [45]. Multilamellar POPC at $P/L \geq 1/30$ show pore size is independent of concentration with inner diameter of 4.4 nm [46]. The standard melittin pore model is four to seven monomers stabilize a toroidal pore in which membrane phosphates participate in lining the transmembrane pore to shield the lipid tails, similar to magainin [46, 47].

Discerning the structure of the pore by neutron scattering suffers from low contrast between the peptides and water and the lipid membrane [46]. It is necessary to study

zwitterionic membranes in the relevant phase as this influences the peptide topology [48]. The electron density cannot be determined for the fluid membrane by X-ray diffraction due to the phase problem [49]. Anomalous diffraction of bromine tethered lipids [50] can only infer whether the structure of the pore is barrel-stave or toroidal based on the extent that lipid headgroups are drawn into the pore [32]. In general it is difficult to get data from solid state NMR experiments because the active part of the system constitutes a small fraction of the peptides [51]. Debate remains over whether pores are fundamentally transient [52] or if they are dynamic equilibrium pores [18].

Controversy over melittin's mechanism of pore formation stems from an inability to establish the leakage mode in ensemble leakage kinetics experiments [53]. Using single GUVs held at constant tension Lee *et al.* show a threshold peptide to lipid ratio (P/L^*) is required to achieve a minimum area expansion before leakage occurs [54]. Membrane expansion correlates well with concomitant membrane thinning preceding the onset of stable pores and an increasing fraction of peptides accessing a transmembrane orientation [32]. According to the two state model no aggregation steps between the peptides are required to explain these observations [55]. In contrast, using GUVs held at zero tension [56] Kokot *et al.* divide melittin activity into four concentration regimes [33] in which melittin dimerization on the membrane surface [57] is the initializing step in each.

The barrier to direct submersion by melittin into the bilayer estimated based on experimental hydrophobicity scales is prohibitive [58, 59, 60]. Detailed atomic level information on melittin's behavior in zwitterionic membranes comes primarily from molecular dynamics simulations. All-atom simulations predict vertical peptides in transmembrane orientation line the pore wall [61, 62]. Insertion of the first peptide to adopt a transmembrane orientation reduces the barrier for the second [63]. Sun *et al.* show the nucleation step involves exposure of a membrane edge [64, 65].

Wimley Melittin Mutants

Melittin's ability to form pores is what makes it a useful starting structure for potential pharmaceuticals. However, activity of a mutant in model membranes does not always translate into efficacy in real applications [66, 67, 68, 69, 70]. Melittin mutants from the Wimley group reveal general principles for introducing membrane specificity and for moderating activity. Krauson *et al.* have shown that membrane specificity is controlled at the level of membrane binding [21]. Mutation of hydrophobic residues that bias the random coil structure rather than the α -helix shift the adsorption equilibrium toward the unbound state [21]. Wiedman *et al.* use the same principle by inserting acidic residue mutations at α -helical intervals within the amino acid sequence such that intrapeptide repulsions bias the random coil structure at neutral pH but not at acidic pH [22, 24].

The Krauson *et al.* gain-of-function (GoF) combinatorial library shows as few as two mutations can confer GoF. Of the ten melittin residues subject to mutation, proline 14, threonine 11 and leucine 16 are conserved. Retention of the proline kink is controversial as its role has not been clearly demonstrated [65, 71, 72]. The single melittin mutation, leucine 16 to glycine, shifts the secondary structure of the C-terminal helix toward the unfolded coil, and prevents the peptide from binding [21]. Mutation of threonine 11 to a nonpolar residue has less of an ability than threonine 10 to reduce the angle of the polar face, hence threonine 10 is generally mutated to alanine while threonine 11 is preserved. Threonine has been documented in the association between transmembrane helices [73]. Diminishing the cationic charge of the C-terminal tail, and reducing the angle of the polar face of the amphipathic helix bring down the barrier to insertion. At P/L=1/200 more than 80 % of MelP5 (GIGAVL-KVLATGLPALISWI-KAAQQL) peptides, the most potent GoF mutant, are in a transmembrane orientation. Cholesterol has an inhibitory effect against melittin but much less so against MelP5 [20].

Mutations to acidic residues aspartic acid and glutamic acid, as well as to glutamine, can

further enhance MelP5 potency [20, 22, 23]. Combinatorial mutagenesis on MelP5 reveals the highly conserved sequence consisting of acidic mutations at positions four and eight and glutamine at position 17 in mutants that facilitate macro-molecule sized pores [22, 23]. Furthermore, this mutational motif can be made pH sensitive with additional acidic residue mutations [22]. Li et al. hypothesize a parallel orientation between peptides in the pore to facilitate interaction between the cationic residue at melittin position seven and the acidic mutation at position eight [23].

Research Statement on Melittin Dimerization :

The persistence of hypotheses that melittin aggregation facilitates pore formation [74], and in particular of dimerization on the membrane surface [33, 57, 75, 76] warrant a review of the evidence in the context of competing theories, presented below. Given impediments to structural studies of protein association by the presence of the membrane molecular dynamics simulation provides an invaluable benchmark for real processes with molecular detail at the nanoscale [77]. Fully atomistic simulation of the AMP pore formation is prohibitive at current computational capacity. Only recently with the advent of special purpose machines [78] has it become possible to simulate protein association in membrane systems without sacrificing atomistic detail. In general implicit solvent models and enhanced sampling methods [79] are needed to observe peptide dimerization due to obstruction by intervening lipids [80] that limit sampling along the dimerization pathway. The Poisson-Boltzmann equation [81] treats the solvent as a dielectric continuum but this method is still too slow for practical molecular dynamics simulations. The generalized Born [82] approximation has produced attempts to solve this problem [83] and permits introduction of a heterogeneous dielectric to represent the membrane [84]. Lazaridis's effective energy function provides an implicit model based on solvent-exclusion [85, 86] and is the fastest realistic alternative to generalized Born and coarse-grained simulations [87, 88]. Umbrella sampling [89, 90] is used for implicit

as well as all-atom simulations along the reaction pathway [91], defined as dimerization on the membrane surface, and the potential of mean force (PMF) [92] is reconstructed using the weighted histogram analysis method (WHAM) [93].

Rational design of synthetic AMPs is limited by a lack of detailed structural information [94], while a strictly combinatorial mutagenesis approach is impractical. Studies using a rational design approach [24] precede resourceful and efficient combinatorial methods [22, 23], and results from molecular dynamics simulation have recently been incorporated into design methodology [94]. The Wimley group’s MelP5 combinatorial library isolated the mutational motif of glutamic acid at positions four and eight and glutamine at position 17 (Glu(4,8), Qln17), which contributes to macro-molecule sized pores and increased potency by the melittin mutant [22, 23]. Aspartic acid is also possible but glutamic acid is preferred. The Glu(4,8), Q17 motif, additional acidic residue mutations at positions 11 and 15, leucine mutation at position 12, and conservation of serine 18 largely define the macrolittins [23]. In addition to histidine in place of lysine, the macrolittins can be made pH sensitive with additional acidic mutations at positions 12 and 18, known as the pH dependent peptides [22, 95]. Any details of how the conserved and variable mutations among the macrolittins and the pH dependent peptides contribute to macro-molecule sized pores and increased potency remains largely unknown. Given the complications with obtaining structural data *in situ* [72] an emblematic member of the macrolittins and of the pH dependent peptides, macrolittin70 (GIGEVL-KELATLLPDLQSWI-KAAQQL) and pHD15 (GIGEVL-HELADDLPDLQEWI-HAAQQL), respectively, are chosen for 10 μ s all-atom molecular dynamics simulation. Macrolittin70 (mac70) is chosen to represent the macrolittins as it is the least modified and the most similar to MelP5. pHD15 is chosen to represent the macrolittins for its rigid pH dependence. Both peptides have the same version of the highly conserved mutational motif composed of E(4,8) and Q17, as well as a variable region of less regularly placed acidic residues. To model peptides at pH 5 and 7 we protonate and deprotonate acidic residue

sidechains, respectively. Microsecond simulations are needed for equilibration of membrane pores by AMPs [96, 97]. Macro-molecule sized pores are prohibitive such that hexameric pores are prepared based on concentrations suitable for stable melittin pores [61, 62], using a putative structure for the parent peptide MelP5 [62]. The parallel orientation among peptides was hypothesized to facilitate interaction between the cationic residue at melittin position seven and the acidic mutation at position eight [23]. The key questions posed by Wimley group [22, 23, 95] are addressed; namely, do the peptides associate? What is the structure of the pore? Are the N- and C-terminal helices independent?

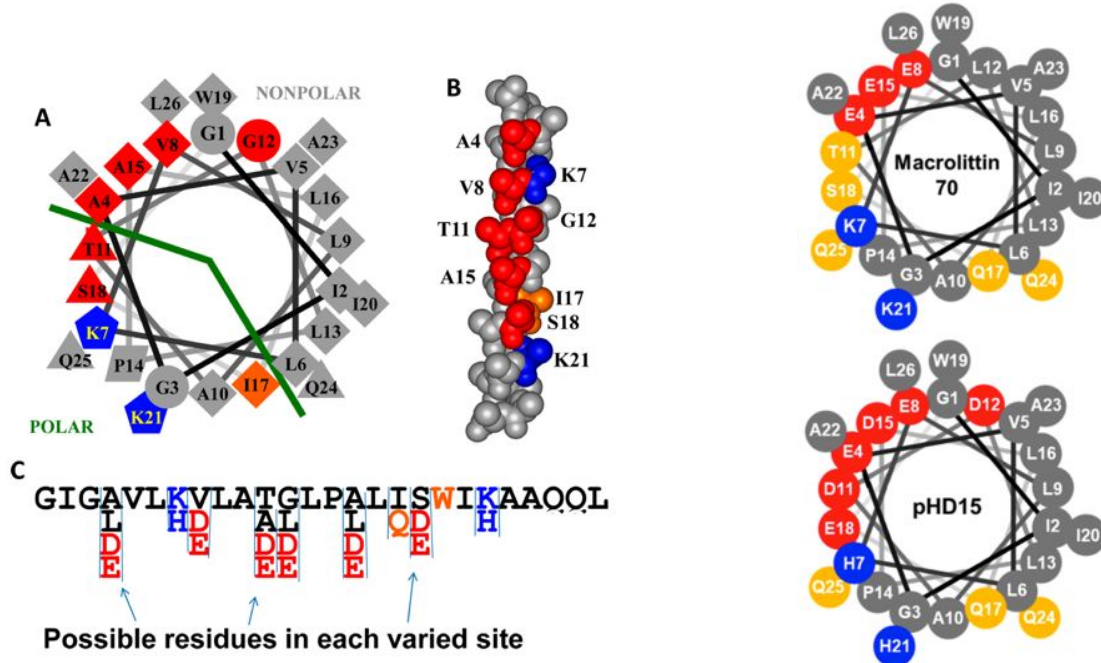


Figure 1.1: (Left, figure taken from [22]) A. Helical wheel diagram of the MelP5 scaffold (grey and blue) with mutation sites (red and orange) with the partition between the polar and nonpolar faces shown in by the green line. B. Molecular representation of the MelP5 scaffold (grey and blue) with mutation sites (red and orange). C. Sequence representation of the MelP5 scaffold (grey and blue) with possible mutations listed below (red and orange). (Right, figure taken from [23]) Helical wheel representation of macrolittin70 and pHD15.

Mini-Review :

A brief review of essential characteristics of melittin is presented here before reviewing the literature related to aggregation and how it relates to pore formation.

Aggregation in Water :

In solution at low concentration melittin is monomeric and unstructured [98]. At elevated concentration, salt content, or phosphate [99] melittin adopts α -helical secondary structural elements [100] and aggregates form [48, 100]. Early methods utilized melittin's intrinsic tryptophan 19 (Trp19) fluorescence to deduce aggregation. Tryptophan 19's fluorescence emission maximum shifts from 353nm to 337nm upon aggregation [100]. This "blue shift" is characteristic of tryptophan transitioning from an aqueous to a hydrophobic environment. This suggests that Trp19 is somewhat embedded in the hydrophobic lumen of the aqueous aggregate. Gel filtration chromatography shows the aggregate is a tetramer [100]. Fluorescence polarization is a common technique for measuring complex formation involving biological molecules. The fluorophore complex has an higher polarization signal relative to the fluorophore alone. Melittin Trp19 fluorescence polarization increases with increasing concentration, and plateaus at 0.5 mM melittin, or 1-2 M NaCl at 0.2 mM melittin [48]. The tetramer at elevated salt concentration has been crystallized and high resolution X-ray structure has been obtained [101].

Membrane Binding :

The blue shift in Trp19 fluorescence is still used to measure melittin adsorption [22]. Trp fluorescence and EPR [102] spectroscopy show melittin adsorption on the membrane surface is facile. Upon binding to membranes Trp19's fluorescence emission maximum shifts from 352nm to 333nm [103, 104]. In contrast to melittin aggregation in water, concentration and ionic strength do not impact membrane adsorption. Increased ionic strength did not hinder nor enhance binding in DMPC or phosphatidylserine (PS) [104], demonstrating that the monomer and the tetramer both bind either membrane equally well. This observation

was confirmed in additional membrane systems (PS, lysolecithin, dihexanoyl-, dioctanoyl-, lysolauroyl-PC) [105]. The length (lauryl C₁₂, myristoyl C₁₄), palmitoyl C₁₆) of the aliphatic chains do not affect membrane binding. Trp19 fluorescence when melittin is bound to PS, DMPC, or DPPC is sensitive to the phase controlled via the temperature. Melittin is somewhat ejected from the bilayer when it enters an ordered state below the phase transition temperature. For DMPC and PS, the higher the pH the steeper the binding curve. High pH tends to make the head-groups region of these membranes increasingly anionic. The increased affinity for anionic membranes was confirmed by introduction of dicetylphosphate into zwitterionic lipid membranes. Conversely, introducing positive charge into the head-group region with addition of stearylamine decreases melittin's affinity for membranes.

Membrane Binding : IR (Topology and Orientation)

IR has been used to determine the orientation of membrane adsorbed melittin. The results of Vogel and Jähnig using polarized IR spectroscopy reveal melittin is oriented parallel to the membrane normal in both ordered [26] and fluid 1,2-ditetradecyl-sn-glycero-3-phosphocholine (DTPC) membranes [45]. Frey and Tamm using attenuated total reflection IR spectroscopy (ATR-IR) later clarify that melittin is parallel to the bilayer plane when the membrane is adequately hydrated [106]. Polarized attenuated total internal reflection-Fourier transform infrared spectroscopy (PATIR-FTIR) shows the helical segments are preferentially oriented parallel to bilayer plane regardless of sample preparation [107].

Membrane Binding : Raman (Secondary Structure)

Vogel and Jähnig identify the two bands, at 34 cm⁻¹ and 65 cm⁻¹, in the Raman spectra of the melittin tetramer in phosphate buffer and melittin bound to DTPC to accordion-like vibrations of two, 11 and 6 residue, helical segments. The difference in Raman spectra between aqueous tetrameric and membrane bound melittin reveals a high degree of similarity between the two systems. However, the peak at 1,550 cm⁻¹ in the difference spectra suggests

that in each case Trp19 is in a different environment. Vogel and Jähnig attribute the change here in Trp19's raman spectra to an increase in the hydrophobicity of its environment. However, in both of the examples they cite as justification [27, 100] the observable is Trp19's fluorescence blue shift based on monomeric melittin, where Trp19 is initially in a polar environment. The difference here is between the tetramer and the membrane bound form where the fluorescence spectra coincide. Thus, raman contrasts with fluorescence in that tetrameric and membrane bound melittin produce different Trp19 spectra. This may suggest that the blue shift in Trp19 fluorescence by the aqueous aggregate and by membrane bound melittin each occurs by a different mechanism.

Membrane Binding : EPR (Topology and Coil-Helix Transition)

Altenbach and Hubbell observe the EPR profile of a nitroxide radical linked to melittin's different lysines, and N-terminus [102]. Broadening of the spectra in the presence of lipids is attributed to vesicle binding. Addition of excess unlabeled melittin to dilute the labeled peptide and preclude spin interactions as the source of the line broadening has no effect. Bringing the salt concentration up to 2 M to induce aggregation (with line broadening) also has no effect on the EPR spectra. Hence, surface adsorbed melittin is deemed monomeric. Chromium oxalate induces broadening for all labels. This suggests a surface bound conformation that cannot penetrate deep into the membrane hydrophobic core. Lys7 is the most solvent accessible while Lys(21,23) are more membrane buried.

Distance distributions of doubly labeled mutants generally shift to smaller values upon binding to LUVs [108]. This observation may be interpreted as a consequence of the random coil-to-helix transition. This is most apparent with melittin labeled at the N-terminus and at position fifteen. Melittin doubly labeled at position fifteen and twenty seven, however, shows almost no shift. Thus the authors claim that the highly charged C-terminal fragment is helical both in solution (at 0.35mM) and bound to LUVs. This is in contrast to the widely

held consensus that the monomer exists as a coil in solution. Doubly labeled Gd⁺³ melittin mutants confirm the random coil-to-helix transition upon membrane binding [109].

Membrane Binding : Partitioning

The cationic C-term mediates adsorption on the membrane surface [110], which subsequently facilitates the coil-to-helix transition [108, 111]. Melittin's nonpolar face buries into the membrane's hydrophobic region while charged moieties protrude more into solution [112]. Benachir and Lafleur observe fast binding go to completion, which is essentially irreversible (there is no exchange between vesicles) [113]. Rex and Schwarz argue that the cationic C-terminus remains in solution and facilitates migration between vesicles [114].

Melittin Dimerization on the Membrane Surface

Fluorescence :

The first attempts to observe melittin aggregation in membranes employ techniques used to observe melittin aggregation in solution, and membrane binding. Georghiou, Thompson, and Kukhopadhyay interpreted the coincidence in the absorption [115], and fluorescence spectra [116] in egg PC and dibasic phosphate as melittin aggregates in membranes. However, the resemblance between spectra may be purely coincidental. While fluorescence polarization increases in the presence of liposomes [48] it could not assess the association state of the adsorbed melittin [105, 115]. In practice, light scattering from lipids interferes with the fluorescence measurement, making it difficult to determine anisotropy decay parameters [115]. To support their claim, Georghiou et al. showed acrylamide quenches membrane bound melittin's Trp19 fluorescence. Accessibility by a polar quencher suggests Trp19 is not deeply embedded in the hydrophobic core of the membrane, but rather is reasonably solvent exposed [99]. The concavity of the Stern-Volmer plots suggest quenching by both collisional and static mechanisms. Georghiou et al. argue the similarity in the collisional and static

quenching constants in dibasic phosphate and egg PC suggests melittin's blue shift in Trp fluorescence in egg PC and dibasic phosphate share a common origin. They attribute the early section of the decay profile to proximity of Trp19 to the quencher or to another Trp19 [115]. As quenching experiments on indole have shown, there is no clear relationship between shift in fluorescence emission and the extent of solvent exposure [117, 118, 119]. Indeed, water has been shown to induce a blue shift in fluorescence depending on its orientation with respect to Trp [120]. The consensus seems to be that attempts to view aggregation based on melittin's intrinsic tryptophan fluorescence are obscured by the membrane [121]. The discrepancy in the interpretations resulting from fluorescence and quenching experiments means resolving the mechanism of melittin's blue shift cannot rely on these methods alone.

To overcome the limitations of Trp fluorescence properties in membranes, numerous authors resorted to Förster resonance energy transfer methods. Early attempts hearken to the notion of Trp as a means for association. Vogel and Jähnig modified melittin (A-melittin) via the Koshland reaction to convert Trp19 into a nonfluorescent acceptor for Trp19 fluorescence [45]. In DMPC vesicles loaded with melittin, fluorescence diminishes upon addition of A-melittin at low melittin content ($P/L=1:1000$) where peptides are expected to be monomeric. The FRET efficiency increases with increasing melittin content suggesting a shifting towards the aggregate, which they determine corresponds to tetramers.

Talbot et al. again attempt explicit observation of Trp-Trp like interaction in 1,2-dioleoyl-sn-glycero-3-phosphocholine (DOPC) small unilamellar vesicles (SUVs) using oxidized-Trp19 melittin as an acceptor for native Trp19 fluorescence [122]. FRET efficiency (of $1\mu M$ melittin) in DMPC, egg PC, and PG liposomes increases only in the presence of $0.5M$ NaCl. The distance between respective Trp19 residues is estimated to be 16.2 \AA , which they interpret as corresponding to an antiparallel surface adsorbed dimer. They add that this value is likely lower than actuality noting oxidation decreases Trp's hydrophobicity, and the oxidized derivative does not self-associate as well as melittin in solution [122].

Hermetter and Lakowicz monitor FRET using Trp19 as donor and covalently label Lys21 with N-methyl anthraniloyl (NMA) as acceptor [123]. Titration of the melittin tetramer in 2M salt solution with DMPC vesicles progressively reduces the NMA-acceptor's fluorescence emission to that of the NMA-melittin monomer. This suggests that the aggregated melittin state dissociates upon interaction with the lipid membrane.

Schwarz and Beschiaschvili repeat Vogel and Jähnig's FRET experiment at acidic pH of five, where the overlap between acceptor absorption spectrum overlaps more favorably with the fluorescence spectrum of the donor [124]. They confirm FRET occurs, however they argue this need not imply aggregation. Increasing the salt concentration to 1M NaCl does not change the result, in contrast to Talbot et al.'s observations [122]. Schwarz and Beschiaschvili conclude that melittin does not aggregate when bound to the membrane.

Subsequently the Jähnig and Dufourcq groups renounce their position on the aggregation state of membrane bound melittin. John and Jähnig show only about 10% of adsorbed melittin in DMPC may exist as aggregates even at high P/L, and high ionic strength [125]. Using melittin and the same modified melittin species (A-melittin) their results show freely diffusing donors and acceptors. Furthermore, plot of relative quantum yield v. acceptor concentration lies on a universal curve for randomly distributed donors and acceptors. Their analysis does not allow for distinction between dimeric and tetrameric aggregates. In addition, John and Jähnig reanalyze the FRET results of Talbot et al. [122], and of Vogel and Jähnig [45] and show they are consistent with monomeric melittin.

Pérez-Payá and coworkers in collaboration with Dufourcq prepare (DNC-melittin) melittin labeled at Gln25 with the fluorescent probe monodansylcadaverine (acceptor of Trp19 fluorescence) [126]. DNC-melittin retains melittin's lytic activity. They observe dissociation of the tetramer upon titration with PC, PS, lysoPC lipids, and erythrocyte ghosts. They estimate the average distance between fluorophores to be 21 Å.

EPR :

Electron paramagnetic resonance spectroscopy has also been used extensively to explicitly address the homo-oligomerization of melittin on the membrane surface. Melittin has no unpaired electrons so EPR probes are covalently tethered to its various residues. Results for melittin exist using nitroxide and gadolinium based probes. Distance measurements using EPR data in solution are based on broadening of the spectra [127]. However, intermolecular distances between peptides in membranes cannot be deduced from EPR spectra based on line broadening. Any broadening that may occur due to homooligomerization (at high concentration, or salt) is too modest to distinguish from the significant broadening of the spectra upon membrane binding [102]. Double electron-electron resonance (DEER) experiments are designed explicitly to calculate distances between EPR probes, thereby placing bounds on the native conformations. Neither probe detects any degree of homo-oligomerization in the membrane.

Altenbach and Hubbell obtain EPR spectra of the nitroxide radical succinimidyl-2,2,5,5-tetramethyl-3-pyrroline-1-oxyl-3-carboxylate methanethiosulfonate linked to melittin's different lysines(7,21,23), and its N-terminus [102]. Broadening of the spectra in the presence of POPC and POPA(anionic) vesicles (in phosphate buffer at pH=7) is due to membrane binding and restricted motion of the labeled site. Addition of excess unlabeled melittin to dilute the labeled peptide, thereby sharpening the EPR spectra, has no effect. This precludes spin interactions as the source of the line broadening. Bringing the salt concentration up to 2M to possibly induce aggregation, and potentially broaden the EPR spectra, also has no effect. All subsequent EPR studies of melittin in membranes confirm melittin remains monomeric.

Gordon-Grossman et *al.* use pulse double electron-electron resonance (DEER) to measure intramolecular distances of MTSL (1-oxyl-2,2,5,5-tetramethyl-3-pyrroline-3-methyl) methanethio-sulfonate labeled melittin [108]. Pulse DEER extends distance accessible (7-20Å) from line

broadening in presence of second spin probe to 70Å (refs 12-14). They investigate aggregation in 7:3 DPPC/PG LUVs at P/L ratio of 1:200. The difference in decay profiles of time-resolved DEER traces between singly(mel-C₁₅) and doubly(mel-C₁₅C₂₇ labeled melittin show dipolar interactions are intramolecular. The results of the N-terminal and C-terminal doubly labeled mutant are interesting because they show distances as low as 17Å, about half the end-to-end distance of the peptide. However, fine structure in calculated distance distributions may simply be experimental artifacts. Therefore, melittin exist as a monomer in partly anionic as well as neutral membranes.

In 2011, Gordon-Grossman and co-workers extend the EPR study to higher melittin concentrations (P/L=1:100, 50, 25) [128]. DEER measurements (using X-band (9.5 GHz) on melittin labeled at position fifteen do not detect intermolecular distances in the range of 1.7-4nm. To investigate distances less than 1.5nm, they look at line broadening of continuous wave (CW) EPR spectra (X-band (9.5 GHz)) of frozen (130 K) samples. Second moment analysis of the CW-EPR spectra do not detect distances below 1.5nm. The authors therefore reject the pore-formation hypothesis in the context of anionic membranes. They do not however preclude the possibility of nonspecific aggregates at large distances.

The nitroxide label is hydrophobic and associates with the nonpolar region of the membrane [129, 130]. Manukivsky et al. investigate melittin homo-oligomerization on 7:3 DPPC/PG LUVs using a Gd³⁺ based label. When Gd³⁺-ADO3A labeled melittin binds the membrane the label remains solvated. Gd³⁺ systems generally shows broader distributions. DEER measurements using W-band (95 GHz) on singly labeled melittin-C15 at P/L=1:2000 show no homo-oligomerization [109]. A low P/L ratio ensures complete membrane association, and minimal background decay by aqueous peptide. It also allows extension of the evolution time in the DEER measurement up to 5μs.

NMR :

It is possible to detect inter-molecular interactions using NMR in a manner similar to EPR. The dipolar interactions between ^{13}C labeled sites causes line broadening in NMR spectra. Melittin in zwitterionic lipids has been studied by solid-state ^{13}C NMR spectroscopy in thin DMPC membranes at high P/L=1:10 where melittin adopts a transmembrane orientation [43]. Below the DMPC lipid crystal-to-gel $T_m = 24^\circ\text{C}$ differential-interference microscopy images show porous GUVs made by P/L=1:10 at high hydration. Doubly labeled melittin, at the Gly(3) alpha carbon and the Ala(15) methyl carbon, show line broadening at 20°C . However, this is due to melittin's strong interaction with the bilayer, and not to ^{13}C - ^{13}C dipolar interaction. Above the DMPC T_m differential-interference microscopy images show vesicle fusion, and above 30°C the vesicles elongate and the bilayer plane predominantly orients along the external magnetic field. Under oriented and fast magic angle spinning (MAS) conditions, ^{13}C ssNMR spectra of melittin singly labeled at the α position of Gly³, Val⁵, Gly¹², Ala¹⁵, Leu¹⁶, or Ile²⁰ show line widths of ~ 400 Hz and ~ 300 Hz, respectively. Despite the reduction in line width by fast MAS it is not sufficient to isolate interactions between melittin monomers. A 4 Å ^{13}C - ^{13}C distance is necessary for ^{13}C - ^{13}C dipolar interaction between rigid helices to achieve 100 Hz of line broadening. Comparison between fast MAS ssNMR spectra of lipid, and singly-labeled melittin ^{13}C carbonyl carbon at 40°C shows melittin's chemical shift anisotropy contributes significantly to line broadening as a result of rotational dynamics along the membrane normal. At temperatures above the T_m , the powder pattern from slow MAS indicates significant precessional and orientational oscillations about the average helical axis. They conclude that melittin's dynamics in zwitterionic membranes largely precludes the ^{13}C - ^{13}C dipolar interaction.

Leakage Kinetics :

The dimer hypothesis extends back to DeGrado in RBCs, and Schwarz in vesicles, and persists in the kinetic analyses of more recent experiments.

Leakage Kinetics : Red Blood Cells

DeGrado et al. observe biphasic hemoglobin, and carbonic anhydrase, release from erythrocytes over a large range of concentrations, ionic strengths, and temperatures [75]. Leakage is proportional to peptide concentration, and RBCs remain intact. The first stage is rapid partial release and is roughly ten minutes. The second stage is slow steady state leakage. The fast stage depends on [melittin]/[RBC]. The first order decay of this process (of surface bound melittin) reflects melittin undergoing conformational, and or topographical changes upon binding the membrane. The fast stage is modeled as two consecutive reactions. To observe first order kinetics melittin must translocate across the bilayer via very brief transient pores. The slow stage depends on $([\text{melittin}]/[\text{RBC}])^2$. The second order dependence of the second stage suggests dimerization by surface bound melittin is rate limiting. This suggests that post binding the melittin dimer is the lytic species, and remains the only unrefuted claim of a melittin dimer. However, interpretations of kinetic results in terms of the molecularity must be approached with caution, as the results are highly system dependent. At 295.15K, in iso-osmotic glucose the fast phase has a fourth order dependence on melittin centration [131]. At 277.15K, in isotonic saline, the fast stage is first order, and the slow stage is zeroth order; and at 310.15K, and the slow stage is first order [131].

Leakage Kinetics : SUVs

Schwarz and Robert develop a kinetic model for the rate of pore formation based on efflux of entrapped self-quenching fluorophore from lipid vesicles [132]. The model assumes that a Poisson distribution of pores across vesicles sets in, and that leakage occurs through an “all-or-none” process such that pore-formation is rate limiting. Schwarz, Zong and Popescu apply this model to melittin interacting with POPC SUVs with entrapped self-quencher carboxyfluorescein [76]. At the concentrations used melittin is initially monomeric. They observe biphasic kinetics with initial fast phase followed by moderate leakage after about a

minute. The final fluorescence never reaches its max, suggesting some vesicles remain intact. Increasing the salt concentration produces faster rates, as does the presence of a membrane voltage. They apply a simple kinetic model in which monomers predominate and are in equilibrium with the dimer, and subsequent fundamental aggregation steps are essentially irreversible. Focusing on the first three minutes, the latter phase reproduces the steady leakage in RBCs with a rate-limiting dimerization step. The third order dependence of the initial phase presupposes rapid formation of a body of dimers.

Using Schwarz, Zong and Popescu's kinetics Takei, Remenyi and Dempsey investigate carboxyfluorescein leakage from PC SUVs using disulfide dimerized cysteine mutants [133]. Melittin is compared with single and doubly substituted mutants, (melittin-K23C)₂, and (melittin-K23C,K25C)₂. They focus on the first phase of the leakage process to neglect possible "graded" leakage during the later stage. Dimerization shows a clear shift from second to first order dependence with respect to peptide concentration suggesting dimerization is rate limiting.

Leakage Kinetics : LUVs

The early model was revised to accommodate a graded leakage process via short-lived pores [134], and to address the fluorescence signals' nonlinear dependence on leakage due to dequenching of the entrapped self-quenching dye [135]. Efflux is recast as a retention function in terms of the static and transient quenching by retained dye. The model assumes equivalent, non-interacting pores on uniformly sized vesicles. Rex and Schwarz then repeat the study by Schwarz, Zong, and Popescu and extend it to POPC and DOPC LUVs [114]. The revised theory shows a substantially graded modes for both LUVs and SUVs [44, 114]. Rex and Schwarz propose three monomeric activation steps precede poration that could but may not include any aggregation steps [114]. They propose an alternate model assuming (i) facile peptide exchange between vesicles, (ii) the monomer predominates, (iii) pores are

short-lived, (iv) fundamentally, the observed leakage kinetics is biphasic with a brief initial fast phase followed by a moderate phase, (v) and a first order rate of pore formation. The kinetic scheme is characterized by two slow equilibria preceding formation of the activated monomer prone to pore formation, which may or may not involve additional melittins.

Matsuzaki, Yoneyama and Miyajima apply the Schwarz' kinetic analysis to analyze calcein leakage from POPC/PG(9:1) LUVs [44]. They also conclude that melittin forms short-lived pores. In addition, they demonstrate melittin's ability to translocate to the inner leaflet and suggest that translocation is coupled to pore-formation. Furthermore, they show that the amount of leakage increases with an increase in P/L, and that a larger fluorescent dextran leaks similarly but at higher P/L.

Other groups observe complete leakage within minutes, without a final steady-state [41, 113]. Benachir and Lafleur study calcein release from POPC LUVs in isotonic buffer (150 mM H₂BO₃, 5 mM EDTA, 140 mM NaCl, 5 mM KOH, pH 9). The overall amount of calcein leakage is proportional to the addition of monomeric melittin. Leakage occurs above a threshold at P/L=1/1000, otherwise vesicles remain intact. Total release is achieved at roughly ten times that P/L. The average minimum number of melittins per vesicle (10^5 lipids) that induces lysis is 254 ± 46 . This relatively high number suggests a cooperative interactions lead to membrane perturbations. Following removal of released calcein, the un-lysed vesicles retain self-quenching calcein concentrations. There is no gradual decrease in self quenching, suggesting an all-or-none leakage mechanism. Unprotonated palmitic acid (PA) or POPG lipids work to inhibit melittin action. The same level of release requires more melittin with an increasing proportion of PA or POPG. Benachir and Lafleur propose a statistical model with peptides randomly distributed on the membrane surface, describing a detergent-like mechanism [113].

Knowledge of the leakage mode is needed to calculate the percent leakage, before a kinetic model can be applied. Ladokhin, Wimley and White investigate the melittin leakage mode

using fluorescence re quenching. ANTS/DPX (anion/cation, fluorophore/quencher pair) is entrapped inside LUVs. Post melittin addition, released ANTS is titrated/re quenched with DPX. Rather than observing fluorescence of leaked dye, re quenching focuses on the extent of quenching of entrapped ANTS. No fluorescence from within vesicles post re quenching suggests some vesicles remain in tact while others release their entire contents. A change in quenching suggests a graded mode. However, melittin induced leakage is too fast and too drastic for the re quenching method to accurately distinguish all-or-none from graded. Either all ANTS leaks, or DPX added to re quench leaked dye enters vesicles and quenches ANTS retained by vesicles.

Leakage Kinetics : Single GUVs

Mally et al. continuously monitor shape, and sugar content of a single GUV held at zero tension by phase-contrast microscopy [57]. The phase-contrast image produces a white halo delineating the POPC GUV's circumference based on the difference in refraction index between the internal 0.2M sucrose ($r_s=0.55\text{nm}$), and the external 0.2M glucose ($r_s=0.44\text{nm}$) solutions. The halo around vesicles containing different concentrations of internal sucrose provides a calibration curve for vesicle leakage. Decrease in the halo brightness indicates equilibration between the outer and inner solutions. Results show four distinct melittin concentration regimes.

At low concentration, from 1-3 $\mu\text{g}/\text{mL}$ melittin perturbs the membrane but vesicle contents are preserved. First, the membrane appears to stiffen and thin tethers extend from the outer leaflet. The tethers are retracted with the onset of membrane fluctuations and the surface area increases. Surface area expansion reverses with the disappearance of outer leaflet tethers. The membrane tenses up again and inward protuberances appear, occasionally budding and encapsulating some of the outer solution. A peptide to lipid ratio up to P/L=1:500 is possible without leakage.

At moderate concentration, from 3-7 $\mu\text{g}/\text{mL}$, the vesicle leaks, with periodic bursts about 0.1s long. Glucose enters the GUV more readily than sucrose exits, leading to osmosis. The vesicle swells before opening when a critical membrane tension is reached. Leakage bursts become more frequent over time, and the vesicle radius shrinks at a linear rate (different for different vesicles). Increasing permeability over time may either be due to an increase in the size or the number of pores. At 7 $\mu\text{g}/\text{mL}$, they estimate the initial pore radius to be 1.1 nm.

At high concentration, from 7-12 $\mu\text{g}/\text{mL}$ rapid lysis occurs and the vesicle disintegrates in under a minute. Interestingly, in the range from 12-60 $\mu\text{g}/\text{mL}$ the vesicle initially survives, in some cases for up to 20 minutes, before it eventually disintegrates.

Mally et al. propose that a common mechanism involving melittin spans phenomena seen at all concentrations. They postulate that dimerization on the membrane surface ultimately leads to insertion forming a transmembrane dimer, which monomers may subsequently join to form pores. Three melittins makes a sugar-permeable pore.

Melittin adsorption first expands the outer leaflet. Encapsulation of the exterior solution by the internal budding suggests outer membrane lipids migrate to the inner leaflet. ΔA_0 is the difference in surface area between the outer and the inner leaflet. Melittin adsorption is rapid such that ΔA_0 grows rapidly upon melittin introduction. A square dependence on melittin concentration associated with lipid flip-flop best describes the subsequent decrease in ΔA_0 . The fast rate of ΔA_0 reduction suggests many dimers transport a few lipids, or that dimers are capable of transporting many lipids. In this way the transmembrane dimer may explain the formation of tethers at low melittin concentration.

Kokot et al. attempt to address whether increasing permeability over time at moderate melittin concentration is due to an increase in size or in number of the pores [33]. Again they use phase-contrast microscopy and POPC GUVs, but this time they encapsulate dextran 6000 (large) and Alexa Fluor 594 (AF, small). Each marker leaks to a different extent depending on the pore size. The white halo in the phase-contrast image is used to monitor

the dextran; and its fluorescence intensity is used to monitor AF.

They use a melittin concentration ([melittin]) of $2\mu\text{M}$ in all runs. Leakage of both markers begins simultaneously. Separate curves can be generated for release of each marker. AF leakage is faster than dextran leakage. The leakage rate diminishes when the marker reaches about 50% of its original concentration. There is a consistent lag time in all runs lasting between 30 seconds and eight minutes before leakage begins. Many vesicles are not permeabilized indicating that leakage is initiated stochastically.

The marker outflow is related to the permeability. The permeability is a sum over the pore concentrations, which change over time. They write kinetic expressions for the adsorbed monomer, and for each pore with a given number of monomers. Concentration drives dimerization, and the dimer is more stable in the transmembrane orientation, which is considered a pre-pore. The partition coefficient K_p , as well as the dimer association and dissociation coefficients are taken from Schwarz et al [76]. Association with the pore is proportional to the number of monomers in the pore, $k_{n,n+1} = k_{a0}n$. Dissociation from the pore is proportional to the number of monomers in the pore, as well as to the Boltzmann factor of the energy difference between the initial and final pore states, $k_{n,n-1} = k_{d0}ne^{-\beta\Delta E_{n,n-1}}$. The model includes the possibility of pore disassembly into two smaller pores. The fission coefficients are proportional to the number of possible fission products, and the Boltzmann factor of the difference in energy between the initial, single-pore state and the final, two-pore state. The number of possible fission i -, and $n - i$ -meric products from an n -meric pore, without permutations, is n , thus $k_{n,n-i,i} = k_{d0}ne^{-\beta\Delta E_{n,n-i,i}}$. The phenomenological expression for the pore energy is related to the pore line tension, the electrostatic repulsion between melittins, and the energy released by melittin participating in the pore. They consider up to a decamer. The resulting set of differential equations is solved using the free parameters, k_{a0} and k_{d0} . The permeability for each pore size is proportional to the excess area of the face of the pore when the marker is exiting. The proportionality factor is chosen to be the same for both AF

and dextran 6000.

A continuously changing distribution of pore size and number is seen over time, with a peak appearing around tetrameric pores. The accumulation of pores large enough to permit marker leakage partly explains the lag time before the onset of leakage. The dissociation of pores consisting of $n \geq 3$ monomers subsequently drives the production of pre-pores and pores. Eventually adsorption of additional monomers becomes less favorable due an increase in membrane surface potential. They estimate an average pore radius of 1.3nm, $k_{a0} = 42/\text{s}$, and $k_{d0} = 10^{-18}/\text{s}$. The pore line tension is $\Gamma = 2.6 \times 10^{-11}\text{N}$, within range of values reported for POPC [136]. They estimate the energy release due to melittin joining the pore as $\delta = 1.4 \times 10^{-19}\text{J}$, which is comparable to monomer adsorption [137].

H. W. Huang:

A pore formation mechanism consistent with data from a variety of structural methods, which does not invoke aggregation has been proposed by Prof. H. W. Huang and his many collaborators. The sigmoidal concentration dependence can be correlated with features of both the peptide and the membrane to reconstruct a general description of the series of events leading to pore formation [13]. An advantageous aspect of the combination of methods chosen is that the sample preparation is the same for each of them. Melittin and lipid of a given P/L are codissolved in 1:1 (v/v) methanol and chloroform and spread onto a substrate (ie: quartz) surface. The system is rehydrated with water vapor following evaporation of the solvent, resulting in oriented multilamellar stacks.

H. W. Huang : OCD

Using oriented circular dichroism (OCD) the orientation of the alpha helical elements with respect to the plane of the membrane can be determined [138, 139]. Yang et *al.* and Chen et *al.* demonstrate the relationship between orientation and P/L on a variety of zwitterionic membranes [46, 140]. Below a threshold P/L^* melittin remains adsorbed on the

membrane surface and adopts an orientation parallel to the membrane surface. Above the critical P/L^* an increasing fraction of adsorbed melittin adopts an orientation perpendicular to the membrane surface.

H. W. Huang : X-ray

The membrane thickness can be estimated based on the distance between phosphates of the upper and lower leaflets. To measure the membrane thickness using X-ray diffraction the scattering vector is oriented perpendicular to the bilayer plane to measure the electron density when traversing the membrane. Again a threshold P/L^* is observed for a variety of zwitterionic lipid membranes [13, 140]. Below P/L^* melittin induces membrane thinning linearly with increasing P/L . Above P/L^* the membrane thickness remains constant. The threshold P/L^* is the same as that found using OCD for each lipid type [13, 140].

H. W. Huang : Neutron Scattering

The same sample observed from OCD can be used for neutron scattering experiments. The electron density contrast between peptide and lipid membrane is too low to observe pores with X-rays. D₂O, however, provides sufficient contrast for neutron scattering. Neutron off-plane scattering is able to detect transmembrane water columns, from which one can estimate the pore radius. Yet again, the same P/L^* value is observed for each membrane. In POPC bilayers the inner and outer pore diameter is 4.4 nm and 7.6 nm, respectively [46].

H. W. Huang : Two State Model

These observations are consistent with the two state model in which pore formation is concentration dependent [13, 55]. At low P/L melittin lays horizontally in a surface adsorbed (S) state, as observable by OCD. Embedding of the α -helix into the headgroup region pushes lipids to the side and creates a void in the lipid matrix just below the peptide [101]. Side-chain hydrophobic moieties cannot span the monolayer thickness [101], thus adjacent lipids

tilt [141] enabling hydrocarbon tails to reach beneath the nonpolar face of the amphipathic helix. As lipid tails extend to fill the gap [13], the membrane surface area expands, and concomitant membrane thinning is observable by X-ray diffraction [140]. Above a critical P/L^* , further membrane thinning stops, and additional adsorbed peptides begin to access a vertical transmembrane orientation, the inserted (I)-state. This transition does not require any intermediate states [55]. At this point the continuous creation and destruction of pores is predominant enough that pores appear stable by neutron scattering [46].

The pore energy in a pure lipid bilayer is [136, 142, 143, 144, 145]

$$E_R^0 = 2\pi r\gamma - \pi r^2\tau$$

, where r is the pore radius, and γ is the line tension for the pore rim. For $r < \gamma/\tau$, the line tension tends to close the pore. For $r > \gamma/\tau$, the surface tension tends to expand the pore indefinitely. Mechanically induced pores in pure membranes tend to close or rupture the vesicle. Stable pores by AMPs are the result of a negative feed-back loop created by the transition from the S-state to the I-state, and the intrinsic affinity of amphipathic molecules for the pore edge [54]. Transition from S-state to the I-state removes a peptide from the interface and reduces the surface tension. Amphipathic molecules tend to bind the pore edge and reduce the line tension [145]. These equilibrium results are also supported by kinetic studies using single GUVs.

The first clear observations leading to the current working hypothesis for melittin induced membrane permeability are attributed to M. L. Longo and coworkers [13]. Longo *et al.* monitor single (1-stearoyl-2-oleoyl-sn-glycero-3-phosphocholine) SOPC/POPS (199/1) GUVs held by micropipette aspiration at constant membrane tension between 0.1 and 0.2 dyn/cm using video microscopy [146]. The GUV contains 100 mM sucrose and is surrounded by 100 mM glucose. They infer permeation based on vesicle swelling upon glucose entry with

co-transport of water. At $0.1 \mu\text{M}$ melittin the vesicle surface area expands but no leakage occurs. At $0.5 \mu\text{M}$ melittin the initial surface area expands is followed by subsequent volume expansion. Leakage occurs below 1% in surface area expansion when the maximum achievable via melittin loading is 5%. This suggests leakage is a localized event, consistent with pore formation [146].

The surface area expansion caused by adsorbed melittin can be related to the surface tension by the fractional area expansion $\Delta A/A$ [54]. Lee *et al.* determine the induced surface tension [54] based on $\tau = K_A \Delta A/A$, where $K_A \approx 240 \text{ mN/m}$ (stretch modulus is roughly the same for all lipid bilayers [147]). They show that above a critical peptide to lipid ratio P/L^* the surface tension induced by melittin is comparable with that needed for mechanical rupture. Long chain lipids 1,2-dieicosenoyl-glycero-3-phosphocholine (di20:1PC), and 1,2-dierucoyl-sn-glycero-3-phosphocholine (di22:1PC) are chosen to achieve a large $\Delta A/A$ before rupture occurs. Single GUVs containing 100mM sucrose held at low constant tension [148] are transferred to isotonic glucose/sucrose solution containing melittin. They record surface area and volume expansion by video micrograph, and monitor the phase contrast between inside and outside of the GUV using a phase condenser. Below $10^{-7} \mu\text{M}$ there is no change in contrast, and the $\Delta A/A$ is usually less than 0.05. Above $10^{-7} \mu\text{M}$, $\Delta A/A$ in the range of 0.05 to 0.15 may be followed by sudden vesicle volume increase along with decreased contrast between inside and out of the GUV. The most frequent pore-forming $\Delta A/A$ for di20:1PC and di22:1PC, are 0.06 and 0.08, respectively. The resulting estimates for the induced surface tension $\tau \approx 14.4 \text{ mN/m}$, and $\tau \approx 19.2 \text{ mN/m}$, for di20:1PC and di22:1PC, respectively, are well within the range required for rupture. Evans *et al.* show that for shorter chain lipids a lower surface tension is needed for mechanical rupture of pure lipid GUVs [144]. For di22:1PC the rupture tension ranges from 9-35 mN/m depending on the tension load rate. Some vesicles do not leak although they are laden with melittin, $\Delta A/A$ up to 0.15. Huang argues that as in dynamic tension spectroscopy [144] of pure lipids, pore

formation like mechanical rupture is contingent on nucleation of a membrane defect [54].

Theory of the Two State Model : Monomeric Melittin

The theoretical basis for the two state model supports a mechanism based on monomeric melittin where the membrane thickness remains constant above a threshold P/L^* . While amphipathic peptide (AP) adsorption is favorable through hydrophobic interactions, the resulting membrane deformation is unfavorable. The deformation (change in thickness of the hydrocarbon region) D for adsorption of a single peptide is [141]

$$D = c \text{kei}(r/\lambda) + d \text{ker}(r/\lambda)$$

, where r extends from the edge of the peptide cross-section approximated as a circle of radius r_0 . For a peptide with circular cross-section of radius 10 Å the thickness change at the boundary is -1.9 Å, due to peptide adsorption, based on conservation of chain volume. The total deformation energy is

$$F^{(1)} = (c^2 + d^2)\pi(BK_c/8a)^{1/2}I(r_0/\lambda)$$

, where $I(z) = z(\text{kei}(z)\text{ker}'(z) - \text{ker}(z)\text{kei}'(z))$. For an amphipathic peptide with circular cross-section of radius 10 Å the total deformation energy $F = 1.9k_B T$. For restriction to a one dimensional system the deformation free energy from two amphipathic peptides in the S-state with separation r is $F^{(2)} = 2F^{(1)}v(r)$, where

$$v(r) = 2\left(1 + [\cosh(r/\sqrt{2}\lambda) - \cos(r/\sqrt{2}\lambda)]/[\sinh(r/\sqrt{2}\lambda) + \sin(r/\sqrt{2}\lambda)]\right)^{-1}$$

Therefore membrane deformations for $r < 2\sqrt{2}\lambda$ (~ 37 Å) are repulsive.

Theory of the Two State Model : Origin of Cooperativity

For a single amphipathic peptide the total free energy of adsorption is the sum of interface binding ϵ_B and membrane deformation f_M . For low P/L , $f_M = F^{(1)}$, and $-\epsilon_B + F^{(1)} < -\epsilon_I$, ϵ_I for insertion. For high P/L , $f_M \propto P/L$ as $-\epsilon_B + c(P/L)F^{(1)}$, where $-\epsilon_I$ defines the critical concentration P/L^* , and c is a constant. For peptide concentration of n per unit length, the deformation free energy per unit length is [141]

$$\frac{nF^{(1)}[\sinh(1/n\sqrt{2}\lambda) + \sin(1/n\sqrt{2}\lambda)]}{[\cosh(1/n\sqrt{2}\lambda) - \cos(1/n\sqrt{2}\lambda)]}$$

. For peptide concentrations n less than $1/2\sqrt{2}\lambda$, it is simply $nF^{(1)}$, whereas for concentrations above $1/2\sqrt{2}\lambda$, the energy is $2\sqrt{2}\lambda n^2 F^{(1)}$. When dimple deformations overlap the total deformation energy is proportional to $(P/L)^2 F^{(1)}$ [13]. Eventually the energy of adsorption will be greater than the energy of insertion.

Theory of the Two State Model : Critical Concentration

Assuming that for sufficiently high P/L membrane thinning is approximately uniform, the differential free energy change in the S-state upon small changes in the number of bound peptides δP is

$$\delta F = -\varepsilon_s \delta P + \sigma \delta A$$

, where $\sigma = K_A \Delta A/A$. For $P/L < P/L^*$, $\Delta A = A_p P$, and the free energy change in the S-state normalized to per lipid for a finite (rather than infinitesimal) change in P/L is

$$\begin{aligned} \Delta F/L &= \Delta f = -\varepsilon_s(P/L) + (1/2)K_A A_L (\Delta A/A)^2 \\ &= -\varepsilon_s(P/L) + (1/2)K_A (A_p^2/A_L)(P/L)^2 = -\varepsilon_s(P/L) + \alpha(P/L)^2 \end{aligned}$$

, where A_p and A_L are the cross-sectional area of the peptide and lipid, respectively. For $P/L \geq P/L^*$, a fraction, $\phi(P/L)$, of the adsorbed peptide may insert and form pores, while

the remainder, $(1 - \phi)(P/L)$, are in the S-state [149]. Rewriting the above expression as [149]

$$\Delta f = -\varepsilon_S(1 - \phi)(P/L) - \varepsilon_I\phi(P/L) + \alpha[(1 - \phi)(P/L) + \beta\phi(P/L)]^2$$

, β expresses the ability of the peptide in the I-state relative to the S-state to thin the membrane; $\beta = 0$ is no thinning, $\beta = 1$ is the I-state thinning is equivalent to that of the S-state. Minimization with respect to ϕ gives

$$(1 - \beta)\phi = 1 - \frac{\frac{\varepsilon_S - \varepsilon_I}{2\alpha(1 - \beta)}}{P/L}$$

, and $\phi = 0$ at the onset of thinning when $P/L = P/L^*$ so the threshold P/L^* is given by

$$(P/L)^* = \frac{\varepsilon_S - \varepsilon_I}{2\alpha(1 - \beta)}$$

and

$$\phi = \frac{1}{1 - \beta} \left(1 - \frac{(P/L)^*}{P/L} \right)$$

. This shows ϕ is linear with respect to $(P/L)^{-1}$. The equilibrium condition [140]

$$\frac{(\varepsilon_S - \varepsilon_I)}{2\alpha(1 - \beta)} = [(1 - \phi)(P/L) + \beta\phi(P/L)]$$

shows thinning (right hand side, in square brackets) is constant above P/L^* .

Transient Pores

Fattal et al. observe quenching kinetics using POPC LUVs with inner or outer leaflet labeled with 1-oleoyl-2-[12-[(7-nitro-1,2,3-benzoxadiazol-4-yl)amino]dodecanoyl] phosphatidyl-choline (NBD-PC) donor lipids in the presence of accepter vesicles containing N-(lissamine rhodamine B sulfonyl)phosphatidylethanolamine (Rh-PE) quencher-tethered lipids [150].

They construct a mass-action kinetic model in which aggregation to form pores mediates fast lipid flip-flop, and aggregation induced membrane perturbation mediates a moderate rate of lipid flip-flop. The extent of melittin induced lipid flip-flop is consistent with the formation of transient pores consisting of two to four melittins.

Matsuzaki et *al.* show that melittin translocates by monitoring the population of surface adsorbed melittin, and by monitoring its passage through multiple multi-lamellar vesicles (MLVs). In the former method, Trp19 fluorescence is quenched by the dansyl chromophore in N-[[5-(dimethylamino)naphthyl]-1-sulfonyl]dipalmitoyl-L- α -phosphatidylethanolamine (DNS-PE) added to egg-PC/PG(\sim 9:1) vesicles. Untranslocated melittin remaining on the outer monolayer can be removed by adding excess vesicles. Recovery of fluorescence upon addition of excess unlabeled vesicles diminishes over time suggesting translocation. In the latter method, sodium dithionite is added to solution to quench N-(7-nitrobenz-2-oxa-1,3-diazol-4-yl)dipalmitoyl-L- α -phosphatidylethanolamine (NBD-PE) present in MLVs. At $P/L = 0.0025$ melittin only permeabilizes the outermost bilayers on the timescale viewed. Above $P/L = 0.005$ dithionite quenching of NBD-PE of the innermost bilayers is apparent. Pore formation of internal layers within MLVs clearly demonstrates melittin translocation.

Wiedman et *al.* combine ANTS/DPX leakage from LUVs with electrical impedance spectroscopy (EIS) to measure the resistance and capacitance of the POPC, POPC/Chol, and POPC/PG(9:1) bilayer [40]. In all cases there is an initial resistance drop quickly followed by recovery in the membrane resistance. These results are consistent with initial rapid transient membrane permeabilization, followed by deactivation first proposed by Tosteson [28].

Mally et *al.* and Kokot et *al.* essentially claim translocation at low melittin concentration occurs upon dimerization of adsorbed melittin [33, 57]. Lee et *al.* propose that transient pores occur by Terwillinger's original mechanism [32]. Adsorbed melittin acts as a wedge distorting the outer leaflet [101]. Melittin's amphipathic character might lend it stability at the bilayer edge and thus stabilize pores. Melittin accumulation on the outer leaflet leads

to formation of transient pores, which facilitate melittin translocation across the bilayer. Transient pores may be induced by fluctuations [13]. Lee *et al.* note the simultaneous expansion of the outer and inner leaflet of single GUVs composed of zwitterionic lipids [54]. They correlate the fractional surface area expansion in single GUVs with the fractional thickness decrease in multilayers. The close correlation between these ratios suggests that the melittin distribution is similar in GUVs and in multilayers before the onset of stable pores. Thus, symmetric expansion of outer and inner leaflet is preceded by melittin translocation via transient pores.

Chapter 2

Methods

IMM1:

Implicit membrane simulations using IMM1 [85, 86] are performed in the canonical ensemble using the molecular dynamics program CHARMM [151, 152]. The effective solute energy (W_{eff}) is the sum of the intramolecular energy based on a modified version of the CHARMM19 force field, and a solvation term (ΔG^{slv}) determined as the sum of contributions from reference (ref) molecular moieties according to a Gaussian exclusion model. The membrane is introduced via a switching function that transitions between the solvation parameters for water and cyclohexane ($chex$)

$$\Delta G_i^{ref}(z) = f(z) \Delta G_i^{ref,water} + (1 - f(z)) \Delta G_i^{ref,chex}$$

where the switching function $f(z)$

$$f(z') = \frac{z'^n}{1 + z'^n}$$

is applied along (z) the membrane normal, T is the membrane thickness, $z' = \frac{|z|}{T/2}$, and n is 10. The thickness of the membrane is set to 27 Å to model a 1-palmitoyl-2-oleoyl-sn-glycero-3-

phosphocholine (POPC) bilayer. This places the interface between the nonpolar hydrocarbon region and the polar head-groups at 13.5 Å above the membrane mid-plane. The steepness of the transition is set by $n = 10$ placing the transition from 90%-nonpolar–10%-polar to 10%-nonpolar–90%-polar solvation between 10.8 Å and 16.8 Å along the z -coordinate. A linear dielectric constant is used to model aqueous solvation, preserving short-range hydrogen bonds while screening against long-range electrostatics.

To prepare the system, melittin monomers are constructed as ideal helices and placed hydrophobic-face down on the membrane surface. Side-chain dihedral angles are adjusted to direct charged or polar moieties out of the membrane interior. Short simulations with melittin’s center of mass placed at 0.5 Å increments along the membrane normal put the binding elevation at 17.5 Å above the membrane mid-plane. The dimer is then minimized at this elevation for 300 steps with the Newton Raphson method [151] allowing side-chains to adopt natural configurations at a planar hydrophobic-hydrophilic interface. Five 1 ns simulations of the three possible dimer configurations are performed using the leap-frog integrator and a 1 fs time-step. A group-based cut-off is placed at 10 Å, with a sigmoidal function [153] switching off nonbonding interactions between 7.0 and 9.0 Å [85]. SHAKE is used to impose rigid bonds involving hydrogen [154]. Calculation of the effective dimerization energy is based on $\langle W(\text{dimer}) \rangle - (2) \langle W(\text{monomer}) \rangle$ [155].

Generalized Born Model: HDGBvdW

The generalized Born model by Still [83, 156] is the standard approximation for Poisson-Boltzmann calculations that allows for analytical calculation of energies and derivatives, furnishing a suitable molecular dynamics force field. The solvation free energy (ΔG_{sol}) is given by

$$\Delta G_{sol} = \Delta G_{cav} + \Delta G_{vdW} + \Delta G_{pol}$$

where ΔG_{cav} is the solvent-solvent cavity term, ΔG_{vdW} is the solute-solvent van der Waals

term, and ΔG_{pol} is the solute-solvent electrostatic polarization of the solvent. For a pure solvent

$$\Delta G_{pol} = -166 \left(1 - \frac{1}{\epsilon}\right) \sum_{i=1}^n \sum_{j=1}^n \frac{q_i q_j}{f_{GB}}$$

$$f_{GB} = \sqrt{r_{ij}^2 + \alpha_i \alpha_j \exp(-r_{ij}^2/4\alpha_i \alpha_j)}$$

where the q 's are the atomic charges, and the α 's are the atomic Born radii.

A heterogeneous dielectric environment [84] is introduced into ΔG_{pol} by defining a local environmental dielectric constant such that

$$\Delta G_{pol} = -166 \sum_i^n \sum_j^n \left(\frac{1}{\epsilon_p} - \frac{1}{\epsilon_{ij}(\epsilon_i, \epsilon_j)} \right) \left(\frac{q_i q_j}{\sqrt{r_{ij}^2 + \alpha_i \alpha_j \exp(-r_{ij}^2/4\alpha_i \alpha_j)}} \right)$$

where $\epsilon_{ij}(\epsilon_i, \epsilon_j) = \frac{1}{2}[\epsilon'(z_i) + \epsilon'(z_j)]$ is the arithmetic mean between local dielectrics at positions z_i and z_j . Each $\epsilon'(z)$ is obtained from the Born equation [82] for an ion probe with charge q , radius a (Å), and the electrostatic solvation free energy ($elst$) from Poisson theory

$$\Delta G_{elst}(z) = -166 \left(1 - \frac{1}{\epsilon'(z)}\right) \frac{q^2}{a}$$

The two main approximations associated with calculating Born radii (α_i) are the molecular volume [157, 158] or surface [156] and the Coulomb field approximation (CFA) [159, 160]. The effective Born radius, α_i , depends on the solute and solvent dielectric, and is estimated as [84]

$$\alpha_i(\epsilon_w, \epsilon_p) = \frac{1}{C_0 A_4 + C_1 \left(\frac{3\epsilon_w}{3\epsilon_w + 2\epsilon_p} \right) A_7} + D + \frac{E}{\epsilon_w + 1}$$

where $C_0 = 0.3225$, $C_1 = 1.085$, $D = -0.14$, and $E = -0.15$. A_4 is the CFA

$$A_4 = \left(R_i^{-1} - \frac{1}{4\pi} \int \int_{R_i}^{\infty} \frac{V(\vec{r})}{|\vec{r} - \vec{x}_i|^4} dr d\Omega \right)$$

, and A_7 is an empirical correction term to the CFA [158]

$$A_7 = \left(\frac{1}{4R^4} - \frac{1}{4\pi} \int \int_{R_i}^{\infty} \frac{V(\vec{r})}{|\vec{r} - \vec{x}_i|^7} dr d\Omega \right)^{1/4}$$

The molecular volume is defined based on a switch function that transitions from one inside the molecule to zero at the surface, and the superposition of atomic functions S [158]

$$V(S) = \frac{1}{1 + \exp(\beta(S - \lambda))}$$

where $\lambda = 0.5$ is chosen such that generalized Born solvation energies best match Poisson energies. $\beta = -12$ controls the width of the switching function. The superposition of atomic functions is defined as [158]

$$S(\vec{r}) = S_0 \left[\sum_j F(|\vec{t}_j|) \right] \frac{\sum_j |\vec{t}_j|^2 F^2(|\vec{t}_j|)}{\left\| \sum_j \vec{t}_j F(|\vec{t}_j|) \right\|^2}$$

where $\vec{t}_j = \vec{r} - \vec{x}_j$, and x_j is the atomic position. $S_0 = 0.65$ is an empirical adjustable parameter. The first term in brackets is a superposition of atomic functions. The second term is a scaling factor to enhance the “gap” regions and diminish the “open” regions, which tend to be under and over represented, respectively, by the van der Waals surface. This superposition mimics the standard molecular volume (Lee-Richards surface). The choice of

atomic function is based primarily on computational efficiency

$$F(\vec{t}_j) = \frac{C_j^2}{(C_j + ||\vec{t}_j||^2 - R_j^2)^2}$$

where $C_j = P_1 R_j + P_2$, and $P_1 = 0.45$ and $P_2 = 1.25$ are empirical fitting parameters. The function's tail is smoothly truncated between $1.9 - 2.1$ Å using the switching function

$$f(u) = \begin{cases} 1 & u \leq 0 \\ 1 - 10u^3 + 15u^4 - 6u^5 & 0 < u < 1 \\ 0 & u \geq 1 \end{cases}$$

The cavity term of the solvation free energy is [161]

$$\Delta G_{cav} = \sum_{i=1}^N \gamma S(z) SASA_i$$

where the surface tension γ is 0.038 kcal/mol/Å². The nonpolar profile, $S(z)$, ranges from zero at the middle of the membrane to one in solution (fig.3 in ref. [161]). The solute $SASA_i$ is the solvent accessible surface area of atom i .

The van der Waals term is approximated by

$$\Delta G_{vdW} = \sum_i^N \sum_j^M a_i \frac{A_{i,j}}{(\alpha_i + R_j)^3}$$

where i is the index over all solute atoms, and j is the index over all solvent atom types, including lipid hydrogen, oxygen, as well as tail and head-group (including glycerol backbone) carbons, and water oxygen. There is a dimensionless fitting parameter, a_i , for each solute atom type. The Born radius of solute atom i is α_i . R_j is the radius of the solvent probe

atom. The function $A_{i,j}$ is used to introduce change in solvent type

$$A_{i,j} = -\frac{16\pi}{3}\rho_j(z)\epsilon_{ij}\sigma_{ij}^6$$

where ϵ_{ij} , and σ_{ij} are Lennard-Jones parameters based on dipalmitoylphosphatidylcholine in CHARMM36 [162], and TIP3P water [163]. The density profile for solvent atom type $\rho_j(z)$ is based on the radial distribution function obtained from atomistic simulation. The parameters a_i , $S(z)$, and γ were optimized to reproduce insertion free energy profiles of amino acid side chains.

The radial integration grid goes up to 20 Å (with grid points at 0.1, 0.2, 0.3, 0.4, 0.5, 0.75, 1.0, 1.25, 1.5, 1.75, 2.0, 2.5, 3.0, 3.5, 4.0, 5.0, 6.0, 7.0, 8.0, 10.0, 12.0, 16.0, 20.0). A spherical polar angular integration grid is used with eight ϕ grid angles, and θ angles are chosen in regular intervals varying with ϕ . A lookup table restricts the molecular volume calculation to atoms in the neighborhood of a grid cell. An atom contributes to a grid cell if it is less than a distance r_{max} from the center of the cell, where $r_{max} = R_i + 2.1 + \frac{\sqrt{3}}{2}c + r_{buffer}$. The 2.1 Å term is the tail length of the atomic function. The term c , the cell width of the lookup grid, is 1.0 Å. The distance that any atom is allowed to move before the lookup table is rebuilt, r_{buffer} is 0.2 Å.

All-Atom Simulations for PMF Calculation

The pre-assembled surface adsorbed melittin dimer at the separation of free energy minimum in IMM1, and at 20 Å separation, are oriented along the x -axis and minimized in IMM1 before being introduced into an explicit membrane using the replacement method [164, 165, 166]. 1-palmitoyl-2-oleoyl-sn-glycero-3-phosphatidylcholine (POPC) bilayer systems are built with the CHARMM-GUI [167, 168, 169, 170]. Small and big systems consist of a 9 nm × 9 nm, and a nearly 12 nm × 12 nm membrane patch, respectively (table. 2.1). For each lipid 60 waters are added to super-saturate the system. Chloride ions are included for

electroneutrality.

The molecular dynamics package GROMACSV5.1 [171, 172, 173, 174, 175] is used, employing the CHARMM36 all atom force field [176, 177], with CMAP corrections [178], and updates for lipids parameters [162]. Waters are treated with the CMAP TIP3P model [163, 179, 180].

Production level simulations are performed in the NPT ensemble. The temperature is maintained above the POPC gel-liquid phase transition [181] at 298.15 K using the velocity rescale algorithm [182] with a coupling constant τ of 1 ps. The pressure is set to 1 bar with a semi-isotropic coupling method [183], with a τ of 5.0 ps, and a compressibility of $4.5 \times 10^{-5} \text{ bar}^{-1}$. The equations of motion are integrated using a 2 fs time-step and the leap-frog integrator. Neighbor lists are generated using the Verlet scheme and non-bonded interactions are cut-off at 1.2 nm. A force-based switching-function is switched [184] on at 1.0 nm to smooth the transition near the van der Waals cut-off. Long-range electrostatics are accounted for using the PME method [185, 186]. Covalent bonds to hydrogen are rigidified using the LINCS algorithm [187]. Initial equilibration of the pre-assembled system is achieved using the sequence of steps recommended by the CHARMM-GUI [166].

System	Atoms	Peptides	Lipids (upper, lower)	Waters	Ions	Duration	Dimensions
melittin dimer (small)	71214	2	(104, 120)	13440	10 Cl ⁻	(90, 90, 97)	
melittin dimer (big)	124594	2	(189, 205)	23640	10 Cl ⁻	(118, 118, 99)	
melittin monomers	124914	2	(189, 206)	23700	12 Cl ⁻	(118, 118, 99)	

Table 2.1: System setup for all-atom melittin dimer simulations.

Umbrella Sampling :

In implicit simulations the order parameter (OP) for the dimerization path is defined by a cylindrical harmonic restraint applied to the distance between the center of mass of the respective monomers. In PMF calculations [92, 188] using IMM1 and HDGB umbrella sampling [89, 90] windows are taken every angstrom. Force constants in IMM1 and HDGB

are shown in figs. 5.1, 5.11, respectively. Umbrella sampling windows are made in 1 Å intervals, and each starting configuration is generated according to the above *ad hoc* procedure. In IMM1 simulations the latter half of 5ns including 2500 data points is used for WHAM analysis. In HDGB simulations the last 4 ns of 5 ns simulations including 40000 data points are used for WHAM analysis.

Pulling methods are used in all-atom simulations to generate the starting configuration for each umbrella sampling window. To separate the pre-assembled melittin dimer (helices oriented with the *x*-axis) one peptide is held in place by harmonic restraints of 10 kcal/mol/Å² and 5 kcal/mol/Å² on the backbone and side-chain heavy atoms, respectively, while the other is pulled by its center of mass at a constant velocity of 0.5 Å/ns by a fictitious tether [172, 189] in the *y*-direction. A harmonic pulling force of 5 and 10 kcal/mol/Å² is used in small and big systems, respectively. In the small system umbrella sampling windows are generated every 0.5 Å (fig. 5.22) and a harmonic restraint (fig. 5.23) is applied on the *y*-distance between the peptides' respective center of mass. In the big system umbrella sampling windows are generated every 0.8 Å (fig. 5.25) and a harmonic restraint (fig. 5.26) is applied on the *xy*-distance between the peptides' respective center of mass. An additional 16 windows (fig. 5.27) are introduced between those in the big system starting from 0.945 nm *xy*-separation, and restraints for all windows are shown in fig. 5.28. To assemble the rubin dimer from 20 Å separation between the monomers a constant force of 0.5 kcal/mol/Å is applied along the vector connecting the center of mass of tryptophan 19 residues of respective monomers. Umbrella sampling windows are taken every angstrom and a harmonic bias is applied on the distance between the center of mass of respective tryptophan 19 residues. An additional three windows are generated between those closest to the rubin dimer 5.40 to improve sampling.

Un-biasing of the distributions from each umbrella sampling window is performed using WHAM [93]. The resulting unbiased distributions are used to reconstruct the PMF along

the order parameter (ξ) according to

$$W(\xi) = W(\xi^*) - \beta^{-1} \ln \left[\frac{\langle \rho(\xi) \rangle}{\langle \rho(\xi^*) \rangle} \right]$$

, where ξ^* is the reference configuration. For GROMACS simulations the PMF profile is constructed using gmx_wham [190]. Bootstrapping error analysis is performed to generate error bars for the PMF profile. The bootstrap trajectory for each umbrella sampling window is determined based on the decorrelation time of the order parameter for a particular window. For implicit simulations the PMF profile is constructed using the Grossfield WHAM program [191]. Here the entire trajectory is used for bootstrapping error analysis.

A Jacobian correction [192] arising from the use of restraints may result in a fictitious force [193] acting along the order parameter (ξ)

$$-k_B T \frac{\partial \ln|J|}{\partial \xi}$$

where $|J|$ is the determinant of the Jacobian, k_B is Boltzmann's constant, and T is the temperature. For restraint on the distance (d) in the xy -plane between two non-interacting point particles the contribution to the PMF that must be removed is [194] $-k_B T \ln(d)$. This contribution is ignored given the complexity of the system noting that the correction rigorously applies for point particles.

Free Energy Correction due to PME under PBC :

Free energy calculations based on molecular dynamics simulations under periodic boundary conditions are susceptible to finite-size error due to periodicity-induced net-charge interactions, periodicity-induced undersolvation, discrete solvent effects, and residual integrated potential effects [195]. The formalism for determining such effects for ligand binding by

Rocklin et al.

$$\Delta G_{binding} = \Delta G_{bound} - \Delta G_{free}$$

is adapted here for peptide dimerization on the membrane surface. The error is dominated by the electrostatic contribution, while the influence of van der Waals interactions is negligible

$$\Delta G_{binding} \approx \Delta G_{charge,bound} - \Delta G_{charge,free}$$

. The free energy under non-periodic boundary conditions (NBC) can be obtained by molecular dynamics simulation under periodic boundary conditions (PBC) with a correction for the use of particle mesh Ewald [195] such that

$$\Delta G_{NBC} = \Delta G_{PBC} + \Delta \Delta G_{corr}$$

The correction to the free energy due to periodicity-induced net-charge interactions, periodicity-induced undersolvation, and residual integrated potential effects is accounted for using a numerical correction scheme (*NUM*) [195]

$$\Delta \Delta G_{NUM} = \Delta G_{NBC} - \Delta G_{PBC}$$

. The charging free energy under NBC and under PBC are calculated using Poisson-Boltzmann calculations under NBC and PBC, respectively. The maximum dimer separation tested is considered the monomeric or free state. The correction to the PMF is computed for each umbrella sampling window as the difference between the correction for a particular window minus the correction for the monomer. The starting dimer configuration of umbrella sampling windows is used to ensure proper membrane binding in the Poisson-Boltzmann

calculations.

Finite-size effects are investigated generally. If counter-ions are included in the molecular dynamics to neutralize the system then a neutralizing charge density should be included in the Poisson-Boltzmann calculation [195]. Rocklin et *al.* place a distribution of partial counter chargers around the negatively and positively charged atoms to neutralize the protein. Here, a sodium or chloride counter-ion is placed 2 Å above each charged peptide atom and the system is minimized for 300 steps with the Newton Raphson method [151]. Rocklin et *al.* also include bound waters as part of the solute. Bound waters are ignored here. The most relevant corrections to the PMF profile occur at the larger values of dimer separation, where artifacts from PBC are most likely to occur.

Poisson-Boltzmann calculations are performed in CHARMM [151, 152] with CHARMM 36 [176] for protein [177, 196, 197] and ions [198]. To obtain $\Delta G_{N\!B\!C}$ we solve the Poisson-Boltzmann equation at twice the box size of the all-atom simulations. The parameters are identical for solving the Poisson-Boltzmann equation under NBCs and PBCs. Grid spacing is 0.05 nm, and the dielectric permitivity of water, protein, and membrane are set to 97.0, 1.0, and 4.0, respectively. The solute boundary is defined using the Lee-Richards reentrant model with a water radius of 1.4 Å [199]. The Debye-Huckel approximation is used to determine the boundary potential under both NBCs and PBCs [200]. The Poisson-Boltzmann equation is solved using the method of successive over relaxation [201, 202]. The membrane thickness is 27 Å, and the temperature is set to 298.15 K.

Anton Simulations :

Anton simulations of the pre-assembled melittin dimer at 8.5 Å and 20 Å dimer separation are prepared in the same way as for umbrella sampling simulations. Macrolittin70 and pHD15 hexameric pores suitable for pore formation by the parent peptide MelP5 are prepared as previously described [62, 203]. Neutral systems with balancing counter ions were built with

the CHARMM-GUI [167, 168, 169, 170] using 180 POPC lipids and a water slab at least 17.5 Å thick above and below the bilayer (table. 2.2). Simulations were performed on Anton 2 [78] in the NPT ensemble using the CHARMM 36 force field [196, 204] and TIP3P water [163]. The equations of motion are integrated using the multigrigator [205] with a 2.5 fs time-step. 310 Kelvin and 1 bar pressure are maintained using the Nose-Hoover [206] thermostat and MTK [207] barostat, respectively. The thermostat and barostat are implemented every 240 and 24 steps, respectively. Long-range electrostatics are computed using the Gaussian split Ewald [208] method. Short-range electrostatics are cut-off between 10-13 Å as determined by Anton based on the atom pair, and are computed every 3 steps.

Table 1.

System	Atoms	Peptides	Lipids	Waters	Ions	Duration	Dimensions
macrolittin70 (neutral pH)	49257	6	180	7541	6 K ⁺	10 μs	(84.8, 84.8, 77)
macrolittin70 (acidic pH)	49227	6	180	7523	12 Cl ⁻	10 μs	(84.8, 84.8, 77)
pHD15 (acidic pH)	49131	6	180	7517	12 Cl ⁻	10 μs	(84.2, 84.2, 77.2)
pHD15 (neutral pH)	49110	6	180	7518	36 K ⁺	10 μs	(84.2, 84.2, 77.2)

Table 2.2: System setup.

Analysis of Transmembrane Pores:

Minimum pore radius is measured based on the water column spanning the bilayer [62]. Helix tilt angle is computed using the algorithm by Chothia [209] implemented in the CHARMM `coor helix` command. The average membrane thickness based on phosphorus is calculated with GridMAT [210] using 25 grid points in each dimension; protein and waters are ignored. Level curves are shown in the appendix (figs. 5.41, 5.42, 5.43, 5.44). Interaction energies are calculated with the CHARMM `inte` command, and H-bonding and van der Waals contacts are identified with the CHARMM commands `coor hbond`, and `coor cont`. The H-bonding criteria, 2.4 Å bond length and bond angle $\leq 120^\circ$, of DeLoof [211] and Aqvist is used [212].

The R `cor()` [213] function is used to measure the Pearson [214] correlation coefficient

between N- and C-terminal helices within and between peptides. The Pearson correlation ($\in [-1, 1]$) is a parametric measure of the linear relationship between two time series. Pearson's r is suitable for analysis given the lack of measurement noise in simulation data [215]. First differences, $x'_i = x_{i+1} - x_i$, of the time series are used to control for underlying trend in the data. When the p-value is less than $\alpha = 1^{-10}$ the null hypothesis (H_0 : no correlation) is rejected. A two-sided test is used for positive or negative correlation. The R program is also used to demonstrate the underlying assumptions. The `shapiro.test()` function is used to demonstrate the underlying distributions are normal using the Shapiro-Wilk [216] test, with $\alpha = 0.05$. The `bptest()` function of the `lmtest` package [217] is used to test for homoscedasticity between the two time series using the Breusch-Pagan [218] test, with $\alpha = 0.05$.

Chapter 3

Results

IMM1: Melittin Dimerization on the Membrane Surface

When melittin is horizontally adsorbed on the membrane surface the unique tryptophan 19 (Trp19) residue is positioned on the left side of the helix with respect to the N-terminus. The nomenclature, rubin and janus, is used to distinguish between the two possible anti-parallel dimer configurations. The rubin dimer has Trp19 oriented toward the dimer interface. Janus orientation places respective Trp19 residues facing in opposite directions, away from the dimer interface. IMM1 simulations to determine the relative effective energies for lateral melittin dimer formation on the membrane surface show the rubin dimer is slightly preferred to the janus dimer, which is more stable than the parallel configuration (table. 5.1).

There is good overlap between umbrella sampling windows (fig. 5.2). The PMF profile (fig.3.1) shows the rubin dimer is stable. As the simulation for each window becomes longer, and as more of the initial equilibration phase is removed, the PMF profiles tend to converge (figs. 5.3 – 5.10). The last 2.5 ns of 5 ns simulations are considered sufficiently equilibrated. The free energy minimum occurs between 10–11 Å with a 24 kcal/mol barrier to separate the dimer. The rubin dimer is fully separated at 40 Å.

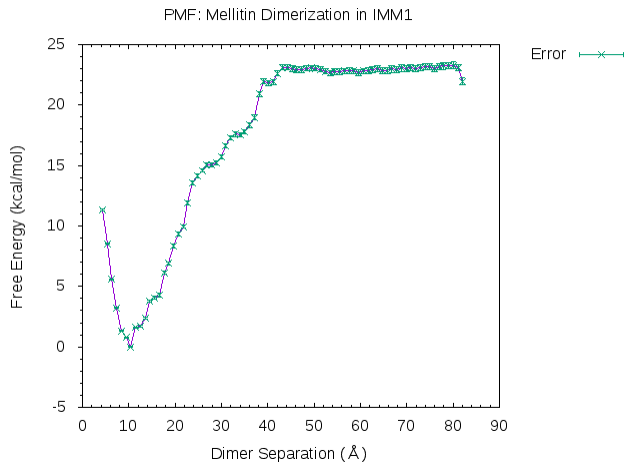


Figure 3.1: The PMF profile for the rubin dimer in IMM1 using a cylindrical restraint. Each umbrella sampling window corresponds to the last 2.5 ns of a 5 ns simulation.

HDGBvdW: Melittin Dimerization on the Membrane Surface

Repeating the PMF calculation with the HDGBvdW model [161] shows good overlap between umbrella sampling windows (fig. 5.12). Again, as the simulation for each window becomes longer, and as more of the initial equilibration phase is removed, the PMF profiles tend to converge (figs. 5.13 – 5.20). The last 4 of 5 ns of each window is used to generate the final PMF profile (fig. 3.2), which suggests the rubin dimer is difficult to access. The ascent along the rubin dimerization path begins between 22 to 23 Å separation with a 7 kcal/mol barrier to bring the monomers within 12 Å of each other.

Unrestrained simulations of pre-assembled melittin dimers on the HDGBvdW surface confirm dimers are unstable. Over the course of 0.5 ns both the pre-assembled rubin 3.3 and janus 3.4 melittin dimers separate.

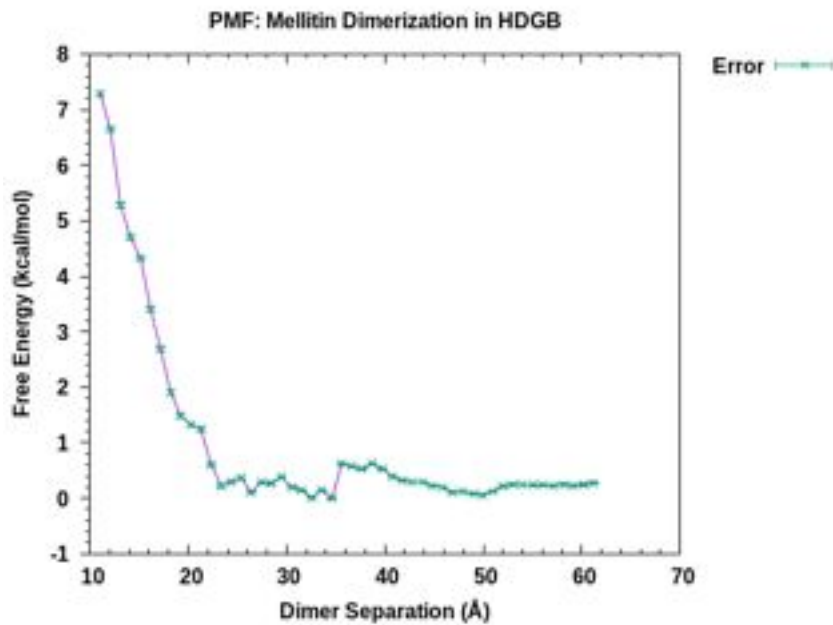


Figure 3.2: PMF profile for the rubin dimer in vdwHDGB using a cylindrical restraint. Last 4 of 5 ns of each US windows were used to compute the PMF profile. Error estimate involves 200 bootstrap trajectories.

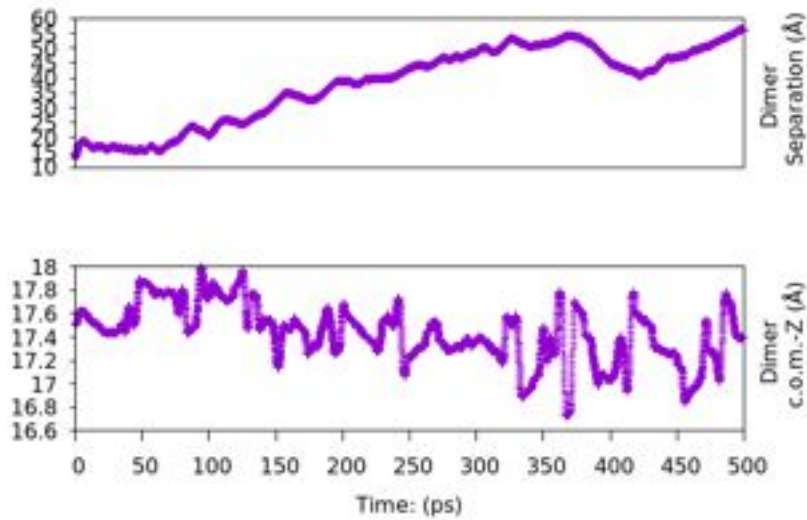


Figure 3.3: Unrestrained simulations of melittin on the HDGB membrane surface starting from the pre-assembled rubin dimer.

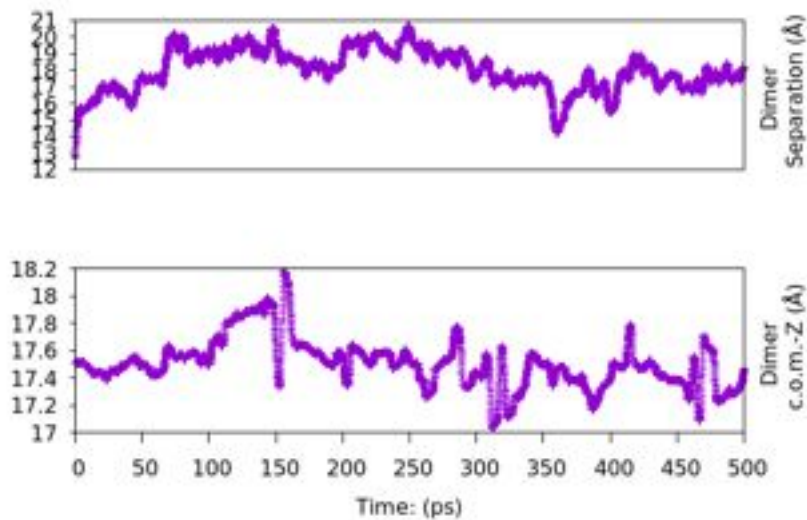


Figure 3.4: Unrestrained simulations of melittin on the HDGB membrane surface starting from the pre-assembled janus dimer.

All-Atom Simulations: Melittin Dimerization on the Membrane Surface

The PMF profile for formation of the rubin dimer is explored along the separation process on a small as well as a big membrane patch. Using a $9\text{ nm} \times 9\text{ nm}$ membrane patch the pre-assembled rubin melittin dimer (with helices oriented with the x -axis) is separated along the distance between the peptides' respective center of mass in the y -direction. For the same peptide setup on a roughly $12\text{ nm} \times 12\text{ nm}$ membrane patch the dimer separation is measured in terms of the distance between the peptides' respective center of mass within the xy -plane. The results of 50 ns umbrella sampling windows for PMF calculations for both systems are shown in fig. 3.5. The PMF profile for the small system shows the rubin dimer is stable and increases monotonically with separation. The PMF profile for the big system has the same functional form as the IMM1 PMF. Both small and big systems show a global minimum at a slightly smaller dimer separation in explicit solvent compared to IMM1, around 8 Å. There should not be such a large difference between the two profiles despite the difference in order parameter, suggesting a dependence on system size in the all-atom PMFs.

The simulations are far from being fully equilibrated. When each umbrella sampling window in the big system is brought up to 100 ns the free energy barrier to separate the dimer falls. Furthermore, progressively removing the early equilibration stages of the windows continues to bring down the PMF profile. The PMF using 40 to 100 ns of the trajectory in each window shows the distance at which monomers are fully separated occurs around 3.0 nm 3.6 with a 9 kcal/mol barrier.

The PMF for formation of the rubin dimer is also investigated along the aggregation process. The distance between the center of mass of respective melittin monomers cannot be used to aggregate the peptides because a layer of lipids persists between the monomers. The distance between tryptophan 19 residues of respective monomers is used to assemble a rubin dimer. The PMF along this pathway shows that there is a significant barrier to aggregation (fig. 3.7). This contradicts the results of all-atom simulations that start from the

pre-assembled dimer. Progressively truncating the initial equilibration stage of the umbrella sampling windows (fig. 5.29) shows an 11 kcal/mol repulsive barrier begins at 0.9 nm that levels off between 0.55 nm and 0.6 nm, when Trp19 residues are adjacent and in direct contact.

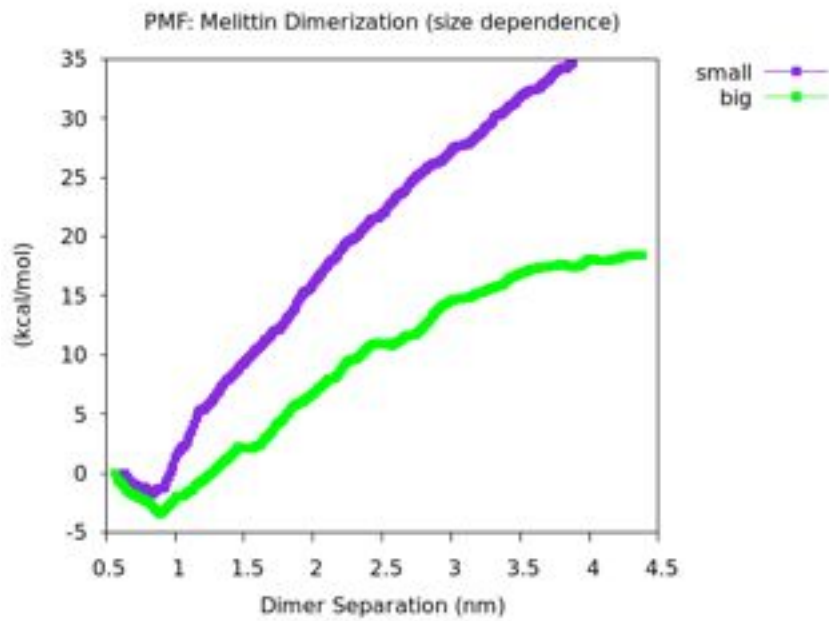


Figure 3.5: The PMF profiles for dimer separation based on US windows generated by pulling the pre-assembled rubin melittin dimer apart demonstrate dependence on system size. The PMF reaches a maximum for the big system (green), while it increases monotonically for the small system (purple) without reaching a plateau.

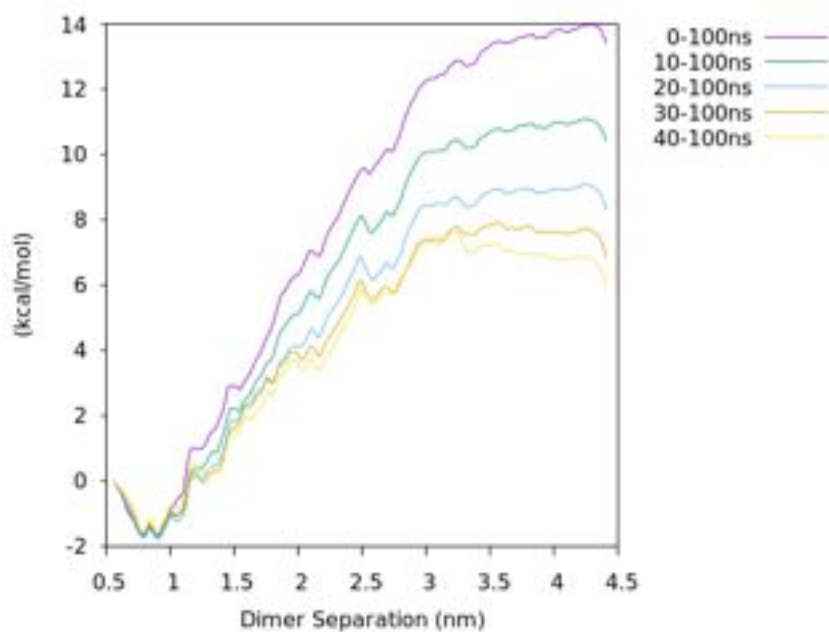


Figure 3.6: PMF profiles for melittin dimerization in the big system with umbrella sampling windows brought up to 100 ns. Different curves show the effect on the PMF when the beginning of the simulation is progressively truncated in each window.

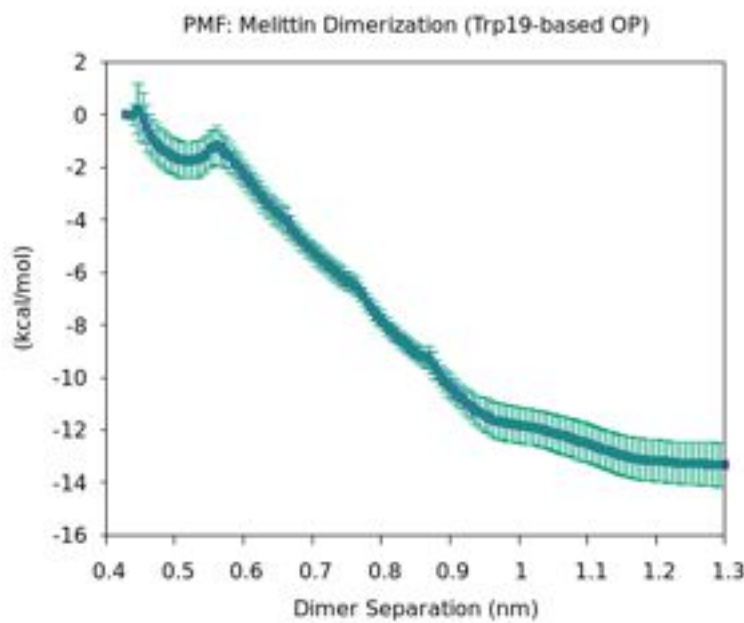


Figure 3.7: The PMF profile with error bars for aggregation along the distance between Trp19 residues of respective melittin monomers. 200 boot-strap trajectories are used to generate error bars.

Correction to the All-Atom PMF Profile

The difference in the PMF profiles for separating the pre-assembled rubin melittin dimer in small and big all-atom systems suggests there is some dependence of the PMF profile on the system size. One possibility is that there are artifacts due to the use of PME in combination with PBCs [195]. A version of the correction scheme proposed by Rocklin *et al.* is used to assess the correction needed in PMF calculations for melittin dimerization on the membrane surface. An estimate for the correction along the dimerization path for the small system is shown in figure 3.8. The values at large separations as peptides approach those in the periodic image are the most relevant. As the distance between the peptides increases the correction oscillates close to zero. This suggests the difference between the PMFs for separating the rubin dimer in the small and in the large systems is not caused by artifacts due to the use of PME and PBCs in all-atom simulations; even a $9\text{ nm} \times 9\text{ nm}$ membrane patch should be sufficiently large to avoid such artifacts.

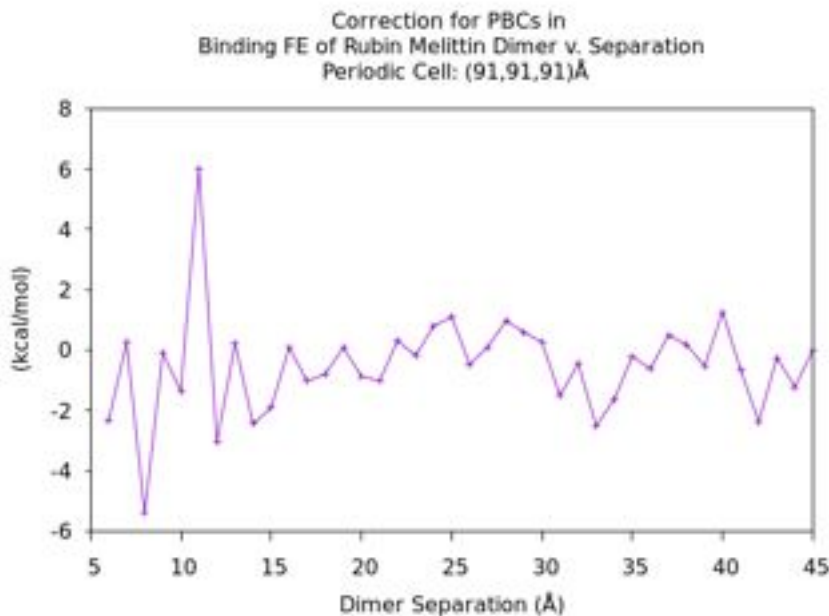


Figure 3.8: Correction to the PMF profile for the use of PME with PBCs at each US window.

Anton Simulations: Melittin Dimerization on the Membrane Surface

The pre-assembled rubin dimer on a roughly $12 \text{ nm} \times 12 \text{ nm}$ membrane patch is simulated on Anton for multiple microseconds. Over $3.5 \mu\text{s}$ monomers of the pre-assembled rubin dimer at 1.75 nm separation between the peptides' respective center of mass remain separated. The pre-assembled rubin dimer at 0.8 nm separation remains intact for $1 \mu\text{s}$ (fig. 3.9) but subsequently disassembles and a dimer aggregate never reforms.

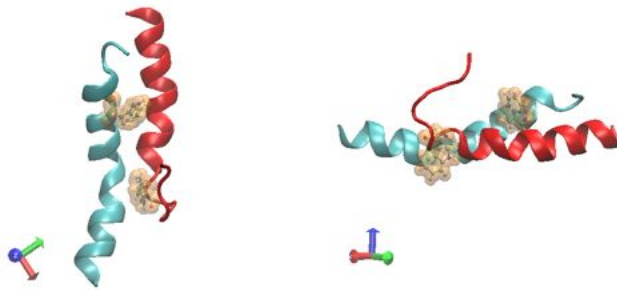


Figure 3.9: Structure of pre-assembled melittin rubin dimer after $1 \mu\text{s}$. (Left) Top view. (Right) Side view.

Anton Simulations: Macrolittins and pH Dependent Peptides

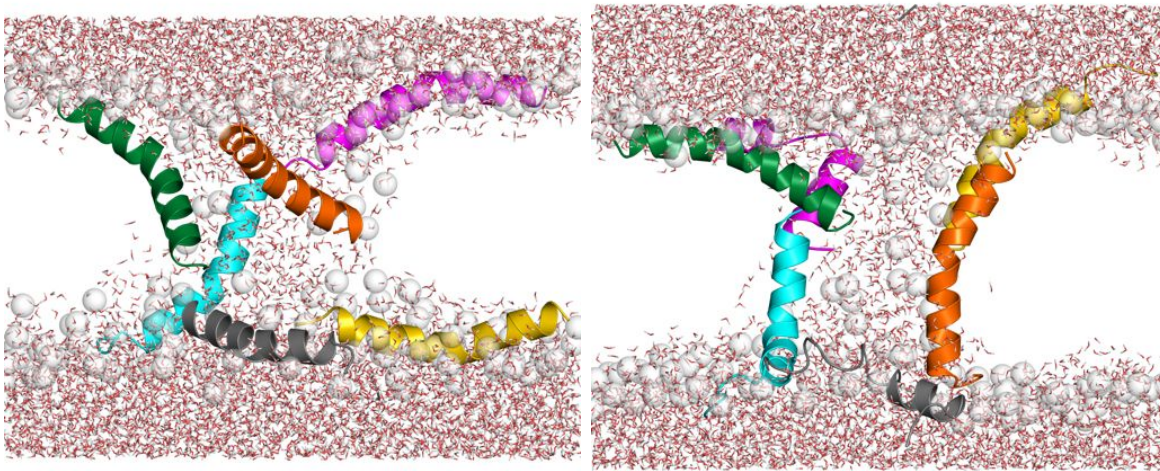


Figure 3.10: (Left) pHD15 at pH 7 at $2 \mu\text{s}$. (Right) pHD15 at pH 7 at $10 \mu\text{s}$. Side view (N-term up). Water shown as sticks colored by atom type. Lipid phosphorus shown as transparent white spheres.

We simulate pHD15 and mac70 pores at P/L ratios suitable for pore formation by the progenitor melittin [46] starting from a putative structure for the parent peptide MelP5 [62]. The parallel orientation of the peptides in the pore assembly was hypothesized for the macrolitins [23] based on the helical wheel diagram for the template monomer (fig. 1.1). Using a helical wheel diagram of the entire helix Li *et al.* propose the parallel orientation facilitates interaction between the cationic residue at position 7 and the anionic mutation at position 8, and maximizes the hydrophobic surface exposed to lipid tails [23]. pHD peptides are random coil and are not fully adsorbed on the membrane surface at neutral pH [22]. The pre-assembled pHD15 pore serves as a control and is destined to collapse. At $2 \mu\text{s}$ half the peptides have left the pore although a large water column remains (fig. 3.10). Most peptides remain helical up until this point but many subsequently unfold at least in part. Over the course of the trajectory multiple peptides are able to move from one leaflet to the other via the aqueous pore. Peptides remain adsorbed near the pore edge biased by the initial

conditions [203]. Numerous membrane phosphates line the water column to accommodate a toroidal pore as the membrane cannot eject peptides to heal itself due to limited available water.

Pore Structures

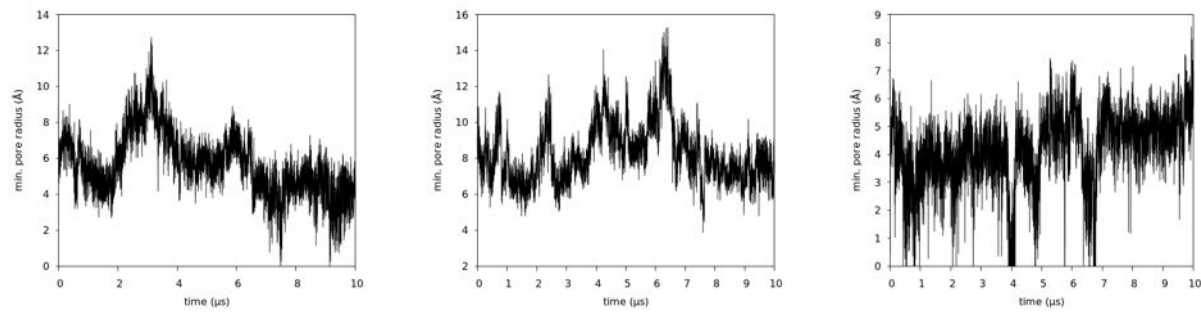


Figure 3.11: pHD15 at acidic pH. Macrolittin70 at neutral pH. Macrolittin70 at acidic pH. Time series of the minimum pore radius.

Stable pores are formed by mac70 and pHD15 under optimal pH, as well as under sub-optimal conditions (pH 5) by mac70, in accordance with leakage experiments [22, 23]. Time series of minimum pore radius show equilibration can be reasonably assumed after about 8 μs for each simulation (fig. 3.11), comparable to alamethicin pores [219]. Mac70 at pH 7 is the only pore that stays open for the entire simulation. The mac70 pore at pH 5 is the most dynamic and closes repeatedly during the 8 μs prior. The pHD15 pore at pH 5 occasionally closes and is the most narrow in the end.

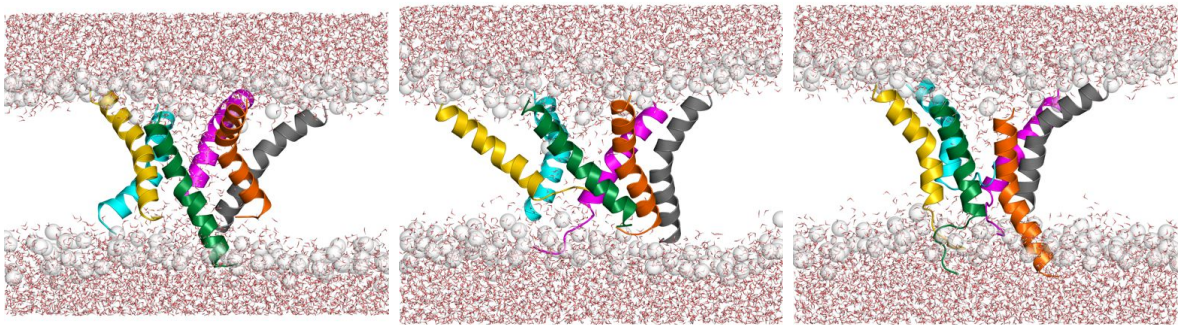


Figure 3.12: (Left) Macrolittin70 at pH 7. (Middle) Macrolittin70 at pH 5. (Right) pHD15 at pH 5. Side view (N-term up) at 10 μ s.

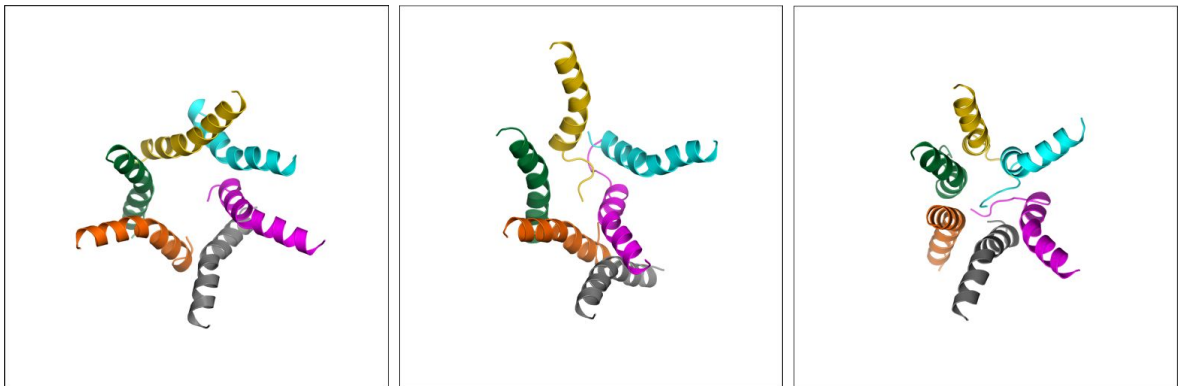


Figure 3.13: (Left) Macrolittin70 at pH 7. (Middle) Macrolittin70 at pH 5. (Right) pHD15 at pH 5. Top view (N-term up) at 10 μ s.

Figures 3.13 and 3.12 show top and side views of pore structures at 10 μ s. In simulations of macrolittin70 at pH 7 and 5, and pHD15 at pH 5, peptides remain transmembrane over the entire trajectory, in contrast to MelP5 in POPC where one of the peptides moves to the surface of the upper leaflet but remains near the pore edge (unpublished work by Dr. Pino-Angeles).

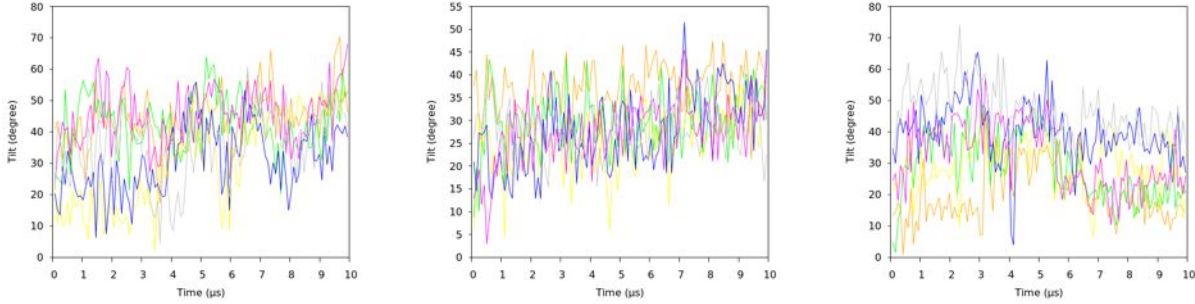


Figure 3.14: (Left) Macrolittin70 pore at pH 7. (Middle) Macrolittin70 pore at pH 5. (Right) pHD15 pore at pH 5. Helix tilt v. time for 10 μ s simulation.

Overall tilt angles are fairly large while peptides remain transmembrane. At pH 5, helix tilt of mac70 and pHD15 equilibrates over the last 2 μ s of the trajectory, while at pH 7 mac70 helix tilt continues to oscillate (fig. 3.14). Peptides are generally in the tilted (T) state (tilt angles 30 – 60°) in contrast to the ancestral peptides, which typically remain in the (I) state (tilt angles 0 – 30°) when participating in the pore [61, 62]. MelP5 in POPC shows three peptides in the T-state and one in the I-state while two are significantly tilted at 60 and 70 degrees (unpublished data by Dr. Pino-Angeles). pHD15 at pH 5 is the most vertically oriented with multiple peptides returning to the I-state. During the last 2 μ s the kink angle between N- and C-terminal helices remain reasonably stabilized (fig. 5.35). Helix kink angles for mac70 and pHD15 are in the range of melittin (140-160° in DMPC) [43] but can be more severely kinked.

Almost all peptides lean to an extent toward the clockwise adjacent peptide in accordance with their neighbors. Time series of the helix cross angle between peptides on opposite (i to $i + 3$) sides of the pore show here left handed knob-into-hole helix packing between adjacent peptides [220] confers a right handed helical spiral to the peptide assembly along its C₆ symmetry axis. Mac70 at pH 7 is the most twisted with the largest cross angles, while pHD15 at pH 5 shows some of the smallest cross angles.

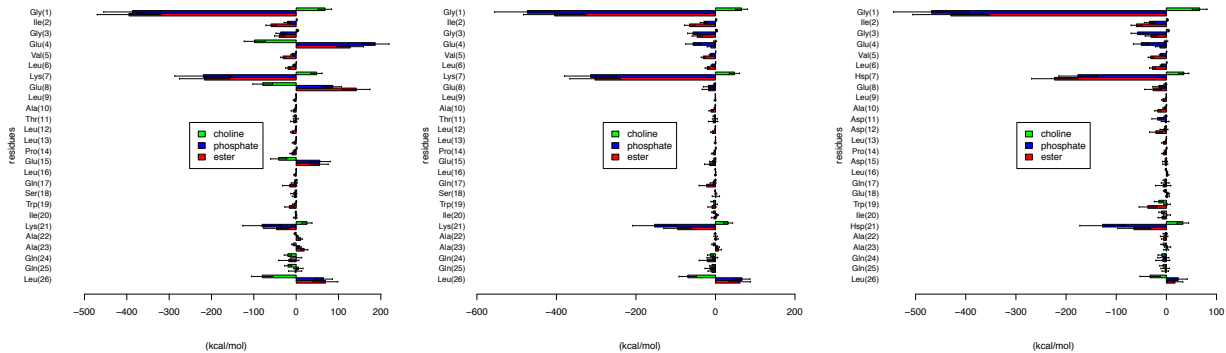


Figure 3.15: (Left) Macrolittin70 pore at pH 7. (Middle) pHD15 pore at pH 5. (Right) Macrolittin70 pore at pH 5. Bar plot of average interaction energy and standard deviation between residues and polar lipid components.

N- and C-terminal halves partition well to opposite sides of the membrane (fig. 3.12).

Figure 3.15 shows average interaction energy between peptide residues and polar moieties of lipid head groups. In all pores the peptides' N-terminal half anchors to phosphate and esters via the cationic residue seven (Cat7) and the N-term. For mac70 at pH 7 these interactions are diminished compared to the others due to repulsion by anionic Glu(4,8). In mac70 at pH 7 attraction by Glu(4,8) overcomes the choline repulsion by the N-term and Lys7 seen at pH 5. At pH 7 the C-terminal half of mac70 has overall unfavorable interactions with phosphate and esters, whereas at pH 5 C-terminal halves of pHD15 and mac70 have overall favorable phosphate and esters interactions. Repulsion of phosphate and esters by mac70's C-terminal half at pH 7 is due to the C-term and the anionic Glu15 overcoming Lys21 attraction. Lys21 attraction to phosphate and esters is partly limited by competition for Lys21 by the C-term, which is also repulsive toward phosphate and esters. In all systems contributions from the C-terminal half accompany choline attraction by the C-term to overcome choline repulsion by Lys21. Deviations from the overall pattern of interaction with lipid polar moieties by individual peptides (figs. 5.45, 5.46, 5.47) are largely due to competition from other peptides (fig. 3.16), which also helps the stabilize transmembrane helices.

Peptide–Peptide Interactions

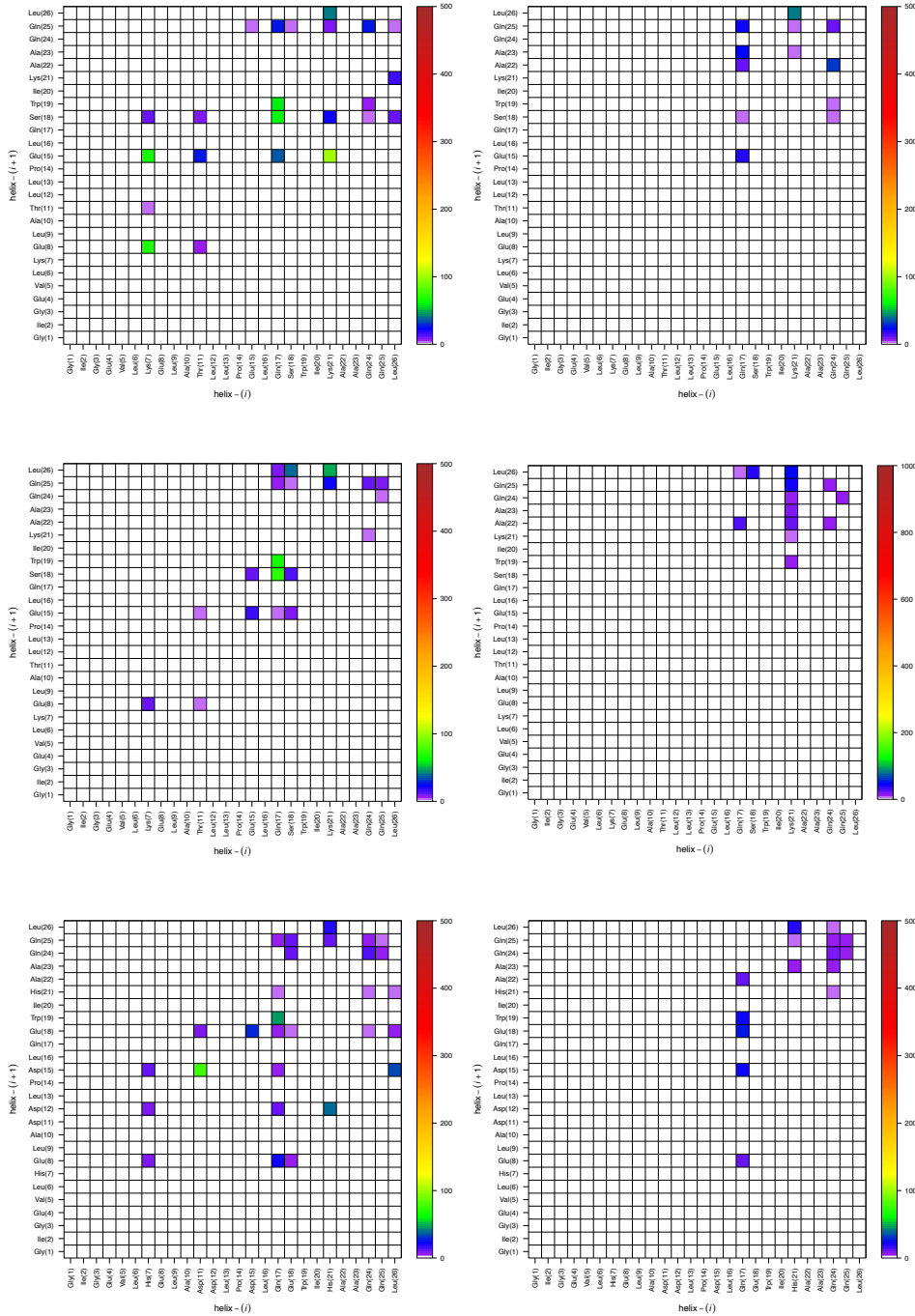


Figure 3.16: (Top to bottom:) Mac70 at pH 7, and pH 5, and pHD15 at pH 5. (Left) Side chain to side chain. (Right) Side chain to backbone. Heat map of the average duration (ns) of the dominant side chain–side chain H-bonding interaction between peptides i (abscissa) and $i + 1$ clockwise (ordinate) during the last 2 μ s.

Molecular dynamics simulations permit direct and detailed examination of electrostatic interactions between residues and along with other techniques are essential to confirm the functionality of combinatorially selected peptides [94]. Based on simulation involving a dry MelP5 trimer in a zwitterionic membrane [62] when peptide association takes place more directly along the polar face the pore tends to close. We focus on lateral association between peptides such that residues on either side of the polar face extend in the opposite direction with respect to the helix axis. In terms of their polar surfaces these interactions between peptides can be termed adjacent rather than face-to-face. For the parallel orientation only one configuration is possible for adjacent peptides.

Figure 3.16 shows the cumulative duration of the dominant side chain interactions between donor and acceptor atoms of adjacent peptides averaged over the pore during the last 2 μ s. The heat map within cells of the residue–residue contact matrix gives a structural overview of peptide–peptide interactions. In mac70 at pH 7 salt bridges dominate and H-bonding plays a lesser role. In mac70 at pH 5 the electrostatic interactions between adjacent peptides are severely diminished. In pHD15 at pH 5 H-bonding replenishes much of the interaction between adjacent peptides lost by lowering the pH on mac70. Pairing between donor and acceptor side chain and backbone atoms of peptide i and the clockwise adjacent peptide $i + 1$ is also shown (fig. 3.16). Such interactions can have detrimental consequences for α -helical structure. The direction shown for side chain to backbone interactions focuses on the role of lysine 21. These interactions show peptide–peptide interactions are likely partly responsible for the unraveling of C-terminal helices, seen by the loss of helical backbone–backbone H-bonding (figs. 5.65, 5.66, 5.67) and intercalation of water bridges along the backbone (figs. 5.69, 5.70, 5.71).

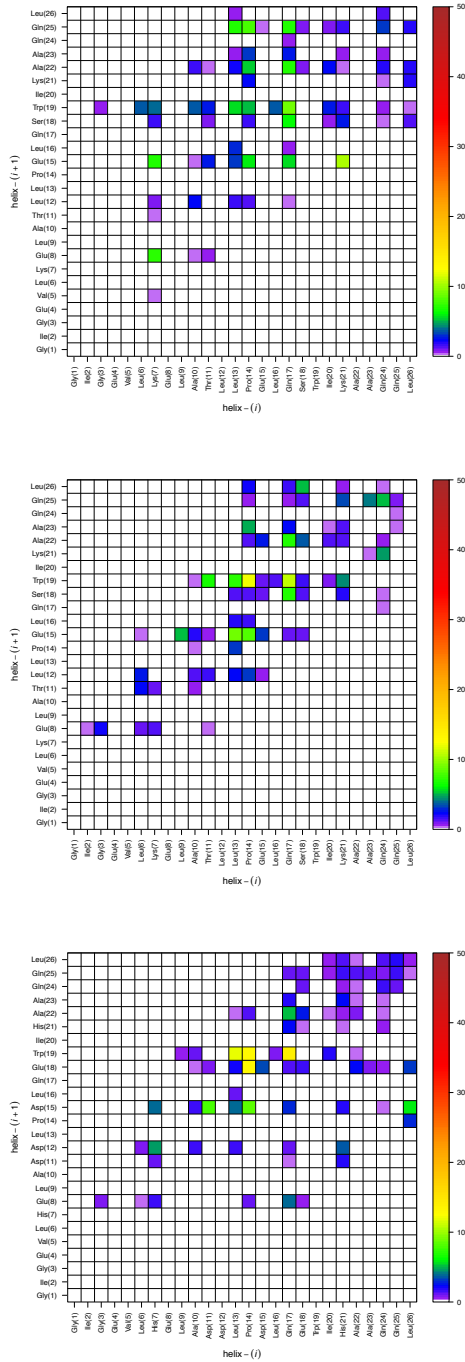


Figure 3.17: (Top to bottom:) Mac70 at pH 7, and pH 5, and pHD15 at pH 5. Heat map of the average duration (ns) of the dominant side chain–side chain interaction within H-bonding distance between peptides i (abscissa) and $i + 1$ clockwise (ordinate) during the last 2 μ s.

We also examine proximity (atoms within H-bonding distance) between side chains regardless of polarity (fig. 3.17). The resulting pattern reveals where inherent peptide-peptide association tendencies occur, and where mutations that bias peptide-peptide association are likely the most favorable. Many positions exhibit the potential for residue pairing between adjacent peptides. Most importantly the heat map shows clear directional preferences by certain positions along the amino acid sequence. Glu8 and Gln17 of the minimal mutation motif (E(4,8),Q17) demonstrate these positions are rigidly oriented toward the counter clockwise and clockwise adjacent peptide, respectively. Detailed visualization below of peptide-peptide interactions reveals most H-bonding takes place within the water column region of the pore, as expected [220]. Gln17 is a rare exception that often H-bonds the tryptophan 19 side chain, which remains largely embedded in the nonpolar region of the membrane. Other residues that are essential to melittin also show rigid directionality at their position within the sequence. Position 19 is perhaps the best suited for engineering peptide-peptide association in the counter clockwise direction, while positions 13 and 14 seem to be the optimum positions for contacting the clockwise adjacent peptide. Position 13 is the preferred mutation site given proline 14 is conserved in the mutational screen [20].

Mac70 (pH 7)	kcal/mol	Mac70 (pH 5)	kcal/mol	pHD15 (pH 5)	kcal/mol
K21-E15	-21.861900 ± 13.765300	K21-L26	-13.304600 ± 10.057700	H21-L26	-2.871110 ± 5.697590
K7-E15	-13.680600 ± 9.409290	Q17-W19	-2.664750 ± 1.547660	H7-D12	-2.622040 ± 1.233230
K7-E8	-13.150100 ± 15.353200	K21-Q25	-2.463940 ± 3.498190	Q17-W19	-2.366310 ± 1.912890
K21-L26	-8.231260 ± 6.566540	Q17-S18	-1.047080 ± 0.631042	H21-D12	-1.832080 ± 0.450933
Q17-E15	-3.178200 ± 3.047400	K7-E8	-0.443539 ± 1.661740	H21-Q25	-1.301470 ± 2.604870
Q17-W19	-2.726790 ± 1.520420	Q24-Q25	-0.420181 ± 0.794015	Q17-D12	-1.271230 ± 0.467928
K21-Q25	-1.521860 ± 2.561540	E15-E15	-0.404619 ± 0.751495	D11-D15	-1.074770 ± 1.092180
Q17-Q25	-1.013420 ± 1.009200	Q24-K21	-0.365080 ± 0.831516	Q24-E18	-0.949201 ± 0.783226
Q17-S18	-0.806433 ± 1.295880	S18-E15	-0.264311 ± 0.365671	H7-E8	-0.857776 ± 1.083620
K21-S18	-0.713028 ± 2.011120	S18-Q25	-0.239585 ± 0.301819	Q17-E18	-0.577244 ± 0.810427
Q24-Q25	-0.486091 ± 1.122880	T11-E15	-0.219663 ± 0.411436	E18-E18	-0.561569 ± 0.365797
T11-E15	-0.365134 ± 1.529100	S18-S18	-0.204073 ± 0.513464	Q17-D15	-0.523035 ± 0.450356
L13-L12	-0.297395 ± 0.204694	E15-S18	-0.193000 ± 0.342460	Q24-Q25	-0.512784 ± 0.990865
T11-E8	-0.157499 ± 0.830764	Q25-Q24	-0.156167 ± 0.375258	Q24-Q24	-0.430470 ± 0.891521
K7-S18	-0.150355 ± 1.233450	Q25-Q25	-0.140274 ± 0.598164	Q17-Q25	-0.349799 ± 0.701317
K7-T11	-0.116922 ± 0.818193	Q17-Q25	-0.121552 ± 0.423986	D11-E18	-0.341808 ± 0.592777
		L13-L12	-0.245550 ± 0.103032	D15-E18	-0.341693 ± 0.597336
				Q25-Q25	-0.319030 ± 0.825599
				Q17-E8	-0.312573 ± 0.291460
				Q25-Q24	-0.252704 ± 0.746926
				E18-Q25	-0.190743 ± 0.539717
				E18-Q24	-0.170115 ± 0.692601
				E18-E8	-0.097504 ± 0.190964

Figure 3.18: Interaction energy for residue pairs to the clockwise adjacent peptide averaged over the pore of (some of the) pairs shown in the heat maps of H-bonding.

Average interaction energies between residue pairs in tables 3.18 include the involvement of backbone atoms and help to quantify the stabilization that is gained, lost, and replenished when comparing mac70 at pH 7, and 5, and pHD15 at pH 5. While electrostatic interactions between side chain and backbone atoms interrupt the backbone's helical structure the attraction may hide the exposed backbone from lipid tails, and ultimately work to maintain the proximity between adjacent peptides. When viewed across systems, these values help to inform whether a residue's directionality is due to energetics of the resulting interaction or the structural rigidity of its position in the amino acid sequence.

Salt bridges are the most favorable and mac70 at pH 7 has the most of them. Interactions between Lys7, and Lys21 and Glu15 are the most favorable. Salt bridges between Lys7 and the clockwise adjacent Glu8, and between Lys21 and the clockwise adjacent C-term, which link the N-terminal and C-terminal helices, respectively, are the next most stabilizing. Salt bridges increase the chances for H-bonding by surrounding residues such as Gln(24,25) of the MelP5 C-terminal tail described previously [62]. Again, proximity to the proline 14 kink is preferred, as Gln17 binding to Glu15 is stronger than to Ser18, Trp19, or Gln25. Lastly, van der Waals interactions between adjacent peptides also play a role. Rather than an acidic mutation at position 12 the macrolittins often possess Leu. This suggests that position 12 is useful for interaction with the counter clockwise peptide, and also important for pH sensitivity in conjunction with the Glu8 of the conserved mutational motif. The average interaction energy shows stabilization between the highly conserved macrolittin mutation Leu12 and the melittin residue Leu13.

In mac70 at pH 5 salt-bridges are converted to H-bonds except those involving the C-term. The charged C-termini allow for direct comparison with simulations of the parent peptide MelP5 [62]. Lysine 7 and 21 can still bind the N- and C-terminal helices, respectively, but communication between Lys7 and the clockwise Glu8 is significantly curtailed, and Lys21 is largely relegated to the clockwise adjacent peptide's C-term where it provides the strongest

attraction. The Lys21 salt bridge to the clockwise Glu15 is replaced by H-bonding to the less centrally positioned Gln25. Glu15 and Ser18 both lose much of their directional preference seen in mac70 at pH 7 and are able to bind the neighboring Glu15 and Ser18, respectively, on either side. In addition, Glu15 and Ser18 can each bind the other in the clockwise as well as counter clockwise directions. This shows positions 15 and 18 are flexible and can bind either the clockwise or the counter clockwise adjacent peptide to establish the strongest interaction. The average stabilization between the Leu12 and Leu13 is comparable to that seen at pH 7.

With introduction of additional acidic residues - Glu15 of macrolittin70 is moved to position 18, and positions 11, 12, and 15 are mutated to aspartic acid - the cationic histidines at melittin positions 7 and 21 of pHD15 at pH 5 regain access to binding at internal positions within the clockwise adjacent peptide's sequence (fig. 3.16). Asp12 interacts with His21 and Gln17 in addition to His7 in accordance with the counter clockwise orientation of position 12. The directional flexibility of positions 15 and 18 is confirmed by the Asp15 and Glu18 mutations in pHD15 at pH 5. For pHD15 at pH 5, position 11 is rigidly oriented towards the clockwise adjacent peptide. pHD15 also tests the ability to replace Lys with His, which can contribute to low pH sensitivity. The magnitude of stabilization by salt bridges involving His21 and the clockwise adjacent C-term is diminished but is still the strongest interaction between adjacent peptides. In pHD15 at pH 5 His7 is better fit to engage the clockwise Asp12 rather than Glu8, which both point toward the counter clockwise adjacent peptide (fig. 3.17).

The Glu4 mutation of the conserved mutational motif is almost completely absent from interactions between peptides. Instead Glu4 plays a structural role within individual helices. In all stable pores here Glu4 binds the N-term. This is accompanied by enhanced interaction at the α -helical interval between residues Gly1 and the $i + 4$ Val5 (fig. 5.65, 5.66, 5.67) relative to MelP5 (fig. 5.64). Given water often intercalates along the helix backbone of the

N-terminal tail (figs. 5.68, 5.70, 5.71), the expulsion of water bridges between Gly1 and $i + 3$ Glu4 and $i + 4$ Val5 for mac70 at pH 7 (fig. 5.69) shows Glu4 binding to the N-term biases helical structure.

The heat maps of the average residue–residue interactions between adjacent peptides in the pore (fig. 3.16, 3.17) give a general picture but cannot capture the diverse interaction profiles among the individual peptides. A detailed outline of the most important side chain–side chain pairings for each pore during the last 2 μ s is presented here for completeness, including between non-adjacent peptides. Specific peptide–peptide interactions give insights into deviations (figs. 5.45, 5.46, 5.47) by individual peptides from the general pattern of interaction with lipid polar moieties (figs. 3.15). Individual peptides are named PRO(A,B,C,D,E,F) and amino acids are referred to via the single letter code.

Peptide–Peptide Interactions : Macrolittin70 at pH 7

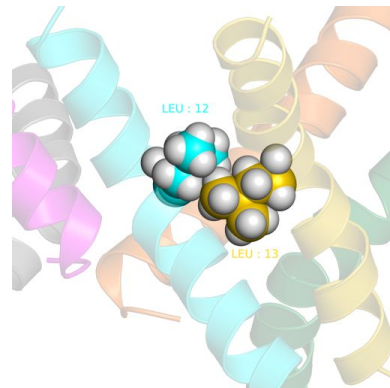


Figure 3.19: Macrolittin70 pore at pH 7. Hydrophobic association between L13 and L12 of the clockwise adjacent peptide.

In mac70 at pH 7 all peptides are in close association with those adjacent given their interactions via the underlying melittin scaffold (fig. 5.75). PRO(A,B,C,D,E) W19 contact the counter clockwise L13. The common macrolittin mutation L12 of PROB contacts the counter clockwise L13 (fig. 3.19).

The side chain of Q17 of the minimal mutation motif is directed toward the clockwise adjacent peptide (fig. 5.75). H-bonding connects Q17 and E15 of every other helix starting from PROA (fig. 5.49). The most ubiquitous contact Q17 to W19 is present in four (PRO(A,C,D,E)) peptides and facilitates H-bonding (fig. 5.49). The next most prevalent H-bond by Q17 is to the melittin residue S18 of PRO(B,D,F). Serine has been previously documented in association between transmembrane helices [73]. PRO(B,F) Q17 H-bond to Q25.

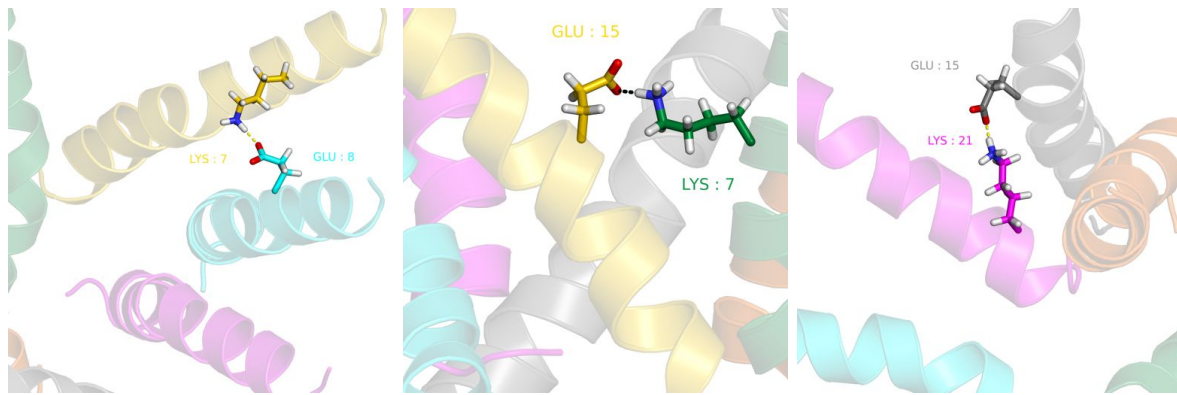


Figure 3.20: Macrolittin70 pore at pH 7. K7 and K21 salt bridges with E8 and E15 of the clockwise adjacent peptide.

The K7 side chain interacts exclusively in the clockwise direction (fig. 5.49), most often with E8 as predicted by Li et al. [23]. Lysine interaction with phosphate and esters is diminished (fig. 5.45) in proportion to how deeply its partner is embedded in the membrane. PRO(B,D) K7 form salt bridges to E15 (fig. 3.20). PRO(B,D) K7 also H-bond to the clockwise S18, bringing these lysines further into the pore interior. PRO(A,C,D) K7 form salt bridges to E8. Overall K21 interaction with phosphate and esters is lower compared to the systems at pH 5 largely due to competition from anionic E15. PRO(A,C,E) K21 salt bridge to E15 (fig. 3.20), and H-bond to S18 (fig. 5.49). Strong interactions with clockwise E15 preclude PRO(C,E) K21 binding to phosphate and esters (fig. 5.45).

The melittin residues T11 [20] and S18 [23] are preserved in mac70. T11 mostly H-bonds

in the clockwise direction and PROD T11 H-bonds to E15. On an ideal continuous helix T11 and S18 are oriented in the same direction (fig. 1.1). Nevertheless, S18 predominantly H-bonds in the counter clockwise direction (fig. 5.49) as described above, despite having a short side chain. This suggests some independence between the N- and C-terminal halves.

Mac70 at pH 7 is also capable of chordal interactions across the pore from i^{th} to the $i+2$ and $i+4$ peptide (fig. 5.50). PROB K21 salt bridges to the PROD C-term. PROA K21 salt bridges to the PROE C-term. There are no interactions between helices on opposite sides of the pore.

Peptide-Peptide Interactions : Macrolittin70 at pH 5

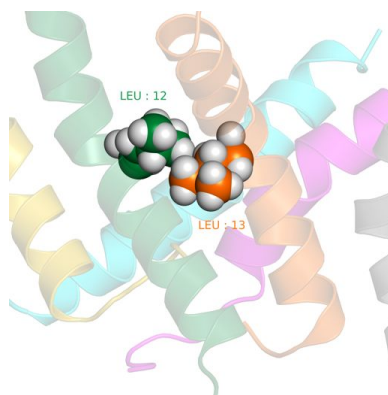


Figure 3.21: Macrolittin70 pore at pH 5. Hydrophobic association between L13 and L12 of the clockwise adjacent peptide.

As at pH 7, peptides of the mac70 pore at pH 5 are in close proximity to adjacent peptides via hydrophobic associations (fig. 5.76). Again, hydrophobic association in the clockwise direction is facilitated by L13 (fig. 3.21), and by W19 and L12 in the counter clockwise direction. PROB L12 associates with the PROA L13. PRO(A,C) W19 associates with the counter clockwise L13. PROD W19 and PROE L12 contact the counter clockwise T11. PROF L12 associates with the counter clockwise L6.

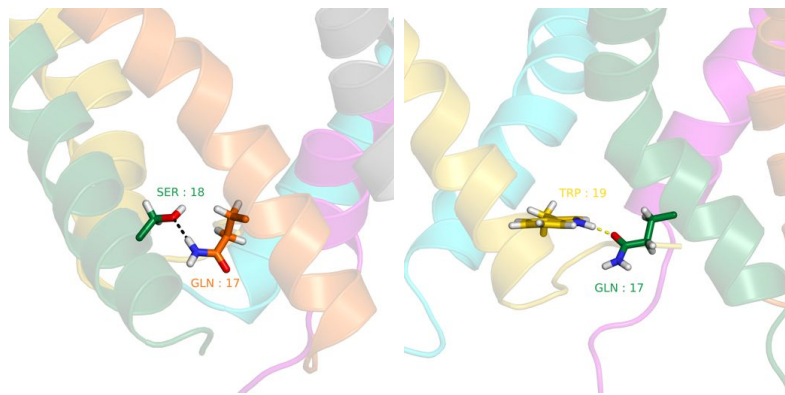


Figure 3.22: Macrolittin70 pore at pH 5. Q17 H-bonding to S18 and W19 and of the clockwise adjacent peptide.

Q17 interacts with the clockwise adjacent peptide in some manner for every monomer participating in the pore. Q17 H-bonding occurs mainly in the clockwise direction alternating between S18 and W19 starting at PROA, except for PROC Q17. The PROC Q17 interrupts the pattern by binding the clockwise C-term.

K7 H-bonds only in the clockwise direction. E8's most significant interaction is to K7 but is less compared to H-bonding at pH 7. PRO(A,B,E) K7 diminished average interaction energy with lipid phosphate and esters (fig.5.46) is primarily due to competition from Cl^- counter ions, rather than peptide-peptide interactions. K21 plays a more significant role than K7 in peptide-peptide interactions, predominantly contacting the clockwise adjacent peptide (fig. 5.53). PRO(B,C) K21 salt bridge to the clockwise adjacent C-terminal tail.

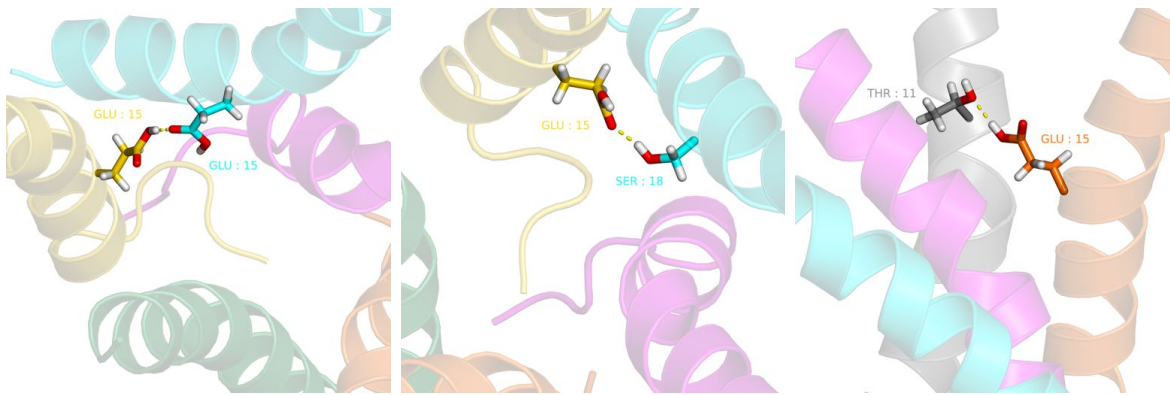


Figure 3.23: Macrolittin70 pore at pH 5. H-bonding of PROC E15 – PROD E15, PROC E15 – PROD S18, and PROC T11 – PROD E15, show loss of rigid directionality of E15.

E15 forms H-bonds with polar residues in both the clockwise and counter clockwise directions (fig. 5.53). PRO(D,E) E15 H-bond the counter clockwise E15 and S18, while PROC E15 H-bonds the clockwise E15 and S18. The PROA E15 H-bonds the E15 of PROF. In addition to counter clockwise H-bonding by S18 to Q17 and E15, S18 can also H-bond in the clockwise direction. PROB S18 H-bonds to the PROC C-term. PROC and PROD S18 H-bond to the clockwise S18. As at pH 7, T11 H-bonds in the clockwise direction. PROD T11 H-bonds the clockwise E8. PROF T11 H-bonds to the clockwise E15.

The mac70 pore is narrower at pH 5 and there are more interactions between the i^{it} and the clockwise $i + 2$, and $i + 4$ peptides (fig. 5.54). PROE Q17 H-bonds the PROA S18. PRO(A,C,E) K21 salt bridges to the $i + 2$ C-term form an internal cycle within the pore. PRO(A,E) K21 salt bridges with the clockwise $i + 2$ C-term preclude K21 binding to lipid phosphate and esters (fig. 5.46). PROC Q24 forms H-bonds to PROE S18 and G24. Interactions across the pore diameter with the $i + 3$ peptide also occur (fig.5.55). K21 of PROB and PROE form salt bridges with each other's C-term.

Peptide-Peptide Interactions : pHD15 at pH 5

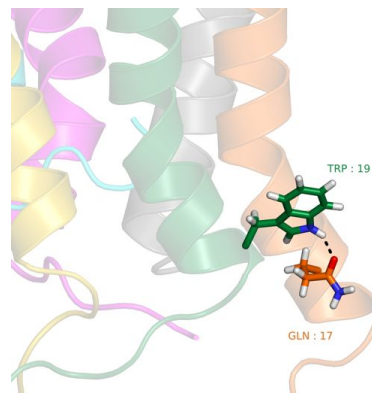


Figure 3.24: pHD15 pore at pH 5. Q17 H-bonding W19 of the clockwise adjacent peptide.

At pH 5 the pHD15 peptides in the pore are in close association with the adjacent peptides (fig. 5.77). Without L12, the melittin residues L13 and W19 plays the dominant role in hydrophobic association between peptides in the clockwise and counter clockwise directions, respectively, but breaks down between PROF and PROA. PRO(A,B,C,E) L13 and PROD I20 contact the clockwise W19.

Q17 of all peptides contacts the clockwise adjacent peptide (fig. 5.57). Q17 of PRO(A,C,D,E) are aligned with W19, and support H-bonding. PROB Q17 H-bonds to E18 and Q25 of PROC. PROD Q17 mostly H-bonds PROE D15. PROF Q17 H-bonds E8 to complete the cycle.

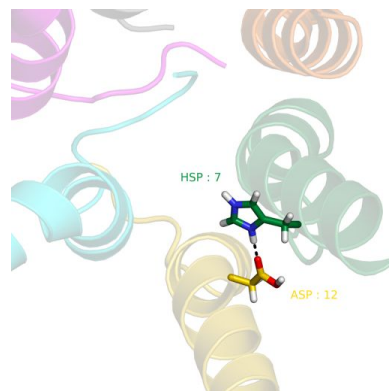


Figure 3.25: pHD15 pore at pH 5. PROB H7 H-bonding to PROC D12.

PROD H7 is capable of H-bonding to the clockwise E8 (fig. 3.25), but overall the relationship between the cationic position seven and E8 is greatly diminished compared to mac70. E8 plays a less significant role in pH15 pores (fig. 5.57). Diminished H7 interaction with phosphate and esters (fig. 5.47) is largely due to competition from peptide-peptide interactions. PRO(A,B) H7 H-bond to D12 (fig. 3.25) and PROB H7 also H-bonds D15. H21 H-bonds predominantly to the clockwise adjacent peptide. PROF H21 H-bonds to the clockwise D12 bringing H21 deep into the water column region of the pore and sequestering it from lipid phosphate and esters (fig. 5.47). PRO(A,B,D) H21 form salt bridges with the clockwise C-term. PROE H21 H-bonds the clockwise Q25.

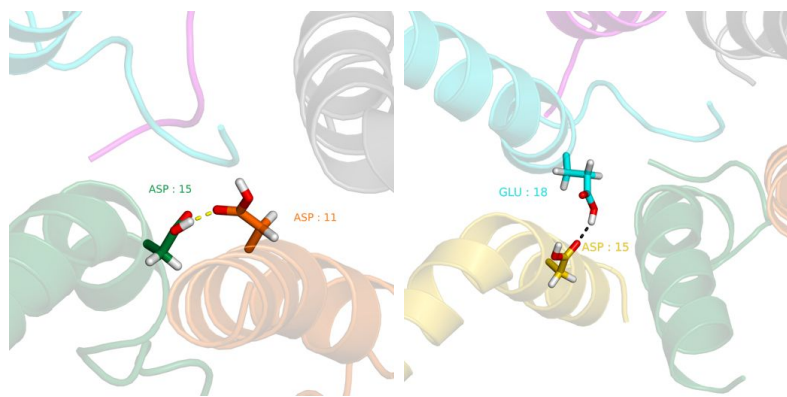


Figure 3.26: pH15 pore at pH 5. H-bonding between PROA-D11–PROB-D15, and PROC-D15–PROD-D18, show lack of directional preference by D15.

Like T11 in mac70, D11 predominantly H-bonds in the clockwise direction. PRO(A,B,C,D) D11 form H-bonds with the clockwise D15. D15 can interact in both clockwise and counter clockwise directions but most D15 H-bonds are in the counter clockwise direction (fig. 3.26). PROA D15 H-bonds to the PROF C-term. PROC D15 H-bonds with the clockwise E18. E18 forms H-bonds the adjacent peptide in both clockwise and counter clockwise directions. In PROD E18 H-bonds the counter clockwise D15. PROC E18 forms H-bond with the clockwise E18 and Q24. PROE E18 H-bonds Q25 in the clockwise direction, and to a lesser extent to Q17 and Q24 in the counter clockwise direction.

At pH 5 pHD15 can make interactions chordal to the pore with peptides in the $i + 2$ and $i + 4$ clockwise positions (figs.5.58). PROC H21 salt bridges to the PROE C-term. Four peptides' E18 form H-bonds to the $i + 4$ peptide. PRO(A,B,F) H-bond the $i + 4$ C-term. In the $i + 4$ clockwise direction, Q24 and Q25 of the PROD C-terminal tail search the polar surface of PROB. PROD Q24 and Q25 both H-bond PROB's E18. PROD E18 H-bonds with PROB D11.

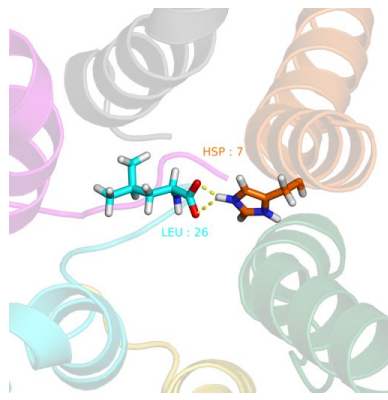


Figure 3.27: pHD15 pore at pH 5. PROA H7 H-bonding to PROD C-term shows the interactions across the diameter of the pore destabilizes the peptide assembly by unfolding the C-terminal tail and preventing it from binding the edge of the pore.

Two peptides pair with another at the $i + 3$ position across the pore diameter (figs.5.59). Unraveling of the PROB C-terminal tail permits H-bonding between the PROE H21 and the PROB C-term. PROA D11 contacts the C-term of PROD. PROD's numerous interactions are due to unraveling of the C-terminal tail. The PROD C-term does not stabilize choline (fig. 5.47) because it resides in the middle of the water column and is insulated from the lipid headgroup region within the membrane interior of the pore. PROA H7 is unavailable for lipid polar moieties (fig.5.47) due to significant H-bonding to the PROD C-term (figs. 3.27, 5.59), which brings H7 into the pore interior. These interactions effectively pull the PROD C-terminal tail off of the wall of the pore.

Membrane Thickness :

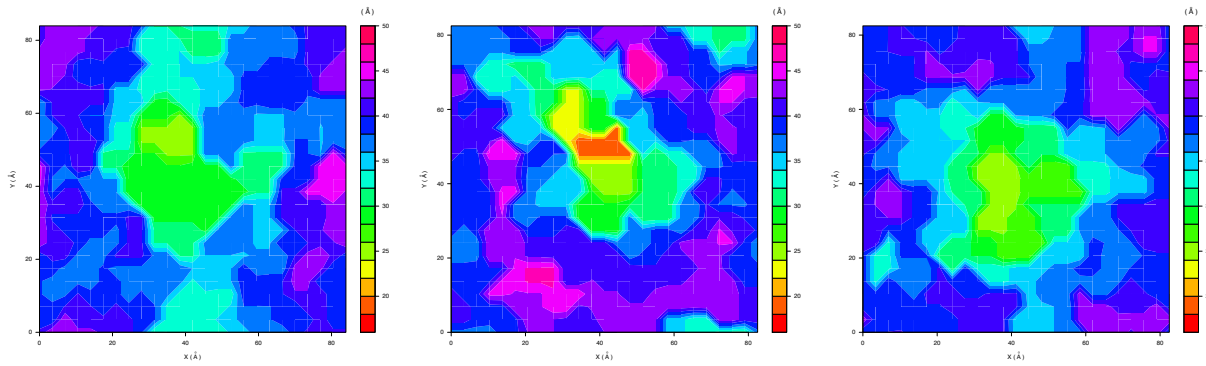


Figure 3.28: Membrane thickness (\AA) of (left) macrolittin70 at pH 7, (middle) macrolittin70 at pH 5, (right) pHD15 at pH 5, based on phosphorus of last frame centered around protein. The average phosphorus-based thickness for pure POPC is $39.36 \pm 0.4 \text{ \AA}$ (based on short Gromacs simulation).

At optimum pH mac70 and pHD15 pore helices remain transmembrane without inducing severe membrane deformations distinguishing them from the parent peptides melittin and MelP5 [61, 62]. Membrane deformations induced by the pore are generally not perfectly uniform and extend beyond the immediate vicinity of the water column (fig. 3.28). Membrane thinning occurs in the region encompassing the pore consistent with the overall tilting of the peptdie helices [221]. Phosphate statistics within the central 10 \AA of the pore are gathered over the last $2 \mu\text{s}$. Mac70 at pH 7 generally has zero, but up to two phosphates, with an average of 0.23 ± 0.42 . pHD15 at pH 5 generally has zero, but can have up to one phosphate, for an average of 0.01 ± 0.12 . Sustained membrane deformations are observed for mac70 at pH 5, which has a mode of one phosphate within the pore interior with as many as two, and an average of 0.56 ± 0.51 . While mac70 at pH 5 can readily deform the membrane it never permits a fully toroidal pore. In contrast, during the last $2 \mu\text{s}$ of a roughly $7 \mu\text{s}$ simulation of MelP5 in POPC (unpublished work by Dr. Pino-Angeles) an average of 0.13 ± 0.39 phosphates enter the central 10 \AA of the pore but as many as four can be present.

Peptides' Correlated Motion :

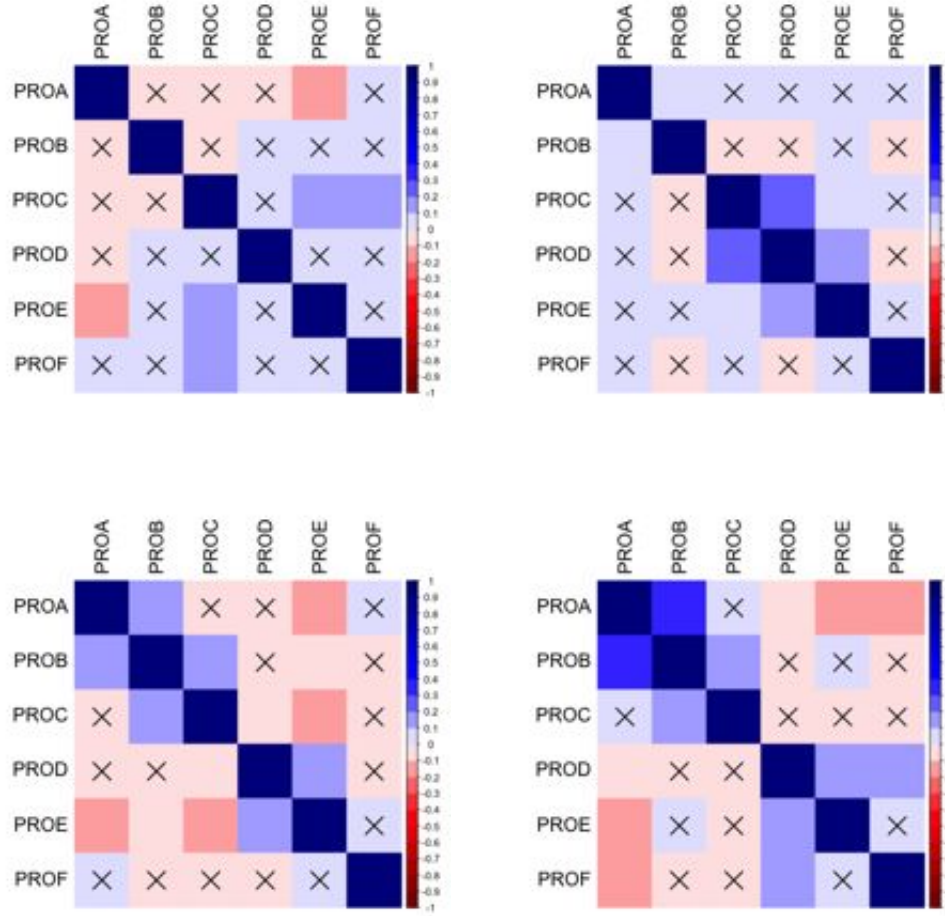


Figure 3.29: Matrices of the Pearson correlation (r) (p -values $> \alpha = 1^{-10}$ are marked with \times) for N-terminal helices is shown for (top left) MelP5, (top right) mac70 at pH 7, (bottom left) mac70 at pH 5, and (bottom right) pHD15 at pH 5.

Correlated motion is important for establishing the role played by dynamics in the structure-function relationships of membrane proteins [222]. The correlation between helix tilt angles is used to assess the independence of large-scale motions within and between peptides. At optimal pH Pearson's r shows pairs of N- and C-terminal helices of the same peptide (diagonal elements of correlation matrices in figs. 5.84, 5.85, 5.86, 5.87) that can rigorously be determined for mac70 and pHD15 are independent in four out of six peptides.

In contrast, two peptides have independent N- and C-terminal helices in the mac70 pore at pH 5, and only one does in MelP5 in POPC (unpublished simulations by Dr. Pino-Angeles). When there are fewer inter-peptide connections intrapeptide N- and C-terminal helices are less independent, and the N- and C-terminal helices behave more like part of a single helix. Their coupled motion is possibly linked to helices anchoring to the membrane. This suggests that peptide–peptide interactions that compete with peptide–membrane interactions decouple peptides from the membrane. The low correlation overall nonetheless suggests large scale motions by the N- and C-terminal helices are generally independent.

Peptides' collective motion in the pore is complicated but some general patterns can be observed. Helices are more likely to be positively correlated with the adjacent helices and uncorrelated or anticorrelated with those farther away. Overall tilt shows that pores are formed of sections of positively correlated peptides followed by intermittent breaks (top row in figs. 5.80, 5.81, 5.82, 5.83). The fundamental unit of association is the dimer, which may expand its correlation network by at most one. The majority of correlations reside with the C-terminal helices for MelP5, as well as for mac70 and pHD15 (bottom row in figs. 5.80, 5.81, 5.82, 5.83). Most notable, however, is the difference in correlation between N-terminal helices between MelP5 and mac70, and pHD15 (middle row in figs. 5.80, 5.81, 5.82, 5.83). MelP5 generally lacks the ability to make connections with adjacent peptides via the N-terminal residues, as Lys7 lacks a partner with a flexible sidechain. Figure 5.80 shows of the five MelP5 N-terminal helices that can be rigorously determined all are uncorrelated with adjacent peptides. This is in stark contrast to mac70 and pHD15, which shows clearly that peptide–peptide interactions between helical segments can lead to correlation in their tilt motion.

Chapter 4

Discussion

Melittin Dimerization On the Membrane Surface

Despite being perhaps the most extensively studied pore-forming peptide [32, 57], melittin's pore formation mechanism continues to be debated [52]. Dimerization on the membrane surface has long been hypothesized as the origin of AMP's sigmoidal concentration dependence [75, 132, 223, 224, 225]. The majority of these claims, with the exception of De-Grado's experiments on RBCs, involve SUVs. As the role played by the membrane became more apparent [226] experiments involving larger vesicles [41, 53, 54, 114, 227] limited the applicability of many of the previous models [76, 132, 228]. The prevailing hypothesis for melittin poration on zwitterionic membranes is the two state model [13, 36, 55, 142, 229]. Huang's two state model is consistent with a continuum elasticity theory based representation of the membrane [141, 230, 231], which shows dimerization on the membrane surface is a rare event, but dimerization by transmembrane helices is favored when the transmembrane helix is accommodated by a dimple deformation in the membrane thickness [141]. X-ray lamellar diffraction [232], surface area expansion of single GUVs [54], OCD [233], neutron in-plane scattering [234], and grazing-angle X-ray anomalous diffraction [32], provide a set of experiments consistent with the two state model that demonstrate the origin of the co-

operative [13] mechanism of AMPs; namely, adsorption on the membrane surface leads to membrane thinning with concomitant surface area expansion [140], and above a threshold concentration peptides begin to adopt a transmembrane orientation and the membrane begins to form pores [13, 32, 46]. Explicit aggregation between peptides is not required at any step for activity [149, 235]. Leakage from single GUVs held at constant tension show poration is a stochastic event mediated by the formation of a membrane defect [54]. Molecular dynamics simulations using CHARMM 36 show that the melittin N-terminus is able to stabilize a membrane defect [64], which may lead to a cascade of N-termini inserting into the defect resulting in a multi-microsecond stable toroidal pore in 1,2-dipalmitoyl-sn-glycero-3-phosphocholine (DPPC) consisting of 4 transmembrane melittins with phosphates lining the channel [65].

Only kinetics experiments in the presence of an applied potential unambiguously suggest peptide aggregation [28, 236]. The formation of the pore can be described as a molecular aggregation step [237] but this does not imply dimerization or association between peptides [62]. Techniques based on melittin's intrinsic tryptophan fluorescence used to observe aggregation in solution are obscured by the membrane [99, 104, 105, 115, 116]. The FRET experiments [238] of Hermetter and Lakowitz, and the EPR experiments [102] of Altenbach and Hubbell are a milestone in the conception of membrane adsorbed melittin as monomeric. Melittin aggregation on the membrane surface based on FRET [45, 122] has been refuted [124, 125, 238, 239]. Subsequent EPR experiments confirm melittin is monomeric [108, 109] even at high concentration [128]. NMR experiments [43] on thin DMPC membranes show melittin is monomeric even when predominantly in the inserted transmembrane (I)-state [43, 46], in agreement with microsecond all-atom molecular dynamics simulations of melittin pores from pre-assembled transmembrane bundles [61, 62].

The covalently linked melittin dimer continues to find applications [38], and new experimental techniques continue to challenge the prevailing assumptions regarding AMP's

activity. Prior to the recognition of pore formation by AMPs as a stochastic event, kinetics based on ensemble approaches had to assume monomeric insertion for lack of evidence of aggregation on the membrane surface [43, 114]. In spite of a wave in the opinion of melittin’s activity as fundamentally monomeric Mally *et al.* and Kokot *et al.*, based on leakage experiments involving single POPC GUVs held at zero tension [56], claim melittin dimerization on the membrane surface [57] is the initiation step for peptide insertion and poration in every concentration regime [33]. The appeal of the two state model is partly due to its generality. In addition to melittin, the two state model has been applied to alamethicin [149], which forms barrel-stave pores [46, 219], and to magainin [47, 240], which forms disordered toroidal pores [46, 203], among others [241]. While the two state model does not require a molecular aggregation step it does not prohibit it. Alamethicin forms barrel-stave pores in which peptides participating in the pore remain in close association [46]. Solid-state NMR experiments on ¹⁹F labeled alamethicin show a pentamer [242] at peptide to lipid ratio of 1:13 where nearly all peptides are in the inserted transmembrane (I)-state [13], drop to a dimer [242] when the fraction in the I-state falls to roughly half [13]. PELDOR EPR experiments by Syryamina *et al.* on ¹⁹F labeled alamethicin show dimers at peptide to lipid ratios as low as 1:1500 [243]. Furthermore, they demonstrate dimerization is coupled to reorientation within the membrane to an inserted transmembrane state using ESEEM [243]. These developments suggest a more nuanced perspective on AMP activity in lipid membranes.

Molecular dynamics simulations provide an invaluable comparison with structural data from spectroscopic experiments [244]. Fully atomistic simulation of the full pore formation process is prohibitive [97]; melittin adsorption on the membrane surface alone occurs on the timescale of milliseconds [237]. Thus, all-atom molecular dynamics simulations are often restricted to a single molecular step in the mechanism. Mechanistic simulations using CHARMM 36 that conform to the two state model show the N-terminal tail mediates melittin insertion [63, 64, 65, 245], which in the absence of an applied potential is a rare

event [246], and confirm [64, 65] that insertion requires formation of a membrane defect [54]. Coarse-grained MARTINI [87, 88] simulations of a 13 nm × 13 nm 512 1,2-dilauroyl-sn-glycero-3-phosphocholine (DLPC) lipid membrane patch show that above a concentration threshold as many as four melittins aggregate on the membrane surface and subsequently insert, albeit in a U-shaped conformation with termini anchored to lipid head groups [247]. Furthermore, melittin above the threshold concentration adsorbed solely on the upper leaflet forms aggregates at around 4 μ s, which are able to translocate to the lower leaflet at roughly 8 μ s. CHARMM 36 simulations also show melittin tends to aggregate at the site of exposed lipid tails caused by irregular packing [64]. The basic unit of aggregation is the dimer, however, despite recent suggestions of its utility no preferred dimer has been identified. Numerous dimer configurations are valid. The simplest cases, the maximally aggregated lateral dimers, are considered here. The parallel dimer is obviously less stable than the antiparallel dimers given the repulsion between cationic C-terminal tails. The principle tenet of the alternative model, dimerization on the membrane surface, is investigated using umbrella sampling.

Simulations from implicit solvent models IMM1 and HDGBvdW disagree. IMM1 shows dimers are stable while HDGBvdW shows they are unstable. IMM1 and HDGBvdW PMF profiles for formation of the most stable dimer in IMM1, the rubin dimer, contradict each other. Whereas formation of the rubin melittin dimer is initiated at 4.0 nm separation in IMM1, in HDGBvdW repulsion between monomers begins at 2.0 nm separation.

The implicit PMFs are sufficiently converged but neither matches those obtained by all-atom simulations. Explicit PMF profiles for separating the pre-assembled rubin dimer reaffirm the presence of a minima upon dimerization seen in IMM1, at 0.8 nm. However, the all-atom PMF tends to depart from the IMM1 profile as the equilibration stage is shed from the 100 ns all-atom umbrella sampling windows (fig. 3.6). Furthermore, microseconds of simulation time are required to equilibrate the surface bound [244, 248] melittin dimer [249].

The difference between the profiles generated on small and big membrane patches (fig. 3.5) suggests the PMF for peptide dimerization on the membrane surface using atomistic simulations depends on the system size. The small 90 nm × 90 nm membrane patch should be large enough (fig. 3.8) to avoid major artifacts due to the use of PME under PBCs [195]. The atomistic details of the lipids likely play a role in determining the PMF profile that cannot be accounted for in implicit simulations. The dependence of the PMF profile on system size has been demonstrated for translocation of amino acid side chains [250, 251] across lipid bilayers.

To validate the PMF and the order parameter the profile must be computed based on umbrella sampling windows obtained from pulling simulations along the reverse as well as the forward process. When pulling the monomers together by their respective center of mass with a small linear force a layer of intervening lipids prevent formation of the rubin dimer starting from 2 nm dimer separation. This behavior is consistent with melittin [249] and other well known α -helical AMPs horizontally adsorbed on the membrane surface [252]. The distance between respective tryptophan 19 residues is chosen as the aggregation order parameter based on historical precedent [45, 122, 124], Trp19's importance to melittin's activity [253], and because it can unambiguously be applied to directly assemble the rubin dimer. The Trp19 based order parameter is effective at occluding lipids from the dimerization interface. However, this all-atom PMF profile disagrees with the PMF profile for separating the dimer, and resembles the PMF profile from HDGBvdW. The difference in the onset of repulsion between monomers suggests different origins for the repulsion between melittins in all-atom and HDGBvdW simulations. In the case of HDGBvdW the membrane does not play a role so it is the electrostatic contribution that has the dominant influence.

The anton simulations suggest the true PMF, if all umbrella sampling windows are in the microsecond range, is most similar to that shown here for aggregation via Trp19 residues. The fully aggregated rubin dimer is likely metastable but a sizable energy barrier impedes

its formation through a direct process. If melittin dimerization does occur it is likely via a complicated mechanism involving the participation of multiple lipids as they are occluded from the dimerization interface.

Comparison between implicit and all-atom based PMF profiles provides a guide for re-parameterizing implicit models based on the results of all-atom simulations. All-atom PMF calculations of melittin dimerization are aimed at using peptide processes on the membrane surface to parameterize IMM1. The lack of correspondence between the dimerization PMF along the reverse and forward processes, based on the order parameters employed here, makes it impossible to provide any insights for improving implicit simulations. Overestimation of the well depth in IMM1 is likely due to overestimation of electrostatic attractions [254, 255]. Improvements for peptide aggregation on the membrane surface in IMM1 can be made via modifications to account for results from amino acid side-chains in all-atom simulations [256], as done for the generalized Born model [161, 257].

The role played by the membrane in all-atom PMF calculations of dimerization on the membrane surface is nontrivial [258]. Katira et *al.* show motility of intervening lipids is a precondition for transmembrane protein association [80]. A multicomponent order parameter that includes intervening lipids along the dimerization process is possibly needed to generate the forward and reverse path using the same order parameter for umbrella sampling on the membrane surface. This additional restraint might be based on the coordination number of lipids to melittin.

Transmembrane Dimerization by Melittin Mutants: pH-Dependent Peptides and Macrolittins

Notwithstanding continued debate over its fundamental mechanism of action melittin has proven its utility as an amino acid template in the development of membrane targeting therapeutics. The Krauson et *al.* gain-of-function (GoF) combinatorial library shows a reduction in charge and improved amphipathicity can increase melittin activity [20]. MelP5,

the most potent GoF mutant, permits small molecule leakage at $P/L = 1/1000$ [20], and release of a 10 kDa dextran at $P/L = 1/500$ [259]. Thr11 is mutated to alanine, and the C-terminal tail is remodeled by shifting Gln25 and Gln26, removing charged residues Arg22, Lys23, and Arg24, and mutating the resulting vacancies with residues that contribute amphipathic character. MelP5 mutations demonstrate melittin's potency is principally limited by peptide insertion.

The Wimley group has pioneered membrane binding [21] and pore size [259] as effective screens [20] for membrane selectivity [22] and potency [23], respectively, by synthetic AMPs. The macrolittins [23] and the pH dependent (pHD) peptides [22, 95] show MelP5's potency can be increased by introduction of acidic residues. Furthermore, the pHD peptides show increased MelP5 potency can be accompanied by low pH sensitivity via strategic mutations to acidic residues. Macrolittins permit release of a 40 kDa dextran at P/L as low as 1/5000, and 50% leakage occurs at P/L as low as 1/1000 [23]. The more potent members of the pHD peptides can achieve 50% leakage of the 40 kDa dextran at P/L as low as 1/900 [22]. The macrolittins are oriented similarly to MelP5 in the membrane [23], and the pHD peptides are expected to do the same (although OCD data is more difficult to obtain at low pH) [95]. The macrolittins and the pHD peptides come from the same combinatorial library and most members share the mutational motif consisting of Gln17 and acidic residues at positions four and eight. The macrolittins typically have an additional acidic mutation at position 11 or 15 for a total of three, as well as the mutation glycine 12 to leucine. Acidic mutations at positions 12 and 18 are rarely seen in macrolittins but are common among the pHD peptides, which typically have five acidic mutations suggesting these positions are useful for pH sensitivity.

All-atom simulation of the entire pore formation process is prohibitive for systems of this size. Preformed pores are simulated at P/L suitable for melittin equilibrium pores [46] according to a putative structure for MelP5 [62] with peptides oriented as hypothesized by Li

et al. [23]. This allows for establishment of peptide sequence-structure-function relationships in molecular detail, as well as pore structure, unencumbered by peptide aggregation in membranes [258]. Mac70 and pH15 of the macrolittins and the pH peptides, respectively, are investigated via multi-microsecond all-atom molecular dynamics simulation to learn how the conserved and variable mutations influence potency. Macrolittin70 has a strictly sigmoidal P:L dependence, thereby serving as reference for the rest of the macrolittins, which also obey a sigmoidal P/L dependence although not necessarily as smoothly. pH15 is an outlier and among the less potent of the pH peptides with six acidic mutations. pH15 is one of the most pH-sensitive, differentiating it from the macrolittins, and making it comparable to the rest of the pH peptides. Given the lack of structural information simulation of preformed pores of mac70 at acidic pH, and of pH15 at neutral pH are also performed to verify the simulation protocol. Mac70 at pH 5 is a positive control as it still forms pores albeit not as effectively as at pH 7. This is confirmed by the reduction in pore size upon protonation of mac70's acidic residues. pH15 at pH 7 serves as a negative control as a system that should not form pores. The formation of a massive toroidal pore by pH15 upon deprotonation of acidic residues shows that pore formation by preformed pores is not conclusive evidence that a given peptide facilitates pore formation. Nonetheless, the difference in pore structure between pH15 at pH 5 and pH 7 convincingly demonstrates pH15 at pH 5 forms stable pores.

Interaction with lipid polar moieties shows pH plays a significant role in determining how peptides' N- and C-terminal halves anchor to the membrane. At pH 7, the N-terminal half anchors via all polar moieties, and the C-terminal half anchors via choline. At pH 5, the N-terminal half anchors via cationic residues to anionic polar moieties, while the C-terminal half anchors via all polar moieties. The peptides' ability to anchor to opposite leaflets ensures they remain transmembrane. There is no obvious difference between Lys and His in terms of membrane binding when each is cationic.

Peptide-peptide interactions can compete with peptide-membrane interactions. Glu4 of the conserved mutational motif (Glu(4,8), Gln17) in mac70 at pH 7 binds the intrapeptide N-term and limits anchoring of the N-term to lipid phosphate and esters. Glu4 is almost completely absent from peptide-peptide interactions and functions more as an N-term capping residue, similar to lysine bias of helical structure by binding the C-term [260]. Interactions by specific residues with neighboring peptides varies, but some residue positions show clear directional preference for the clockwise or counter clockwise adjacent peptide. Glu8 and Gln17 are oriented toward the counter clockwise, and clockwise adjacent peptide, respectively. Gln17's special relationship with Trp19 in all cases here is potentially to sequester the tryptophan indole amine from the lipid tails. Interpeptide H-bonding via the Gln amide to sidechain and backbone atoms has been shown to stabilize dimerization of simple model transmembrane helices [261]. In contrast, lack of strict preference by long and short chain polar residues at variable positions 15 and 18 as shown by mac70 and pHD15 demonstrates directional flexibility at these positions. The cationic residues at melittin position 7 and 21 both point toward the clockwise adjacent peptide, but position 21 is in general more flexible. Inherent directionality appears reinforced when consecutive residues in the amino acid sequence point toward the opposite adjacent neighboring peptide. Examples include cationic position seven and Glu8, Gln17 and position 18, Asp11 and Asp12 in pHD15, and Leu12 and Leu13 in mac70. Interaction between transmembrane leucines has been reported before as stabilizing the transmembrane dimer of the GCN4 leucine zipper [261]. Leu13 association with clockwise Leu12 could be more uniform throughout for simulation of a larger pore with more monomers. There is a noticeable preference for interactions with residues centrally located along the adjacent peptide. Mac70 Lys7 and Lys21 both form stronger salt bridges with Glu15 of the clockwise adjacent peptide than with Glu8 and the C-term, respectively. These interactions are lost at pH 5 due to competition from membrane polar moieties for Lys7, and because peptides' C-term form salt bridges with Lys21. Gln17 con-

tinues to establish relationships with Trp19 and Ser18. With the introduction of additional acidic mutations at central locations within the amino acid sequence, pHD15 at pH 5, again shows that centrally located residues are preferable for peptide-peptide interactions, as H7 has stronger interactions with Asp12 than Glu8. Lastly, not all peptide-peptide interactions encourage stable pores. Interactions across the pore diameter tend to close the pore as shown by the restricted diameter of pores at pH 5, and the prevalence of interactions between peptides i to $i + 2$ and $i + 3$. Interactions across the pore diameter by pHD15 at pH 5 can pull parts of a peptide off of the pore wall 3.27, detaching the hydrophobic face from the lipid tails and preventing it from being able to stabilize the membrane edge [95].

The barrel-stave model is typically disfavored for large diameter (> 3.0 nm) pores such as melittin's given the instability of a bundle of at least 12 peptides to shape deformation [46]. The majority of endogenous AMPs form toroidal pores, albeit via varied arrangements of the peptides, in which lipids bend allowing headgroups to intercalate between peptides to participate in the pore. Alamethicin is a rare exception, forming barrel-stave pores that occlude lipids from the pore lumen. Mac70 and pHD15 peptides associate and remain transmembrane, more similar to alamethicin [219] than to their melittin ancestor, which generally forms transient pore assemblies [40] while peptides remaining monomeric [61]. Furthermore, thickness profiles (figs. 5.41, 5.42, 5.43, 5.44) and phosphate statistics recapitulate the results of AFM experiments [23] that demonstrate macrolittins' and pHD peptides' contrasts with their predecessor MelP5, which induces local thinning in the vicinity of the pore [95]. Mac70 and pHD15 simulations are consistent with the lateral close-packing description proposed by Li *et al.* [23]. While macrolittin and pHD peptide pores are compatible with the barrel-stave model they bear an important distinction, which likens them to toroidal pores. Alamethicin pores are small and display a narrow size distribution, whereas toroidal pores can vary significantly in diameter [13]. This suggests the macrolittins and pHD peptides establish a new class of pore structure being barrel-stave and able to take on large dimensions.

The lack of congruence in the directionality of positions 11 and 18 suggests independence between the N- and C-terminal helices. In general, the correlation is useful for establishing the structure-function relationships of membrane proteins based on collective motion [222].

Macrolittins and pHD peptides retain much of the C-terminal half of MelP5 including the C-terminal tail. Pino-Angeles and Lazaridis have shown salt bridges between Lys21 and the C-term, and H-bonding involving Q24 and Q25 contribute to association between peptides in the MelP5 pore [62]. The ensuing correlation between tilt angles of MelP5 C-terminal helices in the pore extends to the macrolittins and pHD peptides. Regular interactions are absent between MelP5 N-terminal helices as Lys7 lacks a consistent binding partner, and no correlation is seen. In contrast, macrolittins' and pHD peptides' N-terminal helices possess clear opportunities to interact, and positive correlation is observed in cases where they do and no correlation is generally seen in cases where they do not. Lack of or low correlation in tilt between intrapeptide N- and C-terminal helices in mac70 and pHD15 at optimal pH shows the Pro14 kink is the hinge between relatively independent segments. The increase in correlated motion of relatively rigid helical subunits between peptides comes at an entropic cost [262]. Interpeptide interactions that incur the least entropic penalty are therefore preferred. This general principle is seen by the preference for the more flexible long sidechain Glu mutation over Asp [22, 23]. Additionally, introduction of the glycine zipper motif into the N-terminal helix via the valine 8 to glycine mutation is excluded from the consensus GoF positives [20], including MelP5, which the macrolittins and pHD peptides are based on. By comparison, the glycine zipper in the glycophorin-A transmembrane dimer is more centrally located along the helix and more embedded into the membrane, minimizing the influence of one peptide's tilt on the other [258]. Lastly, sidechain interactions between adjacent peptides by mac70 and pHD15 show preference for residues that are more central within the amino acid sequence when comparable alternatives are available. Interactions closer to the base of the pivot point have less influence on the tilt of the bound helix. At pH

7 both Lys7 and Lys21 have stronger interactions with Glu15 than with Glu8 and the C-term, respectively, of the clockwise adjacent peptide. At pH 5 Lys7 affinity for lipid phosphates and esters dominates sequestering Lys7 from Glu15, and the persistence of the salt bridge interaction with the C-term precludes Lys21's H-bonding to Glu15. Peptide association is not necessary for pore formation and given the tight association between mac70 peptides at pH 7 it is understandable that our simulations produce comparatively narrow pores [62] (given the limited number of peptides that can be included in a practical simulation). One might expect given mac70 at pH 5 has fewer and weaker interactions between adjacent peptides that they would behave more like melittin allowing lipids to intercalate between peptides and expand the pore [6]. This is not the case and the mac70 pore at pH 5 is more narrow than at pH 7 suggesting that maintenance of peptide-peptide interaction albeit at high entropic cost ultimately limits expansion of the pore; conversely interactions that come at a lesser entropic cost can have a positive influence on pore size and stability. While pHD15 at pH 5 also shows this preference, for example Lys7 interaction with Asp12 is stronger than with Glu8 of the clockwise adjacent peptide, it is more difficult to link this behavior to pore stability given pHD15 is significantly different from mac70 (an outlier even among the pHD peptides) and pHD15's natural basis for comparison should not form pores.

Chapter 5

Appendix

IMM1 : Melittin Dimerization on the Membrane Surface

System	$\langle \text{Energy} \rangle$, s.d.	Dimerization F.E.
Monomer	-507.945 ± 2.720175	
Rubin	-1048.428 ± 11.97552	-32.538
Janus	-1043.346 ± 4.081241	-27.456
Paralle	-1039.65 ± 6.384011	-23.76

Table 5.1: $\langle \text{TOTE(dimer)} \rangle - (2) \langle \text{TOTE(monomer)} \rangle$

IMM1 : Melittin Dimerization on the Membrane Surface

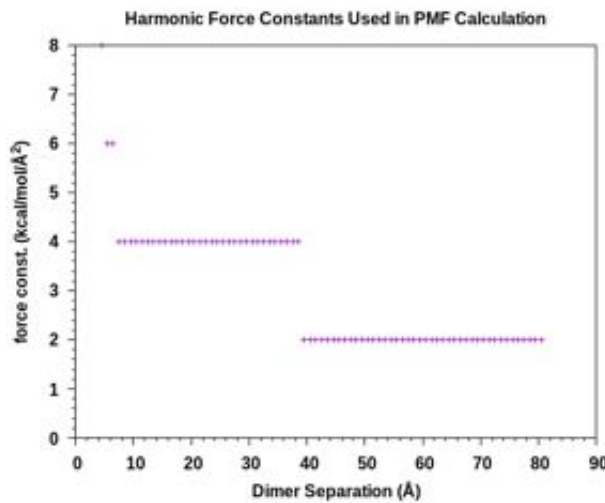


Figure 5.1: Force constants used in PMF calculation associated with each dimer separation sampled.

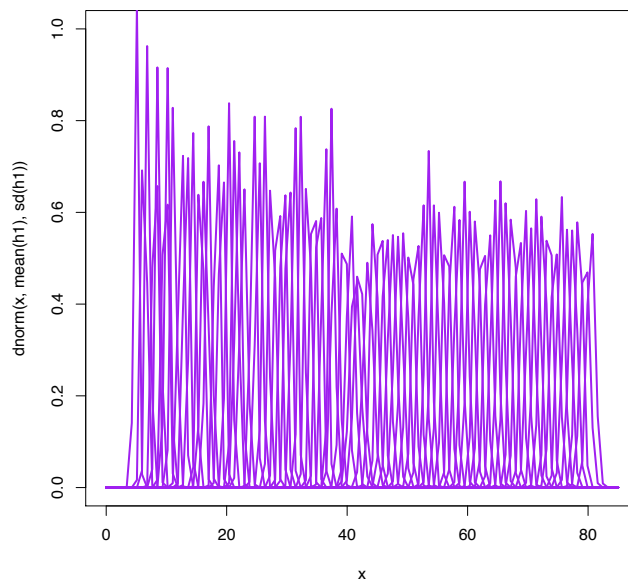


Figure 5.2: Histograms for umbrella sampling windows used in IMM1 PMF profile.

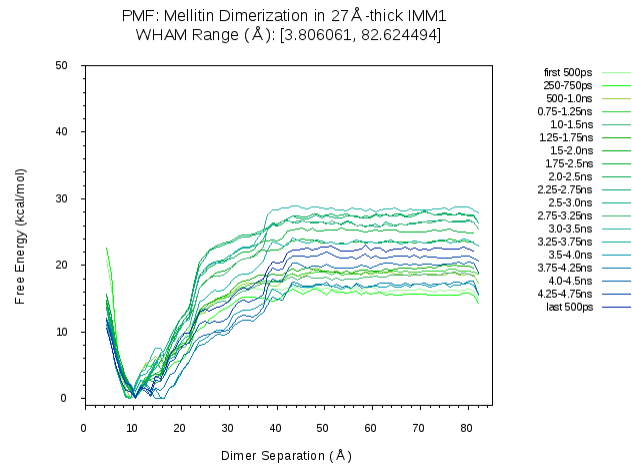


Figure 5.3: PMF profiles at different sections of the trajectory. Each umbrella sampling window consists of 500frames.

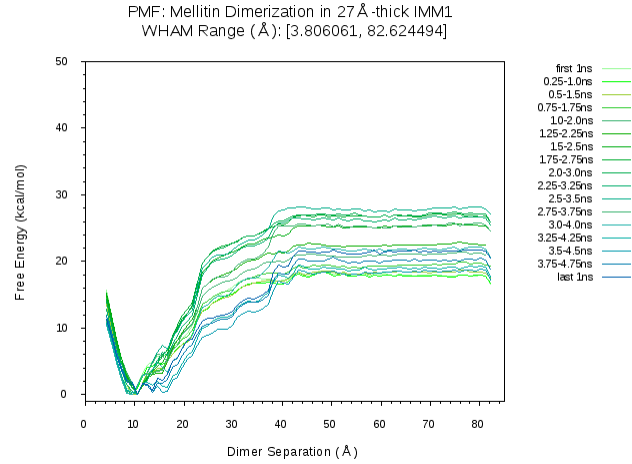


Figure 5.4: PMF profiles at different sections of the trajectory. Each umbrella sampling window consists of 1000frames.

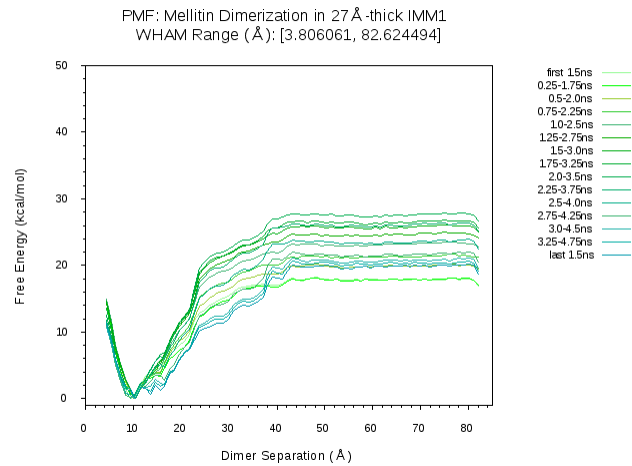


Figure 5.5: PMF profiles at different sections of the trajectory. Each umbrella sampling window consists of 1500frames.

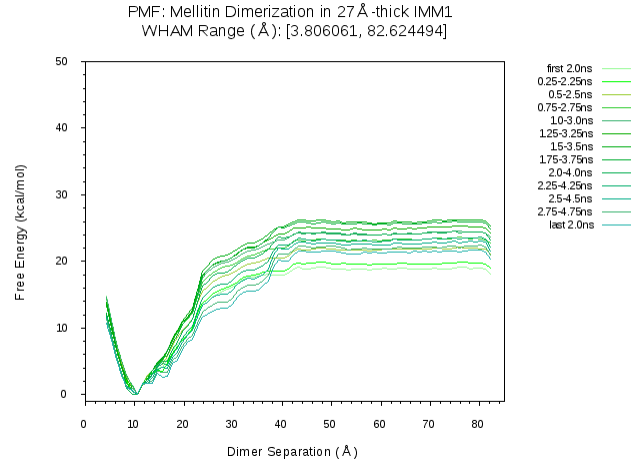


Figure 5.6: PMF profiles at different sections of the trajectory. Each umbrella sampling window consists of 2000frames.

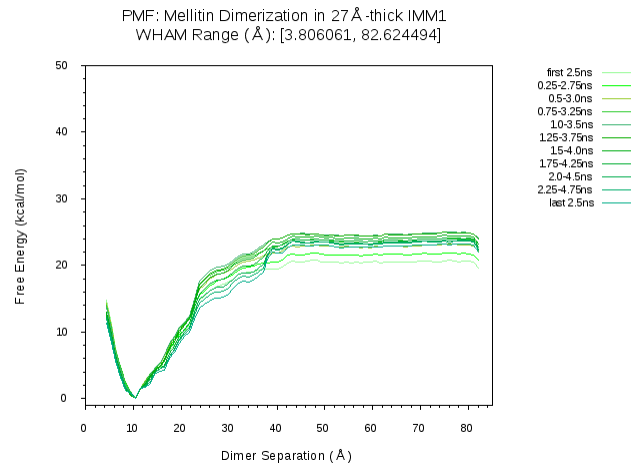


Figure 5.7: PMF profiles at different sections of the trajectory. Each umbrella sampling window consists of 2500frames.

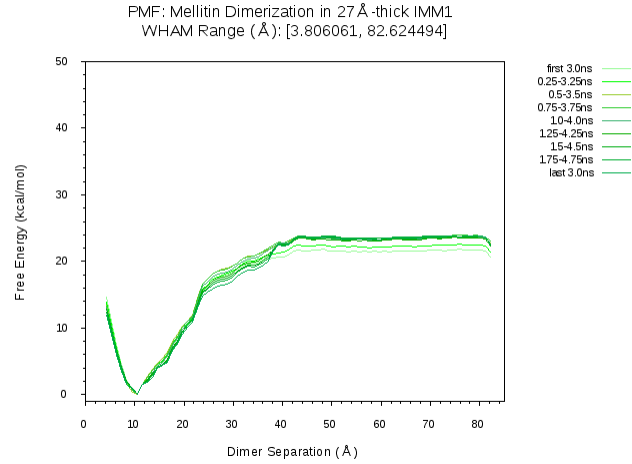


Figure 5.8: PMF profiles at different sections of the trajectory. Each umbrella sampling window consists of 3000frames.

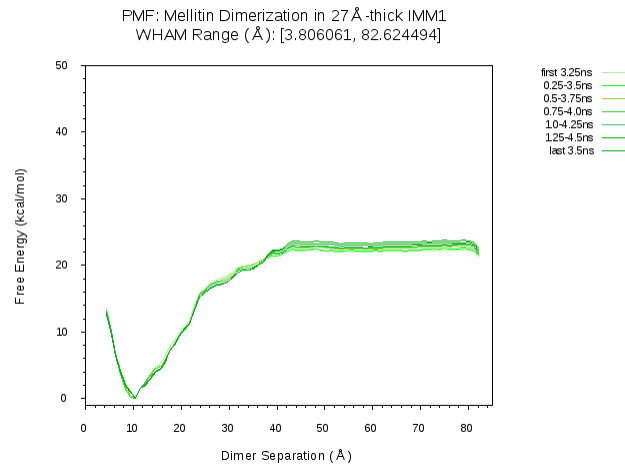


Figure 5.9: PMF profiles at different sections of the trajectory. Each umbrella sampling window consists of 3500frames.

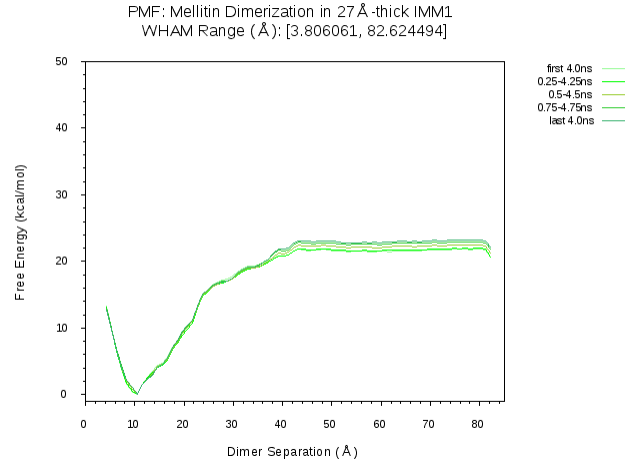


Figure 5.10: PMF profiles at different sections of the trajectory. Each umbrella sampling window consists of 4000frames.

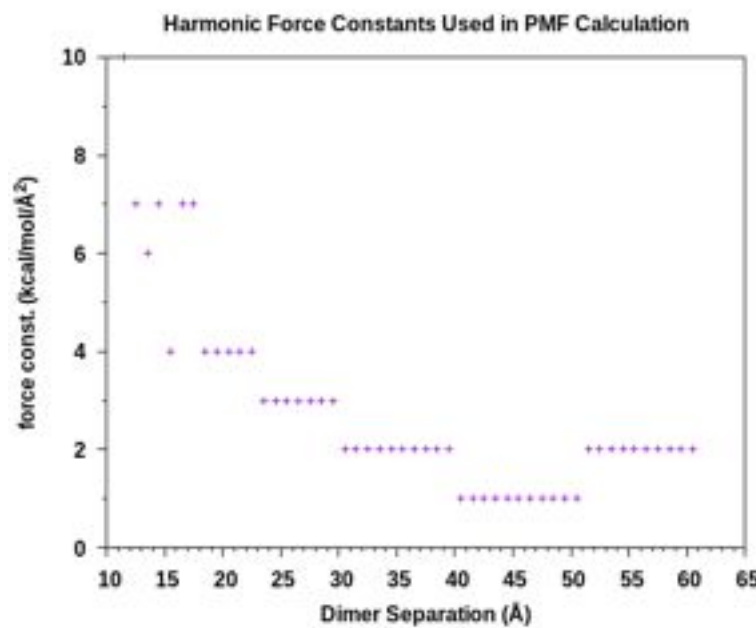
HDGB : Melittin Dimerization on the Membrane Surface

Figure 5.11: Force constants used in PMF calculation associated with each dimer separation sampled.

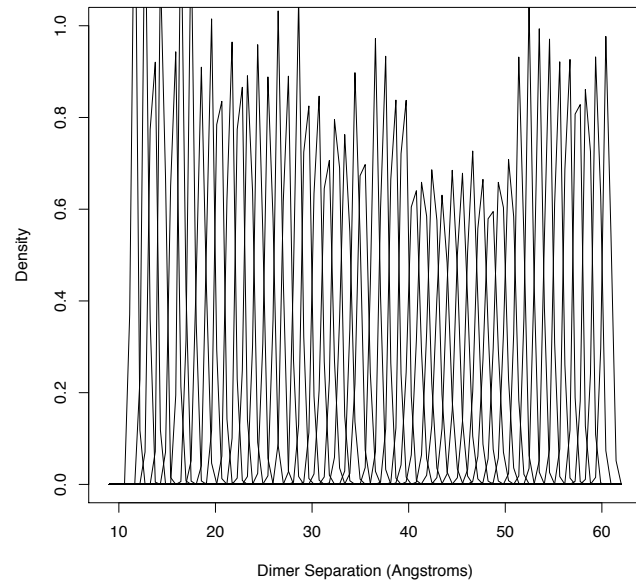


Figure 5.12: Histograms for umbrella sampling windows used in PMF calculation.

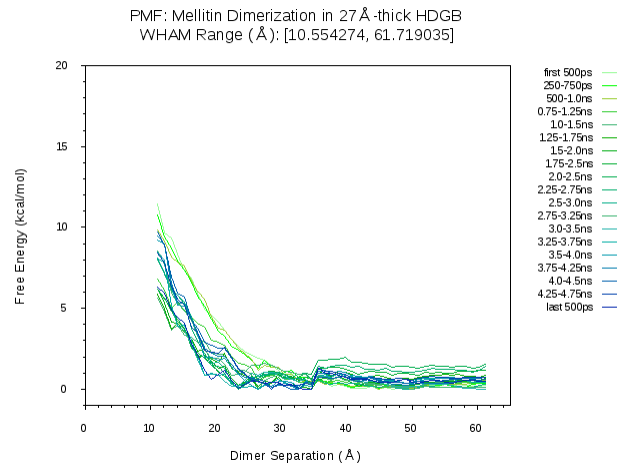


Figure 5.13: PMFs at different sections of the trajectory. Each umbrella sampling window consists of 5000 frames.

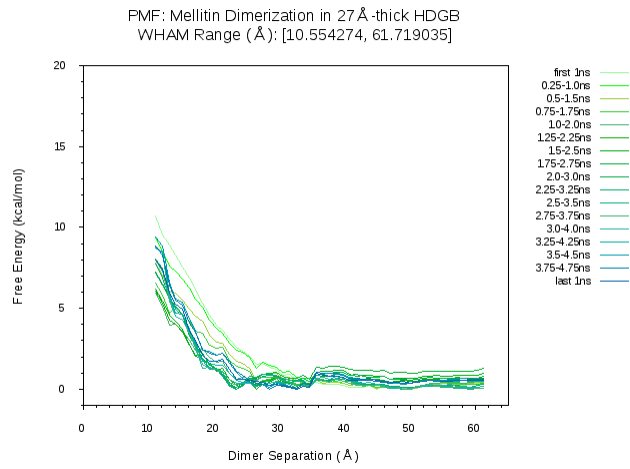


Figure 5.14: PMFs at different sections of the trajectory. Each umbrella sampling window consists of 10000frames.

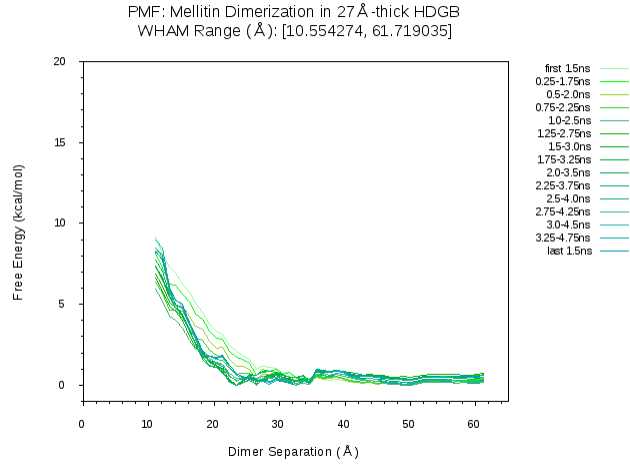


Figure 5.15: PMFs at different sections of the trajectory. Each umbrella sampling window consists of 15000frames.

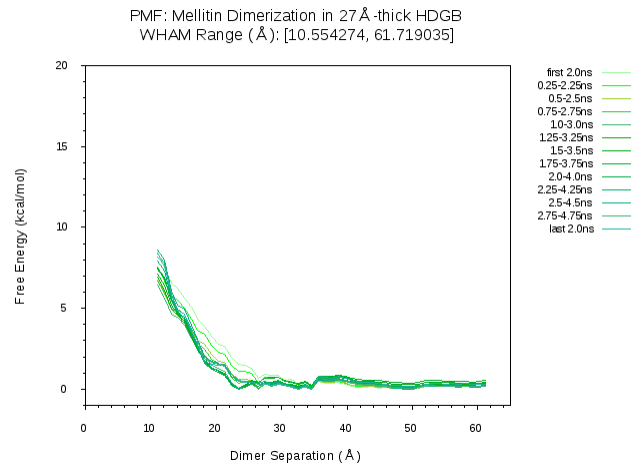


Figure 5.16: PMFs at different sections of the trajectory. Each umbrella sampling window consists of 20000frames.

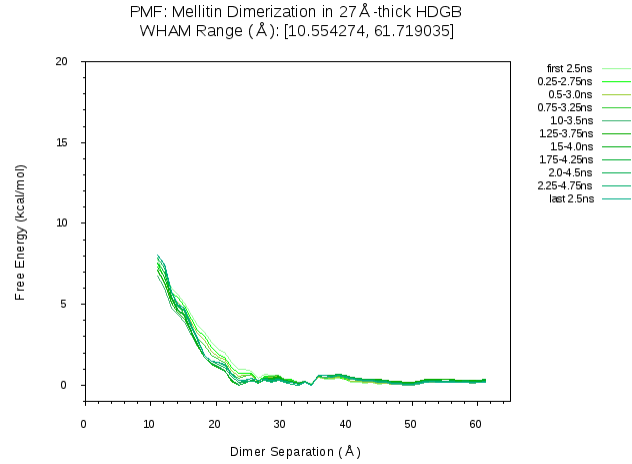


Figure 5.17: PMFs at different sections of the trajectory. Each umbrella sampling window consists of 25000frames.

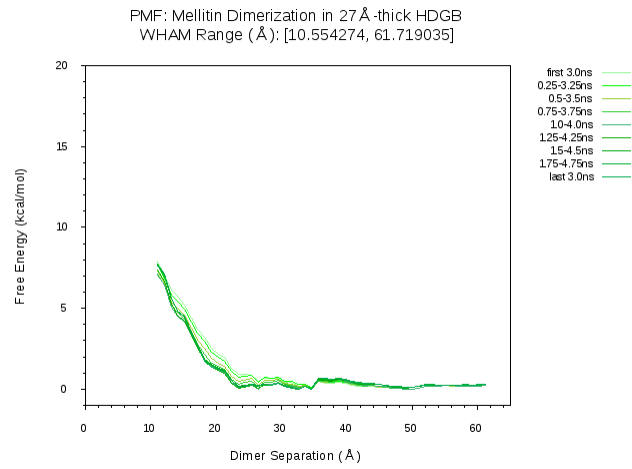


Figure 5.18: PMFs at different sections of the trajectory. Each umbrella sampling window consists of 30000frames.

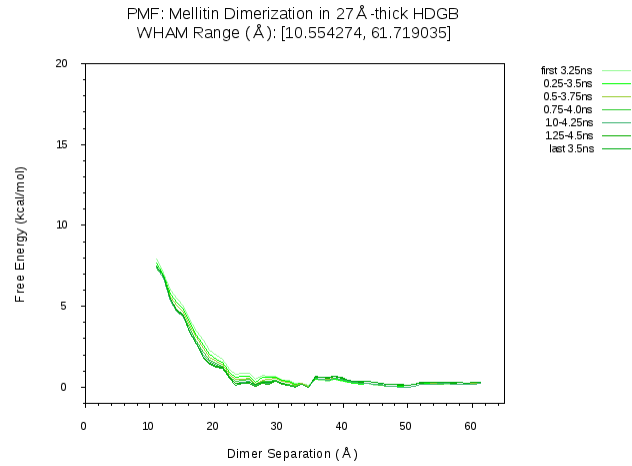


Figure 5.19: PMFs at different sections of the trajectory. Each umbrella sampling window consists of 35000frames.

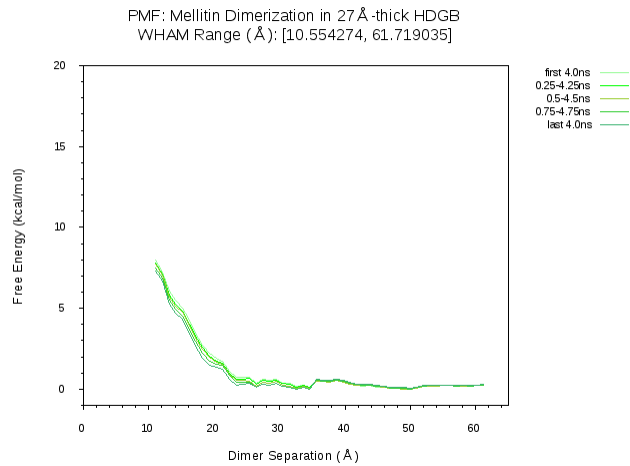


Figure 5.20: PMFs at different sections of the trajectory. Each umbrella sampling window consists of 40000frames.

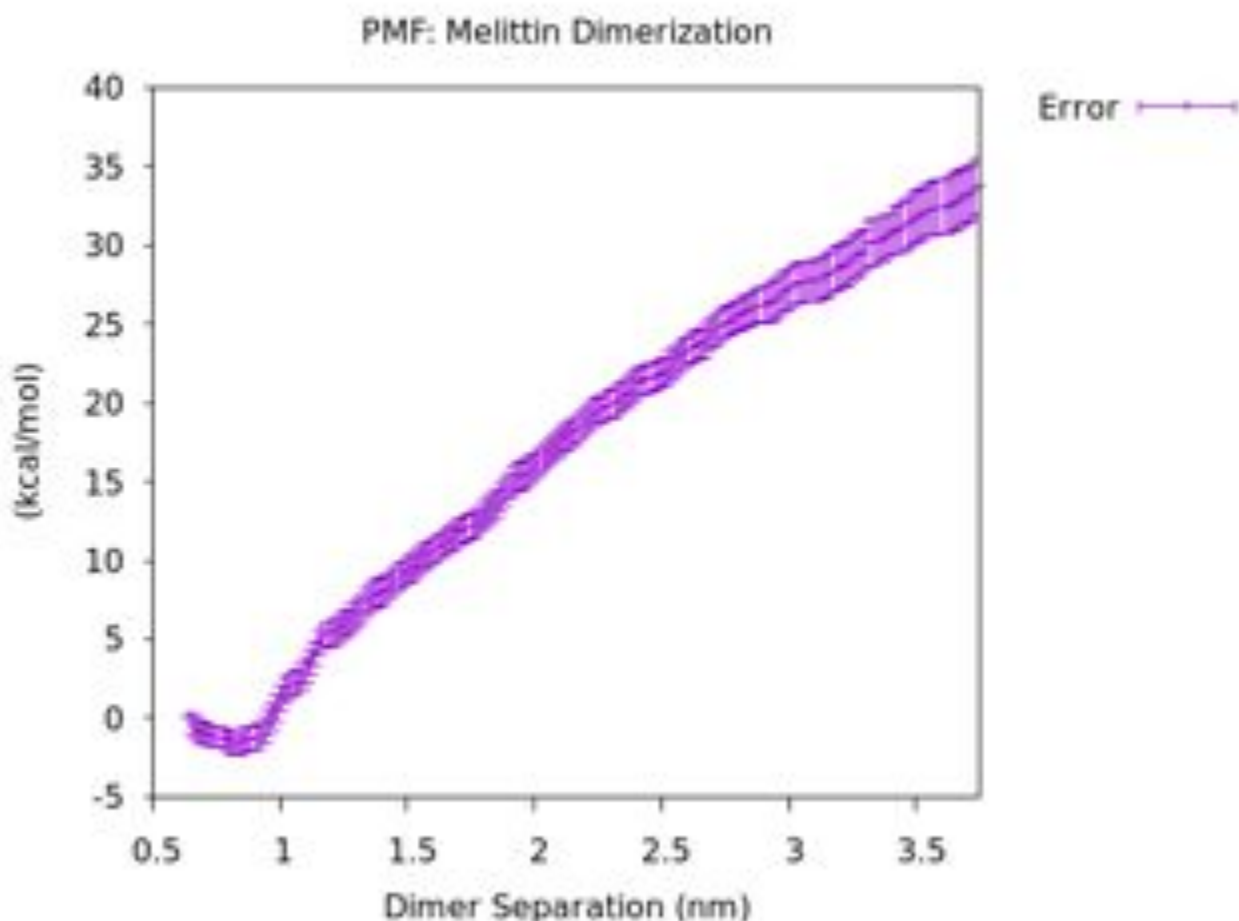
All-Atom Simulations : Melittin Dimerization on the Membrane Surface

Figure 5.21: PMF with error bars for separating the melittin dimer (helices parallel to the x -axis) along the y -direction for the small system shown in fig. 3.5. The windows are each 50 ns long. 20 bootstrap trajectories are used to generate error bars.

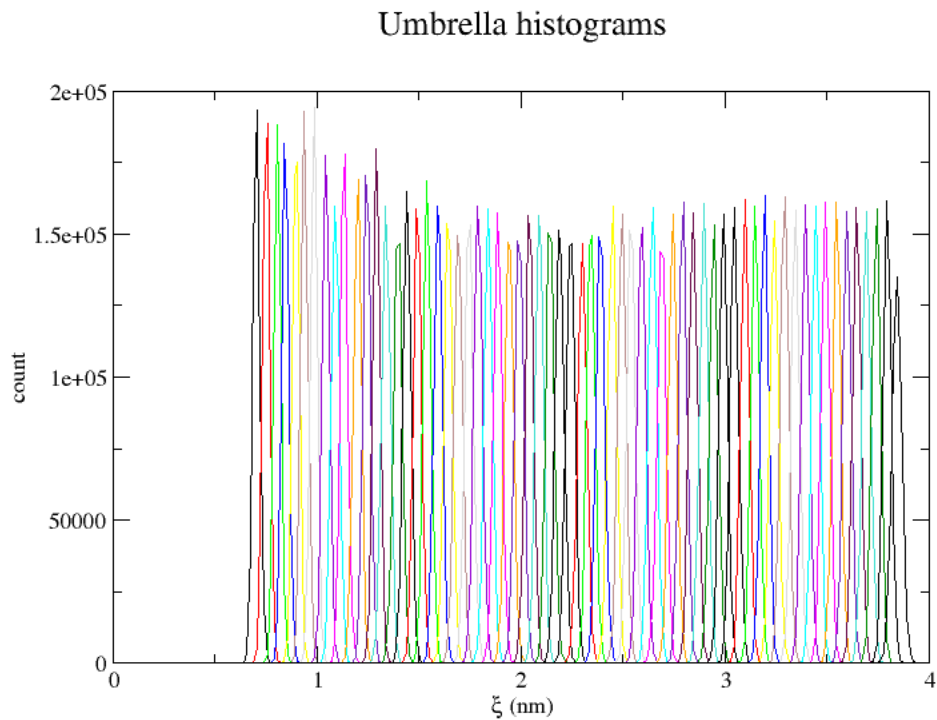


Figure 5.22: Histograms for umbrella sampling windows for the small system in fig. 3.5.

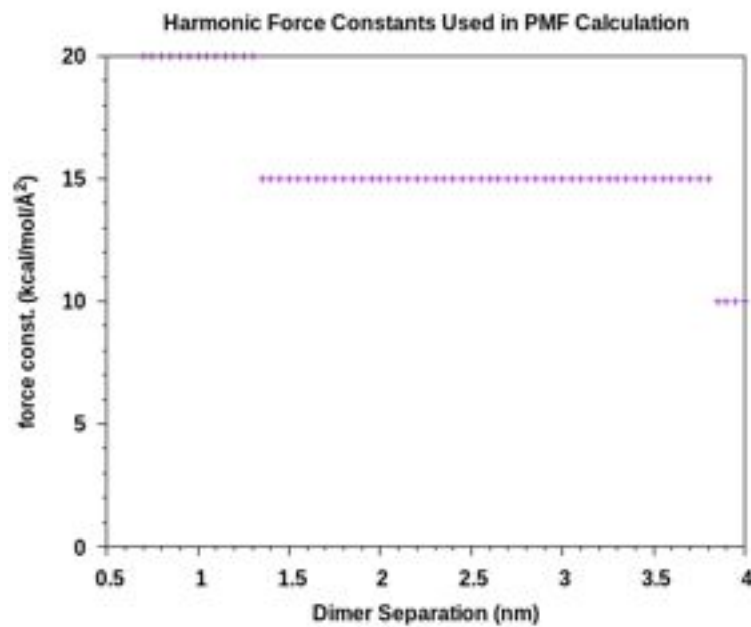


Figure 5.23: Force constants used in 50 ns umbrella sampling windows for the small system PMF in fig. 3.5.

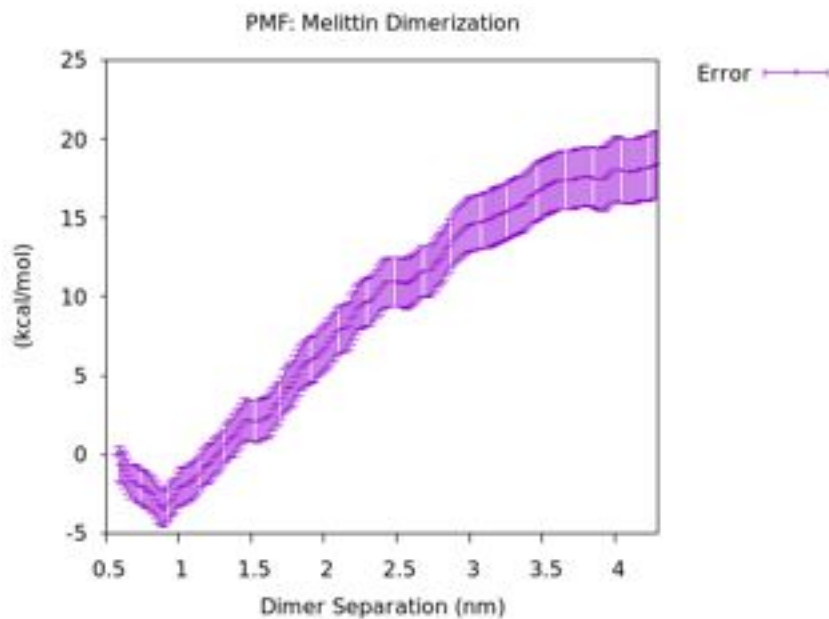


Figure 5.24: PMF for dimer separation along the xy -plane with error bars for the big system show in fig. 3.5. The windows are 50 ns long. 200 bootstrap trajectories are used to generate the error bars.

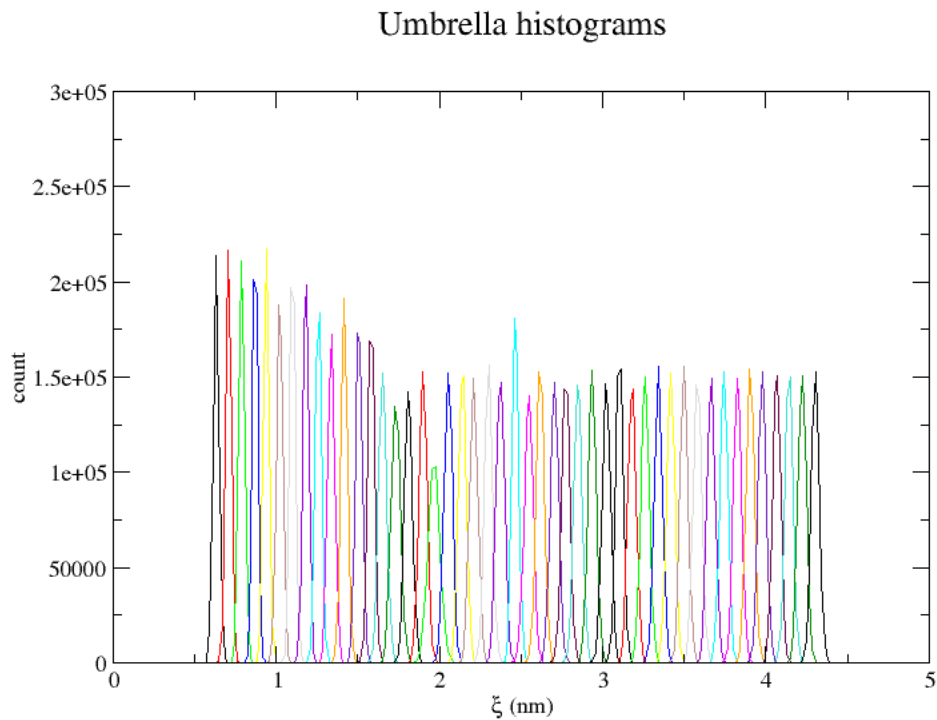


Figure 5.25: Histograms for windows used to generate error bars in the big system.

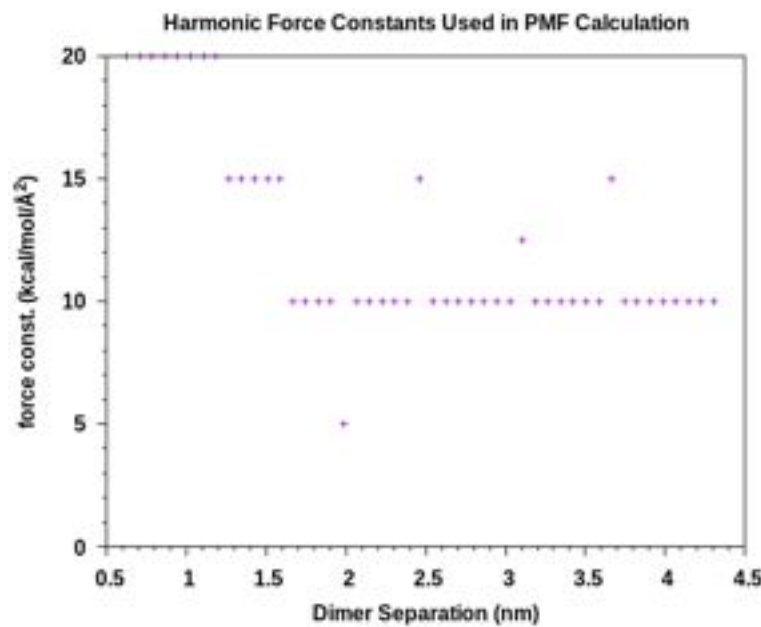


Figure 5.26: Force constants used in umbrella sampling windows for 50 ns windows used for the PMF in fig. 3.5.

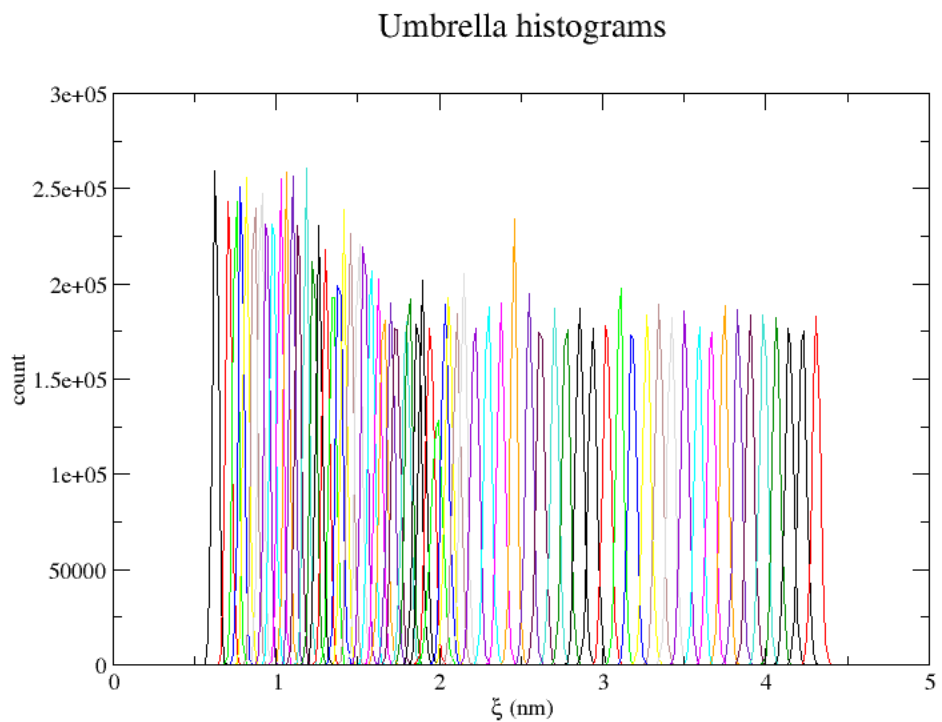


Figure 5.27: Histograms for 100 ns windows used in PMF in fig. 3.6.

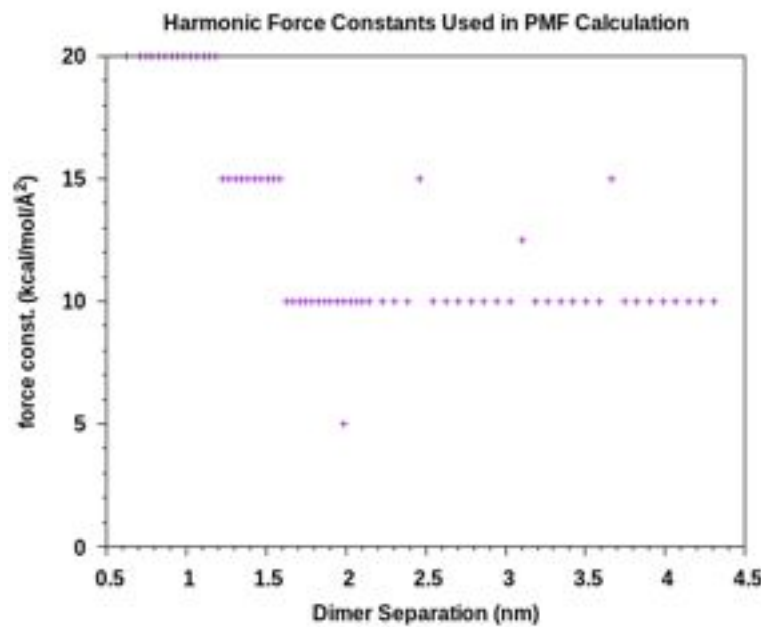


Figure 5.28: Force constants used in umbrella sampling windows for 100 ns windows used for the PMFs in fig. 3.6.

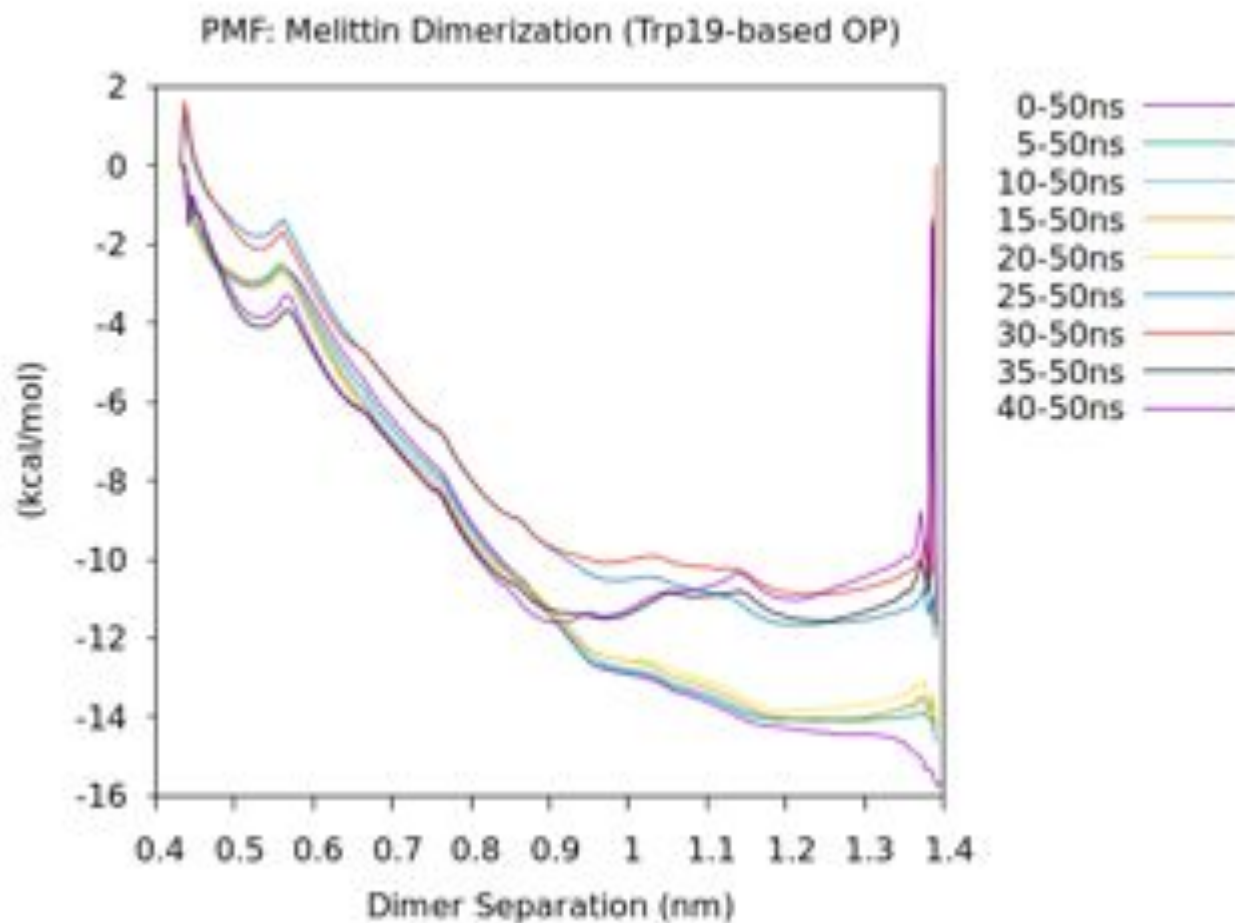


Figure 5.29: PMF profiles showing the influence of truncation of the initial equilibration stage of the simulation.

Umbrella histograms

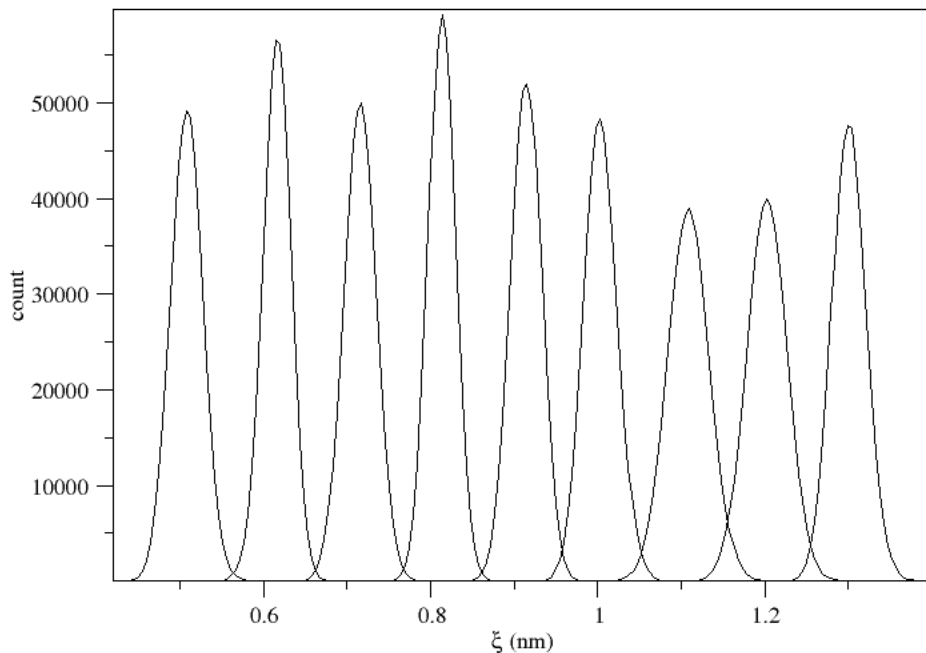


Figure 5.30: Histograms for the PMFs using the Trp19 based order parameter.

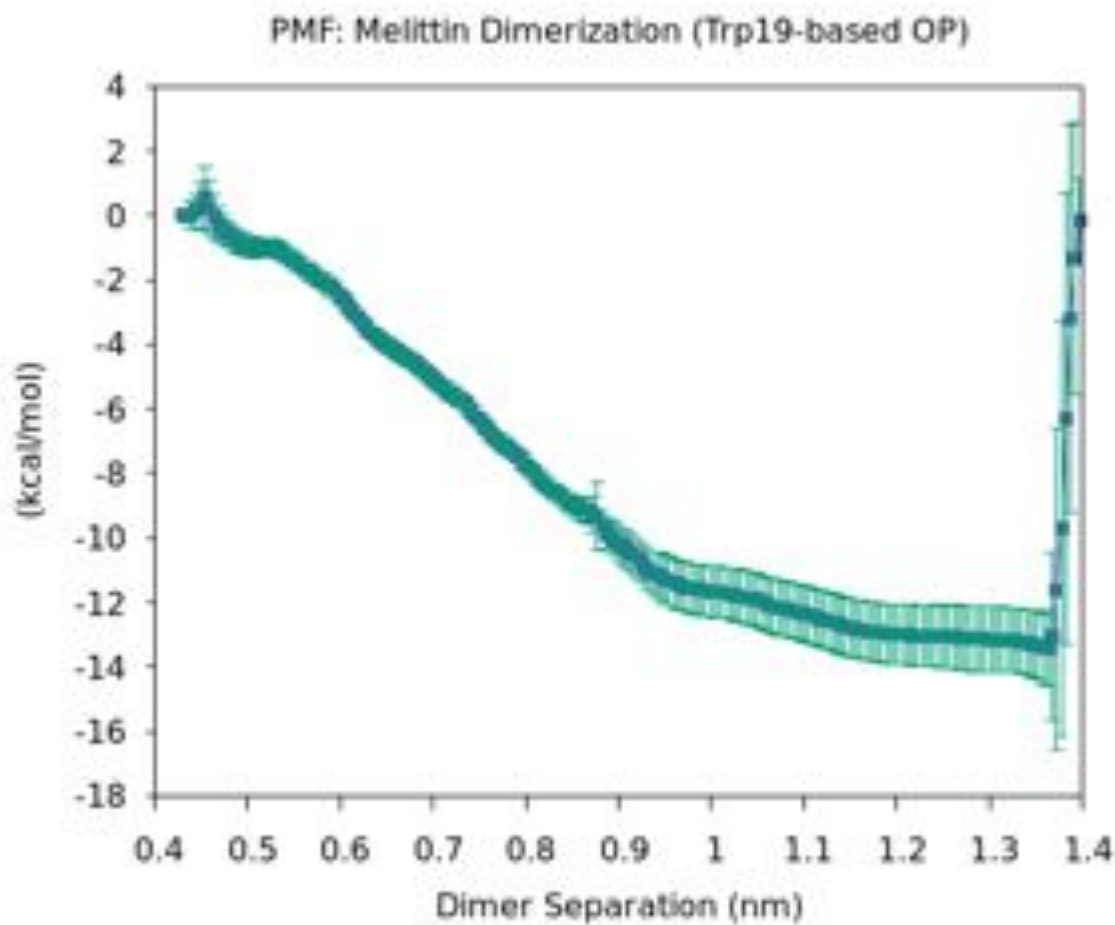


Figure 5.31: PMF profile with error bars. 200 boot-straps.

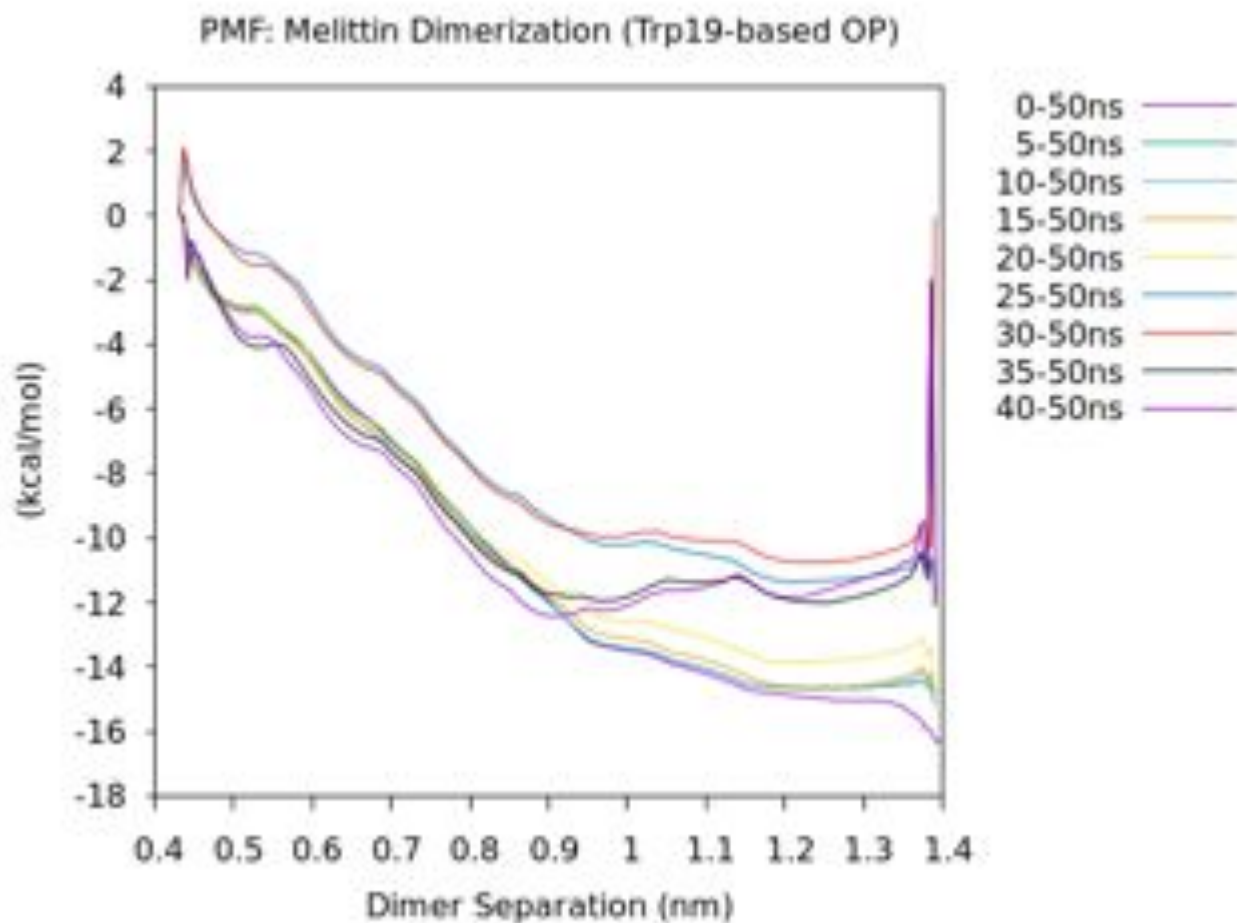


Figure 5.32: PMF profiles with the beginning of the umbrella sampling windows progressively truncated for the tryptophan 19 based order parameter.

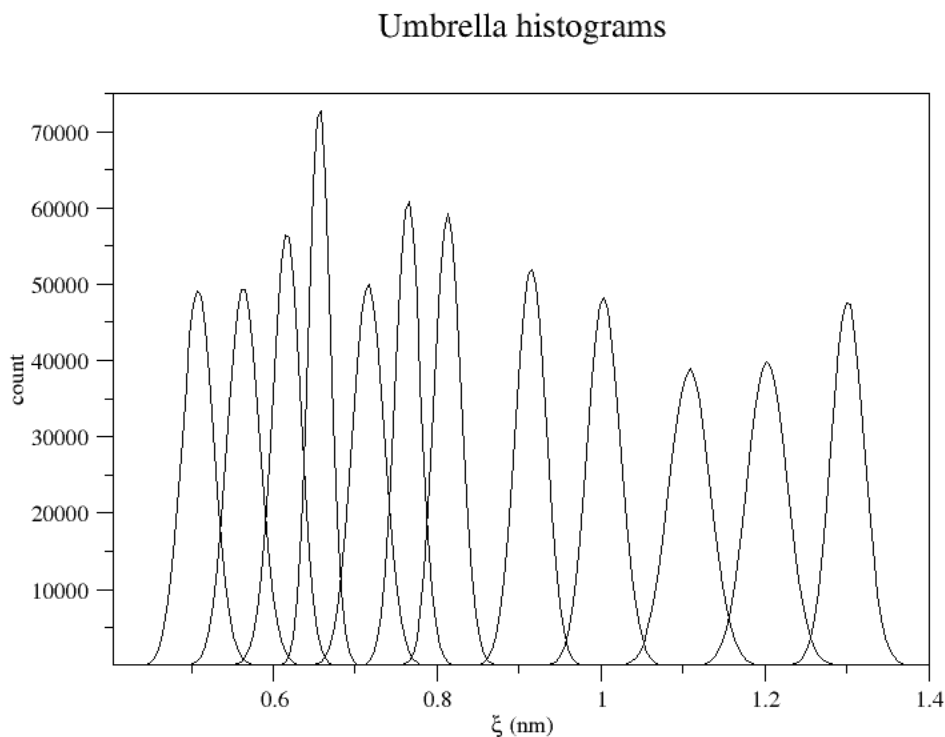


Figure 5.33: Histograms with additional umbrella sampling windows for the tryptophan 19 based order parameter.

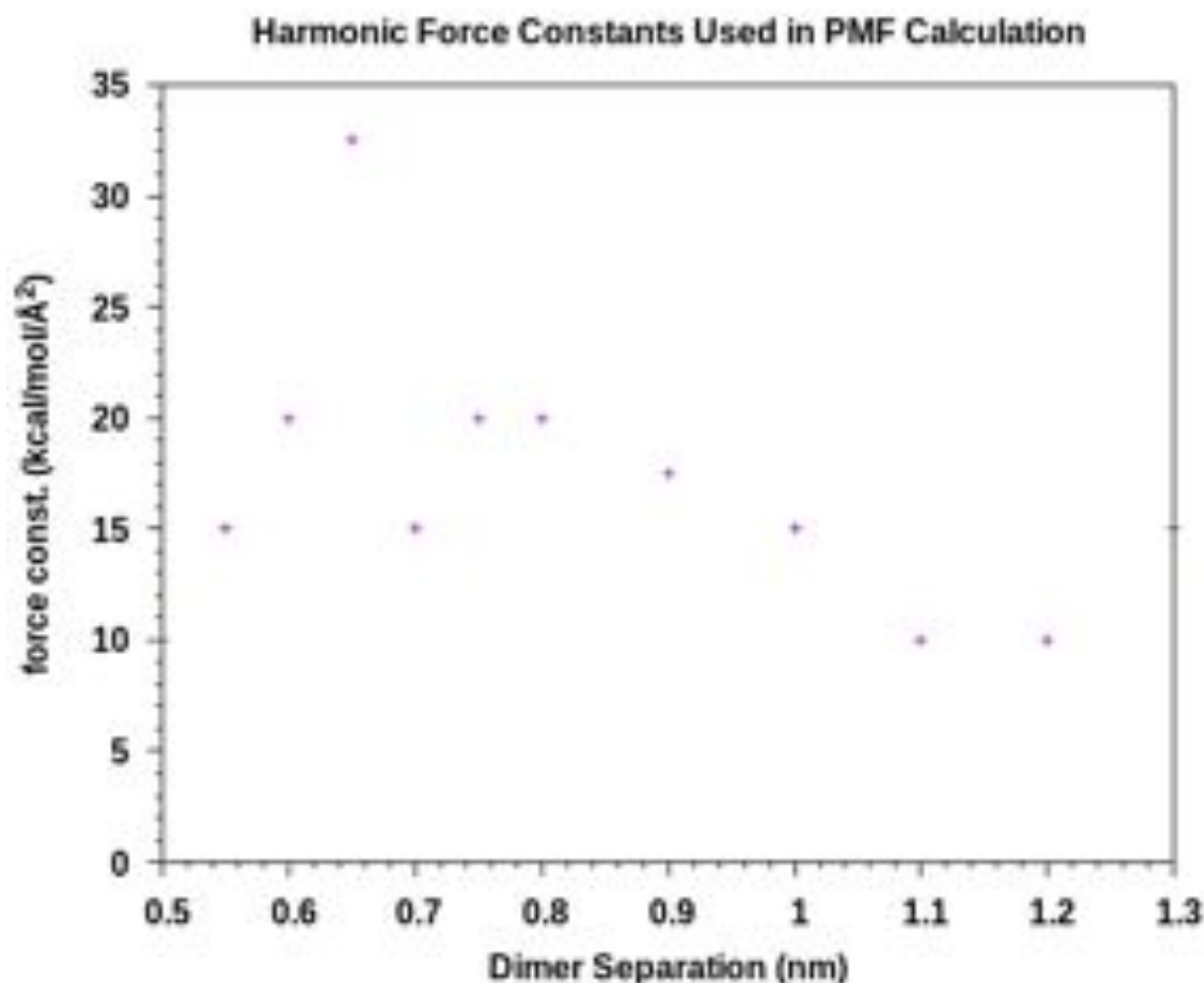


Figure 5.34: Force constants for umbrella sampling windows for the tryptophan 19 based order parameter.

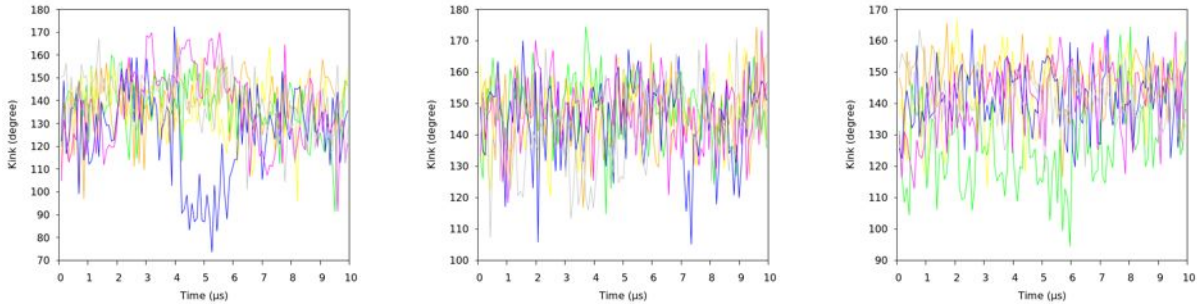
Anton Simulations : Macrolittin70 and pHD15

Figure 5.35: Macrolittin70 pore at pH 7. Macrolittin70 pore at pH 5. pHD15 pore at pH 5. Helix kink v. time for 10 μ s simulation. The N-terminal and C-terminal helix tilt is measured between residues 1 to 13, and between residues 15 to 21, respectively, for all systems.

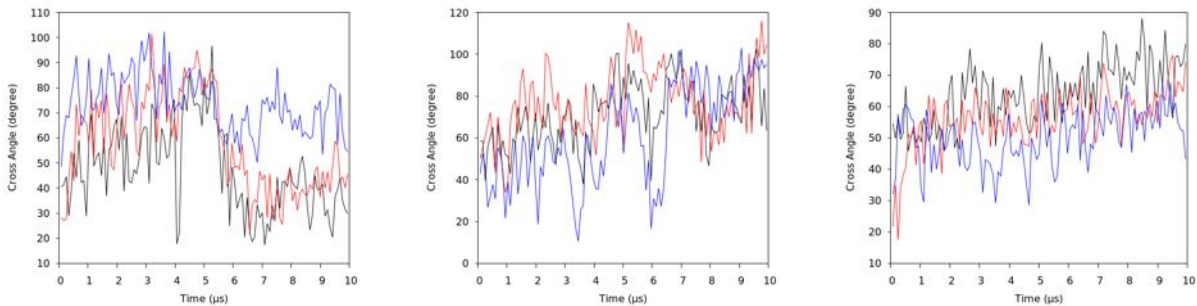


Figure 5.36: Macrolittin70 pore at pH 7. Macrolittin70 pore at pH 5. pHD15 pore at pH 5. Helix cross angle v. time for 10 μ s simulation. Black: cross angle between PROA and PROD helices. Red: cross angle between PROB and PROE helices. Blue: cross angle between PROC and PROF helices.

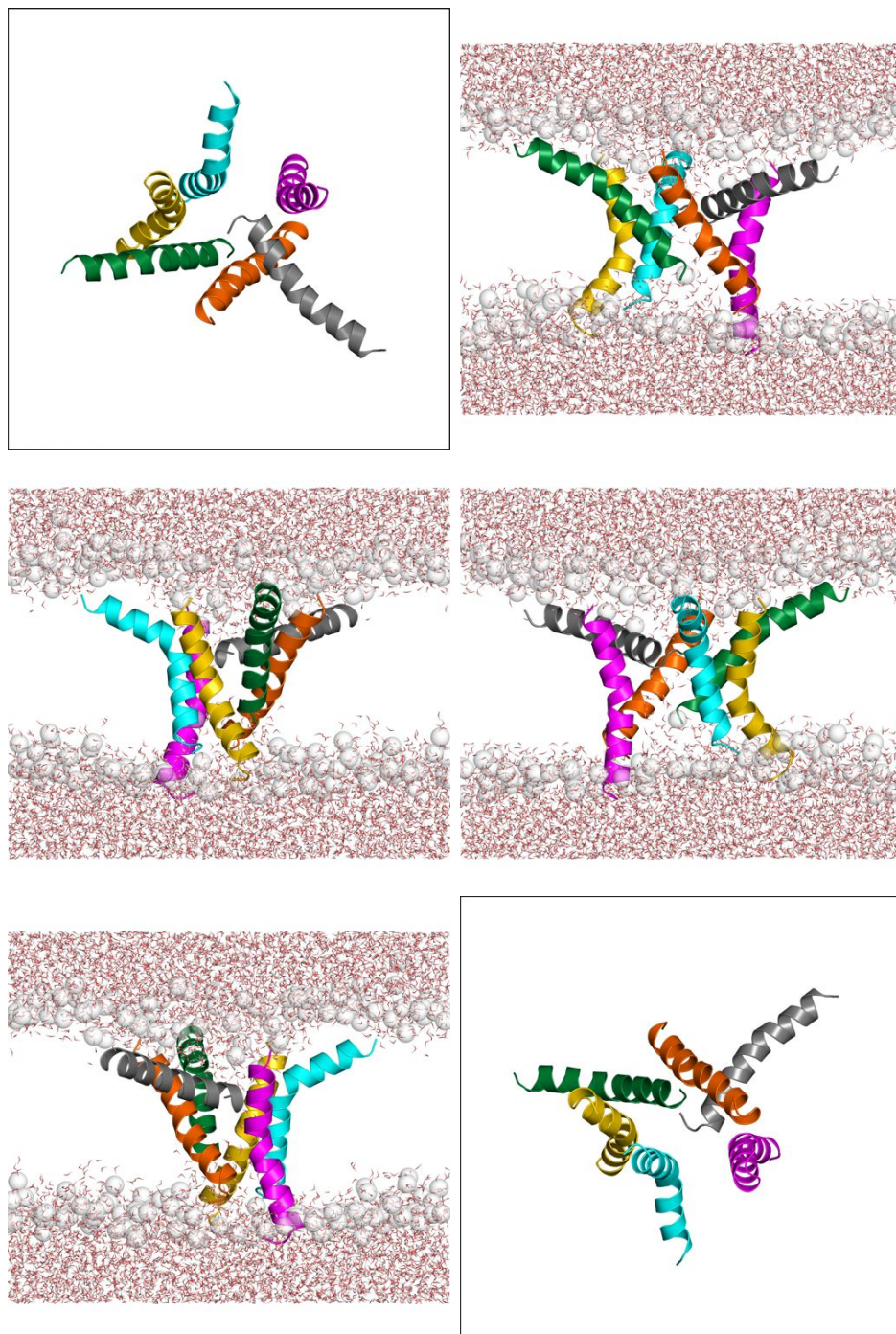


Figure 5.37: MelP5 at 10 μ s. (Top Left) Top view with N-term up. (Top Right) Top view with C-term up. Side views with (N-term up) PROA (orange), PROB (gray), PROC (magenta), PROD (cyan), PROE (yellow), PROF (green).

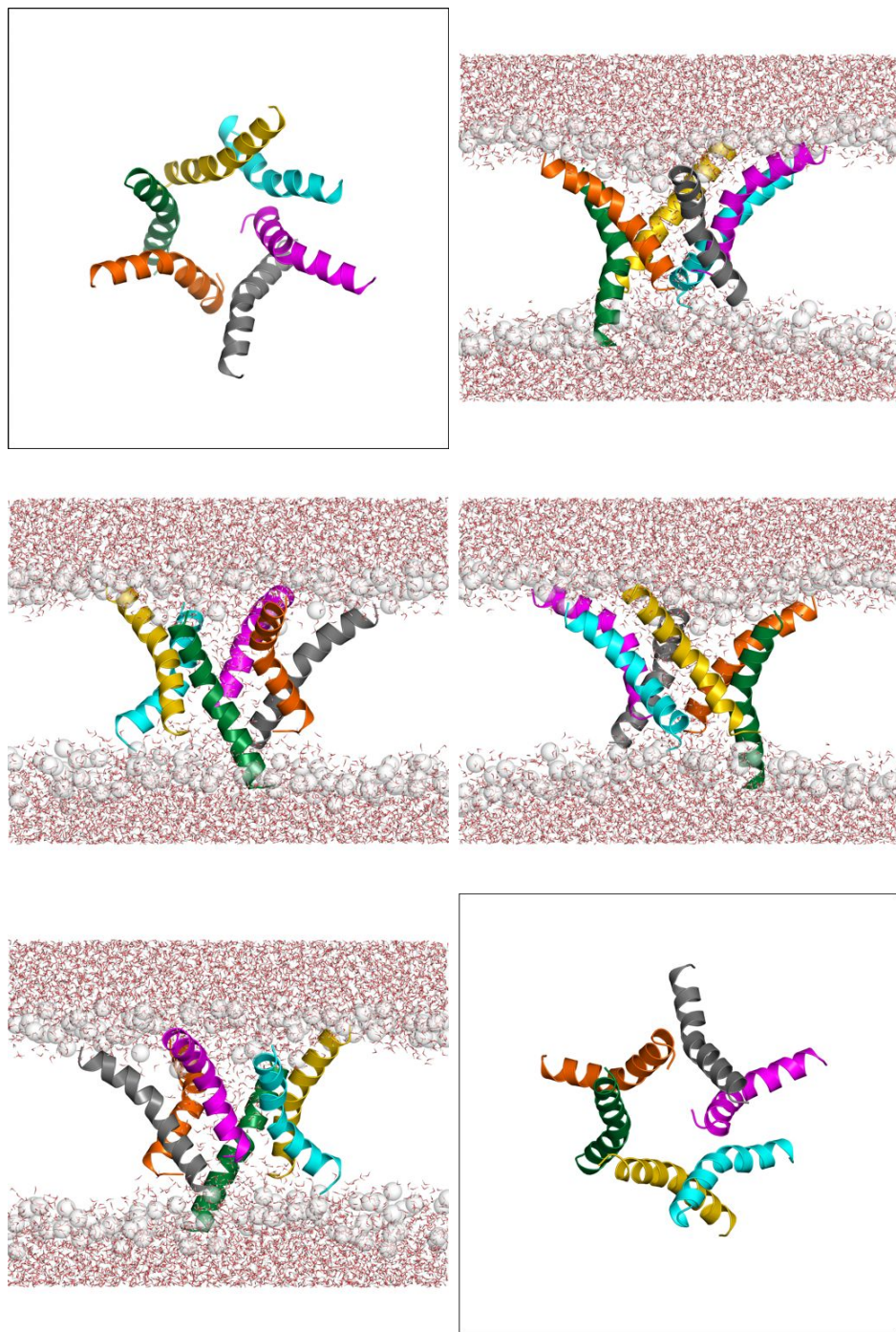


Figure 5.38: Macrolittin60 at pH 7 last frame. Side view (N-term up) at $10 \mu\text{s}$. PROA (orange), PROB (green), PROC (yellow), PROD (cyan), PROE (magenta), PROF (gray).

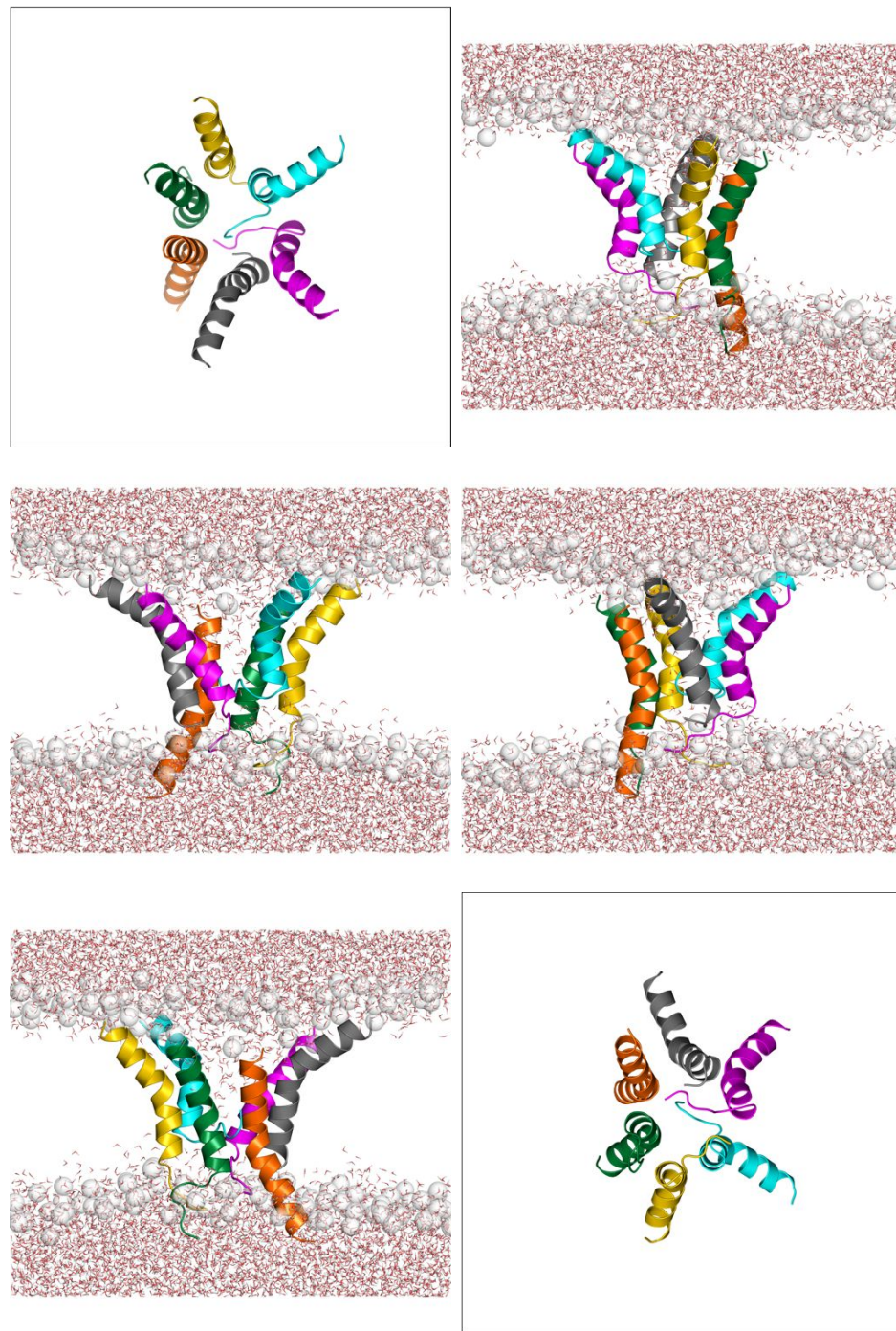


Figure 5.39: Macrolittin60 pore at pH 7 last frame. Side view (N-term up) at 10 μ s. PROA (orange), PROB (green), PROC (yellow), PROD (cyan), PROE (magenta), PROF (gray).

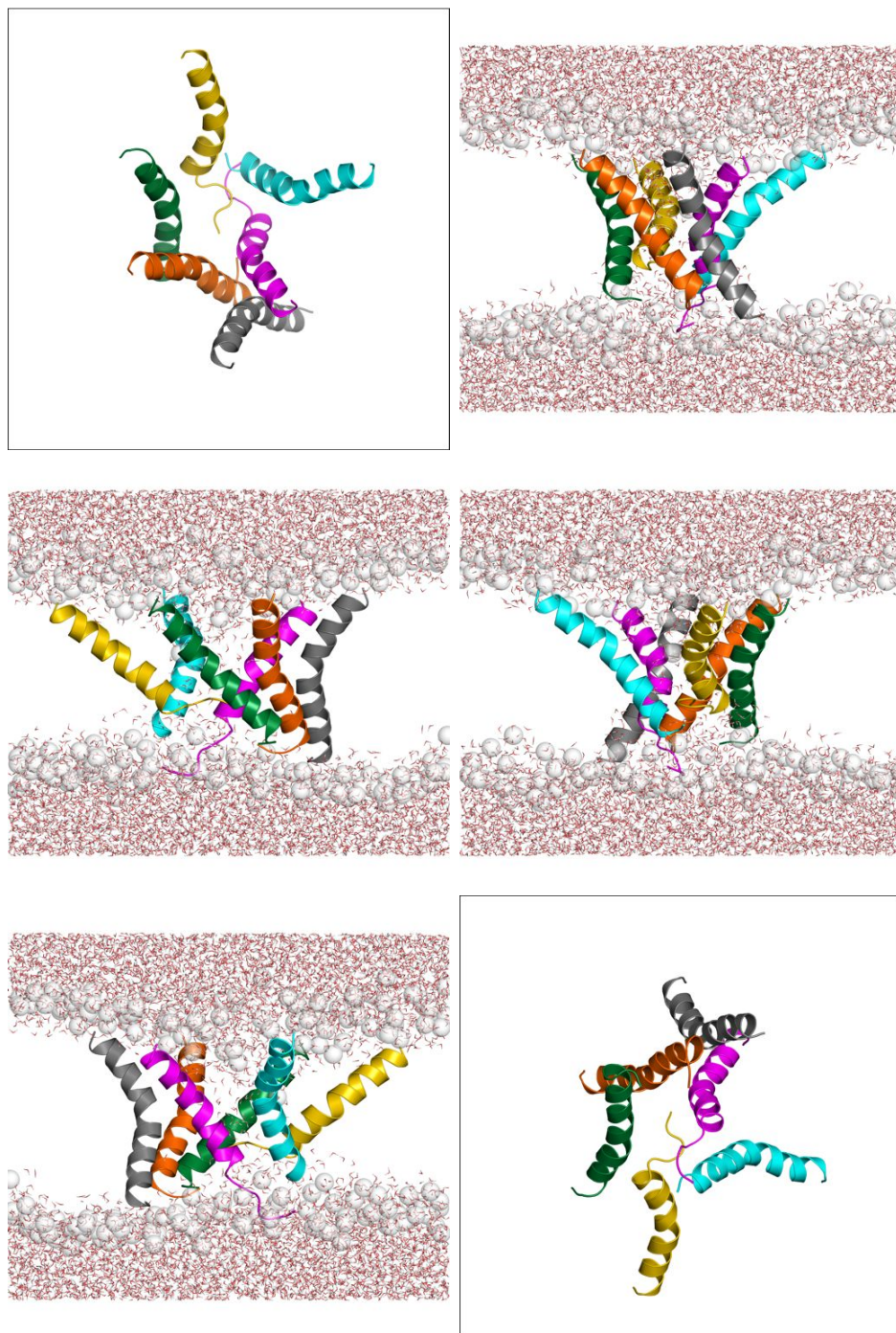


Figure 5.40: Macrolittin70 at pH 5 last frame. Side view (N-term up) at $10 \mu\text{s}$. PROA (orange), PROB (green), PROC (yellow), PROD (cyan), PROE (magenta), PROF (gray).

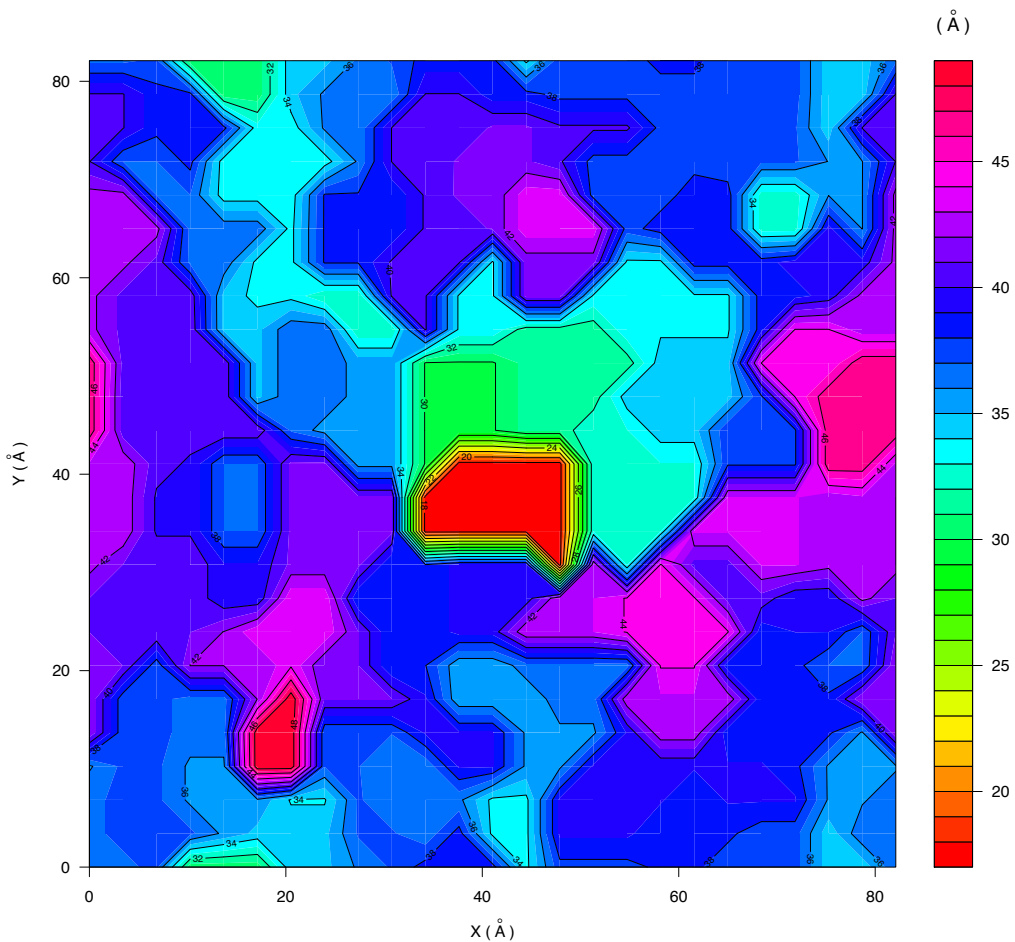
Membrane Thickness :

Figure 5.41: MelP5. Membrane thickness according to phosphorus in \AA . Last frame, centered (and wrapped) around protein.

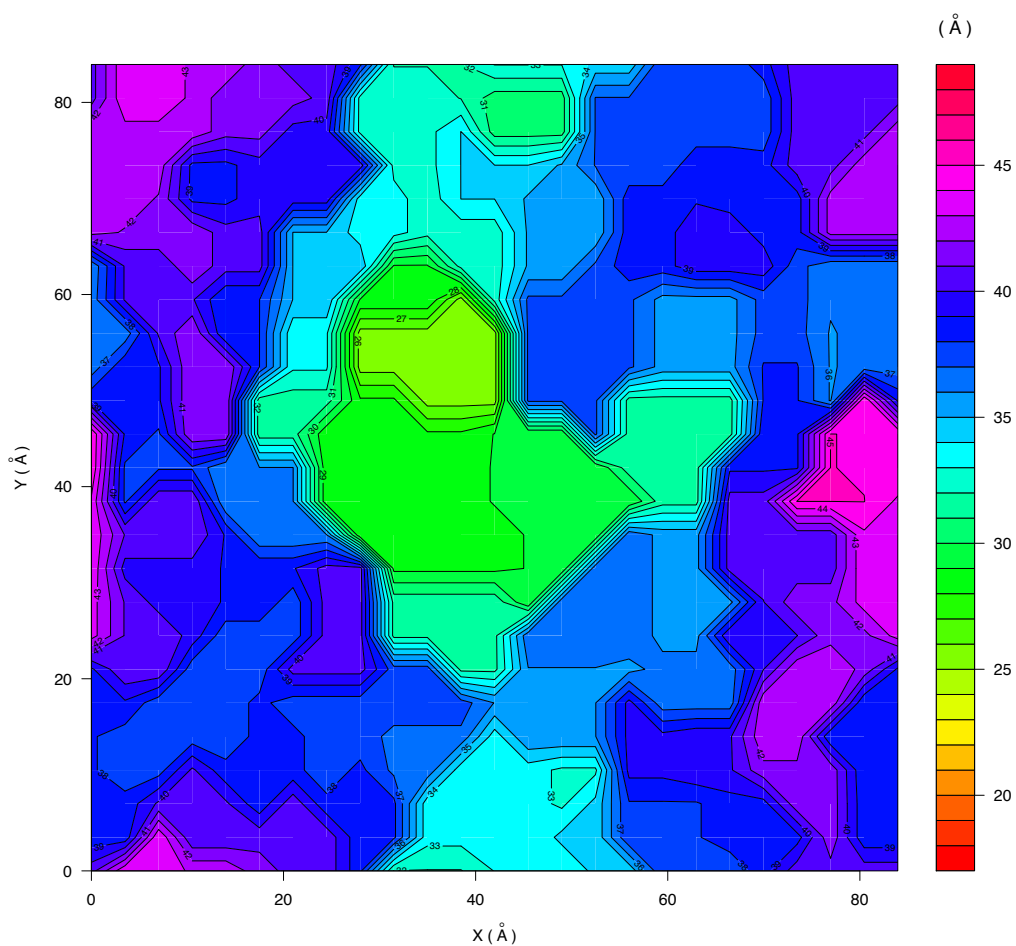


Figure 5.42: Macrolittin70 at pH 7. Membrane thickness according to phosphorus in Å. Last frame, centered (and wrapped) around protein.

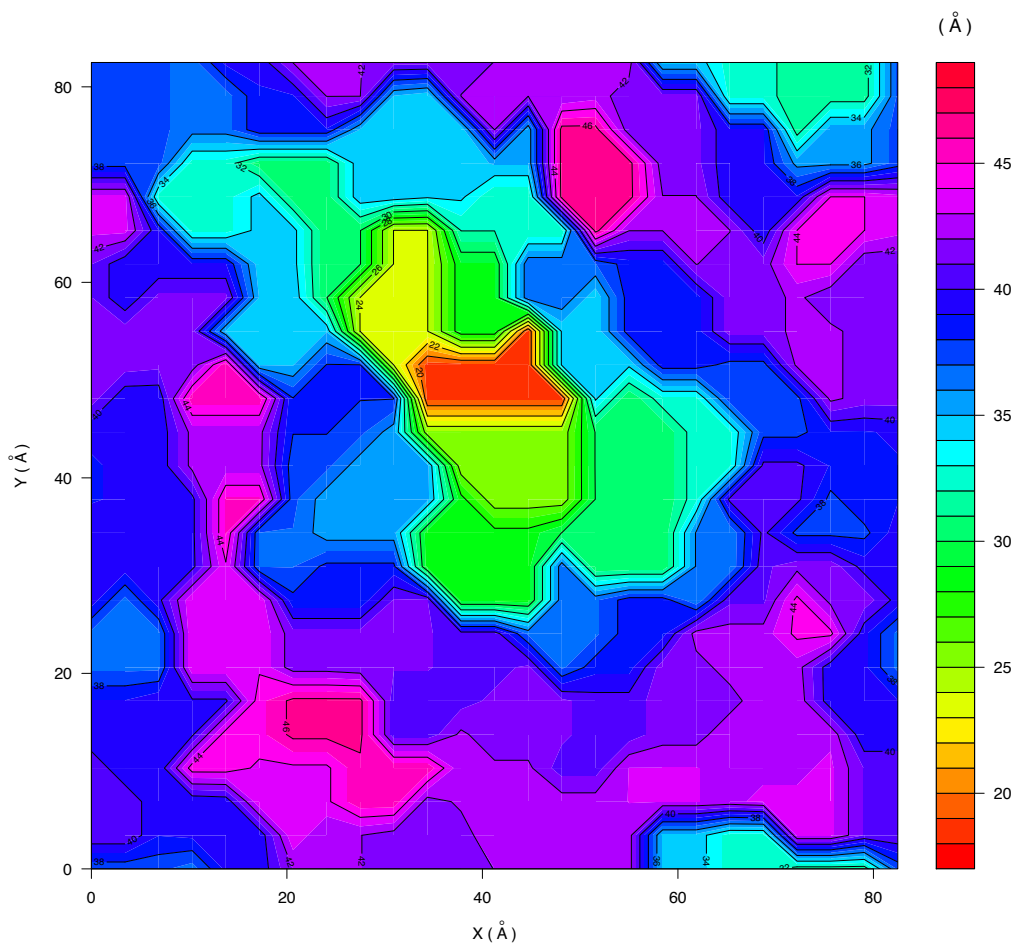


Figure 5.43: Macrolittin70 at pH 5. Membrane thickness according to phosphorus in \AA . Last frame, centered (and wrapped) around protein.

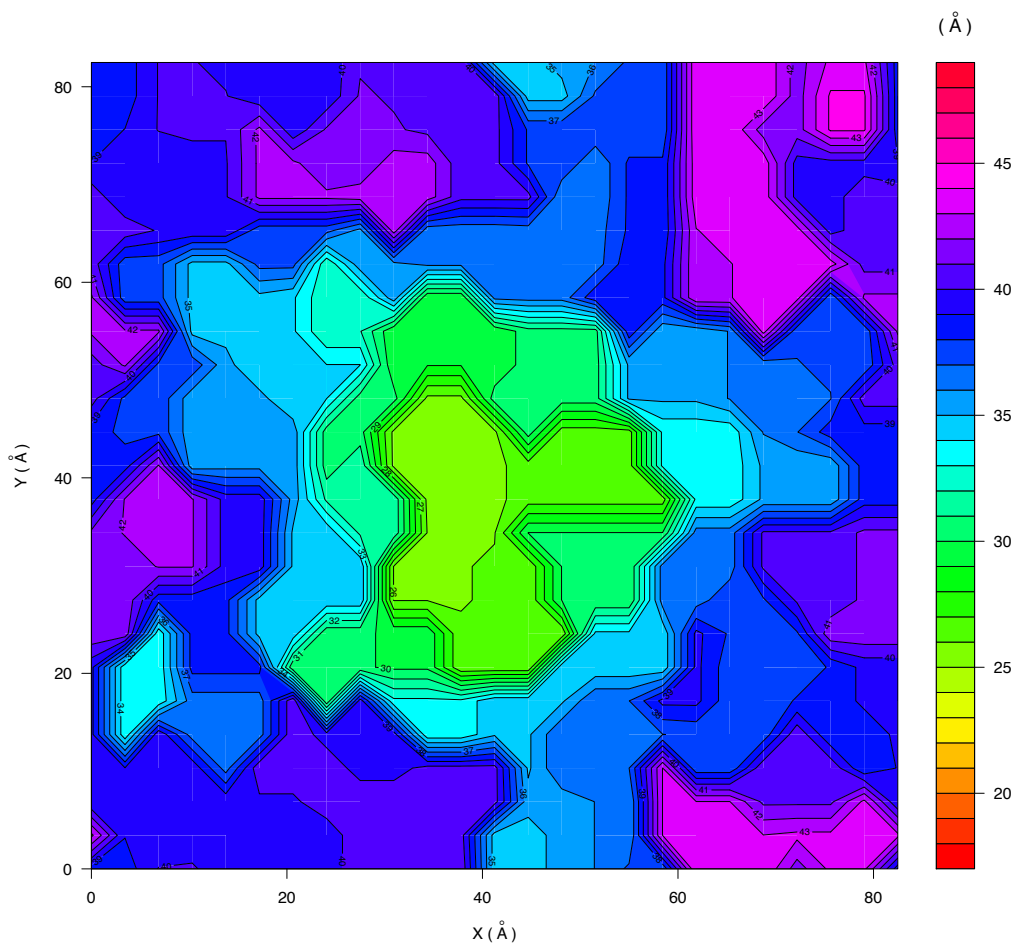


Figure 5.44: pHD15 at acidic pH. Membrane thickness according to phosphorus in \AA . Last frame, centered (and wrapped) around protein.

Interaction Energy between Peptide & Polar Lipid Components :

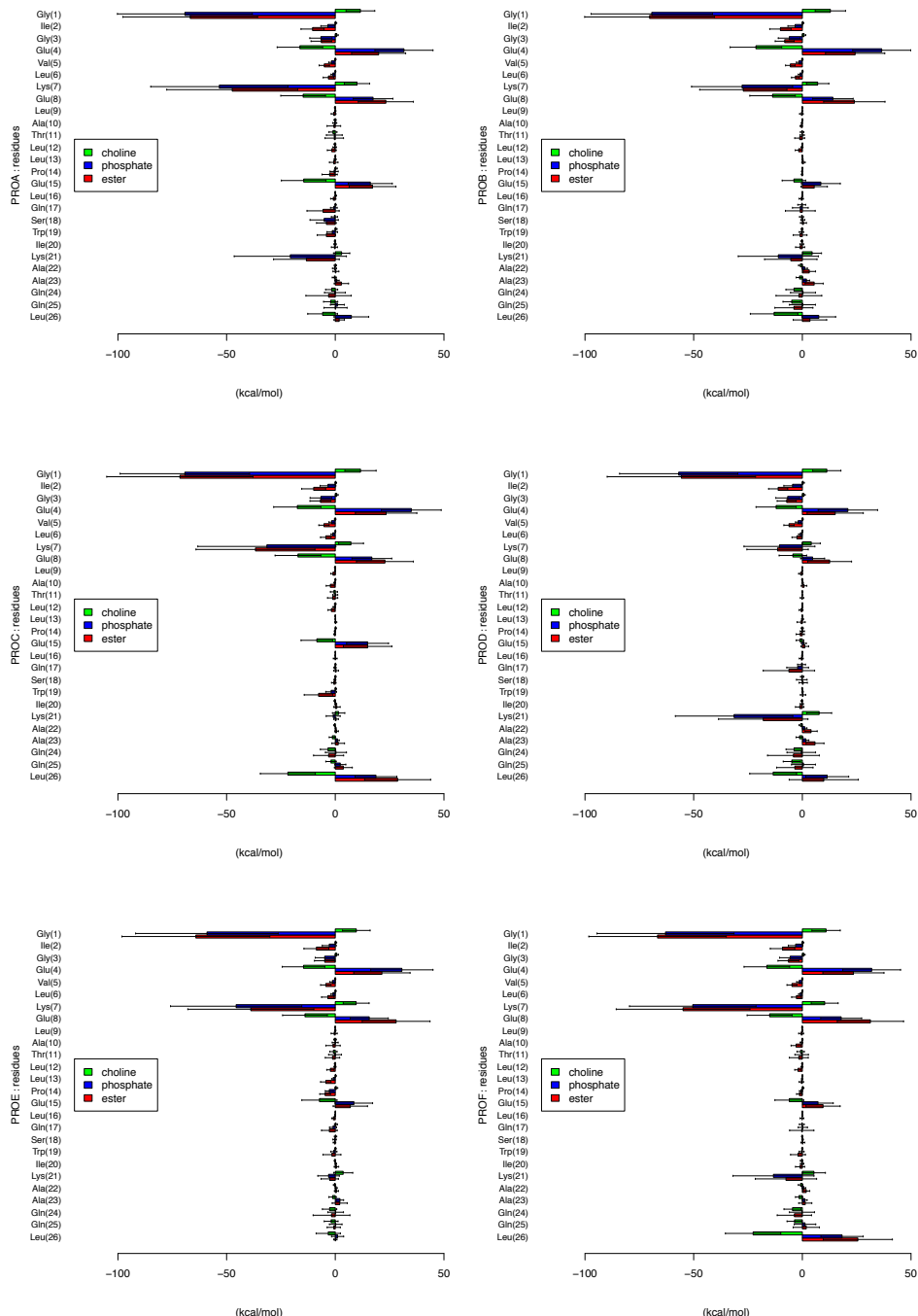


Figure 5.45: Bar plot of average interaction energy and standard deviation between residues of individual macrolittin70 helices at pH 7 and lipid components, choline head-group, phosphate, and ester oxygens.

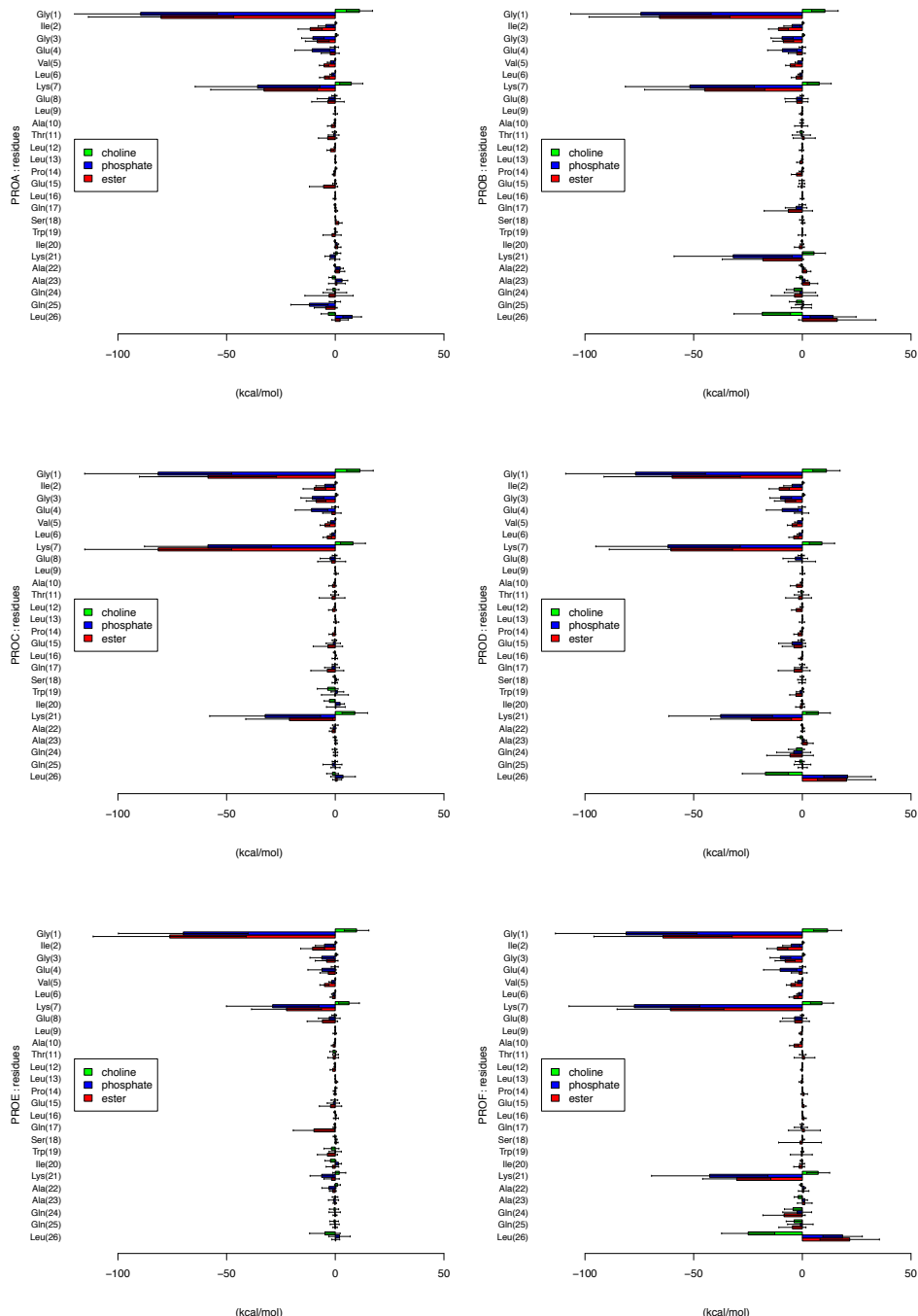


Figure 5.46: Bar plot of average interaction energy and standard deviation between residues of individual macrolittin70 helices at pH 5 and lipid components, choline head-group, phosphate, and ester oxygens.

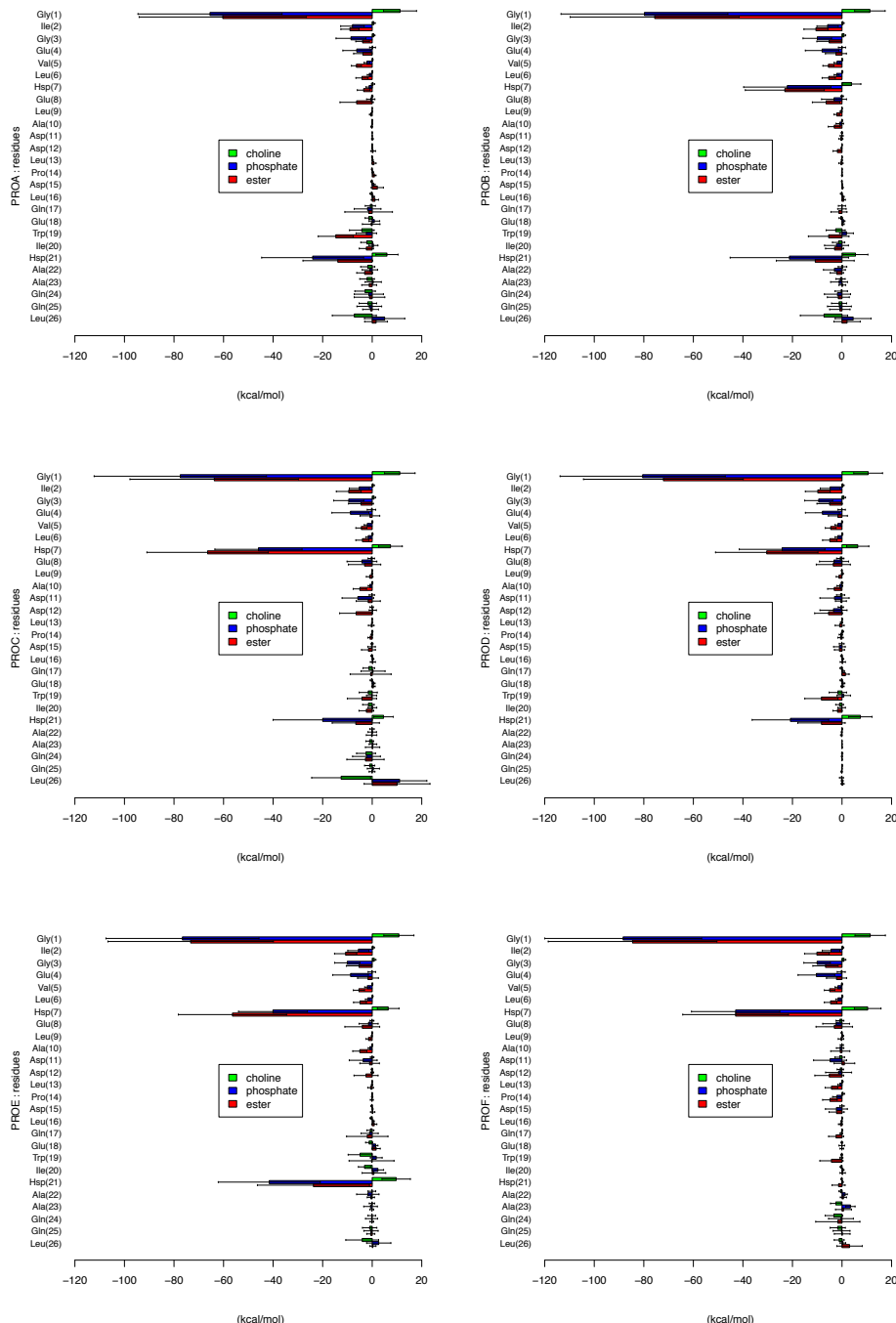


Figure 5.47: Bar plot of average interaction energy and standard deviation between residues of individual pHD15 helices at pH 5 and lipid components, choline head-group, phosphate, and ester oxygens.

Sidechain-Sidechain H-bonding

Sidechain-Sidechain H-bonding : Macrolittin70 at pH 7

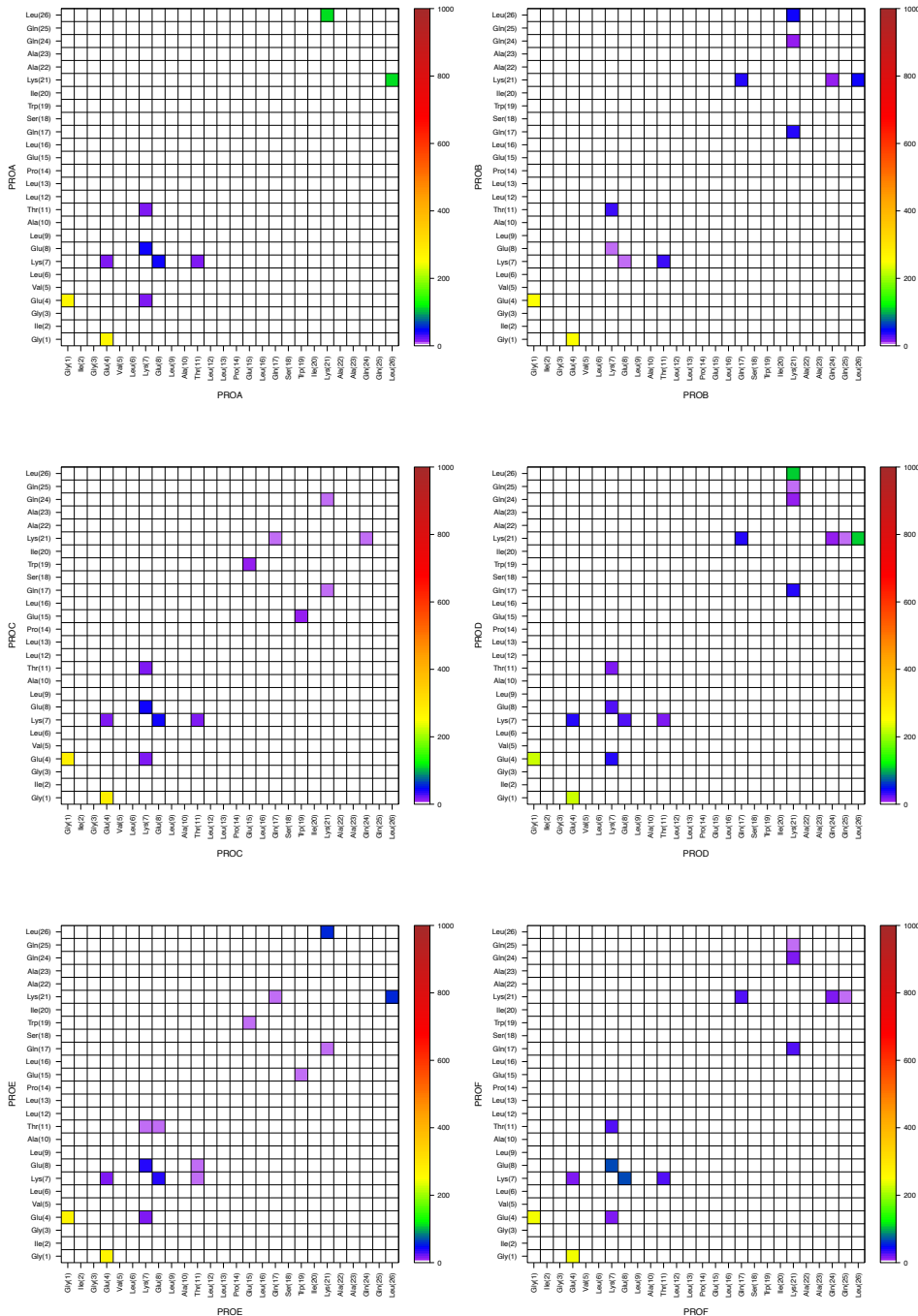


Figure 5.48: Macrolittin70 hexameric pore at pH 7 during last 2 μ s. Heat map of duration (ns) of dominant sidechain–sidechain intra-peptide H-bonding interaction.

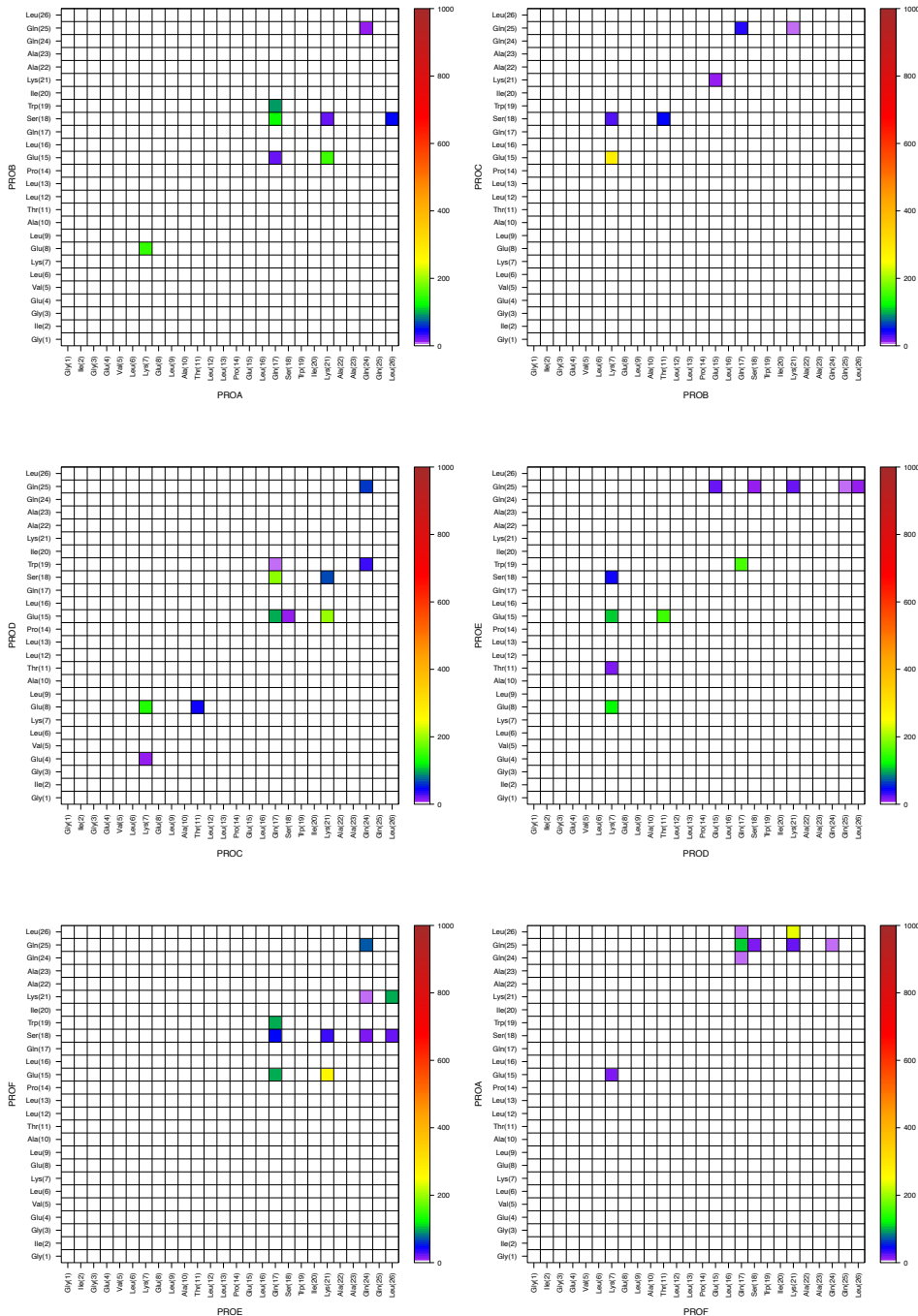


Figure 5.49: Macrolittin70 hexameric pore at pH 7 during last 2 μ s. Heat map of duration (ns) of the dominant sidechain–sidechain H-bonding interaction between peptides i and $i+1$ clockwise (N-term up).

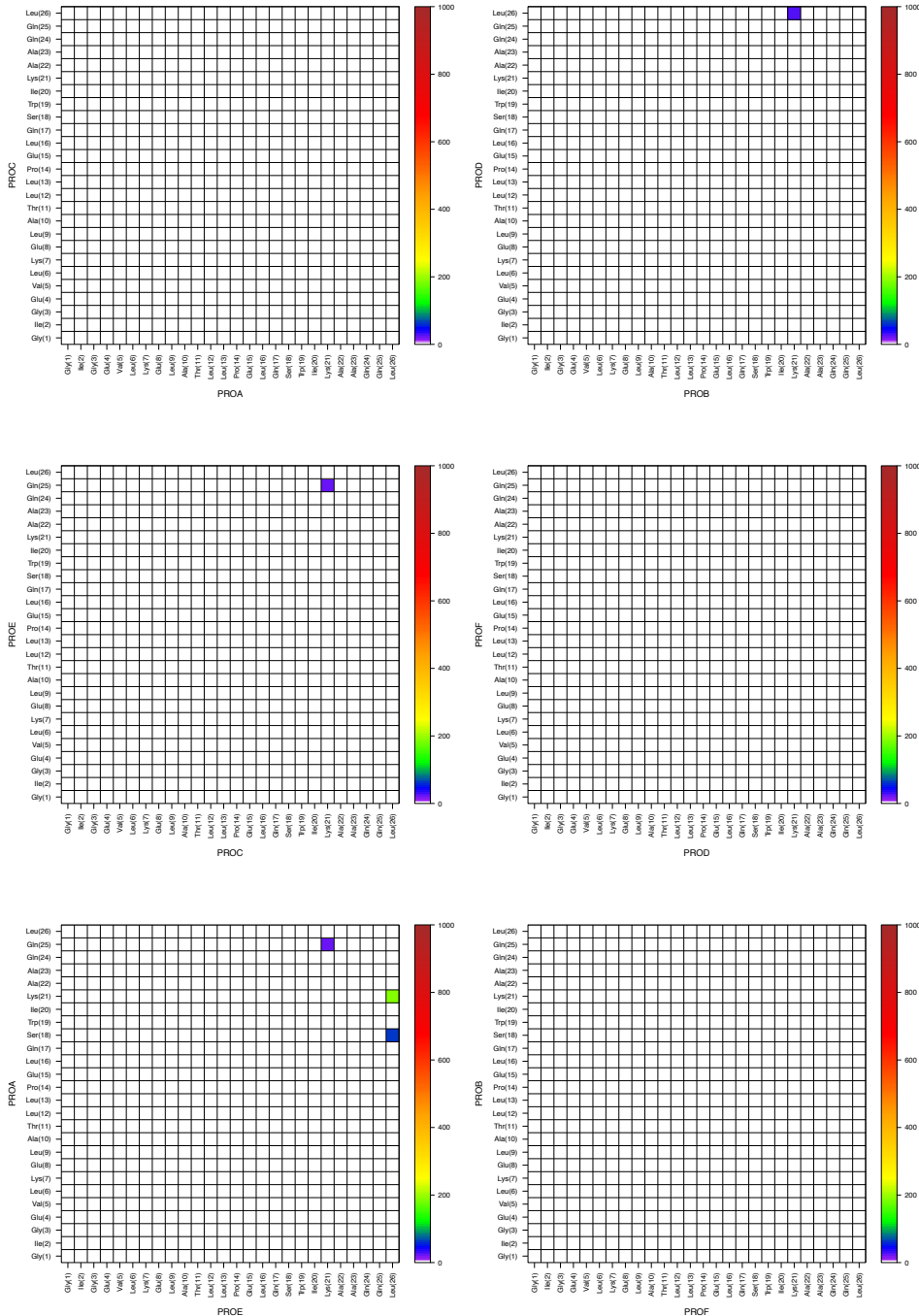


Figure 5.50: Macrolittin70 hexameric pore at pH 7 during last 2 μ s. Heat map of duration (ns) of the dominant sidechain–sidechain H-bonding interaction between peptides i and $i+2$ clockwise (N-term up).

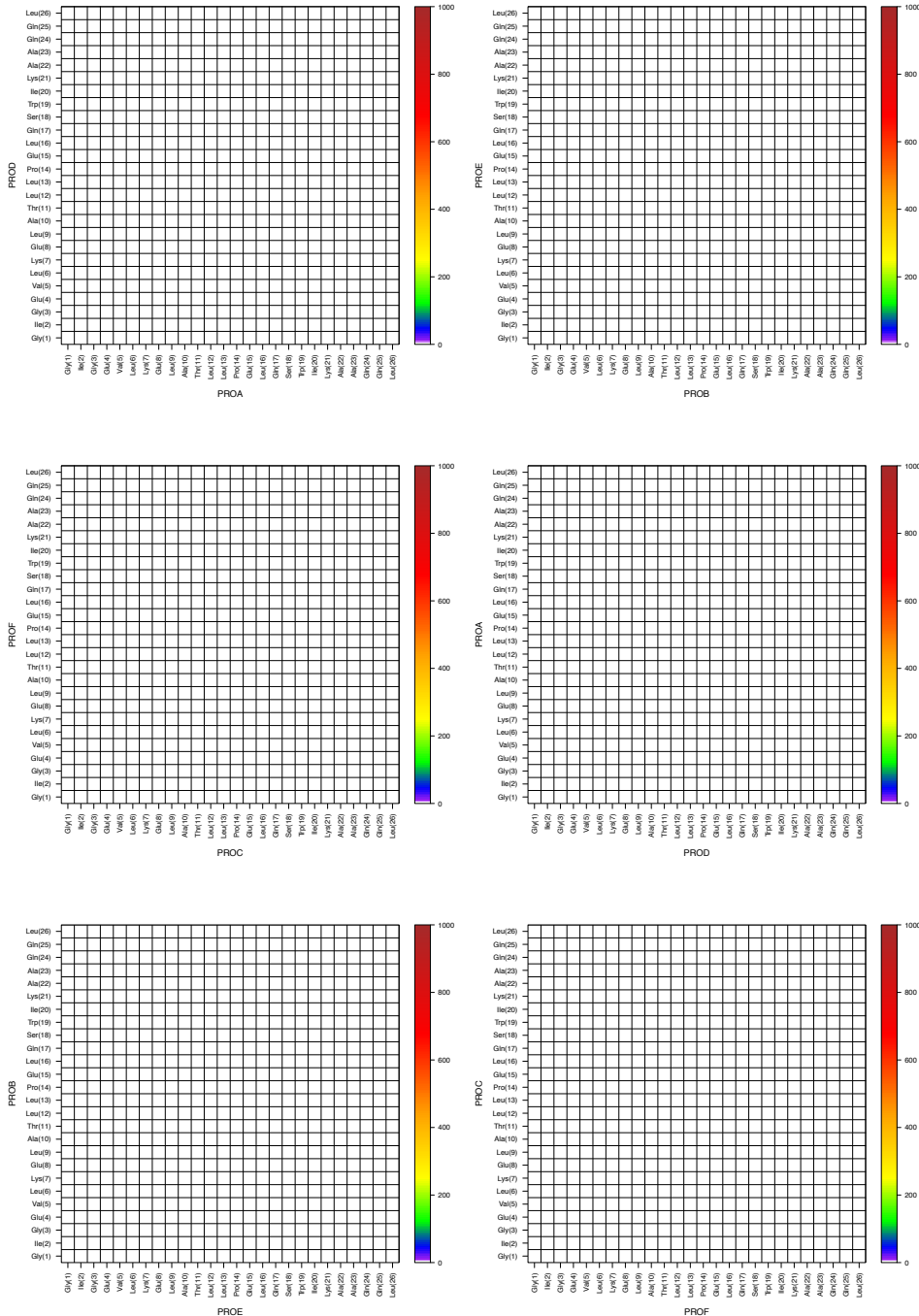


Figure 5.51: Macrolittin70 hexameric pore at pH 7 during last 2 μ s. Heat map of duration (ns) of the dominant sidechain–sidechain H-bonding interaction between peptides i and $i+3$ clockwise (N-term up).

Sidechain-Sidechain H-bonding : Macrolittin70 at pH 5

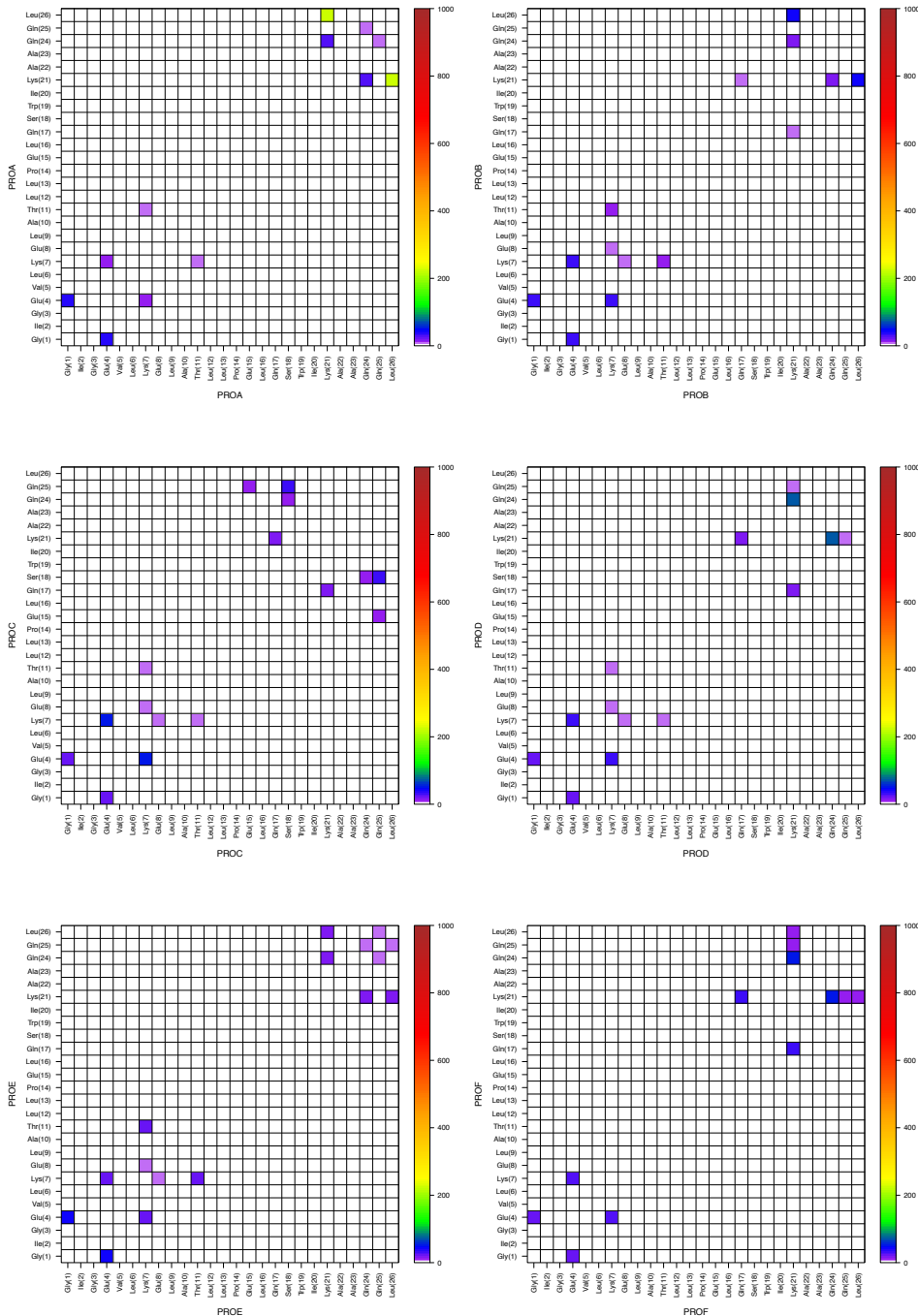


Figure 5.52: Macrolittin70 hexameric pore at pH 5 during last 2 μ s. Heat map of duration (ns) of dominant sidechain–sidechain intra-peptide H-bonding interaction.

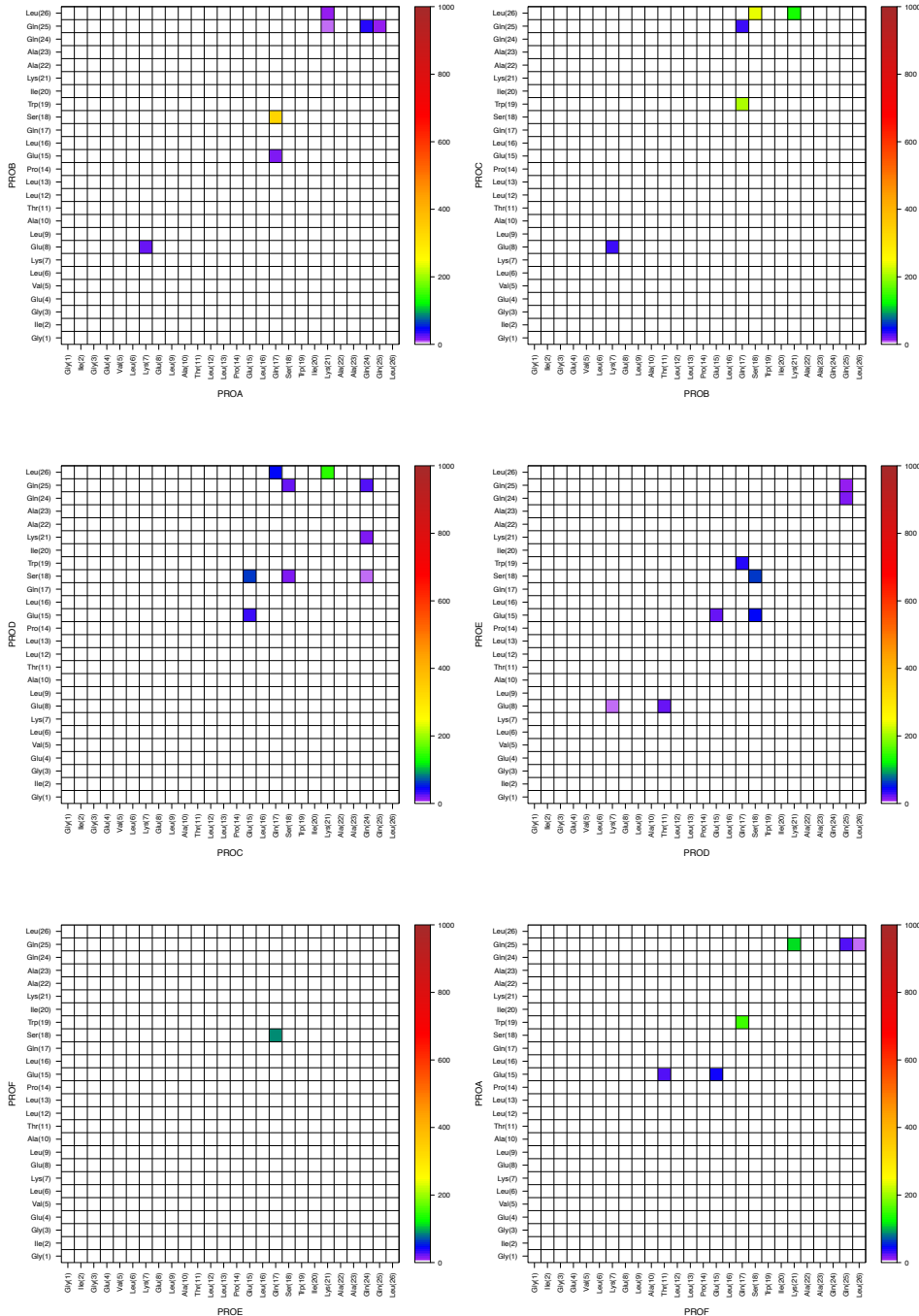


Figure 5.53: Macrolittin70 hexameric pore at pH 5 during last 2 μ s. Heat map of duration (ns) of the dominant sidechain–sidechain H-bonding interaction between peptides i and $i + 1$ clockwise (N-term up).

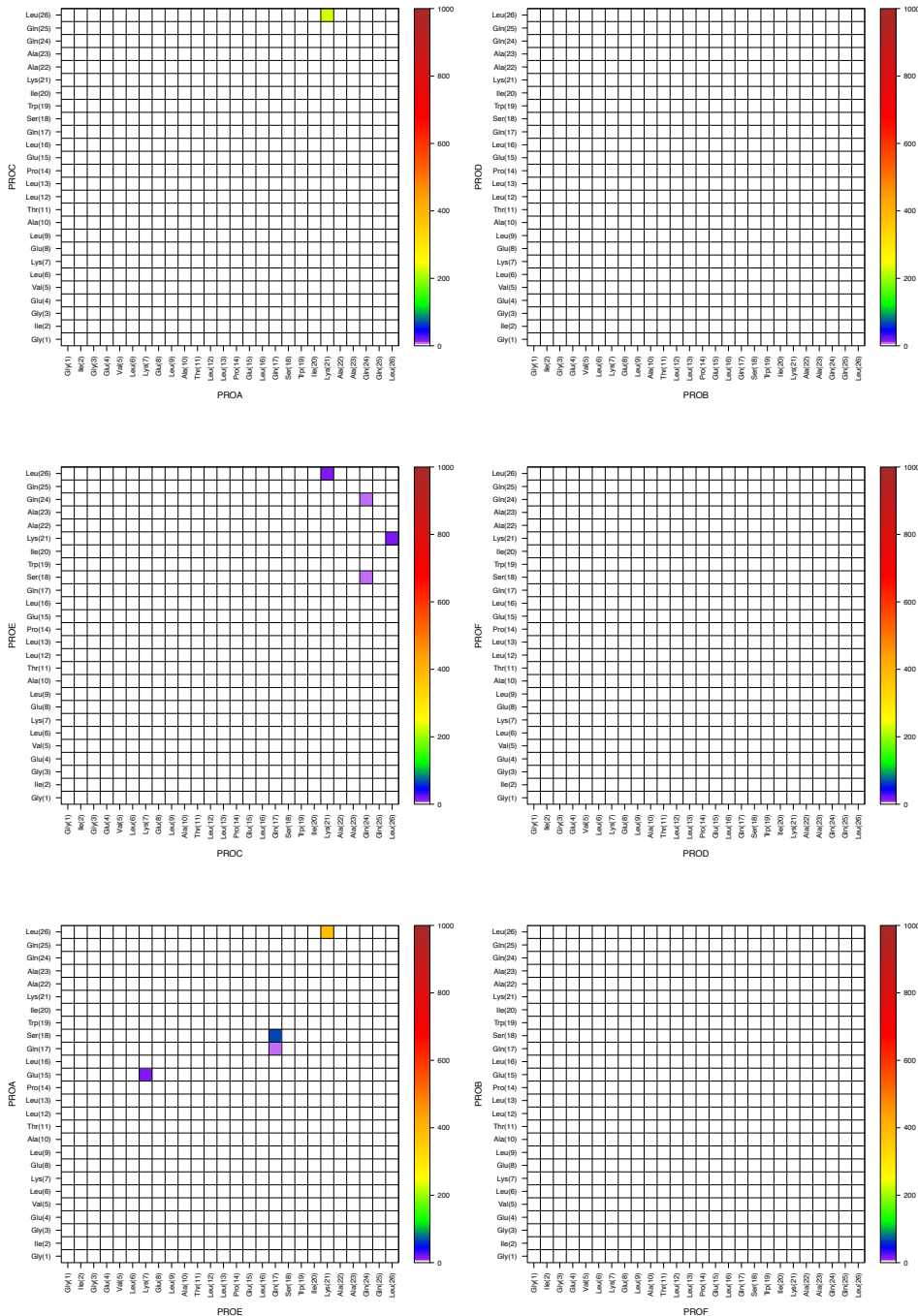


Figure 5.54: Macrolittin70 hexameric pore at pH 5 during last 2 μ s. Heat map of duration (ns) of the dominant sidechain–sidechain H-bonding interaction between peptides i and $i+2$ clockwise (N-term up).

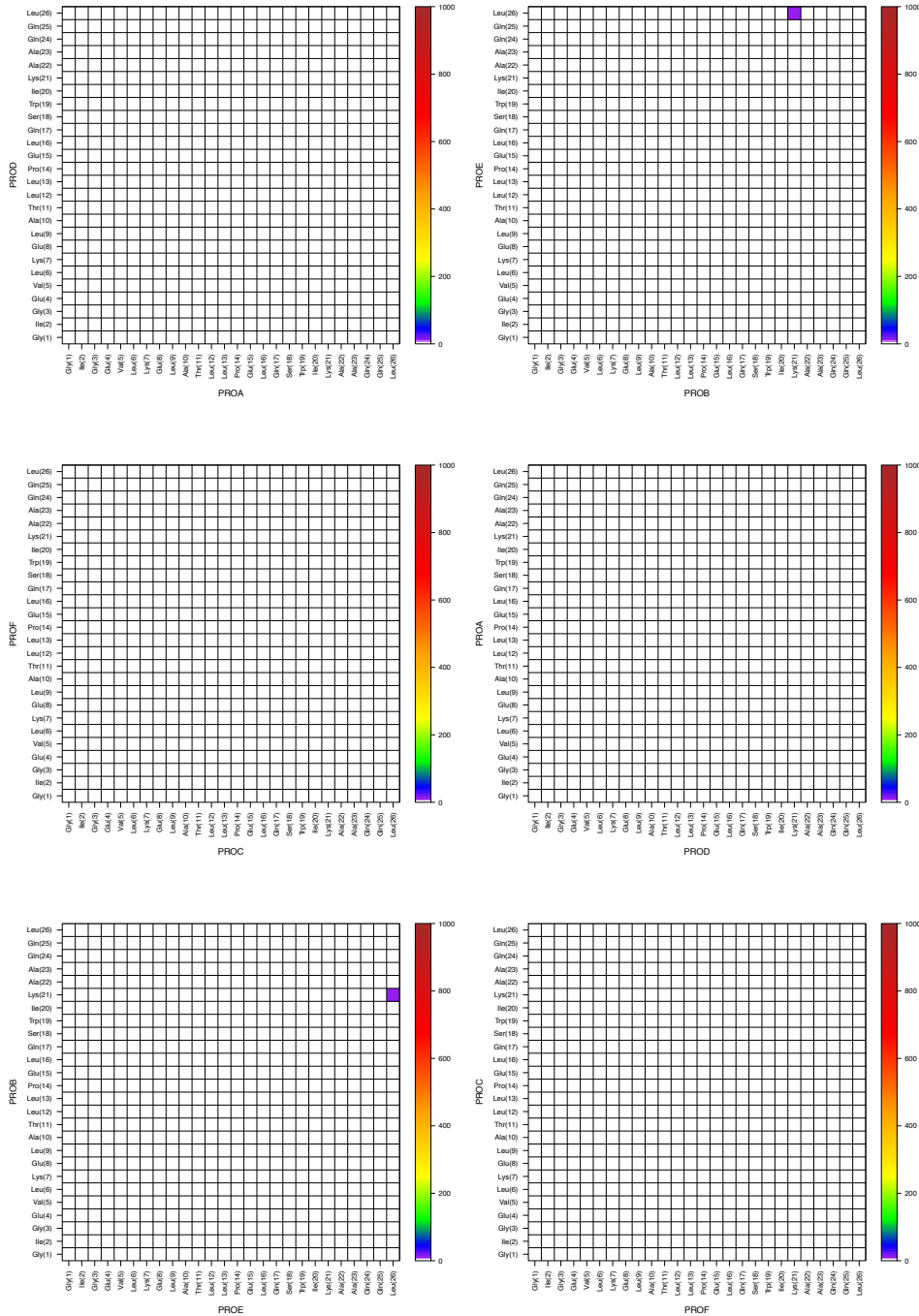


Figure 5.55: Macrolittin70 hexameric pore at pH 5 during last 2 μ s. Heat map of duration (ns) of the dominant sidechain–sidechain H-bonding interaction between peptides i and $i+3$ clockwise (N-term up).

Sidechain-Sidechain H-bonding : pHD15 at pH 5

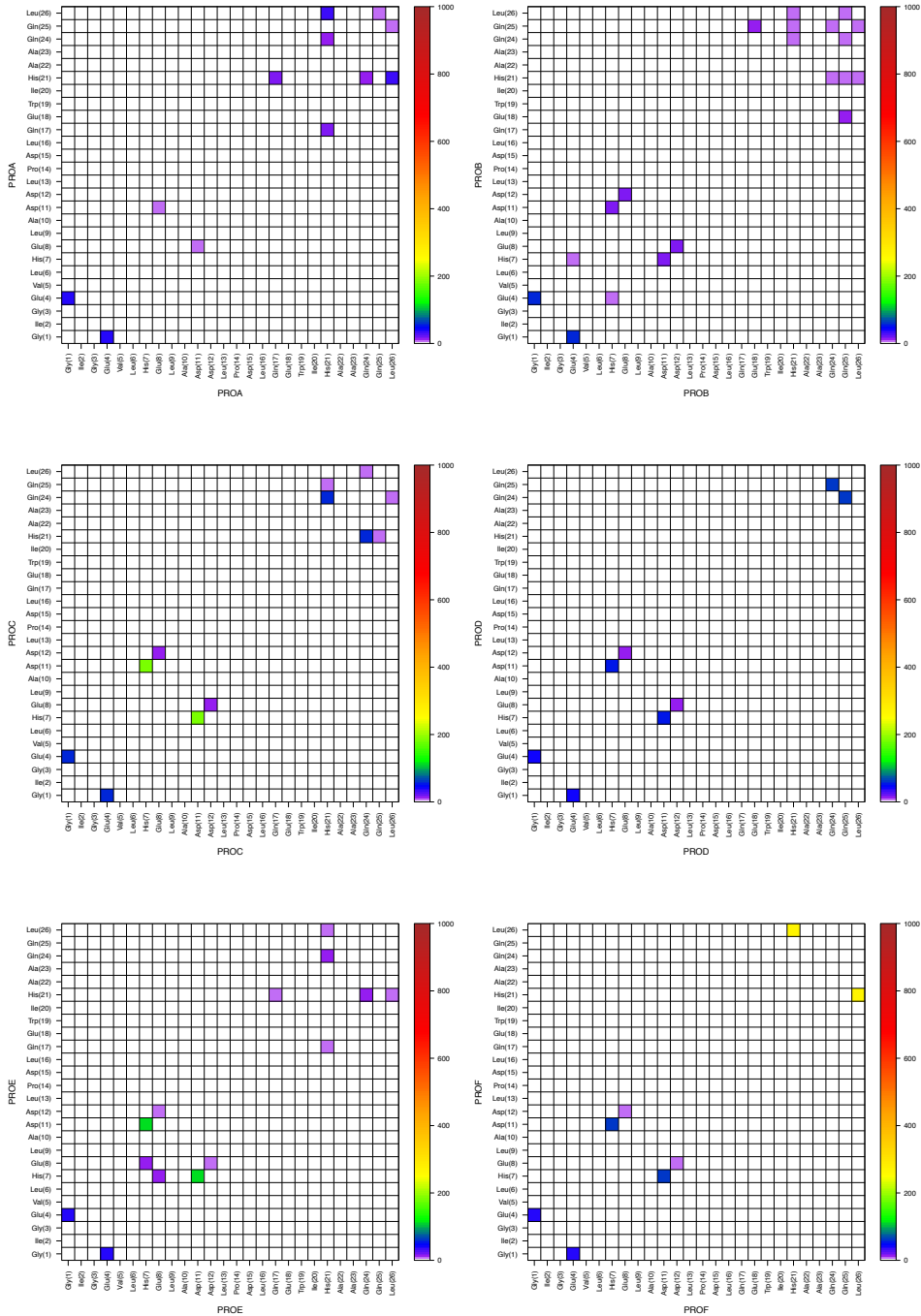


Figure 5.56: pHD15 hexameric pore at pH 5 during last 2 μ s. Heat map of duration (ns) of dominant sidechain–sidechain intra-peptide H-bonding interaction.

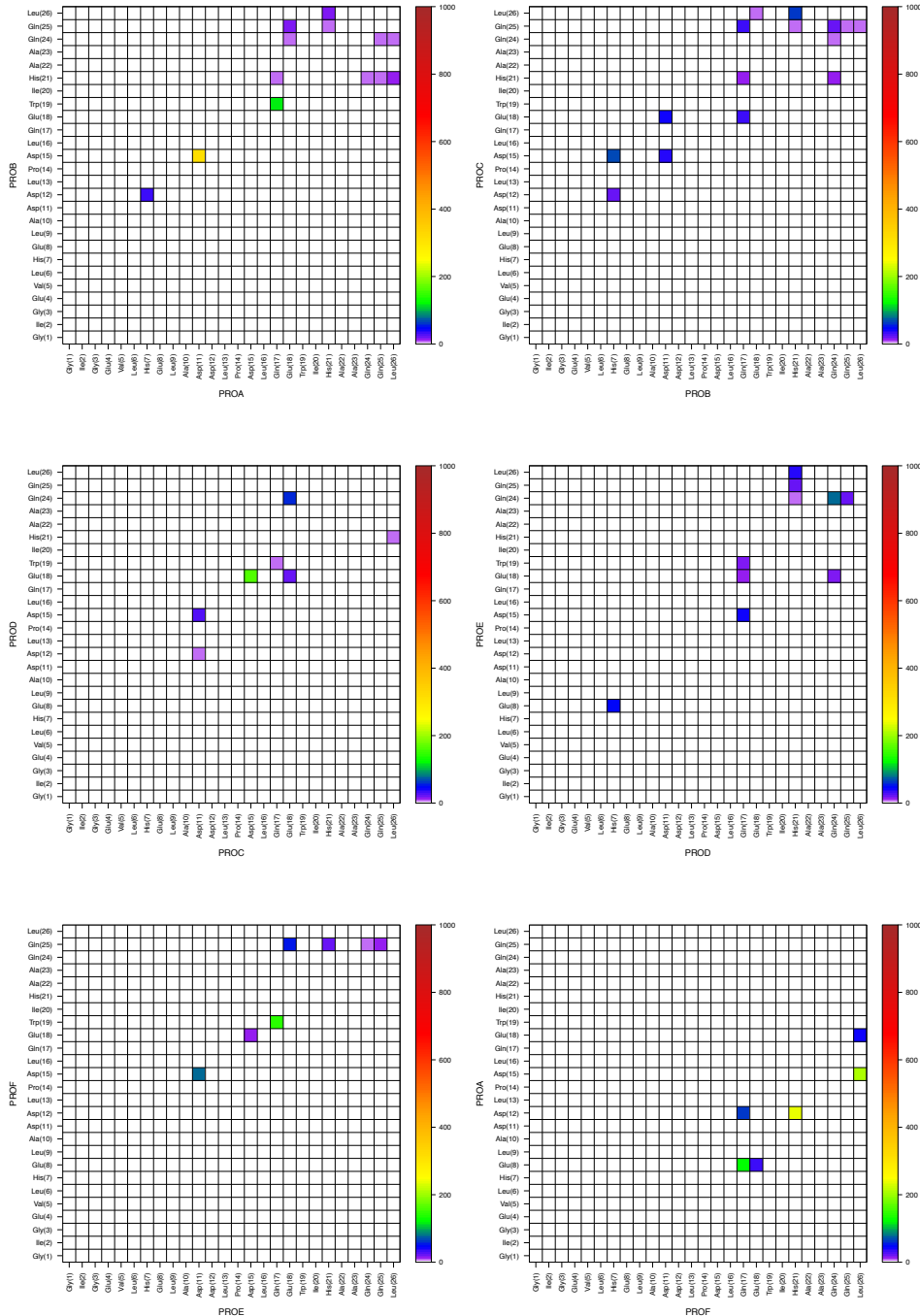


Figure 5.57: pHD15 hexameric pore at pH 5 during last 2 μ s. Heat map of duration (ns) of the dominant sidechain–sidechain H-bonding interaction between peptides i and $i + 1$ clockwise (N-term up).

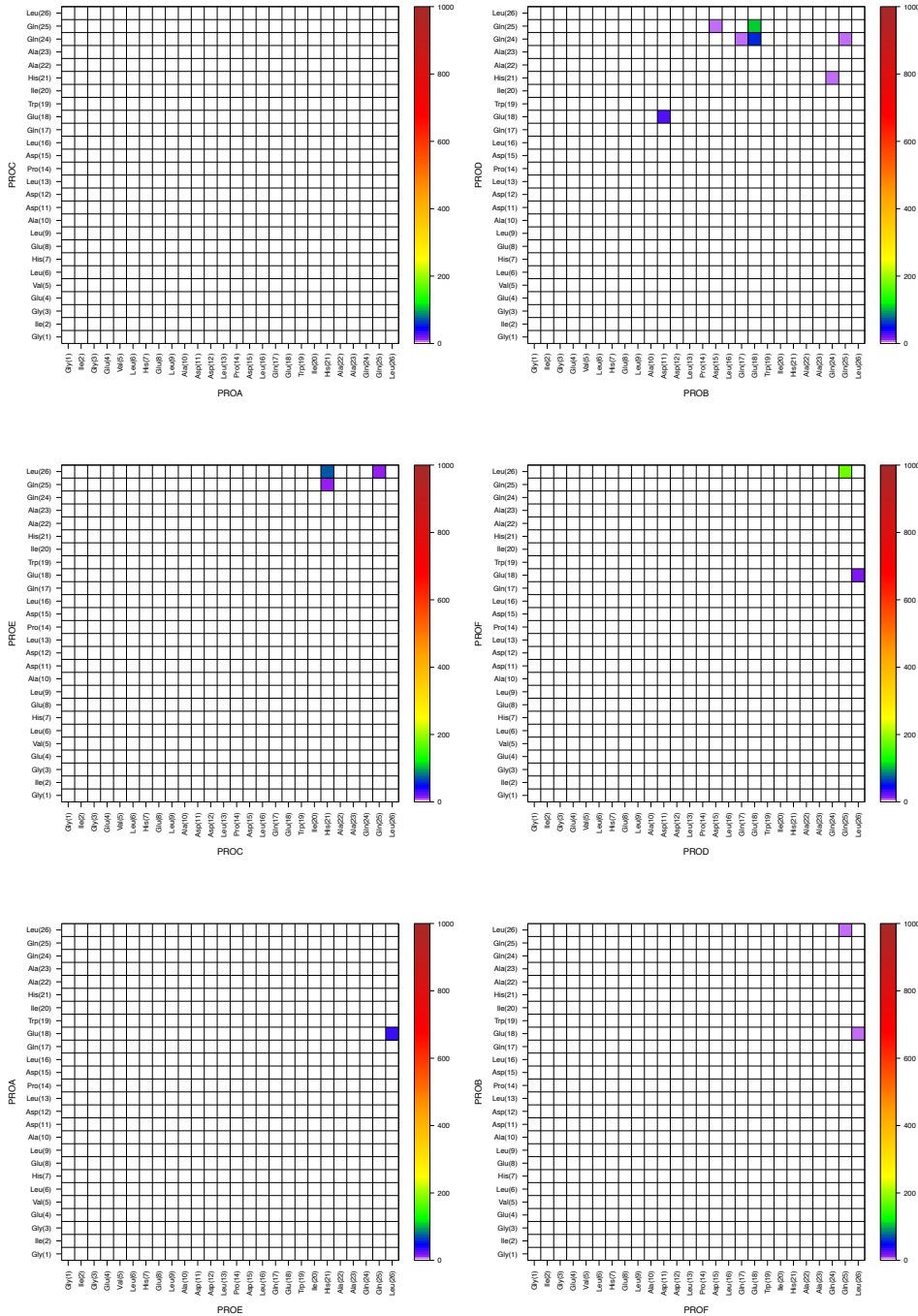


Figure 5.58: pHD15 hexameric pore at pH 5 during last 2 μ s. Heat map of duration (ns) of the dominant sidechain–sidechain H-bonding interaction between peptides i and $i + 2$ clockwise (N-term up).

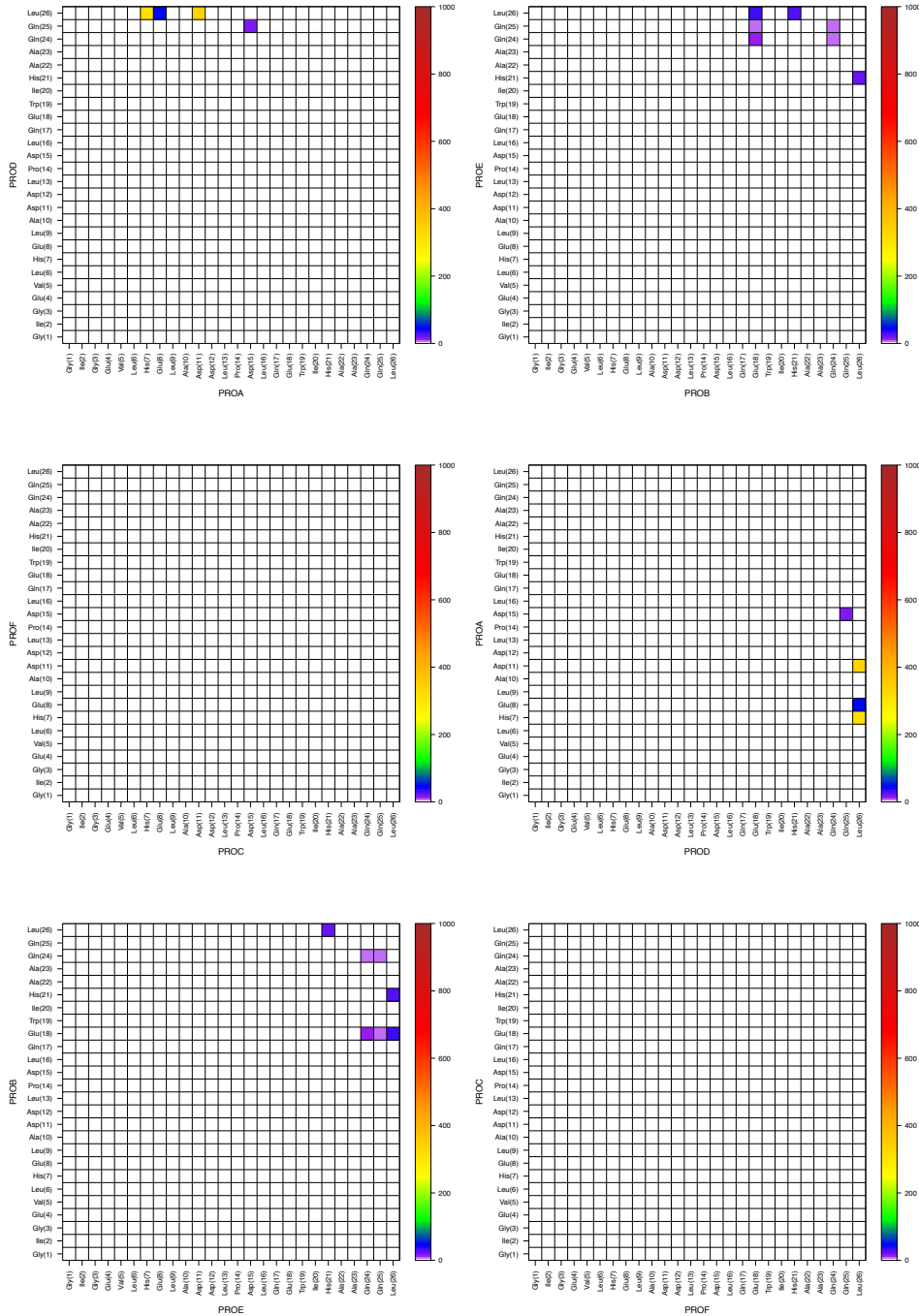


Figure 5.59: pHD15 hexameric pore at pH 5 during last 2 μ s. Heat map of duration (ns) of the dominant sidechain–sidechain H-bonding interaction between peptides i and $i + 3$ clockwise (N-term up).

Sidechain–Backbone H-bonding

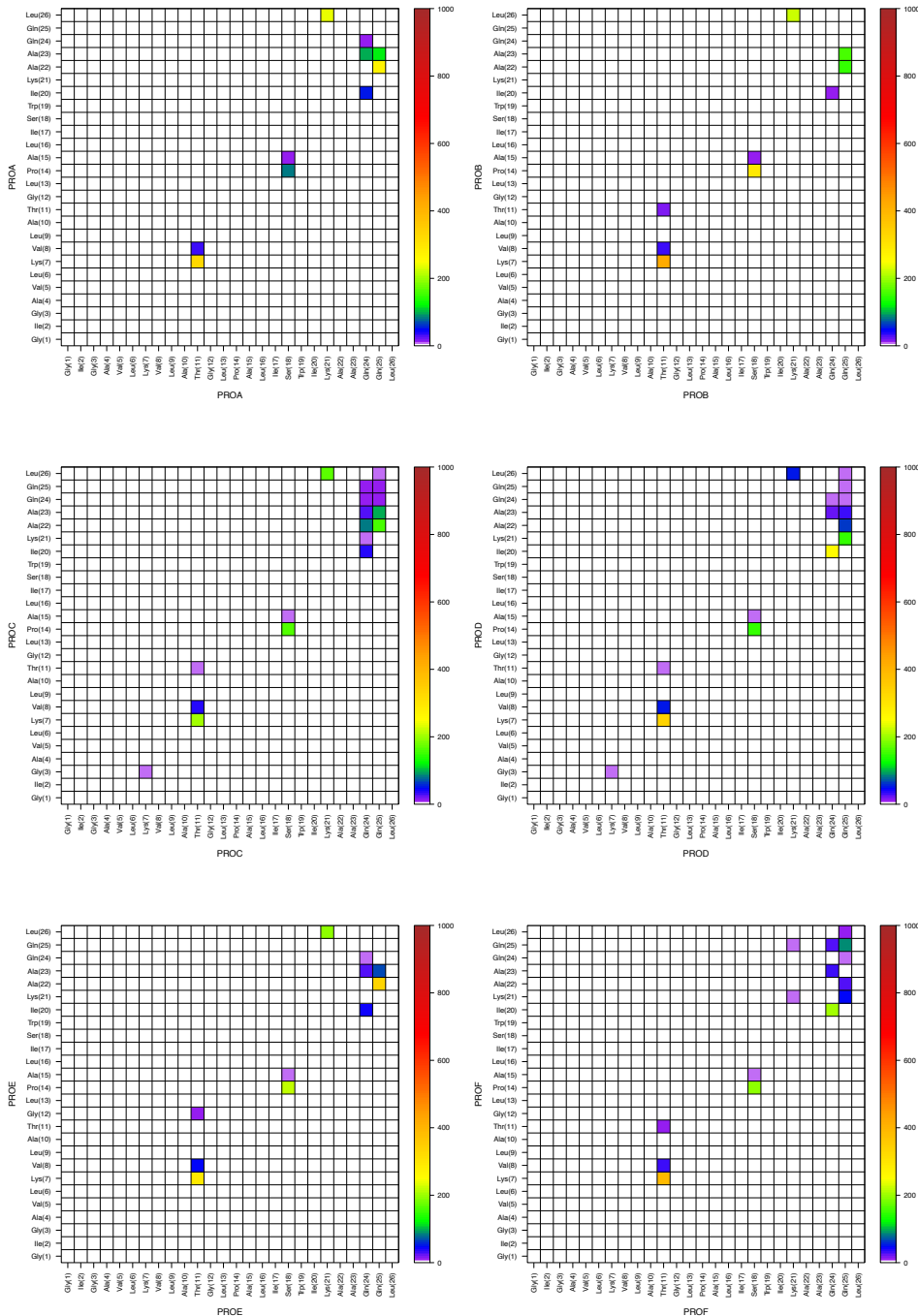


Figure 5.60: MelP5 hexameric pore during last 2 μ s. Heat map of duration (ns) of dominant sidechain–backbone intra-peptide H-bonding interaction.

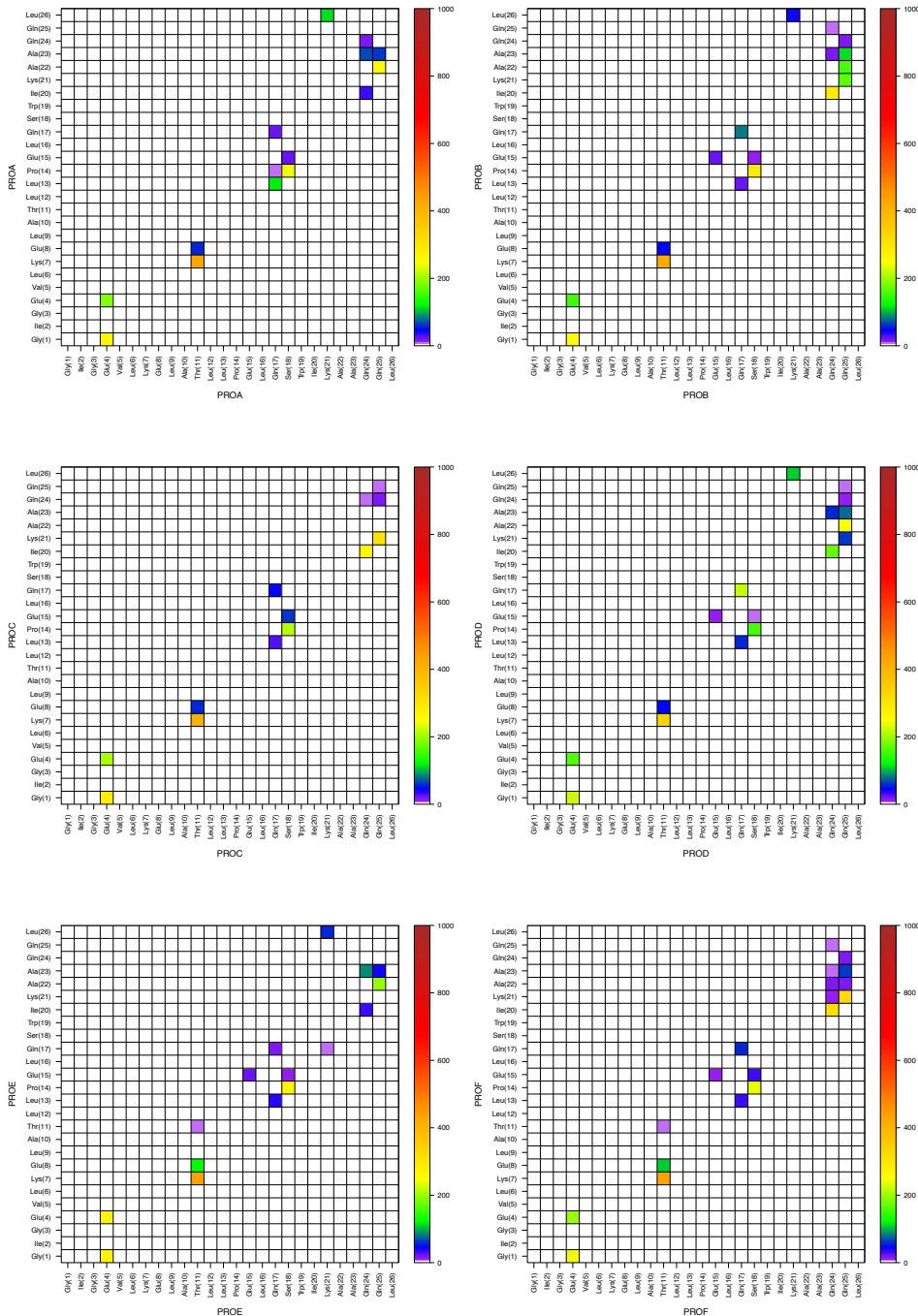


Figure 5.61: Macrolittin70 hexameric pore at pH 7 during last 2 μ s. Heat map of duration (ns) of dominant sidechain–backbone intra-peptide H-bonding interaction.

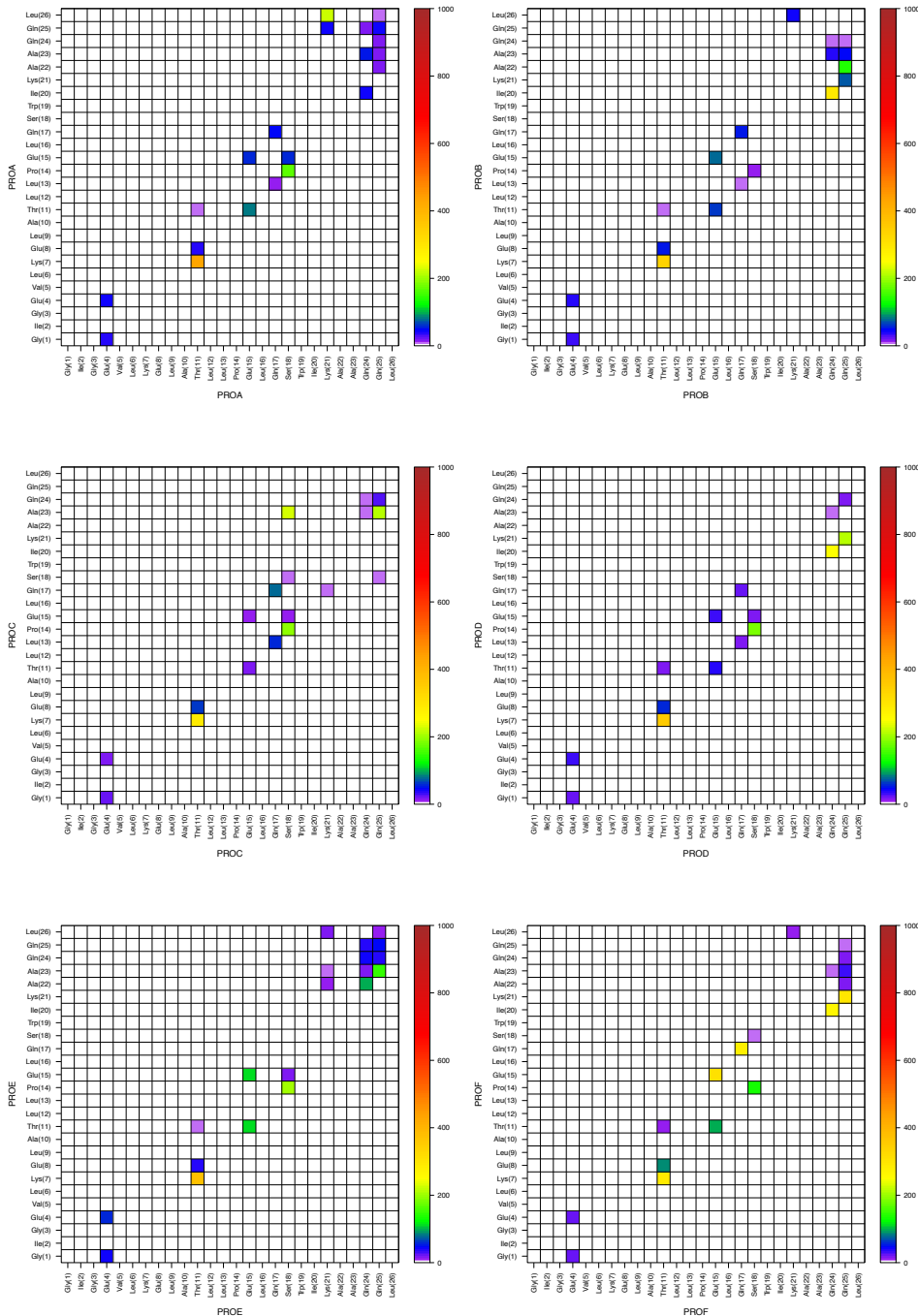


Figure 5.62: Macrolittin70 hexameric pore at pH 5 during last 2 μ s. Heat map of duration (ns) of dominant sidechain–backbone intra-peptide H-bonding interaction.

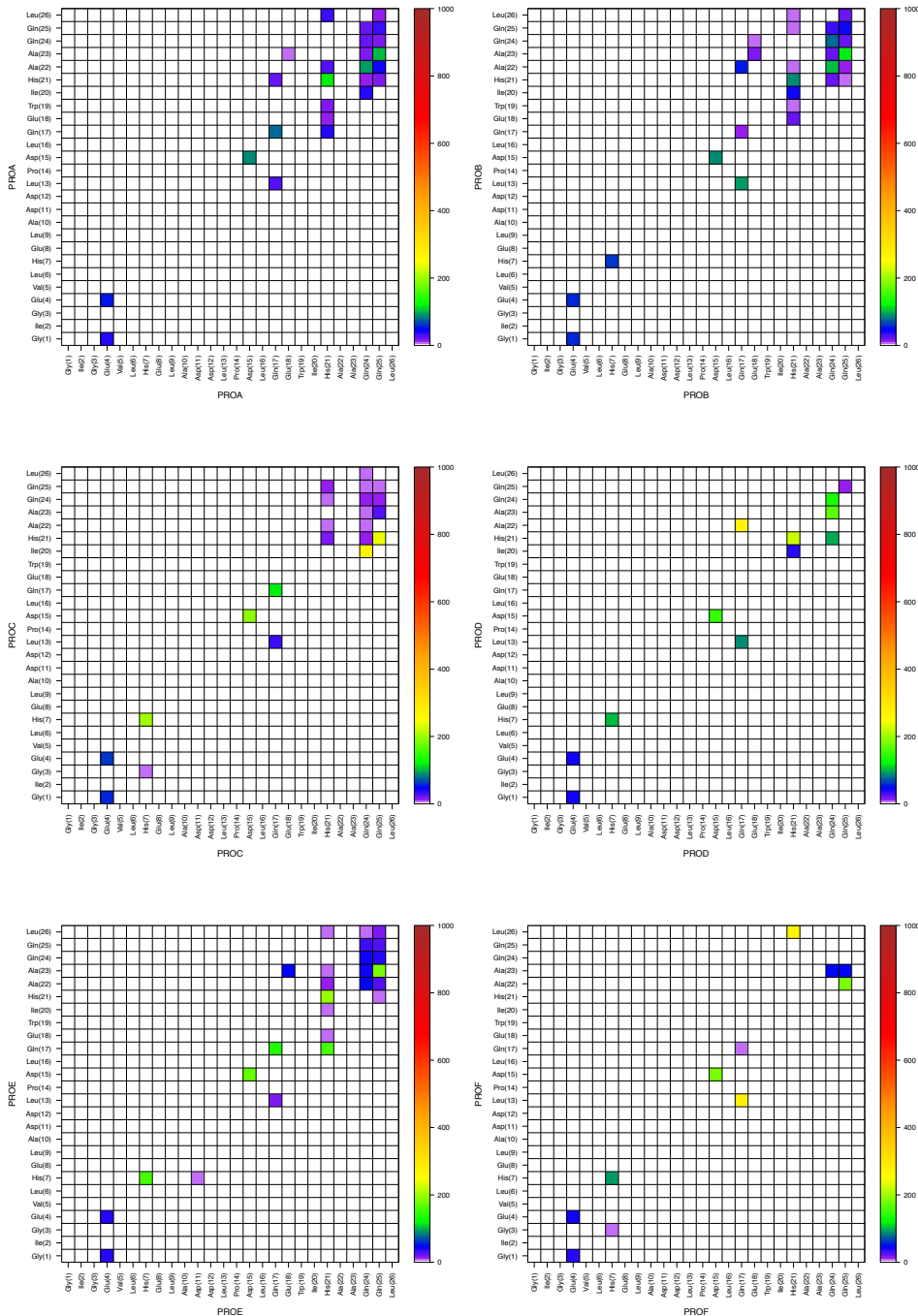


Figure 5.63: pHD15 hexameric pore at pH 5 during last 2 μ s. Heat map of duration (ns) of dominant sidechain-backbone intra-peptide H-bonding interaction.

Backbone–Backbone H-bonding

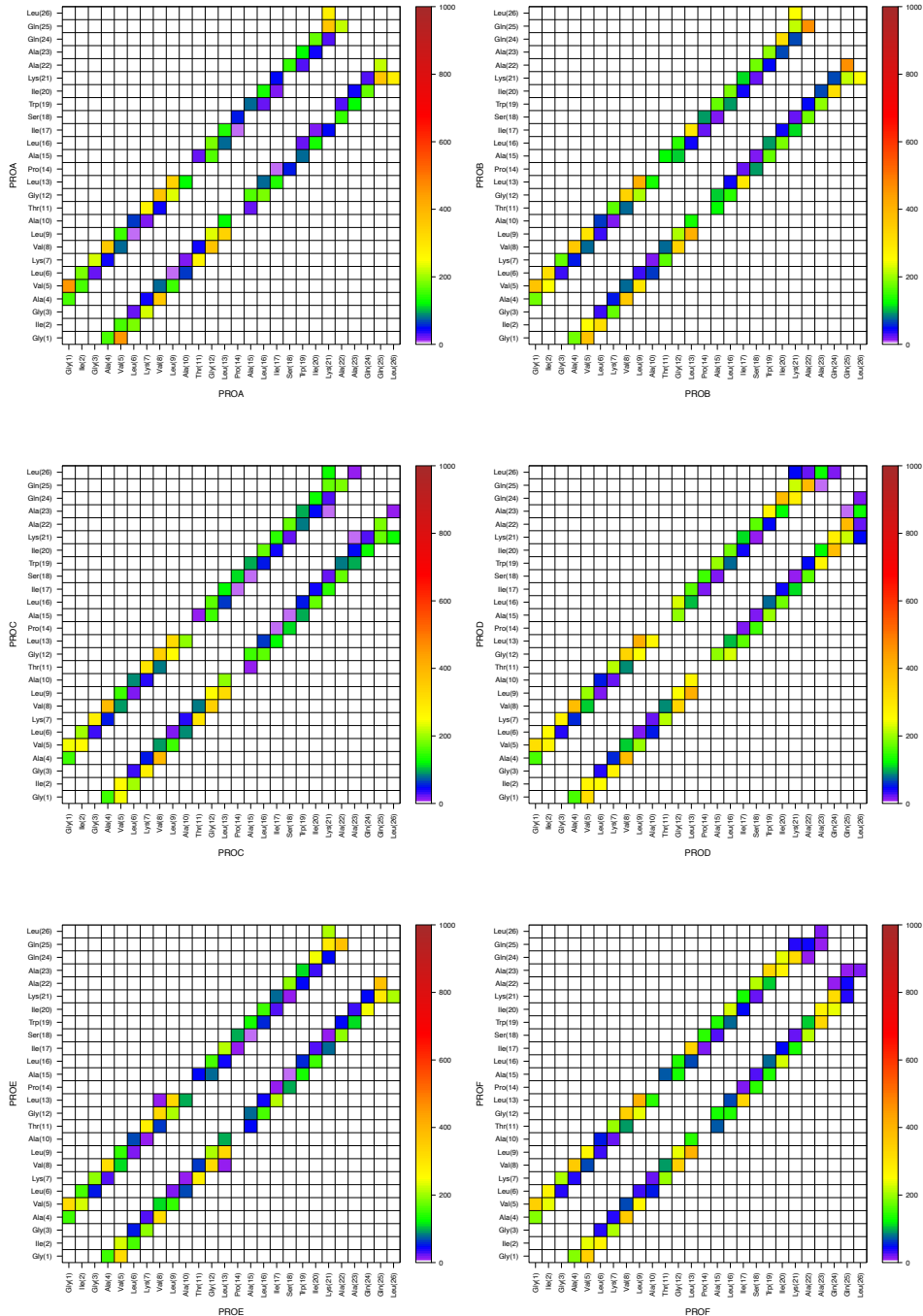


Figure 5.64: MelP5 hexameric pore during last 2 μ s. Heat map of duration (ns) of dominant backbone-backbone intra-peptide H-bonding interaction.

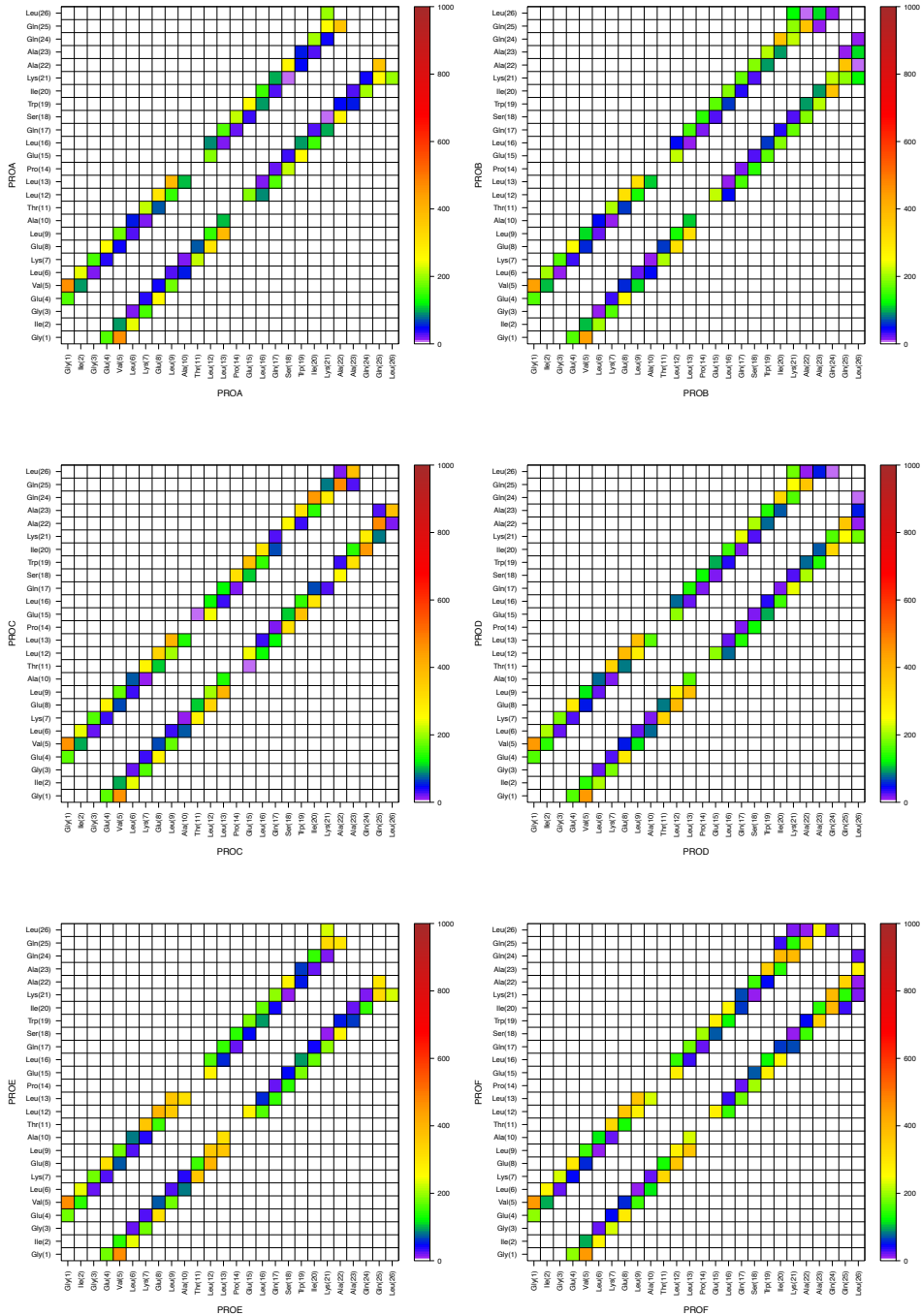


Figure 5.65: Macrolittin70 hexameric pore at pH 7 during last 2 μ s. Heat map of duration (ns) of dominant backbone-backbone intra-peptide H-bonding interaction.

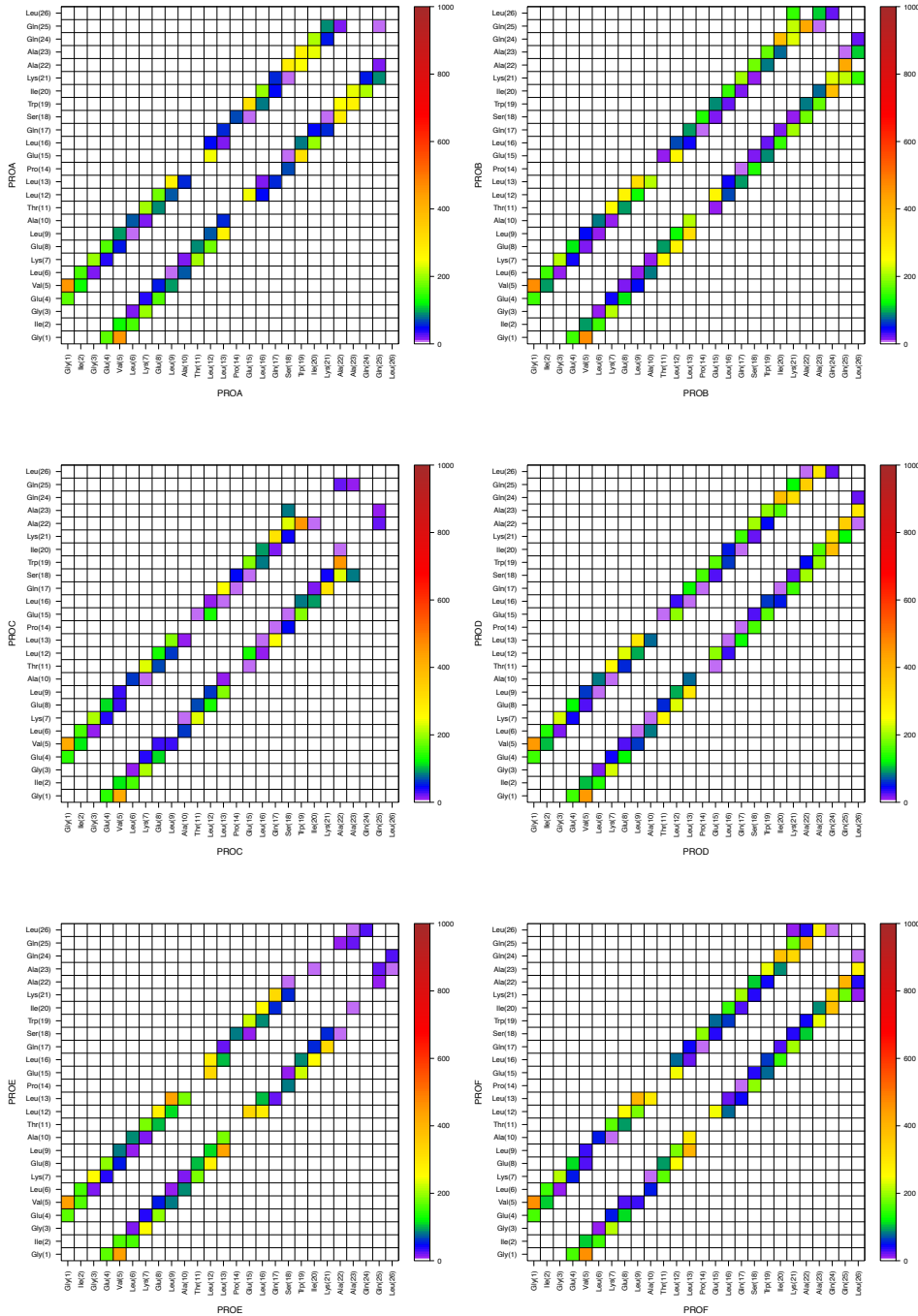


Figure 5.66: Macrolittin70 hexameric pore at pH 5 during last 2 μ s. Heat map of duration (ns) of dominant backbone-backbone intra-peptide H-bonding interaction.

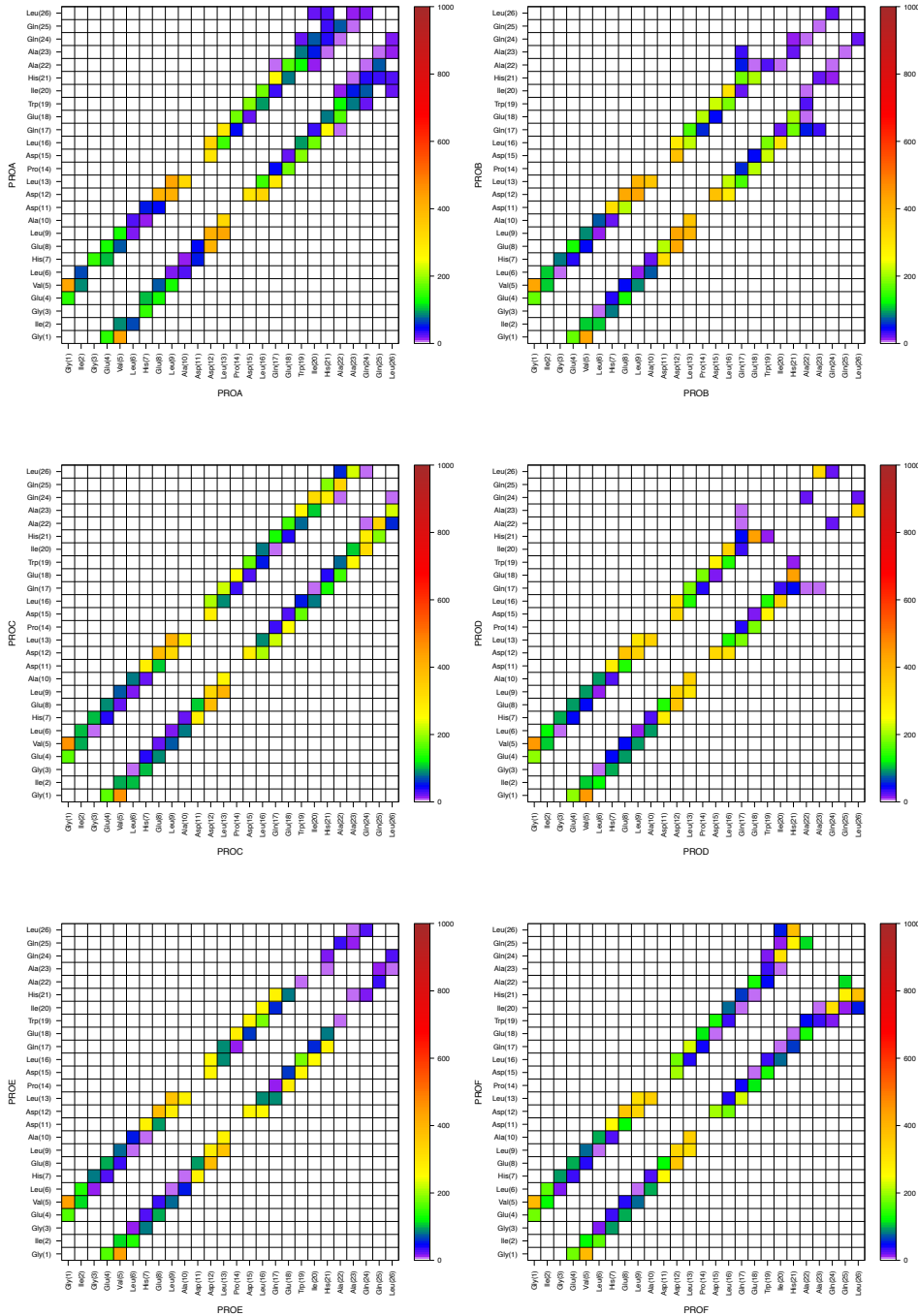


Figure 5.67: pHD15 hexameric pore at pH 5 during last 2 μ s. Heat map of duration (ns) of dominant backbone-backbone intra-peptide H-bonding interaction.

Backbone–Backbone Water Bridges

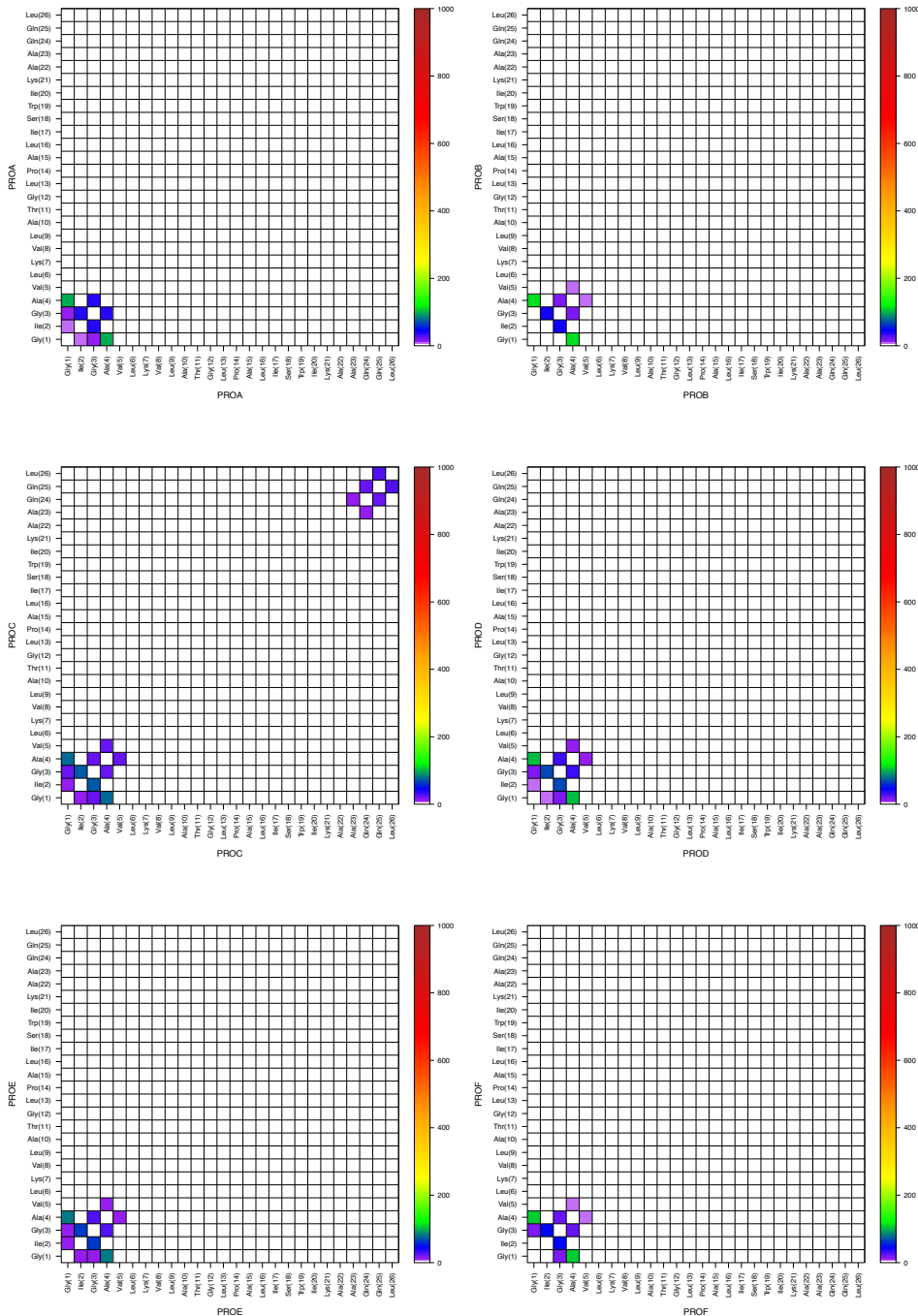


Figure 5.68: MelP5 hexameric pore during last 2 μ s. Heat map of duration (ns) of dominant backbone-backbone intra-peptide water bridging interaction.

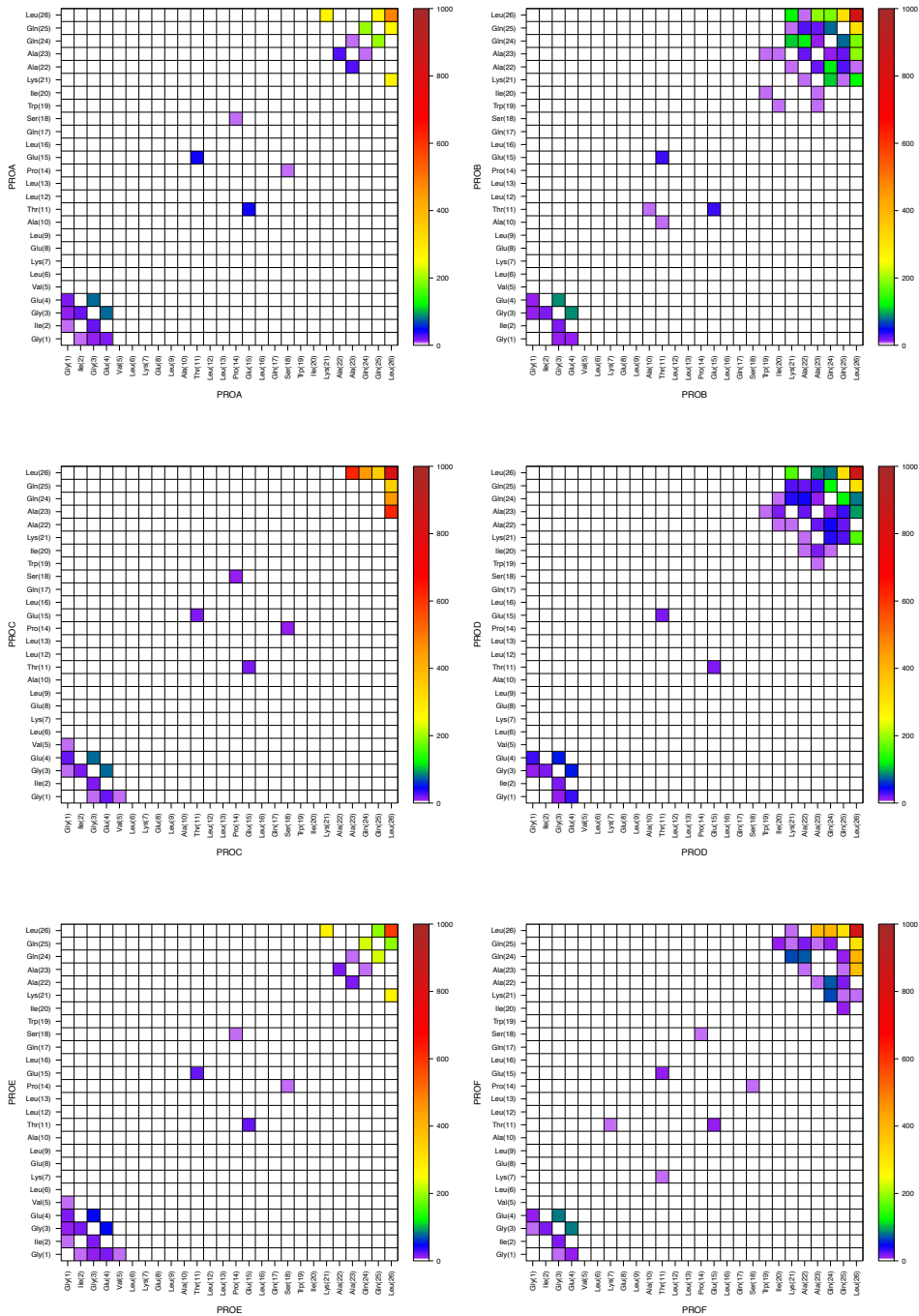


Figure 5.69: Macrolittin70 hexameric pore at pH 7 during last 2 μ s. Heat map of duration (ns) of dominant backbone-backbone intra-peptide water bridging interaction.

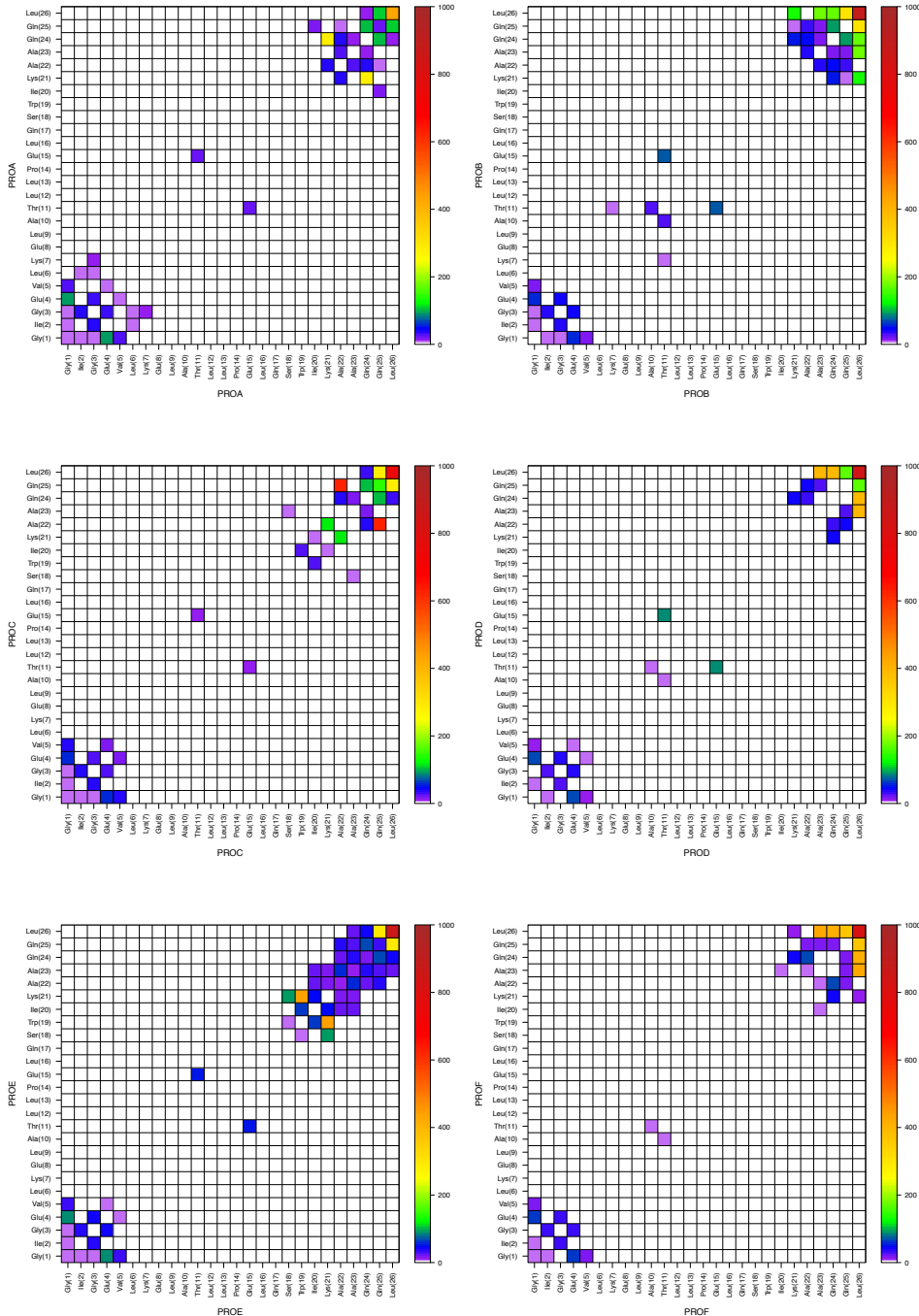


Figure 5.70: Macrolittin70 hexameric pore at pH 5 during last 2 μ s. Heat map of duration (ns) of dominant backbone-backbone intra-peptide water bridging interaction.

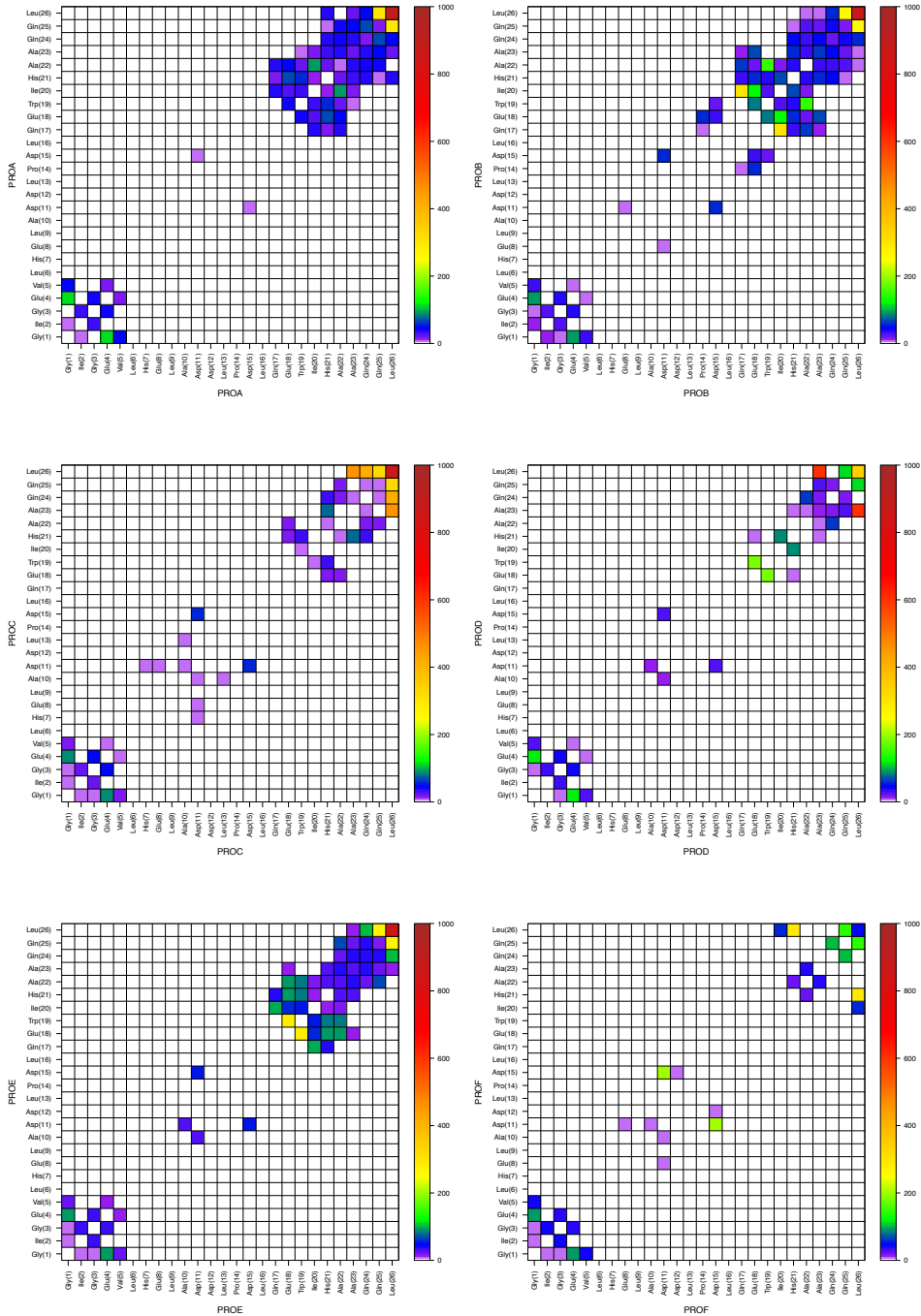


Figure 5.71: pHD15 hexameric pore at pH 5 during last 2 μ s. Heat map of duration (ns) of dominant backbone-backbone intra-peptide water bridging interaction.

Sidechain-Sidechain Contacts

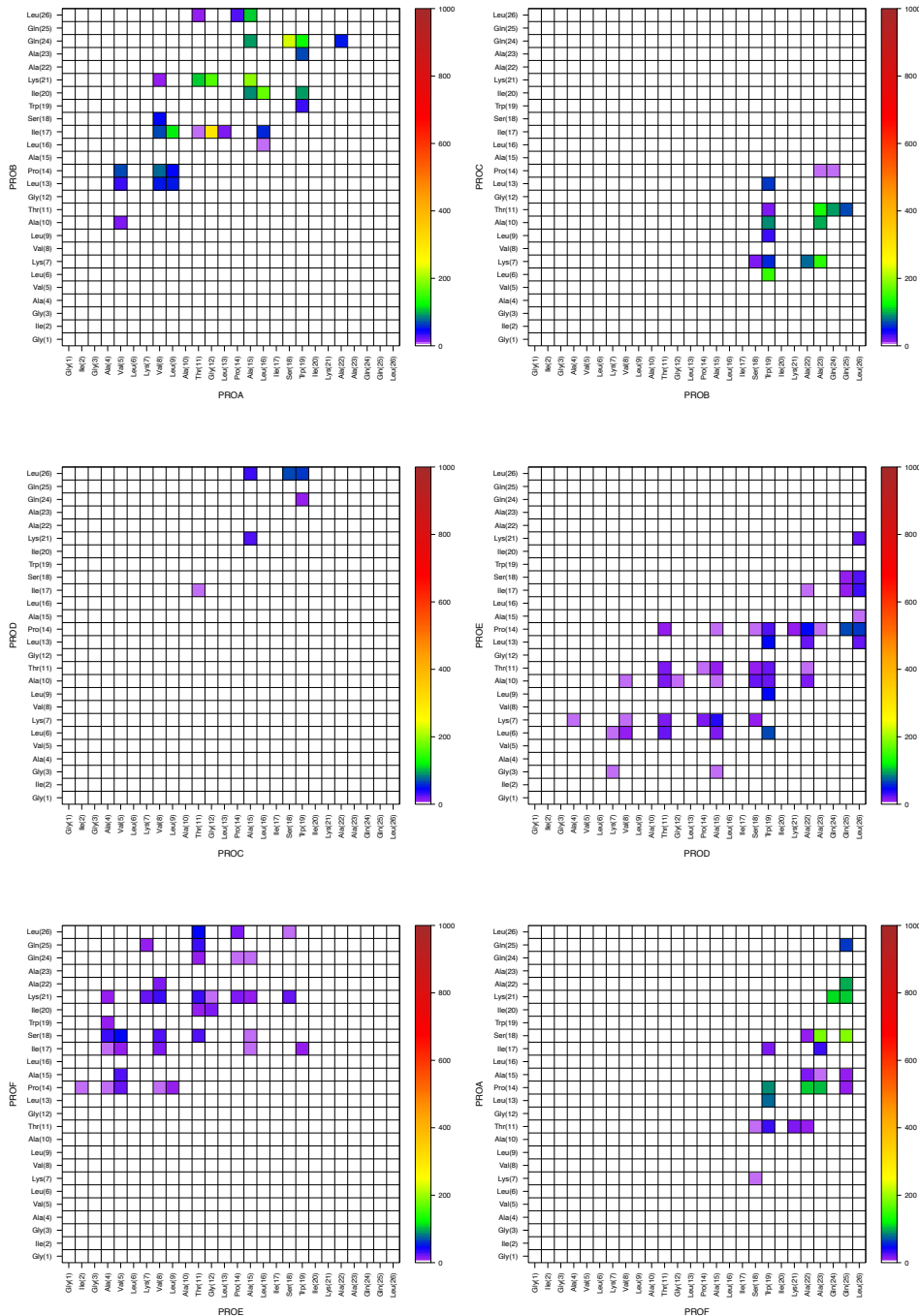


Figure 5.72: MelP5 hexameric pore during last 2 μ s. Heat map of duration (ns) of the dominant sidechain–sidechain contact interaction between peptides i and $i + 1$ clockwise (N-term up).

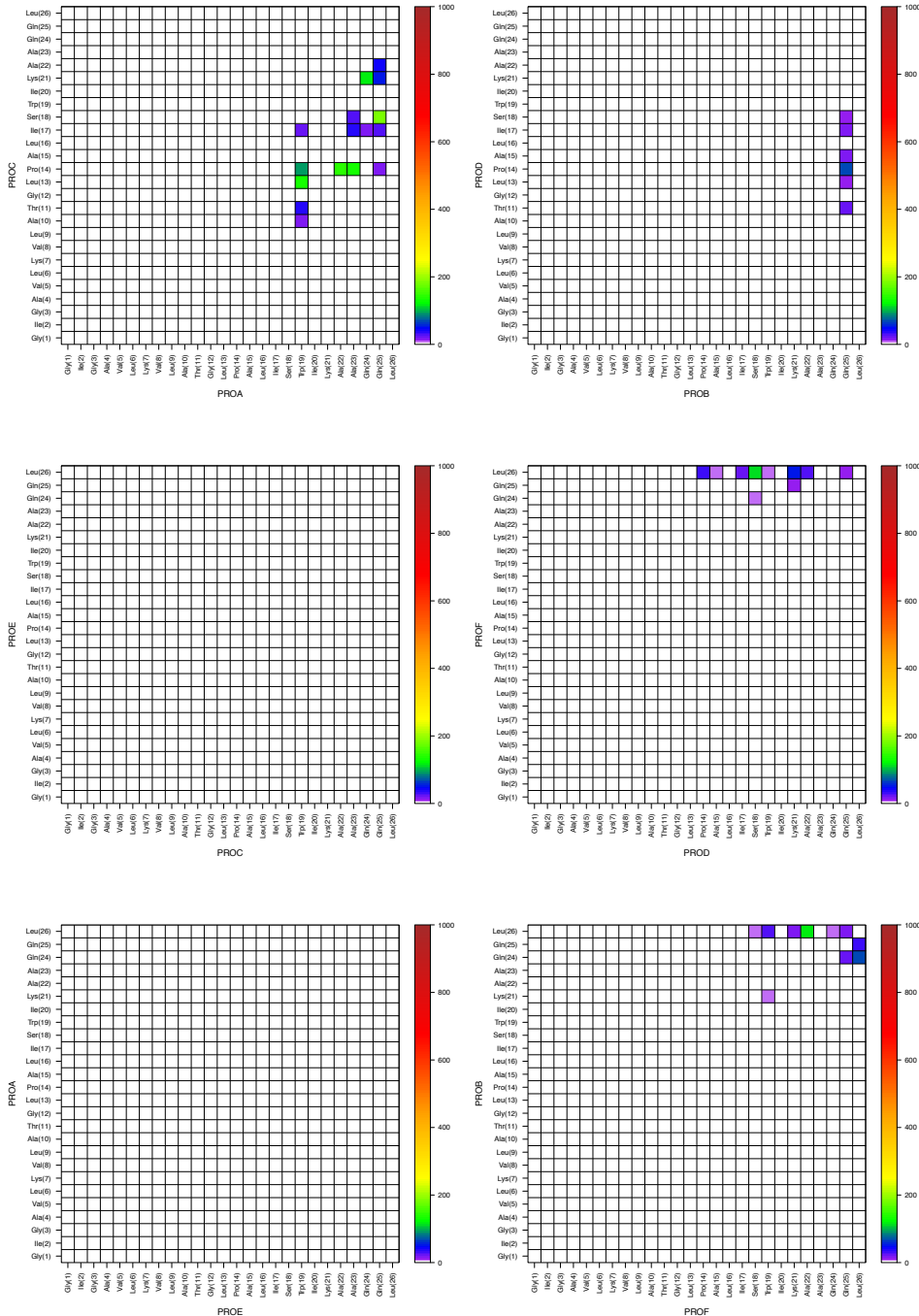


Figure 5.73: MelP5 hexameric pore during last 2 μ s. Heat map of duration (ns) of the dominant sidechain–sidechain contact interaction between peptides i and $i + 2$ clockwise (N-term up).

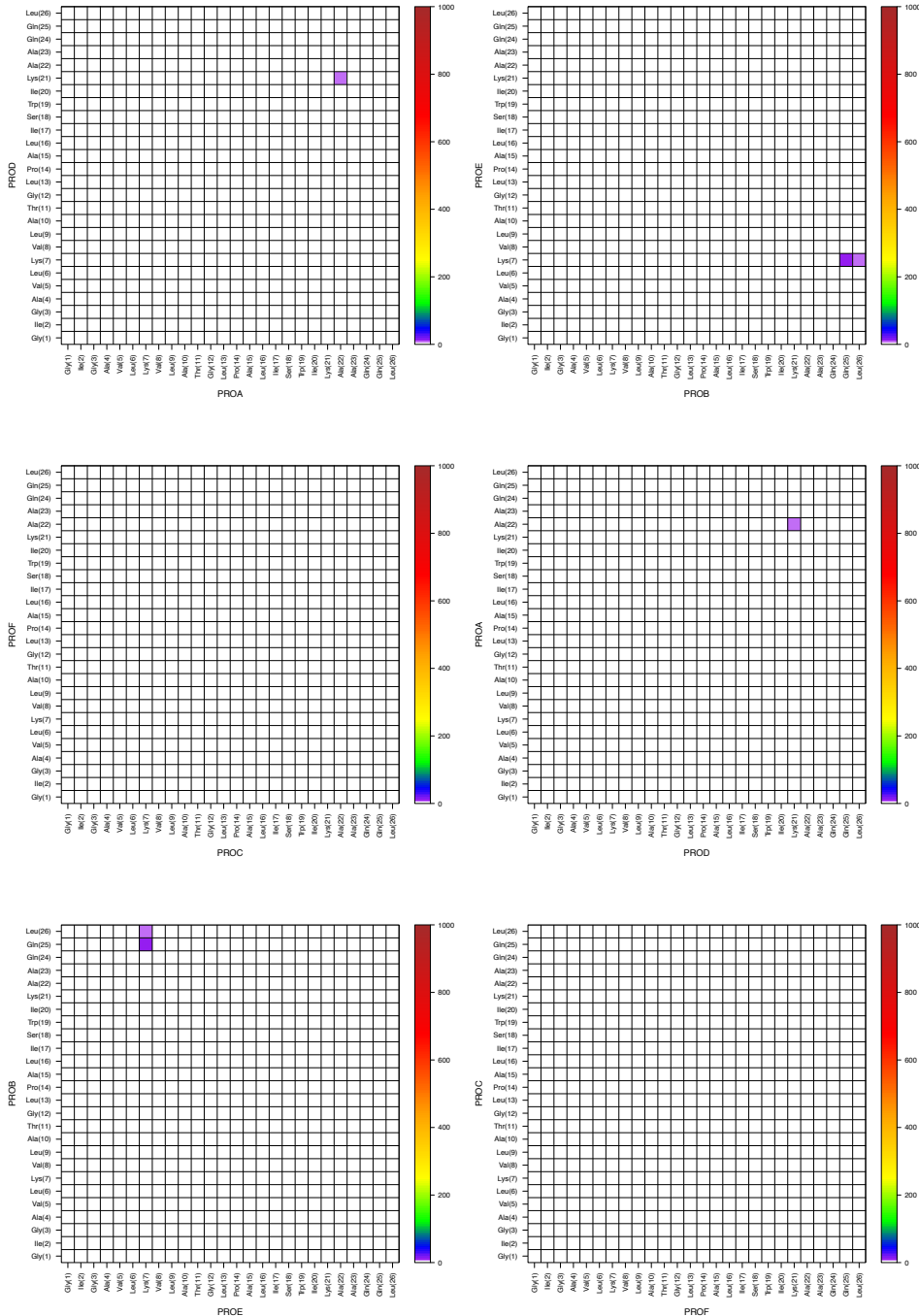


Figure 5.74: MelP5 hexameric pore during last 2 μ s. Heat map of duration (ns) of the dominant sidechain–sidechain contact interaction between peptides i and $i + 3$ clockwise (N-term up).

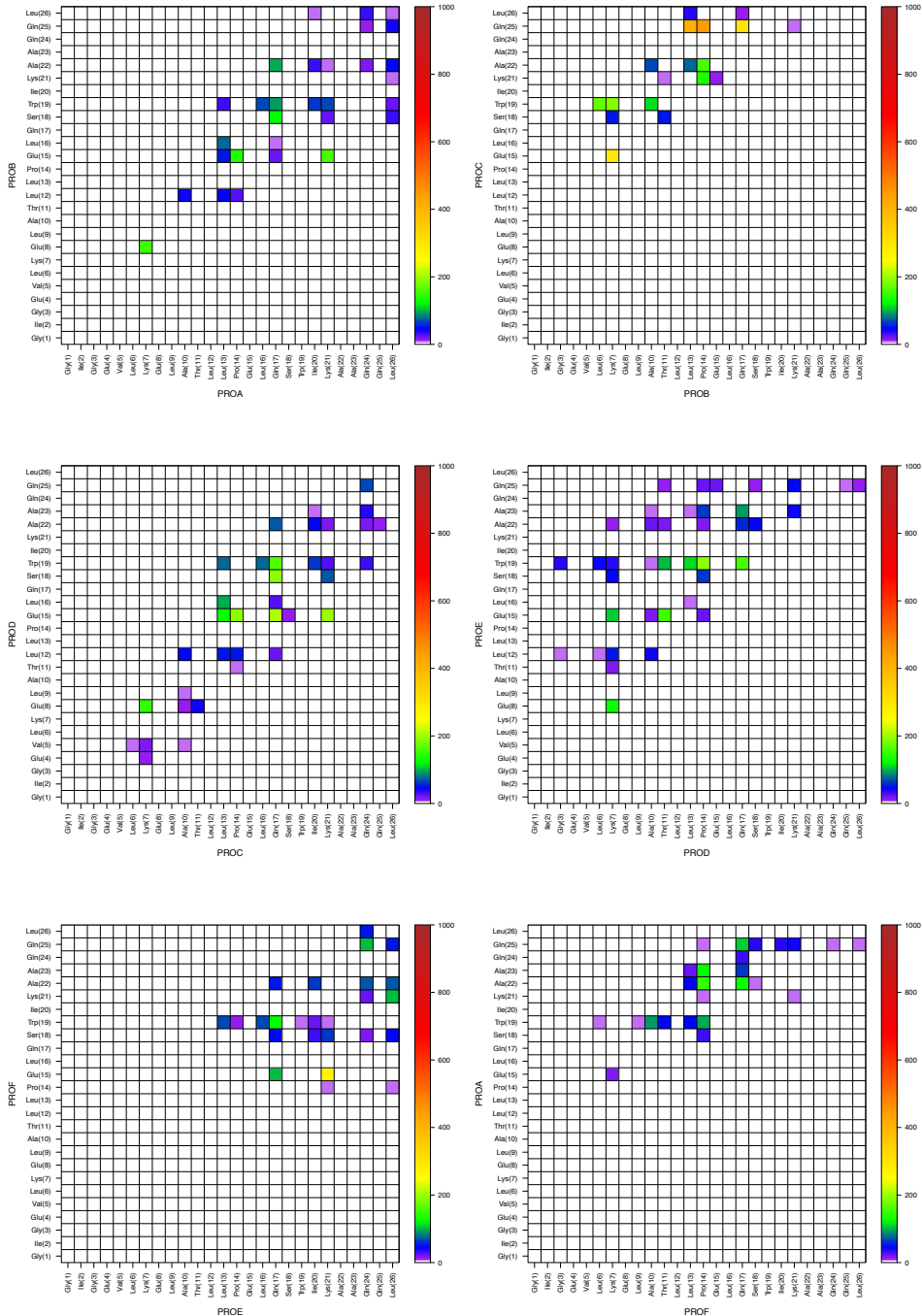


Figure 5.75: Macrolittin70 hexameric pore at pH 7 during last 2 μ s. Heat map of duration (ns) of the dominant sidechain–sidechain contact interaction between peptides i and $i + 1$ clockwise (N-term up).

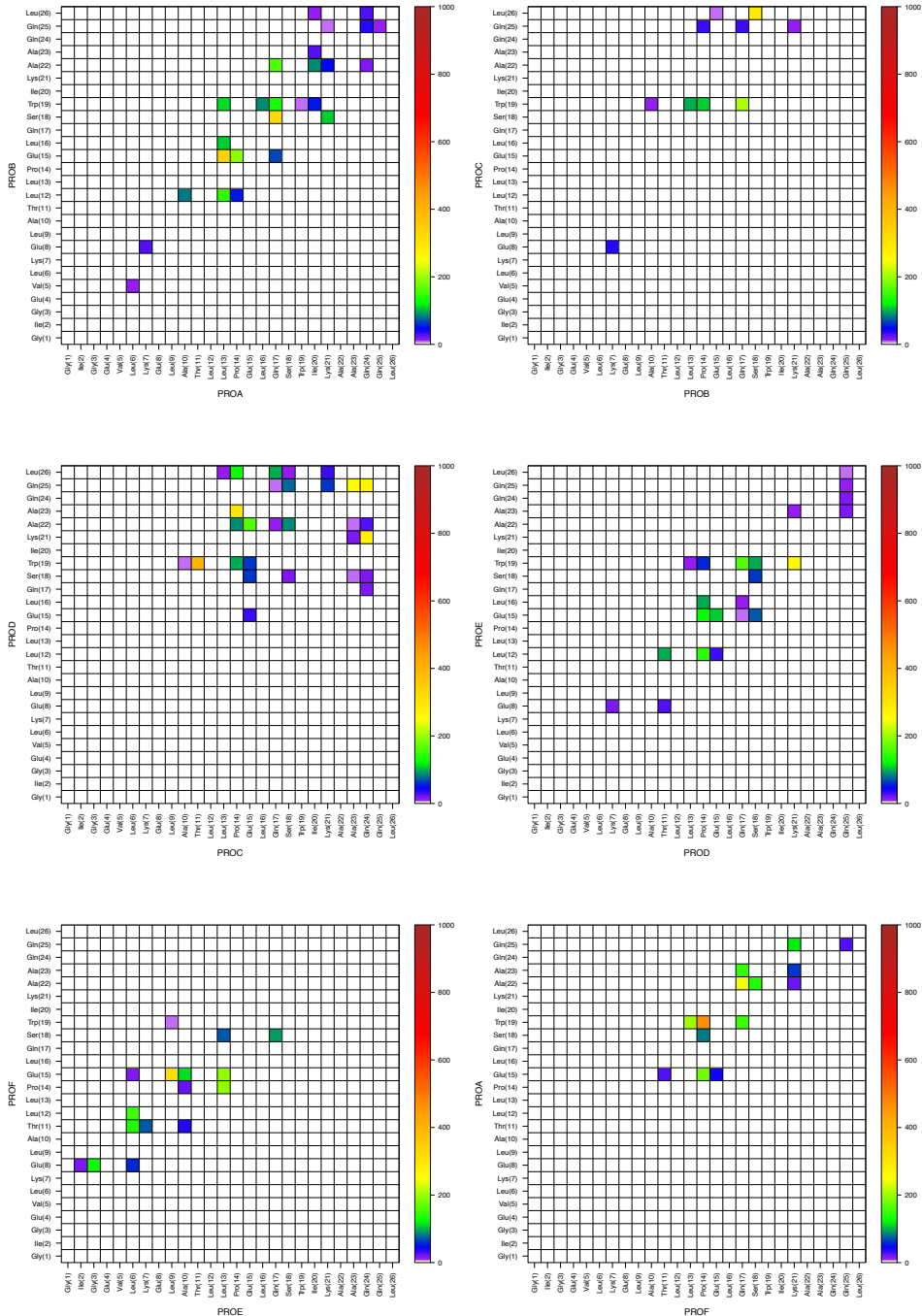


Figure 5.76: Macrolittin70 hexameric pore at pH 5 during last 2 μ s. Heat map of duration (ns) of the dominant sidechain–sidechain contact interaction between peptides i and $i + 1$ clockwise (N-term up).

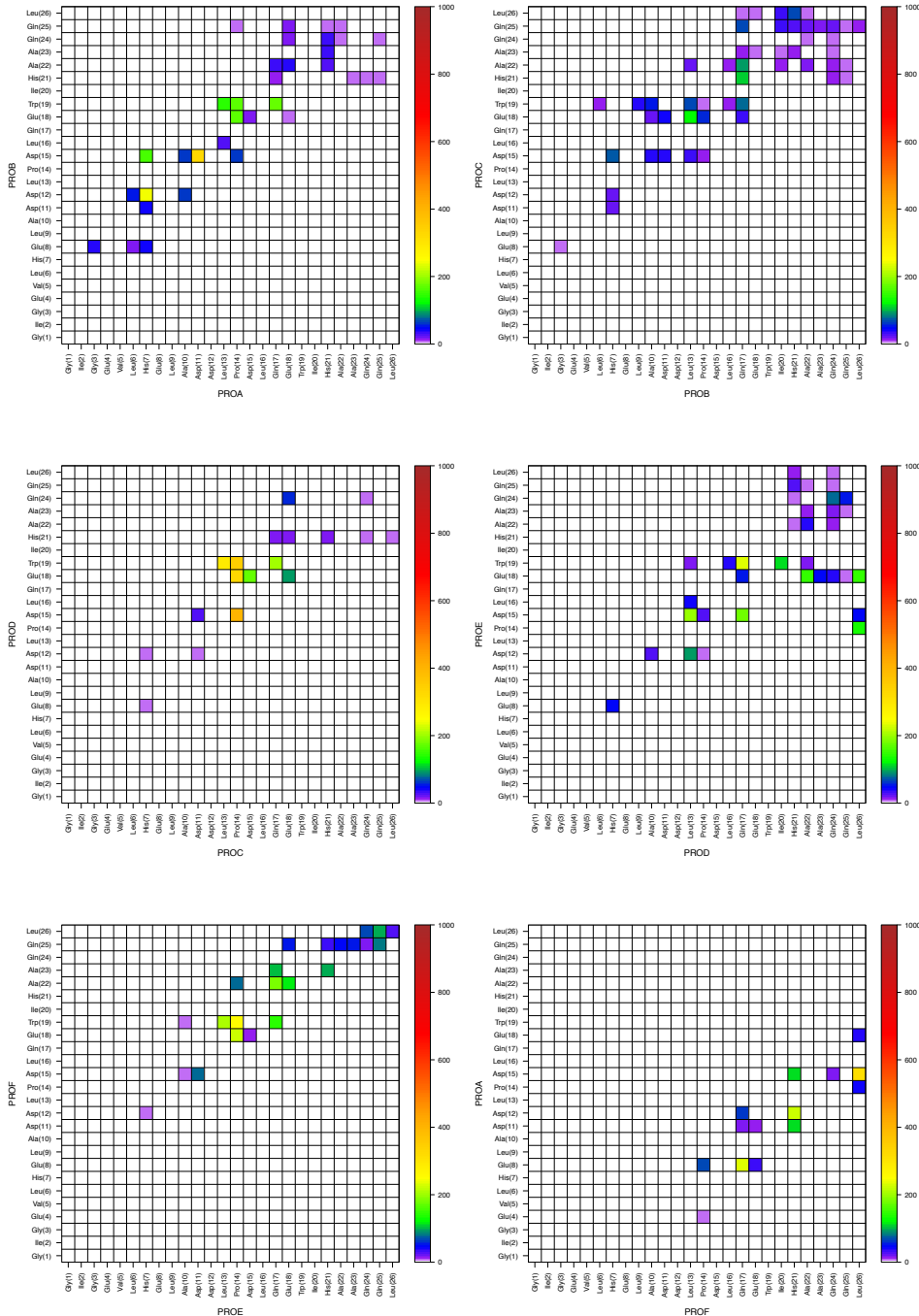


Figure 5.77: pHD15 hexameric pore at pH 5 during last 2 μ s. Heat map of duration (ns) of the dominant sidechain–sidechain contact interaction between peptides i and $i+1$ clockwise (N-term up).

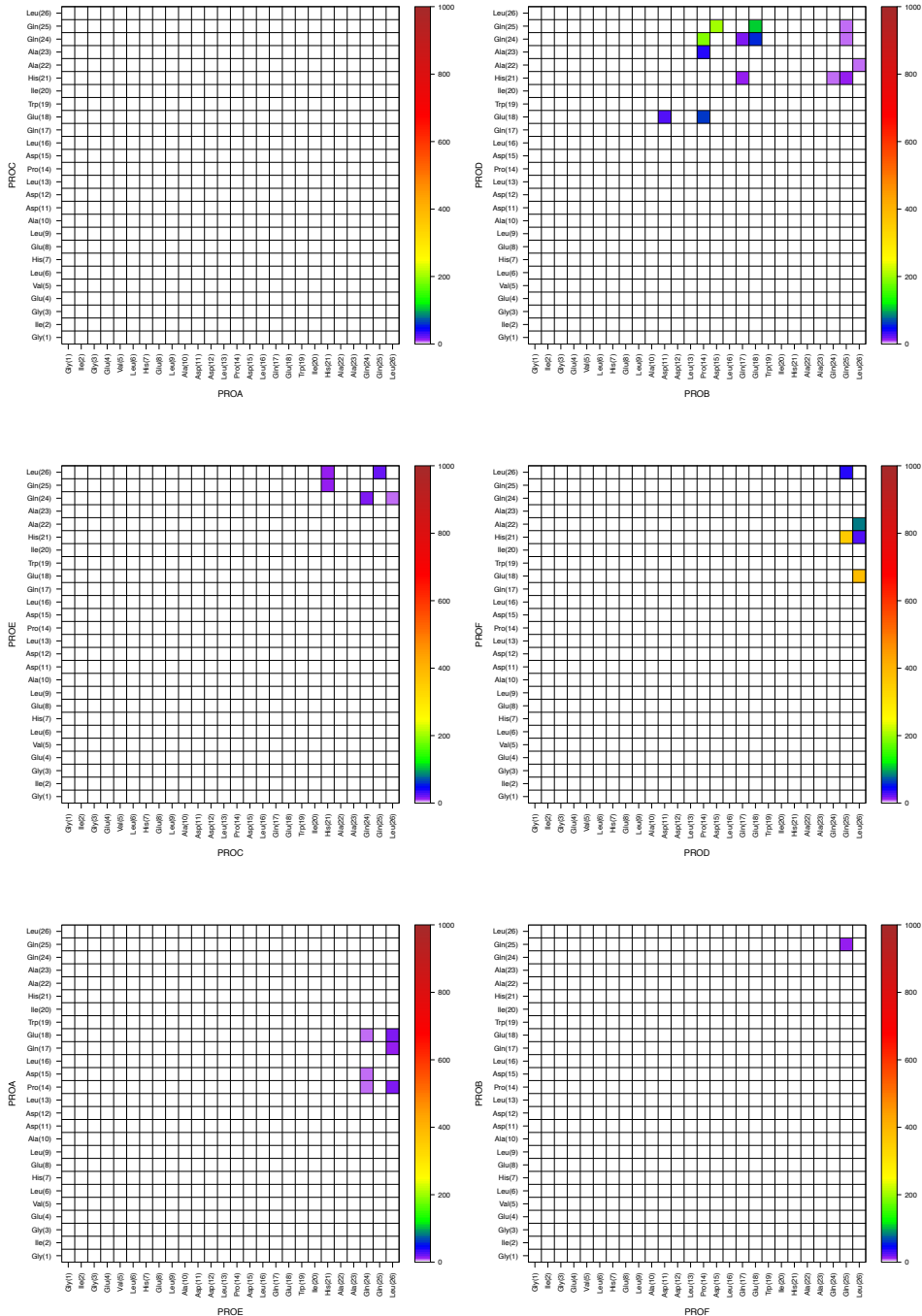


Figure 5.78: pHD15 hexameric pore at pH 5 during last 2 μ s. Heat map of duration (ns) of the dominant sidechain–sidechain contact interaction between peptides i and $i+2$ clockwise (N-term up).

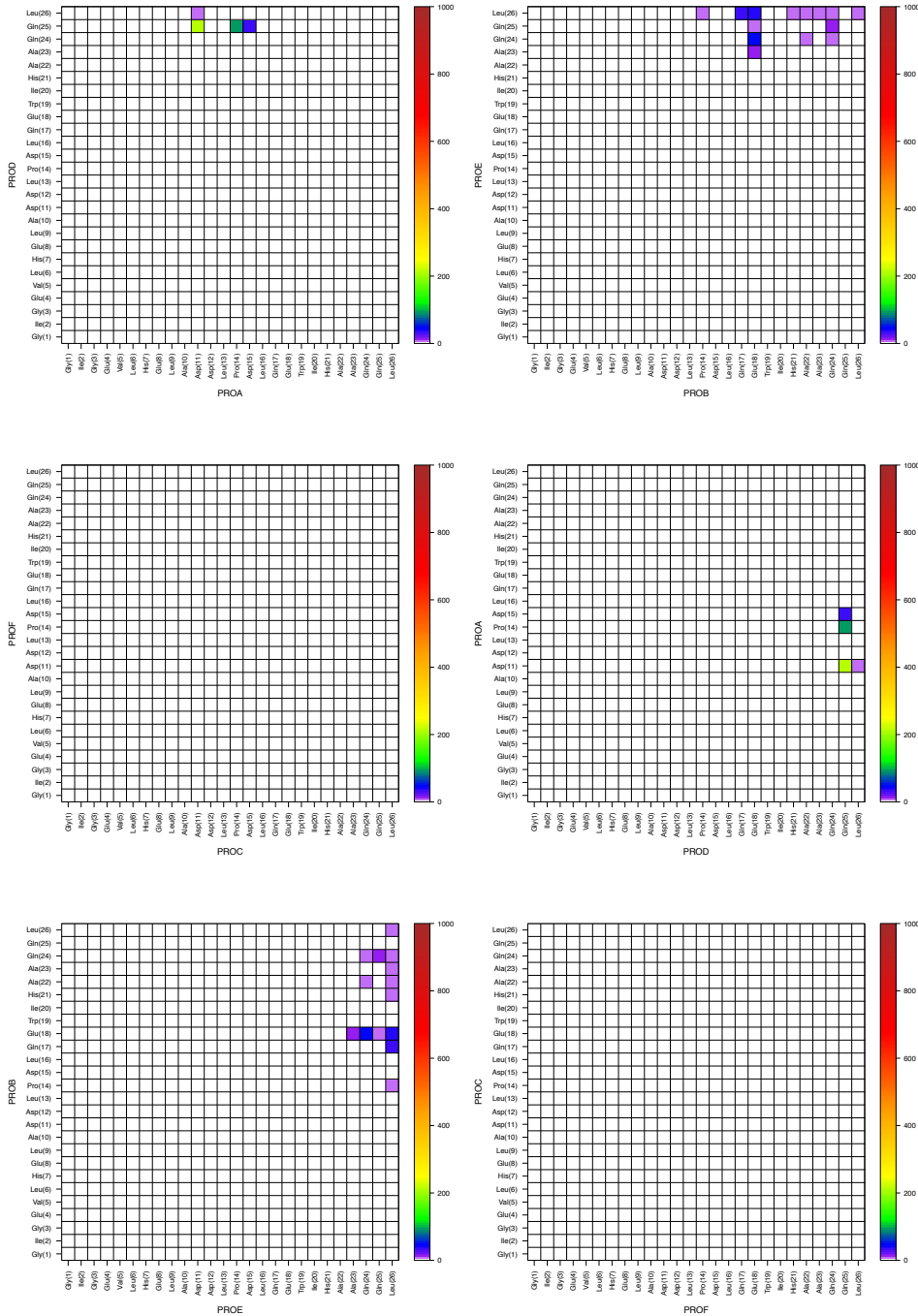


Figure 5.79: pHD15 hexameric pore at pH 5 during last 2 μ s. Heat map of duration (ns) of the dominant sidechain–sidechain contact interaction between peptides i and $i+3$ clockwise (N-term up).

Tilt Angle Correlation:

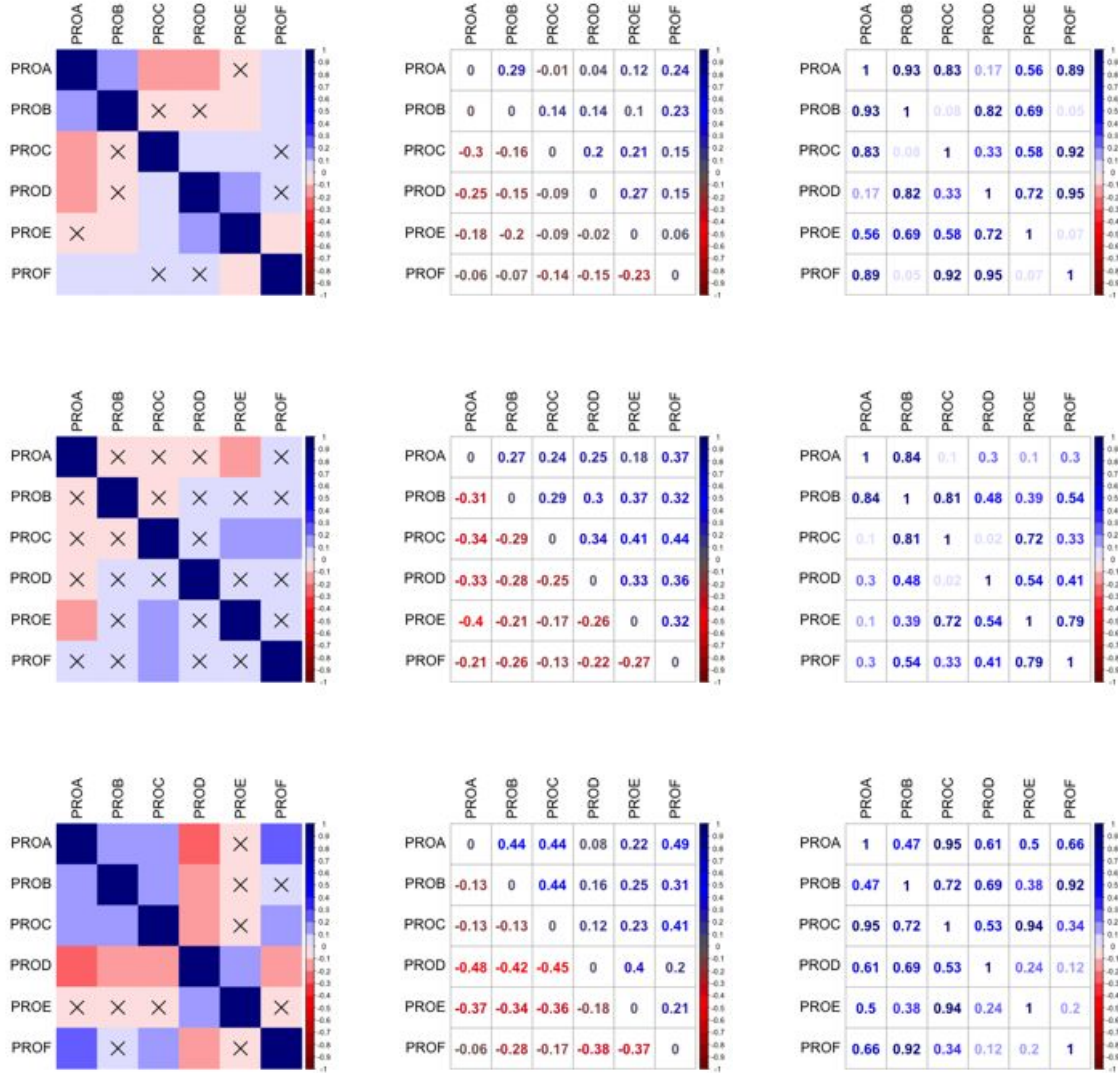


Figure 5.80: MelP5 matrices of **(Left column)** Pearson correlation (r) (p-values $> \alpha = 1 \times 10^{-10}$ are marked with \times), **(Middle column)** 99.9999999% confidence intervals (lower and upper limits in lower and upper-triangular matrix regions, respectively), and **(Right column)** p-values of Breusch-Pagan homoscedasticity test (reject H_0 (homoscedasticity assumption) if p-value < 0.05), for tilt angles of **(Top row)** peptides, and of **(Middle row)** N-terminal, and **(Bottom row)** C-terminal helices. The **table below** shows p-values for the Shapiro-Wilk normalcy test (reject H_0 (normalcy assumption) if the p-value is < 0.05).

p-values:	proa	prob	proc	prod	proe	prof	trajectory
tilt	0.77	0.77	0.09	0.26	0.61	0.18	last 2 μ s
N-ter	0.35	0.35	0.06	0.61	0.80	0.25	last 0.5 μ s
C-ter	0.27	0.27	0.06	0.34	0.52	0.38	last 0.5 μ s

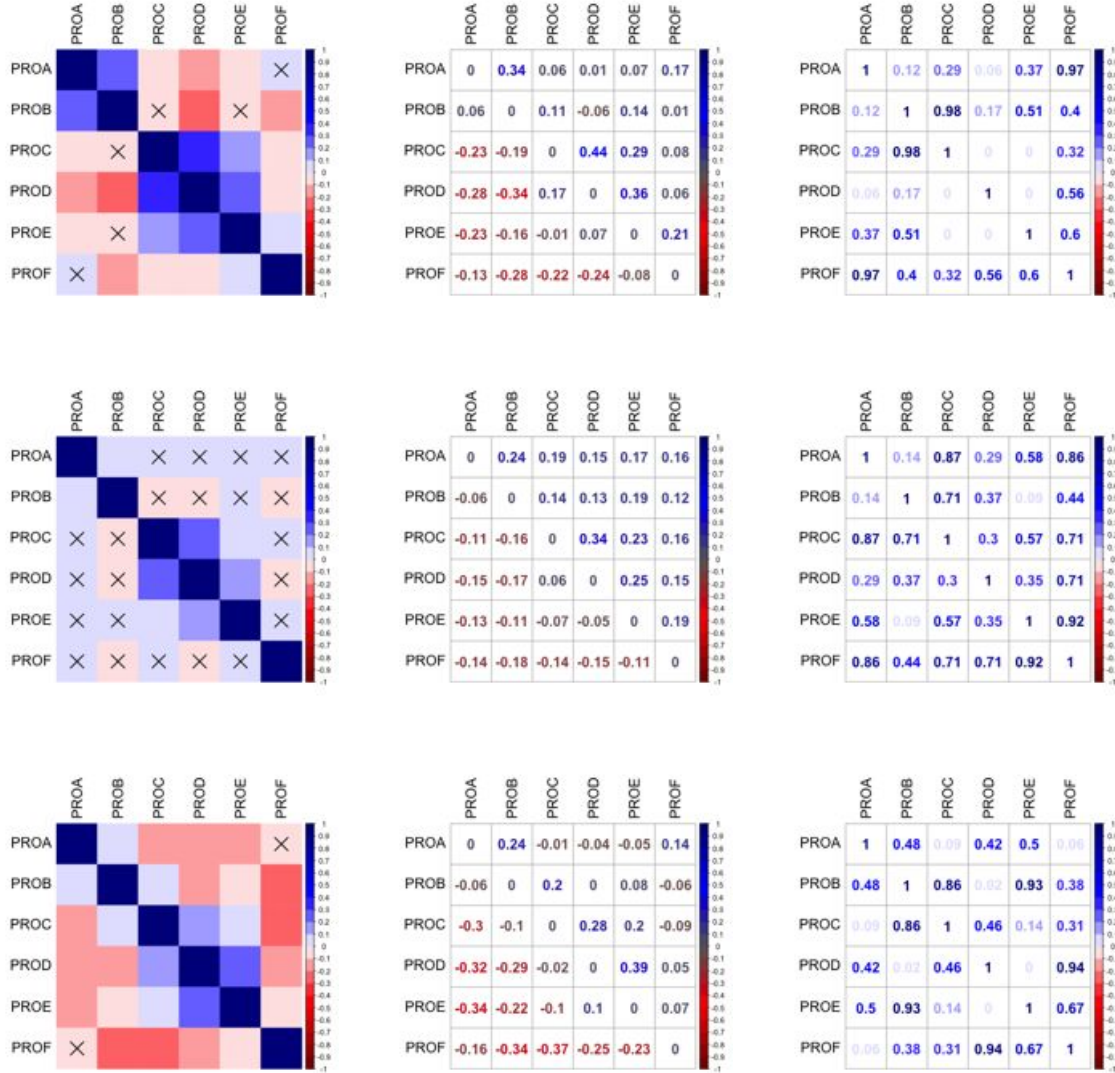


Figure 5.81: Mac70 pore at pH 7 matrices of **(Left column)** Pearson correlation (r) (p-values $> \alpha = 1 \times 10^{-10}$ are marked with \times), **(Middle column)** 99.9999999% confidence intervals (lower and upper limits in lower and upper-triangular matrix regions, respectively), and **(Right column)** p-values of Breusch-Pagan homoscedasticity test (reject H_0 (homoscedasticity assumption) if p-value < 0.05), for tilt angles of **(Top row)** peptides, and of **(Middle row)** N-terminal, and **(Bottom row)** C-terminal helices. The **table below** shows p-values for the Shapiro-Wilk normalcy test (reject H_0 (normalcy assumption) if the p-value is < 0.05).

p-values:	proa	prob	proc	prod	proe	prof	trajectory
tilt	0.06	0.06	0.11	0.97	0.21	0.75	last 2 μ s
N-ter	0.13	0.13	0.14	0.78	0.06	0.54	last 2 μ s
C-ter	0.59	0.60	0.54	0.50	0.16	0.20	last 2 μ s

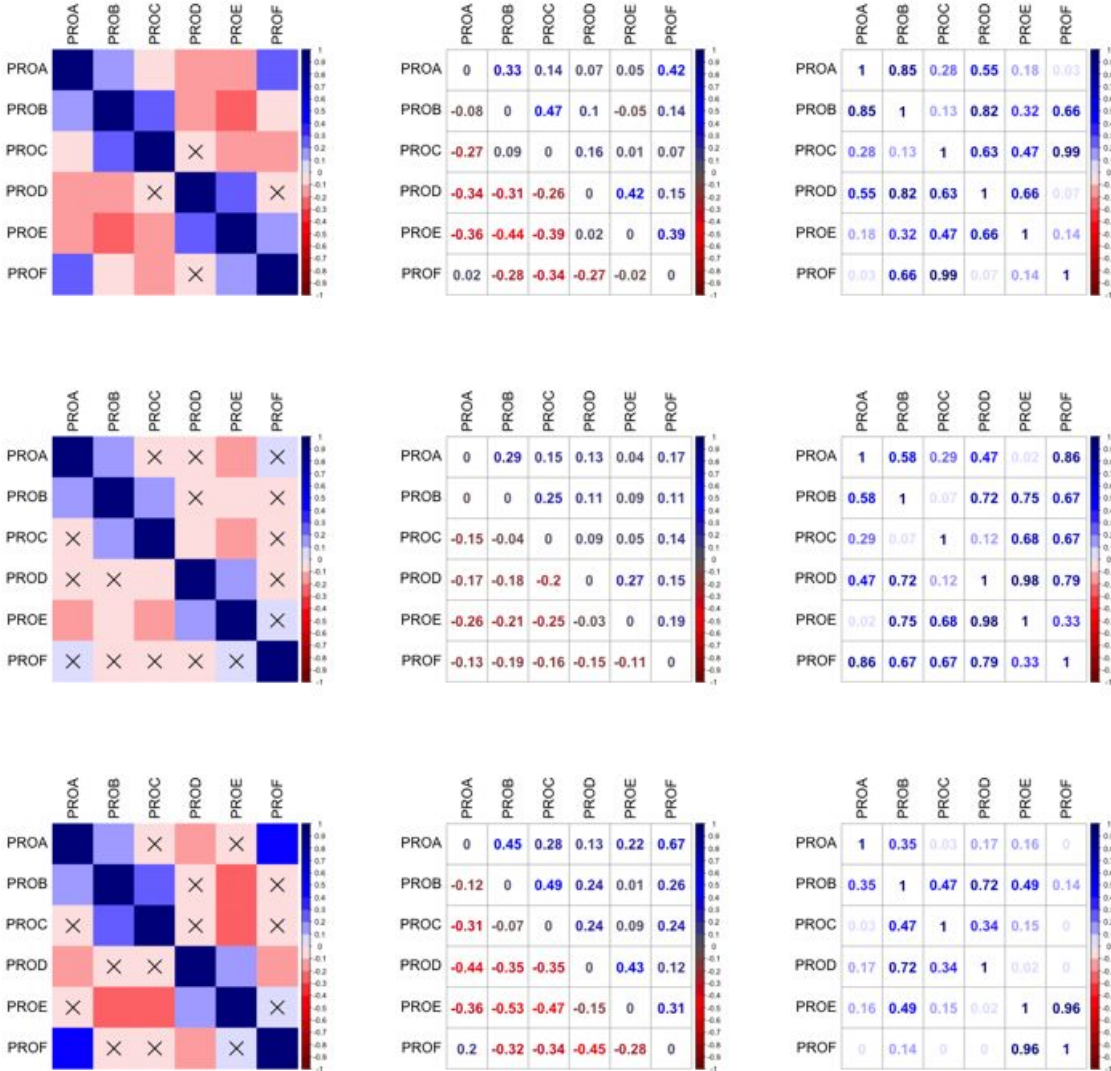


Figure 5.82: Mac70 pore at pH 5 matrices of **(Left column)** Pearson correlation (r) (p-values $> \alpha = 1 \times 10^{-10}$ are marked with \times), **(Middle column)** 99.9999999% confidence intervals (lower and upper limits in lower and upper-triangular matrix regions, respectively), and **(Right column)** p-values of Breusch-Pagan homoscedasticity test (reject H_0 (homoscedasticity assumption) if p-value < 0.05), for tilt angles of **(Top row)** peptides, and of **(Middle row)** N-terminal, and **(Bottom row)** C-terminal helices. The **table below** shows p-values for the Shapiro-Wilk normalcy test (reject H_0 (normalcy assumption) if the p-value is < 0.05).

p-values:	proa	prob	proc	prod	proe	prof	trajectory
tilt	0.40	0.40	0.84	0.50	0.72	0.04	last 1 μ s
N-ter	0.52	0.52	0.63	0.05	0.65	0.11	last 2 μ s
C-ter	0.19	0.19	0.50	0.47	0.74	0.63	last 0.5 μ s

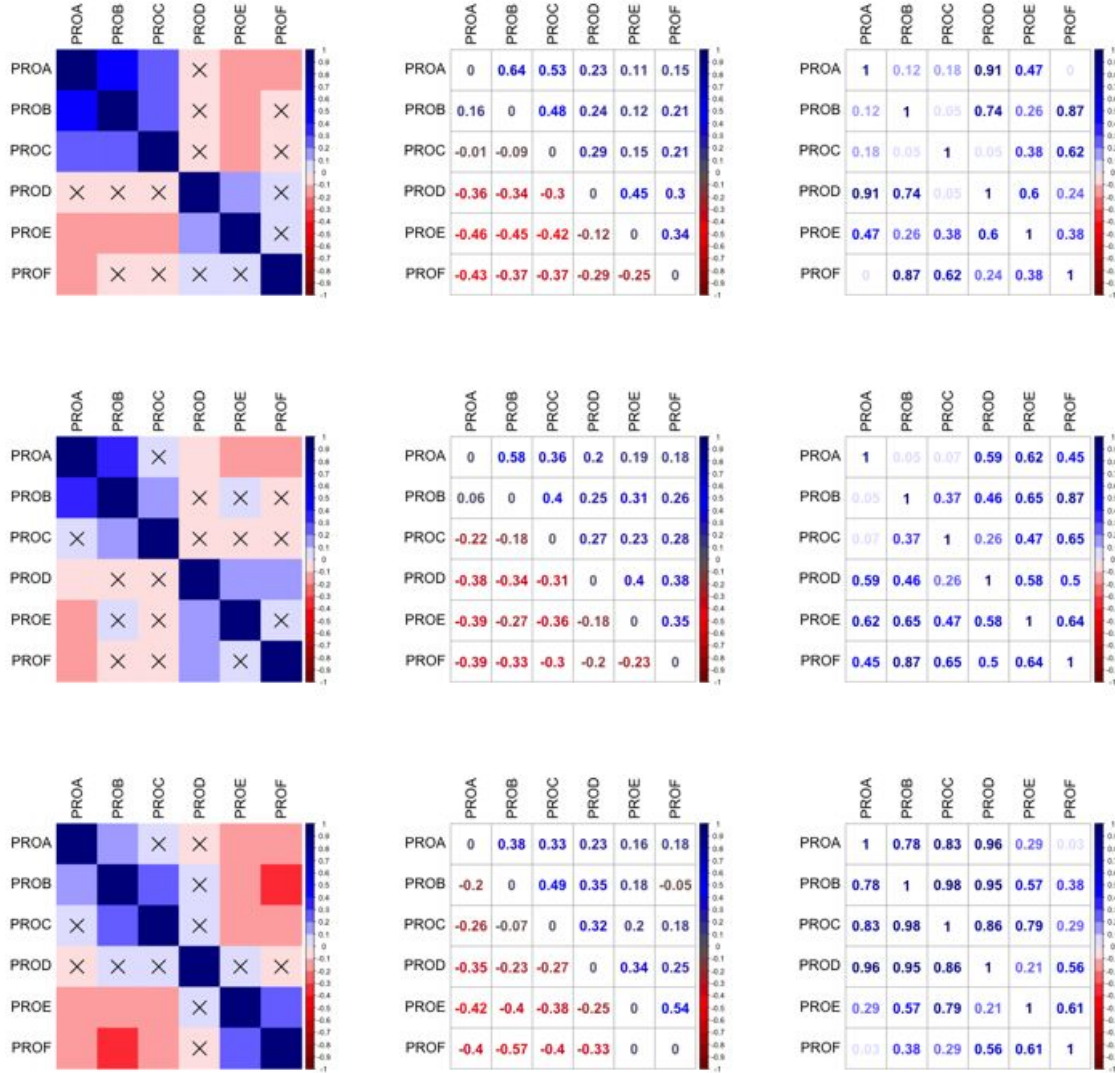


Figure 5.83: pHD15 pore at pH 5 matrices of **(Left column)** Pearson correlation (r) (p -values $> \alpha = 1 \times 10^{-10}$ are marked with \times), **(Middle column)** 99.9999999% confidence intervals (lower and upper limits in lower and upper-triangular matrix regions, respectively), and **(Right column)** p -values of Breusch-Pagan homoscedasticity test (reject H_0 (homoscedasticity assumption) if p -value < 0.05), for tilt angles of **(Top row)** peptides, and of **(Middle row)** N-terminal, and **(Bottom row)** C-terminal helices. The **table below** shows p -values for the Shapiro-Wilk normalcy test (reject H_0 (normalcy assumption) if the p -value is < 0.05).

p-values:	proa	prob	proc	prod	proe	prof	trajectory
tilt	0.96	0.96	0.32	0.22	0.21	0.23	last 0.5 μ s
N-ter	0.69	0.67	0.21	0.16	0.87	0.76	last 0.5 μ s
C-ter	0.83	0.83	0.76	0.35	0.14	0.49	last 0.5 μ s

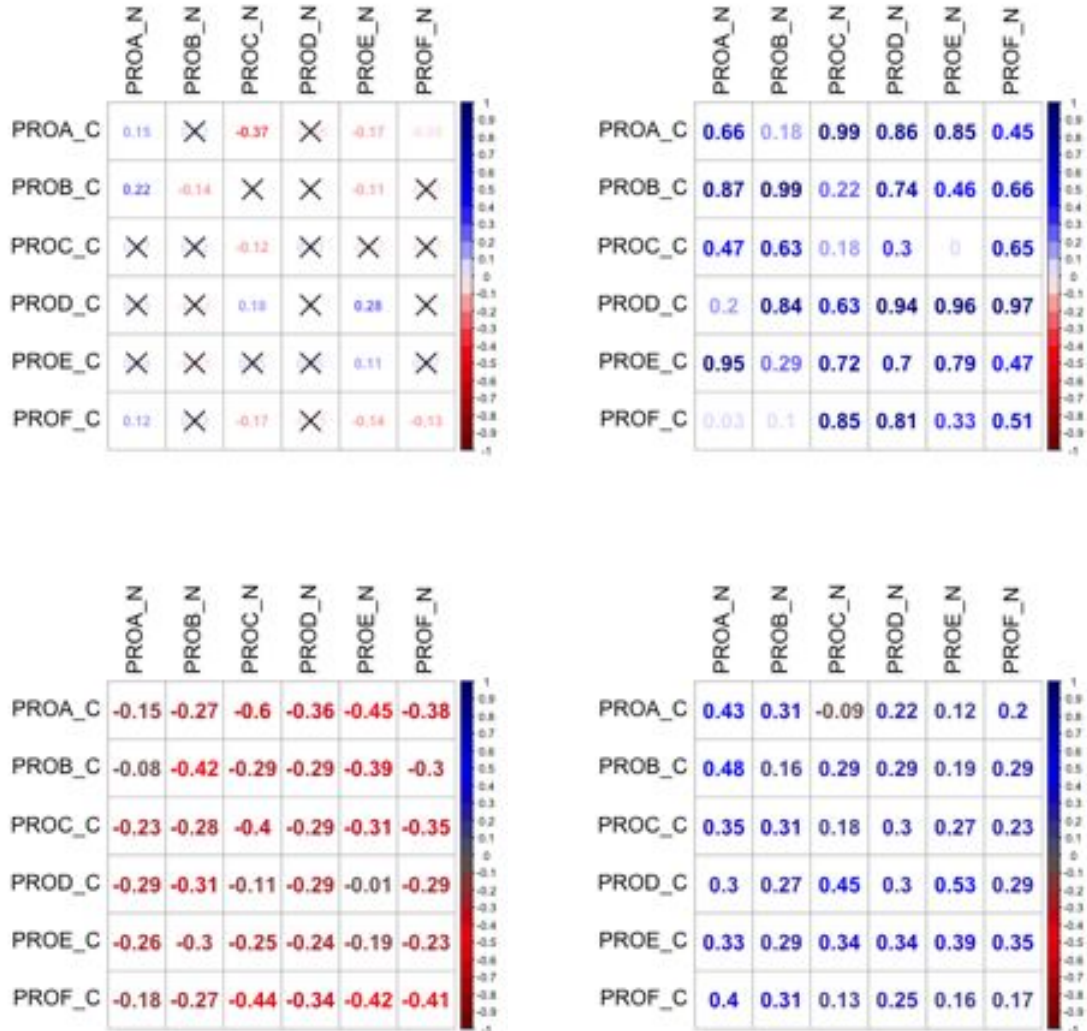


Figure 5.84: **(Left)** Matrix of Pearson correlation (r) between tilt angles of N- and C-terminal helices of the MelP5 pore during the last $0.5 \mu\text{s}$. p-values above 1×10^{-10} are marked with an x. **(Right)** Upper and lower bounds of the 99.9999999% confidence intervals are in the upper and lower triangular regions, respectively.

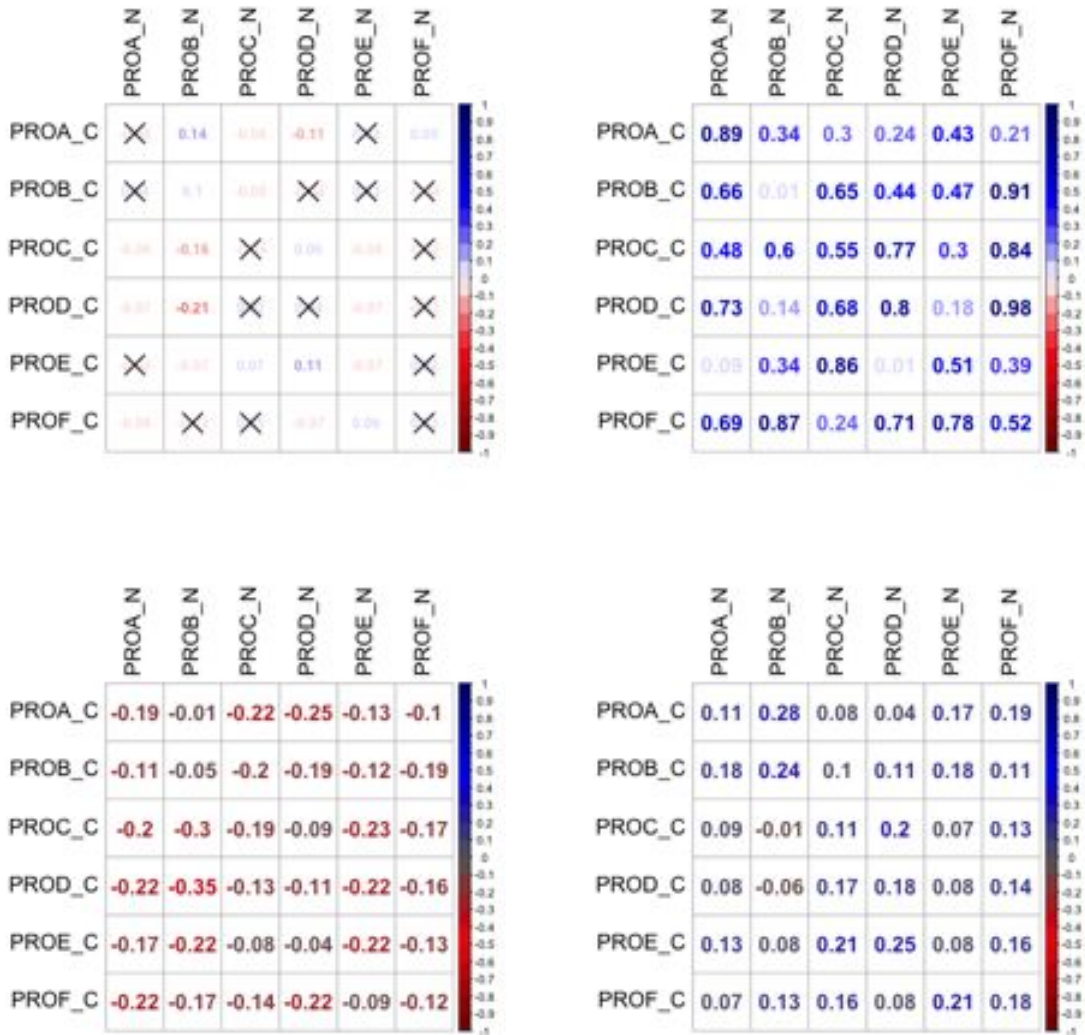


Figure 5.85: **(Left)** Matrix of Pearson correlation (r) between tilt angles of N- and C-terminal helices of the macrolittin70 pore at pH 7 during the last $2 \mu\text{s}$. p-values above 1×10^{-10} are marked with an X. **(Right)** Upper and lower bounds of the 99.9999999% confidence intervals are in the upper and lower triangular regions, respectively.

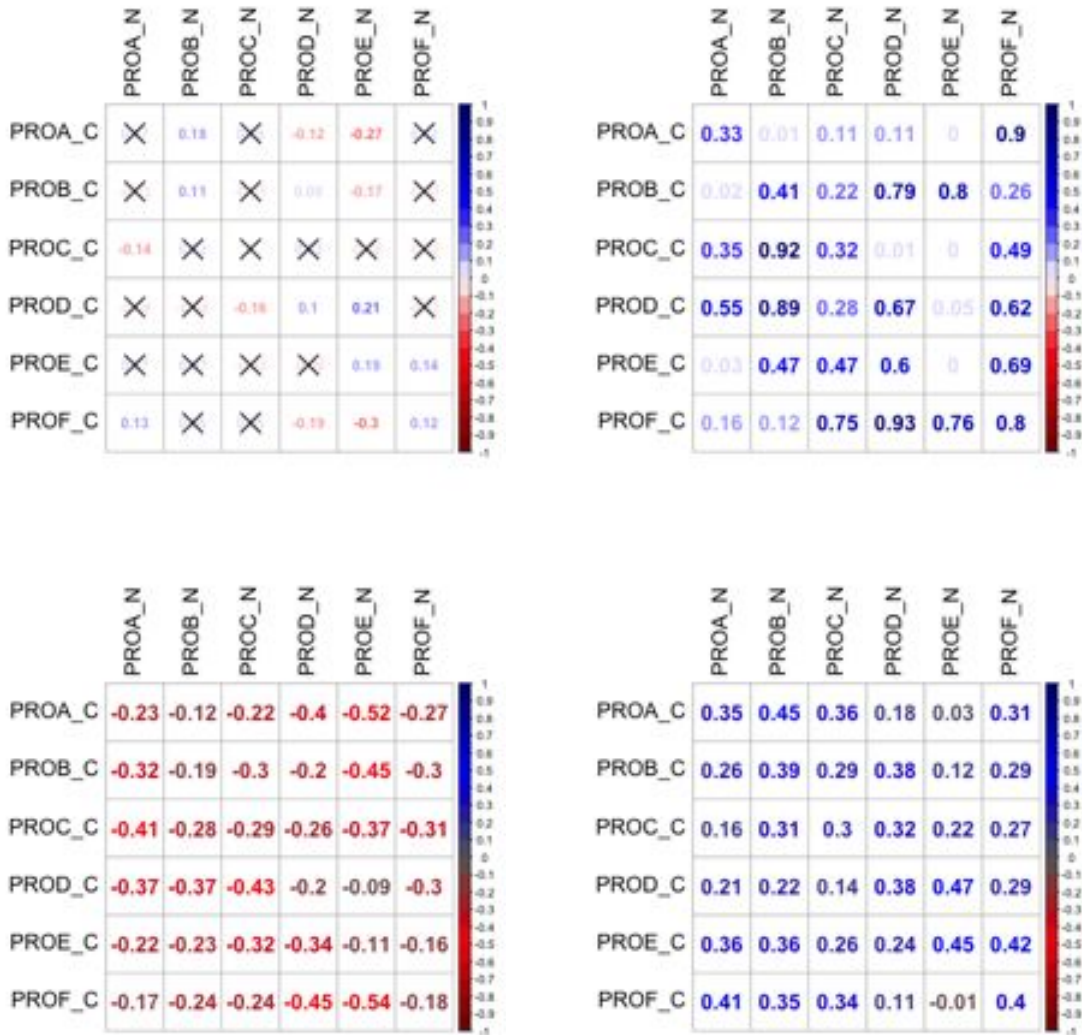


Figure 5.86: **(Left)** Matrix of Pearson correlation (r) between tilt angles of N- and C-terminal helices of the macrolittin70 pore at pH 5 during the last $2 \mu\text{s}$. p-values above 1×10^{-10} are marked with an x. **(Right)** Upper and lower bounds of the 99.9999999% confidence intervals are in the upper and lower triangular regions, respectively.

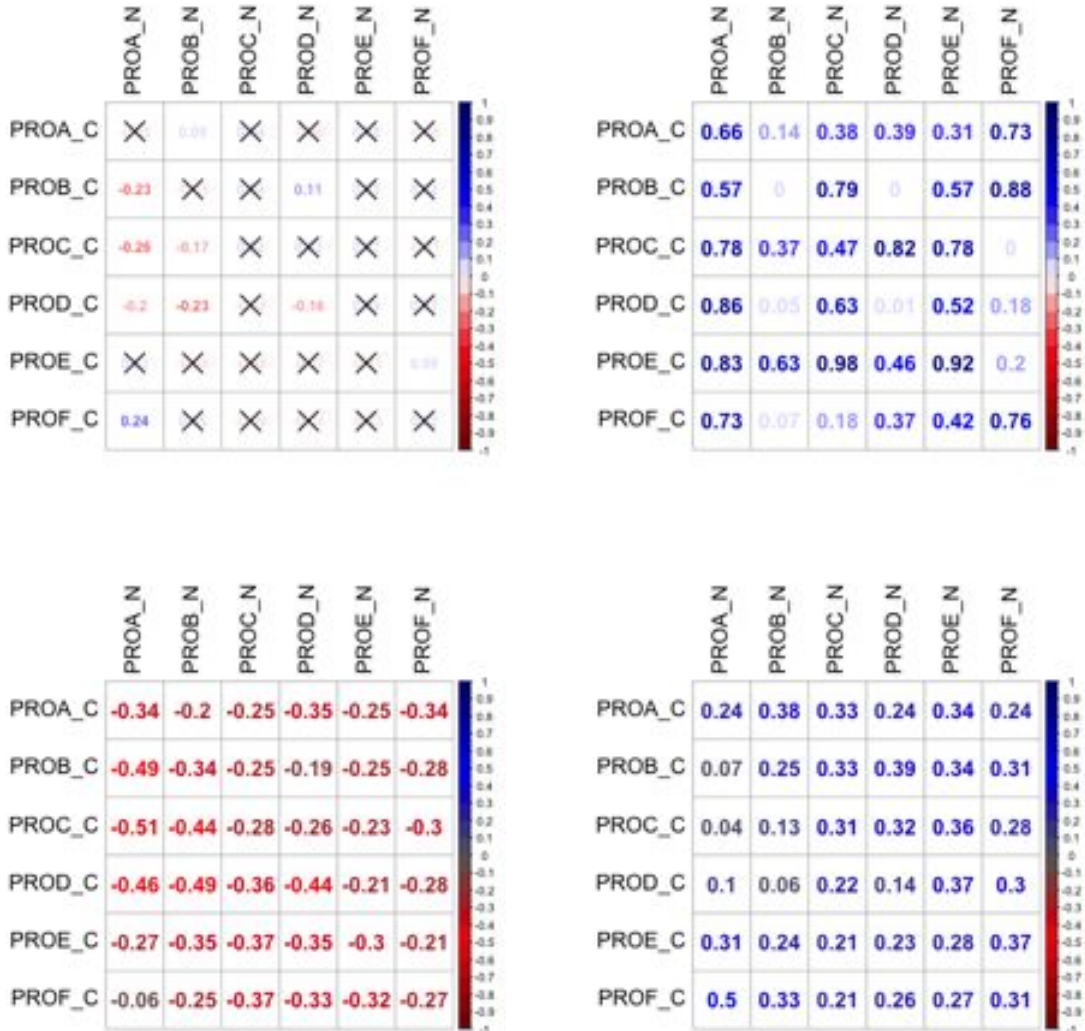


Figure 5.87: **(Left)** Matrix of Pearson correlation (r) between tilt angles of N- and C-terminal helices of the pH15 pore at pH 5 during the last $0.5 \mu\text{s}$. p-values above 1×10^{-10} are marked with an x. **(Right)** Upper and lower bounds of the 99.9999999% confidence intervals are in the upper and lower triangular regions, respectively.

Bibliography

- [1] P. M. Hawkey. Molecular epidemiology of clinically significant antibiotic resistance genes. *Brit. J. Pharmacol.* **2008** 153(Suppl 1):S406–13.
- [2] F. Griffith. The significance of Pneumococcal types. *J. Hyg.* **1928** 27(2):113–159.
- [3] H. E. Alexander and G. Leidy. Induction of streptomycin resistance in sensitive hemophilus influenzae by extracts containing desoxyribonucleic acid from resistant hemophilus influenzae. *J. Exp. Med.* **1953** 97(1):17–31.
- [4] H. E. Alexander, E. Hahn, and G. Leidy. On the specificity of the desoxyribonucleic acid which induces streptomycin resistance in Hemophilus. *J. Exp. Med.* **1956** 104(3):305–320.
- [5] H. W. Boucher, G. H. Talbot, J. S. Bradley, J. E. Edwards, D. Gilbert, L. B. Rice, M. Scheld, B. Spellberg, and J. Bartlett. Bad bugs, no drugs: no ESKAPE! An update from the Infectious Diseases Society of America. *Clin. Infect. Dis.* **2009** 48(1):1–12.
- [6] M. Zasloff. Antimicrobial peptides of multicellular organisms. *Nature* **2002** 415(6870):389–395.
- [7] P. S. Hiemstra, B. a. Fernie-King, J. McMichael, P. J. Lachmann, and J.-M. Sallenave. Antimicrobial peptides: Mediators of innate immunity as templates for the development of novel anti-infective and immune therapeutics. *Curr. Pharm. Des.* **2004** 10(23):2891–2905.
- [8] D. Eisenberg, R. M. Weiss, and T. C. Terwilliger. The helical hydrophobic moment: A measure of the amphiphilicity of a helix. *Nature* **1982** 299(5881):371–374.
- [9] R. M. Hayden, G. K. Goldberg, B. M. Ferguson, M. W. Schoeneck, M. D. J. Libardo, S. E. Mayeux, A. Shrestha, K. A. Bogardus, J. Hammer, S. Pryshchep, H. K. Lehman, M. L. McCormick, J. Blazyk, A. M. Angeles-Boza, R. Fu, and M. L. Cotten. Complementary effects of host defense peptides Piscidin 1 and Piscidin 3 on DNA and lipid membranes: Biophysical insights into contrasting biological activities. *J. Phys. Chem. B* **2015** 119(49):15235–15246.
- [10] S. J. Ludtke, K. He, W. T. Heller, T. A. Harroun, L. Yang, and H. W. Huang. Membrane pores induced by magainin. *Biochemistry* **1996** 35(43):13723–13728.

- [11] K. Matsuzaki, O. Murase, N. Fujii, and K. Miyajima. An antimicrobial peptide, magainin 2, induced rapid flip-flop of phospholipids coupled with pore formation and peptide translocation. *Biochemistry* **1996** 35(35):11361–11368.
- [12] W. WC. Describing the mechanism of antimicrobial peptide action with the interfacial activity model. *ACS Chem. Biol.* **2010** 5(10):905–917.
- [13] H. W. Huang. Molecular mechanism of antimicrobial peptides: The origin of cooperativity. *BBA* **2006** 1758(9):1292–1302.
- [14] R. F. Epand, W. L. Maloy, A. Ramamoorthy, and R. M. Epand. Probing the “charge cluster mechanism” in amphipathic helical cationic antimicrobial peptides. *Biochemistry* **2010** 49(19):4076–4084.
- [15] D. Zweytick, S. Tumer, S. E. Blondelle, and K. Lohner. Membrane curvature stress and antibacterial activity of lactoferricin derivatives. *Biochem. Biophys. Res. Commun.* **2008** 369(2):395–400.
- [16] K. Lohner. Membrane-active antimicrobial peptides as template structures for novel antibiotic agents. *Curr. Top. Med. Chem.* **2017** 17(32):508–519.
- [17] Y. Shai. Mode of action of membrane active antimicrobial peptides. *Biopolymers* **2002** 66(4):236–248.
- [18] J. E. Faust, P. Y. Yang, and H. W. Huang. Action of antimicrobial peptides on bacterial and lipid membranes: A direct comparison. *Biophys. J.* **2017** 112(8):1663–1672.
- [19] R. Rathinakumar and W. C. Wimley. Biomolecular engineering by combinatorial design and high-throughput screening: Small, soluble peptides that permeabilize membranes. *JACS* **2008** 130(30):9849–9858.
- [20] A. J. Krauson, J. He, and W. C. Wimley. Gain-of-function analogues of the pore-forming peptide melittin selected by orthogonal high-throughput screening. *JACS* **2012** 134(30):12732–12741.
- [21] A. J. Krauson, O. M. Hall, T. Fuselier, C. G. Starr, W. B. Kauffman, and W. C. Wimley. Conformational fine-tuning of pore-forming peptide potency and selectivity. *JACS* **2015** 137(51):16144–16152.
- [22] G. Wiedman, S. Y. Kim, E. Zapata-Mercado, W. C. Wimley, and K. Hristova. pH-Triggered, macromolecule-sized poration of lipid bilayers by synthetically evolved peptides. *JACS* **2017** 139(2):937–945.
- [23] S. Li, S. Y. Kim, A. E. Pittman, G. M. King, W. C. Wimley, and K. Hristova. Potent macromolecule-sized poration of lipid bilayers by the macrolittins, a synthetically evolved family of pore-forming peptides. *JACS* **2018** 140(20):6441–6447.

- [24] G. Wiedman, W. C. Wimley, and K. Hristova. Testing the limits of rational design by engineering pH sensitivity into membrane-active peptides. *BBA* **2015** 1848(4):951–957.
- [25] E. Habermann. Bee and wasp venoms. *Science* **1972** 116(4046):314–322.
- [26] H. Vogel, F. Jahnig, V. Hoffmann, and J. Stumpel. The orientation of melittin in lipid membranes. A polarized infrared spectroscopy study. *BBA* **1983** 733(2):201–209.
- [27] H. Vogel. Incorporation of melittin into phosphatidylcholine bilayers. Study of binding and conformational changes. *FEBS Lett.* **1981** 134(1):37–42.
- [28] M. T. Tosteson and D. C. Tosteson. The sting. Melittin forms channels in lipid bilayers. *Biophys. J.* **1981** 36(1):109–116.
- [29] M. S. Sansom. The biophysics of peptide models of ion channels. *Prog. Biophys. Mol. Biol.* **1991** 55(3):139–235.
- [30] M. Zasloff. Magainins, a class of antimicrobial peptides from *Xenopus* skin: isolation, characterization of two active forms, and partial cDNA sequence of a precursor. *PNAS* **1987** 84(15):5449–53.
- [31] J. Y. Lee, A. Boman, C. X. Sun, M. Andersson, H. Jörnvall, V. Mutt, H. G. Boman, H. Jornvall, V. Mutt, and H. G. Boman. Antibacterial peptides from pig intestine: isolation of a mammalian cecropin. *PNAS* **1989** 86(23):9159–9162.
- [32] M.-T. Lee, T.-L. Sun, W.-C. Hung, and H. W. Huang. Process of inducing pores in membranes by melittin. *PNAS* **2013** 110(35):14243–14248.
- [33] G. Kokot, M. Mally, and S. Svetina. The dynamics of melittin-induced membrane permeability. *Eur. Biophys. J.* **2012** 41(5):461–474.
- [34] T. Katsu, C. Ninomiya, M. Kuroko, H. Kobayashi, T. Hirota, and Y. Fujita. Action mechanism of amphipathic peptides gramicidin S and melittin on erythrocyte membrane. *BBA* **1988** 939(1):57–63.
- [35] T. Katsu, M. Kuroko, T. Morikawa, K. Sanchika, Y. Fujita, H. Yamamura, and M. Uda. Mechanism of membrane damage induced by the amphipathic peptides gramicidin S and melittin. *BBA* **1989** 983(2):135–141.
- [36] H. W. Huang. Free energies of molecular bound states in lipid bilayers: Lethal concentrations of antimicrobial peptides. *Biophys. J.* **2009** 96(8):3263–3272.
- [37] G. Beschiashvili and J. Seelig. Melittin binding to mixed phosphatidylglycerol/phosphatidylcholine membranes. *Biochemistry* **2002** 29(1):52–58.
- [38] E. Jamasbi, S. Batinovic, R. A. Sharples, M. A. Sani, R. M. Robins-Browne, J. D. Wade, F. Separovic, and M. A. Hossain. Melittin peptides exhibit different activity on different cells and model membranes. *Amino Acids* **2014** 46(12):2759–2766.

- [39] A. S. Ladokhin and S. H. White. 'Detergent-like' permeabilization of anionic lipid vesicles by melittin. *BBA - Biomembranes* **2001** 1514(2):253–260.
- [40] G. Wiedman, K. Herman, P. Searson, W. C. Wimley, and K. Hristova. The electrical response of bilayers to the bee venom toxin melittin: Evidence for transient bilayer permeabilization. *BBA - Biomembranes* **2013** 1828(5):1357–1364.
- [41] A. S. Ladokhin, M. E. Selsted, and S. H. White. Sizing membrane pores in lipid vesicles by leakage of co-encapsulated markers: Pore formation by melittin. *Biophys. J.* **1997** 72(4):1762–1766.
- [42] A. E. Pittman, B. P. Marsh, and G. M. King. Conformations and dynamic transitions of a melittin derivative that forms macromolecule-sized pores in lipid bilayers. *Langmuir* **2018** 34(28):8393–8399.
- [43] A. Naito, T. Nagao, K. Norisada, T. Mizuno, S. Tuzi, and H. Saito. Conformation and dynamics of melittin bound to magnetically oriented lipid bilayers by solid-state ^{(31)P} and ^{(13)C} NMR spectroscopy. *Biophys. J.* **2000** 78(5):2405–2417.
- [44] K. Matsuzaki, S. Yoneyama, and K. Miyajima. Pore formation and translocation of melittin. *Biophys. J.* **1997** 73(2):831–838.
- [45] H. Vogel and F. Jähnig. The structure of melittin in membranes. *Biophys. J.* **1986** 50(4):573–582.
- [46] L. Yang, T. A. Harroun, T. M. Weiss, L. Ding, and H. W. Huang. Barrel-stave model or toroidal model? A case study on melittin pores. *Biophys. J.* **2001** 81(3):1475–1485.
- [47] S. J. Ludtke, K. He, W. T. Heller, T. A. Harroun, L. Yang, and H. W. Huang. Membrane pores induced by magainin. *Biochemistry* **1996** 35(43):13723–13728.
- [48] J. F. Faucon, J. Dufourcq, and C. Lussan. The self-association of melittin and its binding to lipids - An intrinsic fluorescence polarization study. *FEBS Lett.* **1979** 102(1):187–190.
- [49] M. F. Perutz. X-ray analysis of hemoglobin. *Science* **1963** 140(3569):863–869.
- [50] D. Pan, W. Wang, W. Liu, L. Yang, and H. W. Huang. Chain packing in the inverted hexagonal phase of phospholipids: A study by X-ray anomalous diffraction on bromine-labeled chains. *JACS* **2006** 128(11):3800–3807.
- [51] C. Song, C. Weichbrodt, E. S. Salnikov, M. Dynowski, B. O. Forsberg, B. Bechinger, C. Steinem, B. L. de Groot, U. Zachariae, and K. Zeth. Crystal structure and functional mechanism of a human antimicrobial membrane channel. *PNAS* **2013** 110(12):4586–4591.

- [52] W. C. Wimley. How does melittin permeabilize membranes? *Biophys. J.* **2018** 114(2):251–253.
- [53] A. S. Ladokhin, W. C. Wimley, and S. H. White. Leakage of membrane vesicle contents: determination of mechanism using fluorescence quenching. *Biophys. J.* **1995** 69(5):1964–1971.
- [54] M.-T. Lee, W.-C. Hung, F.-Y. Chen, and H. W. Huang. Mechanism and kinetics of pore formation in membranes by water-soluble amphipathic peptides. *PNAS* **2008** 105(13):5087–5092.
- [55] H. W. Huang. Action of antimicrobial peptides: Two-state model. *Biochemistry* **2000** 39(29):8347–8352.
- [56] M. Mally, J. Majhenc, S. Svetina, and B. Zeks. Mechanisms of equinatoxin II-induced transport through the membrane of a giant phospholipid vesicle. *Biophys. J.* **2002** 83(2):944–953.
- [57] M. Mally, J. Majhenc, S. Svetina, and B. Žekš. The response of giant phospholipid vesicles to pore-forming peptide melittin. *Biochimica et Biophysica Acta (BBA) - Biomembranes* **2007** 1768(5):1179–1189.
- [58] W. C. Wimley, T. P. Creamer, and S. H. White. Solvation energies of amino acid side chains and backbone in a family of host-guest pentapeptides. *Biochemistry* **1996** 35(16):5109–5124.
- [59] T. Hessa, H. Kim, K. Bihlmaier, C. Lundin, J. Boekel, H. Andersson, I. Nilsson, S. H. White, and G. von Heijne. Recognition of transmembrane helices by the endoplasmic reticulum translocon. *Nature* **2005** 433(7024):377–381.
- [60] C. P. Moon and K. G. Fleming. Side-chain hydrophobicity scale derived from transmembrane protein folding into lipid bilayers. *PNAS* **2011** 108(25):10174–10177.
- [61] J. M. Leveritt, A. Pino-Angeles, and T. Lazaridis. The structure of a melittin-stabilized pore. *Biophys. J.* **2015** 108(10):2424–2426.
- [62] A. Pino-Angeles and T. Lazaridis. Effects of peptide charge, orientation, and concentration on melittin transmembrane pores. *Biophys. J.* **2018** 114(12):2865–2874.
- [63] S. J. Irudayam, T. Pobandt, and M. L. Berkowitz. Free energy barrier for melittin reorientation from a membrane-bound state to a transmembrane state. *J.Phys. Chem. B* **2013** 117(43):13457–13463.
- [64] D. Sun, J. Forsman, and C. E. Woodward. Multistep molecular dynamics simulations identify the highly cooperative activity of melittin in recognizing and stabilizing membrane pores. *Langmuir* **2015** 31(34):9388–9401.

- [65] D. Sun, J. Forsman, and C. E. Woodward. Molecular simulations of melittin-induced membrane pores. *J. Phys. Chem. B* **2017** 121(44):10209–10214.
- [66] A. C. Rapson, M. A. Hossain, J. D. Wade, E. C. Nice, T. A. Smith, A. H. Clayton, and M. L. Gee. Structural dynamics of a lytic peptide interacting with a supported lipid bilayer. *Biophys. J.* **2011** 100(5):1353–1361.
- [67] Z. Ningsih, M. A. Hossain, J. D. Wade, A. H. Clayton, and M. L. Gee. Slow insertion kinetics during interaction of a model antimicrobial peptide with unilamellar phospholipid vesicles. *Langmuir* **2012** 28(4):2217–2224.
- [68] M. G. Burton, Q. M. Huang, M. A. Hossain, J. D. Wade, A. H. Clayton, and M. L. Gee. Long-time-scale interaction dynamics between a model antimicrobial peptide and giant unilamellar vesicles. *Langmuir* **2013** 29(47):14613–14621.
- [69] M. G. Burton, Q. M. Huang, M. A. Hossain, J. D. Wade, E. A. Palombo, M. L. Gee, and A. H. Clayton. Direct measurement of pore dynamics and leakage induced by a model antimicrobial peptide in single vesicles and cells. *Langmuir* **2016** 32(25):6496–6505.
- [70] J. He, A. J. Krauson, and W. C. Wimley. Toward the de novo design of antimicrobial peptides: Lack of correlation between peptide permeabilization of lipid vesicles and antimicrobial, cytolytic, or cytotoxic activity in living cells. *Peptide Science* **2014** 102(1):1–6.
- [71] S. Rex. A Pro→Ala substitution in melittin affects self-association, membrane binding and pore-formation kinetics due to changes in structural and electrostatic properties. *Biophys. Chem.* **2000** 85(2):209–228.
- [72] E. Jamasbi, G. D. Ciccotosto, J. Tailhades, R. M. Robins-Browne, C. L. Ugalde, R. A. Sharples, N. Patil, J. D. Wade, M. A. Hossain, and F. Separovic. Site of fluorescent label modifies interaction of melittin with live cells and model membranes. *BBA* **2015** 1848(10):2031–2039.
- [73] J. P. Dawson, J. S. Weinger, and D. M. Engelman. Motifs of serine and threonine can drive association of transmembrane helices. *J. Mol. Biol.* **2002** 316(3):799–805.
- [74] L. Zhou, G. Narsimhan, X. Wu, and F. Du. Pore formation in 1,2-dimyristoyl-sn-glycero-3-phosphocholine/cholesterol mixed bilayers by low concentrations of antimicrobial peptide melittin. *Colloids Surf., B* **2014** 123:419–428.
- [75] W. F. DeGrado, G. F. Musso, M. Lieber, E. T. Kaiser, and F. J. Kézdy. Kinetics and mechanism of hemolysis induced by melittin and by a synthetic melittin analogue. *Biophys. J.* **1982** 37(1):329–338.
- [76] G. Schwarz, R.-t. Zong, and T. Popescu. Kinetics of melittin induced pore formation in the membrane of lipid vesicles. *BBA - Biomembranes* **1992** 1110(1):97–104.

- [77] J. Henin, A. Pohorille, and C. Chipot. Insights into the recognition and association of transmembrane α -helices. The free energy of α -helix dimerization in glycophorin A. *JACS* **2005** 127(23):8478–8484.
- [78] D. E. Shaw, C. H. Fenton, A. Forte, J. Gagliardo, G. Gill, B. Greskamp, C. R. Ho, D. J. Ierardi, L. Iserovich, J. S. Kuskin, R. H. Larson, J. P. Grossman, T. Layman, L.-S. Lee, A. K. Lerer, C. Li, D. Killebrew, K. M. Mackenzie, S. Y.-H. Mok, M. A. Moraes, R. Mueller, L. J. Nociolo, J. A. Bank, J. L. Peticolas, T. Quan, D. Ramot, J. K. Salmon, D. P. Scarpazza, U. B. Schafer, N. Siddique, C. W. Snyder, J. Spengler, P. T. P. Tang, B. Batson, M. Theobald, H. Toma, B. Towles, B. Vitale, S. C. Wang, C. Young, J. A. Butts, J. C. Chao, M. M. Deneroff, R. O. Dror, and A. Even. Anton 2: raising the bar for performance and programmability in a special-purpose molecular dynamics supercomputer. *IEEE* **2014**, 41–53.
- [79] T. Mori, N. Miyashita, W. Im, M. Feig, and Y. Sugita. Molecular dynamics simulations of biological membranes and membrane proteins using enhanced conformational sampling algorithms. *BBA - Biomembranes* **2016** 1858(7, Part B):1635–1651.
- [80] S. Katira, K. K. Mandadapu, S. Vaikuntanathan, B. Smit, and D. Chandler. Pre-transition effects mediate forces of assembly between transmembrane proteins. *eLife* **2016** 5:1–8.
- [81] J. Warwicker and H. C. Watson. Calculation of the electric potential in the active site cleft due to alpha-helix dipoles. *J. Mol. Biol.* **1982** 157(4):671–679.
- [82] M. Born. Volumen und Hydratationswärme der Ionen. *Z. Angew. Phys.* **1920** 1:45–48.
- [83] W. Clark Still, A. Tempczyk, R. C. Hawley, and T. Hendrickson. Semianalytical treatment of solvation for molecular mechanics and dynamics. *JACS* **1990** 112(16):6127–6129.
- [84] S. Tanizaki and M. Feig. A generalized Born formalism for heterogeneous dielectric environments: Application to the implicit modeling of biological membranes. *J. Chem. Phys.* **2005** 122(12):124706.
- [85] T. Lazaridis and M. Karplus. Effective energy functions for protein structure prediction. *Curr. Opin. Struct. Biol.* **2000** 10(2):139–45.
- [86] T. Lazaridis. Effective energy function for proteins in lipid membranes. *Proteins: Structure, Function and Genetics* **2003** 52(2):176–192.
- [87] a. Siewert J. Marrink, A. H. de Vries, , and A. E. Mark. Coarse grained model for semiquantitative lipid simulations. *J. Phys. Chem. B* **2003** 108(2):750–760.
- [88] a. Siewert J. Marrink, †. H. Jelger Risselada, ‡. Serge Yefimov, §. D. Peter Tieleman, , and A. H. de Vries†. The MARTINI force field: Coarse grained model for biomolecular simulations. *J. Phys. Chem. B* **2007** 111(27):7812–7824.

- [89] G. M. Torrie and J. P. Valleau. Nonphysical sampling distributions in Monte Carlo free energy estimation: Umbrella sampling. *J. Comput. Phys.* **1977** 23(2):187–199.
- [90] G. M. Torrie and J. P. Valleau. Monte carlo free energy estimates using non-boltzmann sampling: Application to the sub-critical lennard-jones fluid. *Chem. Phys. Lett.* **1974** 28(4):578–581.
- [91] J. G. Kirkwood. Statistical mechanics of fluid mixtures. *J. Chem. Phys.* **1935** 3(5):300–313.
- [92] B. Roux. The calculation of the potential of mean force using computer simulations. *Comput. Phys. Commun.* **1995** 91(1):275–282.
- [93] S. Kumar, J. M. Rosenberg, D. Bouzida, R. H. Swendsen, and P. A. Kollman. The weighted histogram analysis method for free energy calculations on biomolecules. i. the method. *J. Comput. Chem.* **1992** 13(8):1011–1021.
- [94] C. H. Chen, C. G. Starr, E. Troendle, G. Wiedman, W. C. Wimley, J. P. Ulmschneider, and M. B. Ulmschneider. Simulation-guided rational de Novo design of a small pore-forming antimicrobial peptide. *JACS* **2019** 141(12):4839–4848.
- [95] S. Y. Kim, A. E. Pittman, E. Zapata-Mercado, G. M. King, W. C. Wimley, and K. Hristova. Mechanism of action of peptides that cause the pH-triggered macromolecular poration of lipid bilayers. *JACS* **2019** 141(16):6706–6718.
- [96] W. F. Bennett, C. K. Hong, Y. Wang, and D. P. Tieleman. Antimicrobial peptide simulations and the influence of force field on the free energy for pore formation in lipid bilayers. *J. Chem. Theory Comput.* **2016** 12(9):4524–4533.
- [97] J. P. Ulmschneider and M. B. Ulmschneider. Molecular dynamics simulations are redefining our view of peptides interacting with biological membranes. *Acc. Chem. Res.* **2018** 51(5):1106–1116.
- [98] G. Schwarz and G. Beschiaschvili. Kinetics of melittin self-association in aqueous solution. *Biochemistry* **1988** 27(20):7826–7831.
- [99] S. Georgiou, M. Thompson, and A. Mukhopadhyay. Nature of melittin-phospholipid interaction. *Biophys. J.* **1982** 37(1):159–161.
- [100] J. C. Talbot, J. Dufourcq, J. de Bony, J. F. Faucon, and C. Lussan. Conformational change and self association of monomeric melittin. *FEBS Lett.* **1979** 102(1):191–193.
- [101] T. C. Terwilliger, L. Weissman, and D. Eisenberg. The structure of melittin in the form I crystals and its implication for melittin’s lytic and surface activities. *Biophys. J.* **1982** 37(1):353–361.

- [102] C. Altenbach and W. L. Hubbell. The aggregation state of spin-labeled melittin in solution and bound to phospholipid membranes: Evidence that membrane-bound melittin is monomeric. *Proteins* **1988** 3(4):230–42.
- [103] C. Mollay and G. Kreil. Fluorometric measurements on the interaction of melittin with lecithin. *BBA* **1973** 316(2):196–203.
- [104] J. Dufourcq and J. F. Faucon. Intrinsic fluorescence study of lipid-protein interactions in membrane models. Binding of melittin, an amphipathic peptide, to phospholipid vesicles. *BBA - Biomembranes* **1977** 467(1):1–11.
- [105] J. C. Talbot, J. Lalanne, J. F. Faucon, and J. Dufourcq. Effect of the state of association of melittin and phospholipids on their reciprocal binding. *BBA - Biomembranes* **1982** 689(1):106–112.
- [106] S. Frey and L. K. Tamm. Orientation of melittin in phospholipid bilayers. A polarized attenuated total reflection infrared study. *Biophys. J.* **1991** 60(4):922–930.
- [107] M. J. Citra and P. H. Axelsen. Determination of molecular order in supported lipid membranes by internal reflection Fourier transform infrared spectroscopy. *Biophys. J.* **1996** 71(4):1796–1805.
- [108] M. Gordon-Grossman, Y. Gofman, H. Zimmermann, V. Frydman, Y. Shai, N. Ben-Tal, and D. Goldfarb. A combined pulse EPR and monte carlo simulation study provides molecular insight on peptide-membrane interactions. *J. Phys. Chem. B* **2009** 113(38):12687–12695.
- [109] N. Manukovsky, V. Frydman, and D. Goldfarb. Gd³⁺ spin labels report the conformation and solvent accessibility of solution and vesicle-bound melittin. *J. Phys. Chem. B* **2015** 119(43):13732–13741.
- [110] A. Therrien, A. Fournier, and M. Lafleur. Role of the cationic C-terminal segment of melittin on membrane fragmentation. *J. Phys. Chem. B* **2016** 120(17):3993–4002.
- [111] A. S. Ladokhin and S. H. White. Folding of amphipathic alpha-helices on membranes: Energetics of helix formation by melittin. *J. Mol. Biol.* **1999** 285(4):1363–1369.
- [112] C. Altenbach, W. Froncisz, J. S. Hyde, and W. L. Hubbell. Conformation of spin-labeled melittin at membrane surfaces investigated by pulse saturation recovery and continuous wave power saturation electron paramagnetic resonance. *Biophys. J.* **1989** 56(6):1183–1191.
- [113] T. Benachir and M. Lafleur. Study of vesicle leakage induced by melittin. *BBA - Biomembranes* **1995** 1235(2):452–460.
- [114] S. Rex and G. Schwarz. Quantitative studies on the melittin-induced leakage mechanism of lipid vesicles. *Biochemistry* **1998** 37(8):2336–2345.

- [115] S. Georghiou, M. Thompson, and A. Mukhopadhyay. Melittin-phospholipid interaction studied by employing the single tryptophan residue as an intrinsic fluorescent probe. *BBA* **1982** 688:441–452.
- [116] S. Georghiou, M. Thompson, and A. K. Mukhopadhyay. Melittin-phospholipid interaction: Evidence for melittin aggregation. *BBA - Biomembranes* **1981** 642(2):429–432.
- [117] M. R. Eftink and C. A. Ghiron. Exposure of tryptophanyl residues in proteins. Quantitative determination by fluorescence quenching studies. *Biochemistry* **1976** 15(3):672–680.
- [118] M. R. Eftink and C. A. Ghiron. Fluorescence quenching of indole and model micelle systems. *J. Phys. Chem.* **1976** 80(5):486–493.
- [119] M. R. Eftink and C. A. Ghiron. Fluorescence quenching studies with proteins. *Anal. Biochem.* **1981** 114(2):199–227.
- [120] J. T. Vivian and P. R. Callis. Mechanisms of tryptophan fluorescence shifts in proteins. *Biophys. J.* **2001** 80(5):2093–2109.
- [121] E. John and F. Jähnig. Dynamics of melittin in water and membranes as determined by fluorescence anisotropy decay. *Biophys. J.* **1988** 54(5):817–827.
- [122] J. C. Talbot, J. F. Faucon, and J. Dufourcq. Different states of self-association of melittin in phospholipid bilayers - A resonance energy transfer approach. *Eur. Biophys. J.* **1987** 15(3):147–157.
- [123] A. Hermetter and J. R. Lakowicz. The aggregation state of mellitin in lipid bilayers. An energy transfer study. *J. Biol. Chem.* **1986** 261(18):8243–8248.
- [124] G. Schwarz and G. Beschiaschvifi. Thermodynamic and kinetic studies on the association of melittin with a phospholipid bilayer. *BBA* **1989** 979:82–90.
- [125] E. John and F. Jähnig. Aggregation state of melittin in lipid vesicle membranes. *Biophys. J.* **1991** 60(2):319–328.
- [126] E. Pérez-Payá, J. Dufourcq, L. Braco, and C. Abad. Structural characterisation of the natural membrane-bound state of melittin: A fluorescence study of a dansylated analogue. *BBA* **1997** 1329(2):223–236.
- [127] C. Altenbach and W. L. Hubbell. The aggregation state of spin-labeled melittin in solution and bound to phospholipid membranes: evidence that membrane-bound melittin is monomeric. *Proteins* **1988** 3(4):230–242.
- [128] M. Gordon-Grossman, H. Zimmermann, S. G. Wolf, Y. Shai, and D. Goldfarb. Investigation of model membrane disruption mechanism by melittin using pulse electron paramagnetic resonance spectroscopy and cryogenic transmission electron microscopy. *J. Phys. Chem. B* **2012** 116(1):179–188.

- [129] Y. Polyhach, A. Godt, C. Bauer, and G. Jeschke. Spin pair geometry revealed by high-field DEER in the presence of conformational distributions. *J. Magn. Reson.* **2007** 185(1):118–129.
- [130] I. Tkach, S. Pornsuwan, C. Höbartner, F. Wachowius, S. T. Sigurdsson, T. Y. Baranova, U. Diederichsen, G. Sicoli, and M. Bennati. Orientation selection in distance measurements between nitroxide spin labels at 94 GHz EPR with variable dual frequency irradiation. *PCCP* **2013** 15(10):3433–3437.
- [131] C. E. Dempsey. The actions of melittin on membranes. *BBA* **1990** 1031(2):143–161.
- [132] G. Schwarz and C. H. Robert. Pore formation kinetics in membranes, determined from the release of marker molecules out of liposomes or cells. *Biophys. Chem.* **1990** 58(3):577–583.
- [133] J. Takei, A. Reményi, A. R. Clarke, and C. E. Dempsey. Self-association of disulfide-dimerized melittin analogues. *Biochemistry* **1998** 37(16):5699–5708.
- [134] G. Schwarz and C. H. Robert. Kinetics of pore-mediated release of marker molecules from liposomes or cells. *Biophys. Chem.* **1992** 42(3):291–296.
- [135] G. Schwarz and A. Arbuzova. Pore kinetics reflected in the dequenching of a lipid vesicle entrapped fluorescent dye. *BBA - Biomembranes* **1995** 1239(1):51–57.
- [136] E. Karatekin, O. Sandre, H. Guitouni, N. Borghi, P.-H. Puech, and F. Brochard-Wyart. Cascades of transient pores in giant vesicles: Line tension and transport. *Biophys. J.* **2003** 84(3):1734–1749.
- [137] M. Manna and C. Mukhopadhyay. Cause and effect of melittin-induced pore formation: A computational approach. *Langmuir* **2009** 25(20):12235–12242.
- [138] G. A. Olah and H. W. Huang. Circular dichroism of oriented α helices. I. Proof of the exciton theory. *J. Chem. Phys.* **1988** 89(4):2531–2538.
- [139] Y. Wu, H. W. Huang, and G. A. Olah. Method of oriented circular dichroism. *Biophys. J.* **1990** 57(4):797–806.
- [140] F. Y. Chen, M. T. Lee, and H. W. Huang. Evidence for membrane thinning effect as the mechanism for peptide-induced pore formation. *Biophys. J.* **2003** 84(6):3751–3758.
- [141] H. W. Huang. Elasticity of Lipid Bilayer Interacting with Amphiphilic Helical Peptides. *Journal de Physique II* **1995** 5(10):1427–1431.
- [142] M. T. Lee, F. Y. Chen, and H. W. Huang. Energetics of Pore Formation Induced by Membrane Active Peptides. *Biochemistry* **2004** 43(12):3590–3599.

- [143] F. Brochard-Wyart, P. G. de Gennes, and O. Sandre. Transient pores in stretched vesicles: role of leak-out. *Physica A* **2000** 278(1):32–51.
- [144] E. Evans, V. Heinrich, F. Ludwig, and W. Rawicz. Dynamic Tension Spectroscopy and Strength of Biomembranes. *Biophys. J.* **2003** 85(4):2342–2350.
- [145] P.-H. Puech, N. Borghi, E. Karatekin, and F. Brochard-Wyart. Line Thermodynamics: Adsorption at a Membrane Edge. *Phys. Rev. Lett.* **2003** 90(12):128304.
- [146] †. Marjorie L. Longo, §. Alan J. Waring, §. Larry M. Gordon, , and ‡. Daniel A. Hammer*. Area expansion and permeation of phospholipid membrane bilayers by influenza fusion peptides and melittin. *Langmuir* **1998** 14(9):2385–2395.
- [147] W. Rawicz, K. C. Olbrich, T. McIntosh, D. Needham, and E. Evans. Effect of chain length and unsaturation on elasticity of lipid bilayers. *Biophys. J.* **2000** 79(1):328–339.
- [148] R. Kwok and E. Evans. Thermoelasticity of large lecithin bilayer vesicles. *Biophys. J.* **1981** 35(3):637–652.
- [149] F. Y. Chen, M. T. Lee, and H. W. Huang. Sigmoidal concentration dependence of antimicrobial peptide activities: A case study on alamethicin. *Biophys. J.* **2002** 82(2):908–914.
- [150] E. Fattal, R. A. Parente, F. C. Szoka, and S. Nir. Pore-forming peptides induce rapid phospholipid flip-flop in membranes. *Biochemistry* **1994** 33(21):6721–6731.
- [151] B. R. Brooks, R. E. Bruccoleri, B. D. Olafson, D. J. States, S. Swaminathan, and M. Karplus. CHARMM: A program for macromolecular energy, minimization, and dynamics calculations. *J. Comp. Chem.* **1983** 4(2):187–217.
- [152] Brooks BR, 3rd, Brooks CL, Jr, MacKerell AD, L, Nilsson, RJ, Petrella, B, Roux, Y, Won, G, Archontis, C, Bartels, S, Boresch, A, Caflisch, L, Caves, Q, Cui, AR, Dinner, M, Feig, S, Fischer, J, Gao, M, Hodoscek, W, Im, K, Kuczera, T, Lazaridis, J, Ma, V, Ovchinnikov, E, Paci, RW, Pastor, CB, Post, JZ, Pu, M, Schaefer, B, Tidor, RM, Venable, HL, Woodcock, X, Wu, W, Yang, DM, York, and M., Karplus. CHARMM: The biomolecular simulation program. *J. Comp. Chem.* **2009** 30(16):1545–1614.
- [153] P. J. Steinbach and B. R. Brooks. New spherical-cutoff methods for long-range forces in macromolecular simulation. *J. Comput. Chem.* **1994** 15(7):667–683.
- [154] J. P. Ryckaert, G. Ciccotti, and H. J. C. Berendsen. Numerical integration of the cartesian equations of motion of a system with constraints: molecular dynamics of n-alkanes. *J. Comput. Phys.* **1977** 23(3):327–341.
- [155] J. Zhang and T. Lazaridis. Calculating the free energy of association of transmembrane helices. *Biophys. J.* **2006** 91(5):1710–1723.

- [156] D. Qiu, P. S. Shenkin, F. P. Hollinger, , and W. C. Still*. The GB/SA continuum model for solvation. A fast analytical method for the calculation of approximate Born radii. *J. Phys. Chem. A* **1997** 101(16):3005–3014.
- [157] M. S. Lee, F. R. Salsbury, and C. L. Brooks. Novel generalized Born methods. *J. Chem. Phys.* **2002** 116(24):10606–10614.
- [158] M. S. Lee, M. Feig, F. R. Salsbury, and C. L. Brooks. New analytic approximation to the standard molecular volume definition and its application to generalized born calculations. *J. Comput. Chem.* **2003** 24(11):1348–1356.
- [159] D. Bashford and D. A. Case. Generalized born models of macromolecular solvation effects. *Annu. Rev. Phys. Chem.* **2000** 51:129–152.
- [160] M. Scarsi, J. Apostolakis, and A. Caflisch. Continuum electrostatic energies of macromolecules in aqueous solutions. *J. Phys. Chem. A* **1997** 101(43):8098–8106.
- [161] B. Dutagaci, M. Sayadi, and M. Feig. Heterogeneous dielectric generalized Born model with a van der Waals term provides improved association energetics of membrane-embedded transmembrane helices. *J. Comput. Chem.* **2017** 38(16):1308–1320.
- [162] J. B. Klauda, R. M. Venable, J. A. Freites, J. W. O'Connor, D. J. Tobias, C. Mondragon-Ramirez, I. Vorobyov, A. D. MacKerell, and R. W. Pastor. Update of the CHARMM all-atom additive force field for lipids: validation on six lipid types. *J. Phys. Chem. B* **2010** 114(23):7830–7843.
- [163] W. L. Jorgensen, J. Chandrasekhar, J. D. Madura, R. W. Impey, and M. L. Klein. Comparison of simple potential functions for simulating liquid water. *J. Chem. Phys.* **1983** 79(2):926–935.
- [164] T. B. Woolf and B. Roux. Molecular dynamics simulation of the gramicidin channel in a phospholipid bilayer. *PNAS* **1994** 91(24):11631–11635.
- [165] T. B. Woolf and B. Roux. Structure, energetics, and dynamics of lipid-protein interactions: A molecular dynamics study of the gramicidin A channel in a DMPC bilayer. *Proteins: Structure, Function and Genetics* **1996** 24(1):92–114.
- [166] S. Jo, T. Kim, and W. Im. Automated builder and database of protein/membrane complexes for molecular dynamics simulations. *PLoS ONE* **2007** 2(9):e880.
- [167] S. Jo, T. Kim, V. G. Iyer, and W. Im. CHARMM-GUI: a web-based graphical user interface for CHARMM. *J. Comput. Chem.* **2008** 29(11):1859–1865.
- [168] S. Jo, J. B. Lim, J. B. Klauda, and W. Im. CHARMM-GUI membrane builder for mixed bilayers and its application to yeast membranes. *Biophys. J.* **2009** 97(1):50–58.

- [169] E. L. Wu, X. Cheng, S. Jo, H. Rui, K. C. Song, E. M. Dávila-Contreras, Y. Qi, J. Lee, V. Monje-Galvan, R. M. Venable, J. B. Klauda, and W. Im. CHARMM-GUI membrane builder toward realistic biological membrane simulations. *J. Comput. Chem.* **2014** 35(27):1997–2004.
- [170] J. Lee, X. Cheng, J. M. Swails, M. S. Yeom, P. K. Eastman, J. A. Lemkul, S. Wei, J. Buckner, J. C. Jeong, Y. Qi, S. Jo, V. S. Pande, D. A. Case, I. Charles L. Brooks, A. D. MacKerell, Jr., J. B. Klauda, and W. Im. CHARMM-GUI input generator for NAMD, GROMACS, AMBER, OpenMM, and CHARMM/OpenMM simulations using the CHARMM36 additive force field. *J. Chem. Theory Comput.* **2015** 12(1):405–413.
- [171] H. J. C. Berendsen, D. van der Spoel, and R. van Drunen. GROMACS: A message-passing parallel molecular dynamics implementation. *Computer Physics Communications* **1995** 91(1-3):43–56.
- [172] E. Lindahl, B. Hess, and D. van der Spoel. GROMACS 3.0: A package for molecular simulation and trajectory analysis. *J. Mol. Model.* **2001** 7:306–317.
- [173] D. Van Der Spoel, E. Lindahl, B. Hess, G. Groenhof, A. E. Mark, and H. J. C. Berendsen. GROMACS: Fast, flexible, and free. *J. Comput. Chem.* **2005** 26(16):1701–1718.
- [174] B. Hess, C. Kutzner, D. Van Der Spoel, and E. Lindahl. GRGMACS 4: Algorithms for highly efficient, load-balanced, and scalable molecular simulation. *J. Chem. Theory Comput.* **2008** 4(3):435–447.
- [175] S. Pronk, S. Pál, R. Schulz, P. Larsson, P. Bjelkmar, R. Apostolov, M. R. Shirts, J. C. Smith, P. M. Kasson, D. Van Der Spoel, B. Hess, and E. Lindahl. GROMACS 4.5: A high-throughput and highly parallel open source molecular simulation toolkit. *Bioinformatics* **2013** 29(7):845–854.
- [176] K. Vanommeslaeghe, E. Hatcher, C. Acharya, S. Kundu, S. Zhong, J. Shim, E. Darian, O. Guvench, P. Lopes, I. Vorobyov, and A. D. Mackerell. CHARMM general force field: A force field for drug-like molecules compatible with the CHARMM all-atom additive biological force fields. *J. Comput. Chem.* **2010** 31(4):671–690.
- [177] R. B. Best, X. Zhu, J. Shim, P. E. M. Lopes, J. Mittal, M. Feig, and A. D. MacKerell. Optimization of the additive CHARMM all-atom protein force field targeting improved sampling of the backbone ϕ , ψ and side-chain χ and χ dihedral angles. *J. Chem. Theory Comput.* **2012** 8(9):3257–3273.
- [178] A. D. MacKerell, M. Feig, and C. L. Brooks. Extending the treatment of backbone energetics in protein force fields: Limitations of gas-phase quantum mechanics in reproducing protein conformational distributions in molecular dynamics simulation. *J. Comp. Chem.* **2004** 25(11):1400–1415.

- [179] S. R. Durell, B. R. Brooks, and A. Ben-Naim. Solvent-induced forces between two hydrophilic groups. *J. Phys. Chem.* **1994** 98(8):2198–2202.
- [180] E. Neria, S. Fischer, and M. Karplus. Simulation of activation free energies in molecular systems. *J. Chem. Phys.* **1996** 105(5):1902–1921.
- [181] D. Tieleman. Lipid properties and the orientation of aromatic residues in OmpF, influenza M2, and alamethicin systems: Molecular dynamics simulations. *Biochemistry* **1998** 37(50):17554–17561.
- [182] G. Bussi, D. Donadio, and M. Parrinello. Canonical sampling through velocity rescaling. *J. Chem. Phys.* **2007** 126(1):014101.
- [183] M. Parrinello and A. Rahman. Polymorphic transitions in single crystals: A new molecular dynamics method. *J. Appl. Phys.* **1981** 52(12):7182–7190.
- [184] B. P. Maliwal, A. Hermetter, and J. R. Lakowicz. A study of protein dynamics from anisotropy decays obtained by variable frequency phase-modulation fluorometry: internal motions of N-methylanthraniloyl melittin. *BBA* **1986** 873(2):173–181.
- [185] T. Darden, D. York, and L. Pedersen. Particle mesh Ewald: An N-log(N) method for Ewald sums in large systems. *J. Chem. Phys.* **1993** 98(12):10089.
- [186] U. Essmann, L. Perera, M. L. Berkowitz, T. Darden, H. Lee, and L. G. Pedersen. A smooth particle mesh Ewald method. *J. Chem. Phys.* **1995** 103(1995):8577–8593.
- [187] B. Hess, H. Bekker, H. J. C. Berendsen, and J. G. E. M. Fraaije. LINCS: A linear constraint solver for molecular simulations. *J. Comput. Chem.* **1997** 18(12):1463–1472.
- [188] M. Souaille and B. Roux. Extension to the weighted histogram analysis method: combining umbrella sampling with free energy calculations. *Comput. Phys. Commun.* **2001** 135(1):40–57.
- [189] S. J. Marrink, O. Berger, P. Tieleman, and F. Jähnig. Adhesion forces of lipids in a phospholipid membrane studied by molecular dynamics simulations. *Biophys. J.* **1998** 74(2):931–943.
- [190] J. S. Hub, B. L. De Groot, and D. Van Der Spoel. g_wham-A free Weighted Histogram Analysis implementation including robust error and autocorrelation estimates. *J. Chem. Theory Comput.* **2010** 6(12):3713–3720.
- [191] A. Grossfield. WHAM: the weighted histogram analysis method. *version 2.0.9* <http://membrane.urmc.rochester.edu/content/wham>.
- [192] S. Boresch and M. Karplus. The Jacobian factor in free energy simulations. *J. Chem. Phys.* **1996** 105(12):5145–5154.

- [193] R. M. Neumann. Entropic approach to Brownian movement. *Am. J. Phys.* **1998** 48(5):354.
- [194] W. Im, J. Lee, T. Kim, and H. Rui. Novel free energy calculations to explore mechanisms and energetics of membrane protein structure and function. *J. Comput. Chem.* **2009** 30(11):1622–1633.
- [195] G. J. Rocklin, D. L. Mobley, K. A. Dill, and P. H. Hünenberger. Calculating the binding free energies of charged species based on explicit-solvent simulations employing lattice-sum methods: An accurate correction scheme for electrostatic finite-size effects. *J. Chem. Phys.* **2013** 139(18):184103–32.
- [196] A. MacKerell, D. Bashford, M. Bellott, R. Dunbrack, J. Evanseck, M. Field, S. Fischer, J. Gao, H. Guo, S. Ha, D. Joseph-Mccarthy, L. Kuchnir, K. Kuczera, F. Lau, C. Mattos, S. Michnick, T. Ngo, D. Nguyen, B. Prodhom, W. Reiher, B. Roux, M. Schlenkrich, J. Smith, R. Stote, J. Straub, M. Watanabe, J. Wiorkiewicz-Kuczera, D. Yin, and M. Karplus. All-atom empirical potential for molecular modeling and dynamics studies of proteins. *J. Phys. Chem. B* **1998** 102(18):3586–3616.
- [197] A. D. MacKerell, Jr., M. Feig, and C. L. Brooks. Improved treatment of the protein backbone in empirical force fields. *JACS* **2003** 126(3):698–699.
- [198] D. Beglov and B. Roux. Finite representation of an infinite bulk system: Solvent boundary potential for computer simulations. *J. Chem. Phys.* **1994** 100(12):9050–9063.
- [199] B. Lee and F. M. Richards. The interpretation of protein structures: Estimation of static accessibility. *J. Mol. Biol.* **1971** 55(3):379–400.
- [200] P. H. Hünenberger and J. A. McCammon. Ewald artifacts in computer simulations of ionic solvation and ion–ion interaction: A continuum electrostatics study. *J. Chem. Phys.* **1999** 110(4):1856–1872.
- [201] I. Klapper, R. Hagstrom, R. Fine, K. Sharp, and B. Honig. Focusing of electric fields in the active site of Cu-Zn superoxide dismutase: Effects of ionic strength and amino-acid modification. *Proteins Struct. Funct. Bioinf.* **1986** 1(1):47–59.
- [202] A. Nicholls and B. Honig. A rapid finite difference algorithm, utilizing successive over-relaxation to solve the Poisson–Boltzmann equation. *J. Comput. Chem.* **1991** 12(4):435–445.
- [203] A. Pino-Angeles, J. M. L. Iii, and T. Lazaridis. Pore structure and synergy in antimicrobial peptides of the magainin family. *PLoS Comput. Biol.* **2016** 12(1):e1004570.
- [204] J. Huang and A. D. MacKerell. Charmm36 all-atom additive protein force field: Validation based on comparison to nmr data. *J. Comput. Chem.* **2013** 34(25):2135–2145.

- [205] R. A. Lippert, C. Predescu, D. J. Ierardi, K. M. Mackenzie, M. P. Eastwood, R. O. Dror, and D. E. Shaw. Accurate and efficient integration for molecular dynamics simulations at constant temperature and pressure. *J. Chem. Phys.* **2013** 139(16):164106.
- [206] W. G. Hoover. Canonical dynamics: Equilibrium phase-space distributions. *Phys. Rev. A* **1985** 31(3):1695–1697.
- [207] G. J. Martyna, D. J. Tobias, and M. L. Klein. Constant pressure molecular dynamics algorithms. *J. Chem. Phys.* **1994** 101(5):4177–4189.
- [208] Y. Shan, J. L. Klepeis, M. P. Eastwood, R. O. Dror, and D. E. Shaw. Gaussian split Ewald: A fast Ewald mesh method for molecular simulation. *J. Chem. Phys.* **2005** 122(5):54101.
- [209] C. Chothia, M. Levitt, and D. Richardson. Helix to helix packing in proteins. *J. Mol. Biol.* **1981** 145(1):215–250.
- [210] W. J. Allen, J. A. Lemkul, and D. R. Bevan. GridMAT-MD: a grid-based membrane analysis tool for use with molecular dynamics. *J. Comput. Chem.* **2009** 30(12):1952–1958.
- [211] H. De Loof, L. Nilsson, and R. Rigler. Molecular-dynamics simulation of galanin in aqueous and nonaqueous solution. *JACS* **1992** 114(11):4028–4035.
- [212] J. Aqvist, W. F. van Gunsteren, M. Lijonmarck, and O. Tapia. A molecular dynamics study of the c-terminal fragment of the l7/l12 ribosomal protein. secondary structure motion in a 150 picosecond trajectory. *J. Molec. Biol.* **1985** 183(3):461–477.
- [213] R Core Team. *R: A Language and Environment for Statistical Computing*. R Foundation for Statistical Computing, Vienna, Austria, **2013**.
- [214] J. L. Rodgers and W. A. Nicewander. Thirteen ways to look at the correlation coefficient. *American Statistician* **1988** 42(1):59–66.
- [215] J. A. Hanson and H. Yang. A general statistical test for correlations in a finite-length time series. *J. Chem. Phys.* **2008** 128(21):214101.
- [216] J. P. Royston. Algorithm AS 181: The W test for normality. *Journal of the Royal Statistical Society. Series C (Applied Statistics)* **1982** 31(2):176–180.
- [217] T. Hothorn, A. Zeileis, R. W. Farebrother, C. Cummins, G. Millo, and D. Mitchell. *lmtest: Testing Linear Regression Models*, **2019**. R package version 0.9-37.
- [218] R. D. Cook and S. Weisberg. Diagnostics for heteroscedasticity in regression. *Biometrika* **1983** 70(1):1–10.

- [219] B. S. Perrin and R. W. Pastor. Simulations of membrane-disrupting peptides I: alamethicin pore stability and spontaneous insertion. *Biophys. J.* **2016** 111(6):1248–1257.
- [220] P. W. Hildebrand, S. Günther, A. Goede, L. Forrest, C. Frömmel, and R. Preissner. Hydrogen-bonding and packing features of membrane proteins: Functional implications. *Biophys. J.* **2008** 94(6):1945–1953.
- [221] T. Kim and W. Im. Revisiting hydrophobic mismatch with free energy simulation studies of transmembrane helix tilt and rotation. *Biophys. J.* **2010** 99(1):175–183.
- [222] S. Stolzenberg, M. Michino, M. V. LeVine, H. Weinstein, and L. Shi. Computational approaches to detect allosteric pathways in transmembrane molecular machines. *BBA - Biomembranes* **2016** 1858(7, Part B):1652–1662.
- [223] G. Schwarz, S. Stankowski, and V. Rizzo. Thermodynamic analysis of incorporation and aggregation in a membrane: Application to the pore-forming peptide alamethicin. *BBA - Biomembranes* **1986** 861:141–151.
- [224] G. Schwarz, H. Gerke, V. Rizzo, and S. Stankowski. Incorporation kinetics in a membrane, studied with the pore-forming peptide alamethicin. *Biophys. J.* **1987** 52(5):685–692.
- [225] A. Arbuzova and G. Schwarz. Pore-forming action of mastoparan peptides on liposomes: A quantitative analysis. *BBA - Biomembranes* **1999** 1420(1):139–152.
- [226] A. S. Ladokhin, S. Jayasinghe, and S. H. White. How to measure and analyze tryptophan fluorescence in membranes properly, and why bother? *Anal. Biochem.* **2000** 285(2):235–245.
- [227] W. C. Wimley and S. H. White. Determining the membrane topology of peptides by fluorescence quenching. *Biochemistry* **2000** 39(1):161–170.
- [228] T. D. Bradrick and S. Georgiou. Kinetics of melittin-induced fusion of dipalmitoylphosphatidylcholine small unilamellar vesicles. *BBA - Biomembranes* **1987** 905(2):494–498.
- [229] H. W. Huang, F. Y. Chen, and M. T. Lee. Molecular mechanism of peptide-induced pores in membranes. *Phys. Rev. Lett.* **2004** 92(19):198304–1.
- [230] W. Helfrich. Elastic properties of lipid bilayers: Theory and possible experiments. *Z. Naturforsch. C* **1973** 28(11):693–703.
- [231] H. W. Huang. Deformation free energy of bilayer membrane and its effect on gramicidin channel lifetime. *Biophys. J.* **1986** 50(6):1061–1070.

- [232] Y. Wu, K. He, S. J. Ludtke, and H. W. Huang. X-ray diffraction study of lipid bilayer membranes interacting with amphiphilic helical peptides: diphytanoyl phosphatidyl-choline with alamethicin at low concentrations. *Biophys. J.* **1995** 68(6):2361–2369.
- [233] H. W. Huang and Y. Wu. Lipid-alamethicin interactions influence alamethicin orientation. *Biophys. J.* **1991** 60(5):1079–1087.
- [234] K. He, S. J. Ludtke, H. W. Huang, and D. L. Worcester. Antimicrobial peptide pores in membranes detected by neutron in-plane scattering. *Biochemistry* **1995** 34(48):15614–15618.
- [235] K. He, S. J. Ludtke, W. T. Heller, and H. W. Huang. Mechanism of alamethicin insertion into lipid bilayers. *Biophys. J.* **1996** 71(5):2669–2679.
- [236] M. Pawlak, S. Stankowski, and G. Schwarz. Melittin induced voltage-dependent conductance in DOPC lipid bilayers. *BBA - Biomembranes* **1991** 1062(1):94–102.
- [237] G. Klocek, T. Schulthess, Y. Shai, and J. Seelig. Thermodynamics of melittin binding to lipid bilayers. Aggregation and pore formation. *Biochemistry* **2009** 48(12):2586–2596.
- [238] A. Hermetter and J. R. Lakowicz. The aggregation state of mellitin in lipid bilayers. An energy transfer study. *J. Biol. Chem.* **1986** 261(18):8243–8248.
- [239] E. Pérez-Payá, J. Dufourcq, L. Braco, and C. Abad. Structural characterisation of the natural membrane-bound state of melittin: A fluorescence study of a dansylated analogue. *BBA - Biomembranes* **1997** 1329(2):223–236.
- [240] S. Ludtke, K. He, and H. Huang. Membrane thinning caused by magainin 2. *Biochemistry* **1995** 34(51):16764–16769.
- [241] C.-C. Lee, Y. Sun, S. Qian, and H. W. Huang. Transmembrane pores formed by human antimicrobial peptide LL-37. *Biophys. J.* **2011** 100(7):1688–1696.
- [242] E. S. Salnikov, J. Raya, M. De Zotti, E. Zaitseva, C. Peggion, G. Ballano, C. Toniolo, J. Raap, and B. Bechinger. Alamethicin supramolecular organization in lipid membranes from (19)F solid-state NMR. *Biophys. J.* **2016** 111(11):2450–2459.
- [243] V. N. Syryamina, M. De Zotti, C. Toniolo, F. Formaggio, and S. A. Dzuba. Alamethicin self-assembling in lipid membranes: Concentration dependence from pulsed EPR of spin labels. *Phys. Chem. Chem. Phys.* **2018** 20(5):3592–3601.
- [244] Y. Wang, T. Zhao, D. Wei, E. Strandberg, A. S. Ulrich, and J. P. Ulmschneider. How reliable are molecular dynamics simulations of membrane active antimicrobial peptides? *BBA* **2014** 1838(9):2280–2288.

- [245] S. J. Irudayam and M. L. Berkowitz. Binding and reorientation of melittin in a POPC bilayer: Computer simulations. *BBA* **2012** 1818(12):2975–2981.
- [246] C. Kempf, R. D. Klausner, J. N. Weinstein, J. Van Renswoude, M. Pincus, and R. Blumenthal. Voltage-dependent trans-bilayer orientation of melittin. *J. Biol. Chem.* **1982** 257(5):2469–2476.
- [247] S. Y. Woo and H. Lee. Aggregation and insertion of melittin and its analogue MelP5 into lipid bilayers at different concentrations: effects on pore size, bilayer thickness and dynamics. *Phys. Chem. Chem. Phys.* **2017** 19(10):7195–7203.
- [248] M. Andersson, J. P. Ulmschneider, M. B. Ulmschneider, and S. H. White. Conformational states of melittin at a bilayer interface. *Biophys. J.* **2013** 104(6):12–14.
- [249] S. K. Upadhyay, Y. Wang, T. Zhao, and J. P. Ulmschneider. Insights from Microsecond Atomistic Simulations of Melittin in Thin Lipid Bilayers. *J. Membr. Biol.* **2015** 248(3):497–503.
- [250] Y. Hu, S. Ou, and S. Patel. Free energetics of arginine permeation into model DMPC lipid bilayers: Coupling of effective counterion concentration and lateral bilayer dimensions. *J. Phys. Chem. B* **2013** 117(39):11641–11653.
- [251] Y. Hu, S. K. Sinha, and S. Patel. Reconciling structural and thermodynamic predictions using all-atom and coarse-grain force fields: the case of charged oligo-arginine translocation into DMPC bilayers. *J. Phys. Chem. B* **2014** 118(41):11973–11992.
- [252] M. Schumann, M. Dathe, T. Wieprecht, M. Beyermann, and M. Bienert. The tendency of magainin to associate upon binding to phospholipid bilayers. *Biochemistry* **1997** 36(14):4345–4351.
- [253] S. E. Blondelle and R. A. Houghten. Hemolytic and antimicrobial activities of the twenty-four individual omission analogs of melittin. *Biochemistry* **1991** 30(19):4671–4678.
- [254] A. Masunov and T. Lazaridis. Potentials of mean force between ionizable amino acid side chains in water. *JACS* **2003** 125(7):1722–1730.
- [255] J. Lee, S. Ham, and W. Im. Beta-hairpin restraint potentials for calculations of potentials of mean force as a function of beta-hairpin tilt, rotation, and distance. *J. Comp. Chem.* **2009** 28(1):73–86.
- [256] O. Yuzlenko and T. Lazaridis. Interactions between ionizable amino acid side chains at a lipid bilayer-water interface. *J. Phys. Chem. B* **2011** 115(46):13674–13684.
- [257] V. Mirjalili and M. Feig. Interactions of amino acid side-chain analogs within membrane environments. *J. Phys. Chem. B* **2015** 119(7):2877–2885.

- [258] J. Domański, M. S. P. Sansom, P. J. Stansfeld, and R. B. Best. Balancing force field protein-lipid interactions to capture transmembrane helix-helix association. *J. Chem. Theory Comput.* **2018** 14(3):1706–1715.
- [259] G. Wiedman, T. Fuselier, J. He, P. C. Searson, K. Hristova, and W. C. Wimley. Highly efficient macromolecule-sized poration of lipid bilayers by a synthetically evolved peptide. *JACS* **2014** 136(12):4724–4731.
- [260] W. R. Fiori, K. M. Lundberg, and G. L. Millhauser. A single carboxy-terminal arginine determines the amino-terminal helix conformation of an alanine-based peptide. *Nat. Struct. Biol.* **1994** 1(6):374–377.
- [261] J. Lee and W. Im. Role of hydrogen bonding and helix-lipid interactions in transmembrane helix association. *JACS* **2008** 130(20):6456–6462.
- [262] I. Z. Steinberg and H. A. Scheraga. Entropy changes accompanying association reactions of proteins. *J. Biol. Chem.* **1963** 238:172–181.